Variational approach to model fracture in viscoelastic materials of bituminous type

Rajasekar Gopalsamy

MEMOIRE DE DOCTORAT DE

L'ECOLE CENTRALE DE NANTES

ECOLE DOCTORALE N° 602
Sciences de l'Ingénierie et des Systèmes
Spécialité : *Génie Mécanique*

Par
Rajasekar GOPALSAMY

Variational approach to model fracture in viscoelastic materials of bituminous type

Projet de recherche doctoral présenté et soutenu à l'Université Gustave Eiffel, Campus de Nantes le 8 décembre 2023

Unité de recherche : Département MAST-LAMES, Université Gustave Eiffel, Campus de Nantes

Rapporteurs avant soutenance :

Gilles PIJAUDIER-CABOT	Professeur des universités, Université Pau et Pays de l'Adour
Eshan V.DAVE	Full professor, University of New Hampshire, États-Unis

Composition du Jury :

Présidente	:	Véronique LAZARUS	Professeure des universités, ENSTA Paris
Examinateurs	:	Gilles PIJAUDIER-CABOT	Professeur des universités, Université Pau et Pays de l'Adour
		Eshan V.DAVE	Full professor, University of New Hampshire, États-Unis
		Frédéric DUBOIS	Professeur des universités, Université de Limoges
		Nicolas MOËS	Professeur des universités, École Centrale de Nantes

Directeur de recherches doctorales	:	Ferhat HAMMOUM, Directeur de recherche, Université Gustave Eiffel, Campus de Nantes
Co-enc. de recherches doctorales	:	Olivier CHUPIN, Chargé de recherche, Université Gustave Eiffel, Campus de Nantes
Co-enc. de recherches doctorales	:	Nicolas CHEVAUGEON, Maître de conférences HDR, École Centrale de Nantes

ACKNOWLEDGEMENT

I extend my heartfelt gratitude to my parents and my sister for their unwavering support, and to my supervisor and advisors for their invaluable guidance and assistance throughout my doctoral journey.
I am also grateful for the opportunities and blessings that the universe has bestowed upon me.

Abstract

The deterioration of pavement due to the fracturing of layers made of bituminous materials is a significant challenge, necessitating a deeper understanding of the associated mechanisms and factors. Addressing this issue involves the development of essential theoretical models and numerical tools. Bituminous materials are widely acknowledged for their viscoelastic characteristics, forming the core focus of this thesis. In this context, the present thesis focuses on the cracking of viscoelastic materials in a quasi-static setting. A novel, thermodynamically consistent variational approach is introduced to model damage within viscoelastic solids. This approach enables the integration of local constitutive equations into a global incremental potential, the minimization of which yields the solution to the mechanical problem. To overcome the spurious mesh-dependent results associated with softening damage models, the lip-field approach has been used to regularize the problem. A detailed numerical implementation for both one-dimensional (1D) and two-dimensional (2D) scenarios is presented, complemented by Python-based finite element (FE) codes (link to code). The simulation results for the 2D case show the ability of the model to fit experimental force-displacement curves (for mode-I fracture) and to predict the crack paths (for mixed mode fracture). This work not only provides a robust theoretical and numerical foundation for potential future applications in pavement mechanics but also extends its relevance beyond bituminous materials. The methodology developed here can be applied effectively to model cracking in various viscoelastic materials.

Keywords : Damage, Fracture, Viscoelasticity, Lip-field approach, Bituminous materials, Variational approach

Résumé

La détérioration des chaussées due à la fissuration des couches de matériaux bitumineux représente un défi majeur, nécessitant une compréhension plus approfondie des mécanismes et des facteurs associés. Aborder cette problématique implique le développement de modèles théoriques dédiés et leur implémentation dans des outils numériques. Les matériaux bitumineux sont largement reconnus pour leurs caractéristiques viscoélastiques. Dans ce contexte, la présente thèse se concentre sur la fissuration des matériaux viscoélastiques dans un cadre quasi-statique. Une nouvelle approche variationnelle thermodynamiquement cohérente est introduite pour modéliser l'endommagement dans les solides viscoélastiques. Cette approche permet l'intégration des équations constitutives locales dans un potentiel global incrémental, dont la minimisation conduit à la résolution du problème mécanique. Afin de surmonter les problèmes de dépendance au maillage associés aux modèles d'endommagement adoucissants, l'approche du lip-field a été utilisée pour régulariser le problème. Une mise en œuvre numérique dans des codes à éléments finis (FE) basés sur Python (lien pour le code) est présentée pour des scénarios à une dimension (1D) et à deux dimensions (2D). Les résultats de simulation pour le cas en 2D démontrent la capacité du modèle à reproduire les courbes force-déplacement expérimentales (pour la rupture en mode I) et à prédire les trajectoires de fissuration (pour la rupture en mode mixte). Ce travail fournit non seulement une base théorique et numérique solide pour d'éventuelles applications futures en mécanique des chaussées, mais étend également sa pertinence au-delà des matériaux bitumineux. La méthodologie développée ici peut être efficacement utilisée pour modéliser la fissuration dans divers matériaux viscoélastiques.

Mots clés : Endommagement, Fissuration, Viscoélasticité, Lip-field, Matériaux bitumineux, Approche variationnelle

Table of Contents

List of acronyms

AM	Alternate Minimization
BBR	Bending Beam Rheometer
CDM	Continuum Damage Mechanics
CMOD	Crack Mouth Opening Displacement
CTOD	Crack Tip Opening Displacement
COV	Coefficient Of Variation
CZ(M)	Cohesive Zone (Model)
DCT	Disc-shaped Compact Tension test
DMA	Dynamic Mechanical Analysis
DSR	Dynamic Shear Rheometer
DTT	Direct Tensile Test
FAM	Fine Aggregate Matrix
FPZ	Fracture Process Zone
GKV	Generalized Kelvin-Voigt model
GM	Generalized Maxwell model
ITT	Indirect Tensile Test
KV	Kelvin-Voigt model
LEFM	Linear Elastic Fracture Mechanics
LF	Lip-Field approach
LSA	Linear Stability Analysis
ODE	Ordinary Differential Equation(s)
PF	Phase-Field approach
PDE	Partial Differential Equation(s)
SE(N)B	Single Edge Notched Beam
SCB	Semi Circular Beam
SIF	Stress Intensity Factor
SHRP	Strategic Highway Research Program
TLS	Thick Level Set approach
TTSP	Time-Temperature Superposition Principle
WLF	Williams–Landel–Ferry equation
X-FEM	eXtended-Finite Element Method

List of Figures

List of Tables

INTRODUCTION

In this thesis, our focus lies in the numerical simulation of the mechanical response of viscoelastic materials subjected to fracture, specifically those of the bituminous type. This manuscript presents a compilation of the models developed and the outcomes obtained over the course of three years. The present work is the result of collaboration between the Laboratoire Auscultation, Modélisation, Expérimentation des infrastructures de transport (LAMES) at Université Gustave Eiffel (Nantes) and the laboratory of Génie civil et Mécanique (GeM) at École Centrale de Nantes. The French road network covers over 1 million kilometers, making it one of the densest in Europe. With an estimated value of 2,000 billion euros, the road network represents a primary asset of the state government. Consequently, substantial financial resources are allocated each year for the maintenance and management of this existing infrastructure. Hence, pavement maintenance studies are conducted to ensure efficient maintenance and management practices, resulting in improved safety, reduced deterioration, and cost-effectiveness. Estimating the residual life of pavements is a crucial aspect of pavement maintenance studies. This thesis primarily focuses on this aspect, although the work done during the thesis is still in its early stages concerning anticipated future applications. The main objective is to develop physical models and code them to study crack initiation and propagation in structures composed of materials exhibiting thermo-viscoelastic rheology, characteristic of bituminous materials. It is important to note that this thesis specifically addresses monotonous loadings and does not encompass fatigue aspects resulting from repeated mechanical loading or climatic stresses. The tools developed in this study can initially be applied to analyze cracking tests conducted on bituminous materials in a laboratory setting, considering different conditions such as geometry, loading speed, and temperature. In particular, the interest was limited to developing variational approaches to model fracture in viscoelastic materials, within the framework of damage mechanics. However, such local models are mathematically ill-posed and result in strain localization (or damage accumulation) on a mathematical plane (plane of zero thickness). Consequently, when implemented in finite element codes, the region where damage concentrates becomes dependent on the characteristic length scale of the finite elements, leading to spurious mesh-dependent results. Introducing length scales into the model is often necessary to address this issue. In this regard, we rely on the Lip-field approach, recently developed at the GeM laboratory of École Centrale de Nantes. This approach has been shown in the literature to provide satisfactory

results for brittle fracture in elastic solids under quasi-static conditions. Additionally, the Lip-field approach and its mathematical properties enable efficient computation of damage fields, thereby reducing computational effort. This thesis thus also contributes to extending the Lip-field approach to the field of viscoelastic media, an area not previously addressed in the existing literature.

Here's a comprehensive summary of the manuscript: In the first chapter (Chapter 1), we discuss the mechanical properties of viscoelastic materials (of bituminous type) and the phenomena associated with these materials during rupture tests under monotonous loading. Additionally, we explore relevant references from the bibliography that are considered valuable for understanding the subsequent chapters. We also present different rheological models that aid in modeling the linear viscoelastic behavior. The Cohesive Zone Model (CZM) and various non-local damage models are also examined before detailing the Lip-field approach. This section thus includes selective state-of-the-art information. Chapter 2 deals with the development of a thermodynamically consistent viscoelastic damage model. In particular, a variational approach has been proposed, which results in seeking solutions to an optimization problem. To overcome the aforementioned problem of mesh sensitivity associated with softening damage models, Lipschitz regularization has been used to introduce a length scale into the model. Chapter 3 is dedicated to the development of a variational framework for fracture in viscoelasticity in the case of a homogeneous bar in one dimension (1D). The viscoelastic behavior is represented using a spectral approach by considering both the Generalized Kelvin-Voigt (GKV) model and the Generalized Maxwell (GM) model. We then present the numerical implementation followed by validation with analytical solutions. The simulation results reveal the homogeneous evolution of damage (where the damage does not localize) initially for both models. A Lyapunov stability analysis was performed to understand the aforementioned phenomenon. which indicates the presence of an intrinsic time scale associated with damage. Chapter 4 focuses on extending the variational framework for viscoelastic fracture from one dimension (1D) to two dimensions (2D). To prevent cracks in compression (unilateral effects), we propose an asymmetric tension/compression split of the free energy for the GKV model. The numerical implementation is then presented, followed by validation of the numerical implementation. Having the numerical implementation validated, Chapter 5 deals with calibrating the model with experimental results for fracture in bituminous mortar mix. Simulation results show the ability of the model to fit experimental force-displacement curves under different loading rates for mode-I fracture. The crack path predicted by the model for the case of mixed-mode fracture was also found to be in good agreement with the experiments. The work accomplished during this thesis opens up numerous perspectives and possibilities for future research, which are presented in the conclusion.

Chapter 1

Literature review

1.1 Overview of pavements and bituminous materials

The road pavement structure refers to the layers of materials that are constructed on the ground to provide a durable and stable surface for vehicles to travel on. It plays a crucial role in supporting transportation networks and facilitating economic growth within a country. The most commonly used pavement structure is of flexible type. Figure 1.1 displays the various layers of the flexible pavement structure.

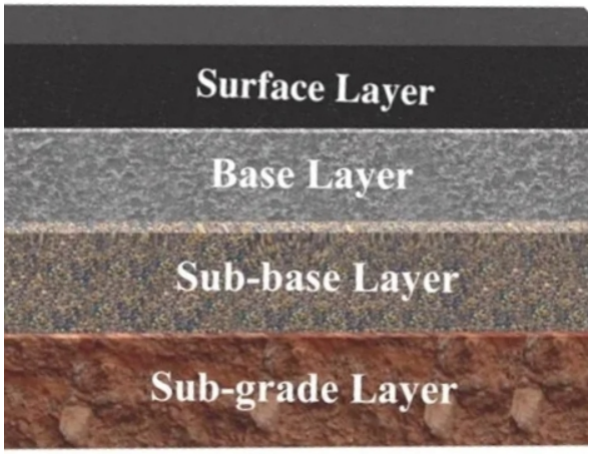

Figure 1.1 – Structure of flexible pavement (Image source)

The functions of the different layers are listed below:

1. Sub-grade: The sub-grade is the natural soil or compacted layer beneath the pavement layers. Its function is to provide support to the entire pavement structure. The sub-grade layer should have sufficient strength to bear the load of the traffic and distribute it evenly to prevent excessive deformation or settlement.
2. Sub-base course: The sub-base course layer, located above the sub-grade, serves as a transition between the sub-grade and the base course. It helps distribute the load from the

traffic and provides additional support to the upper layers. The sub-base layer also aids in drainage, preventing the accumulation of water within the pavement structure.

3. Base Course: The base course is a layer of granular or stabilized material placed above the sub-base. Its primary function is to provide structural support to the upper layers and distribute the traffic load. The base course helps to evenly distribute the load, reducing the stresses on the sub-grade layer and improving the overall stability of the pavement.

4. Surface Course: The surface course is the topmost layer of the pavement structure, directly in contact with the traffic. Its function is to provide a smooth, durable, and skid-resistant driving surface. The surface course protects the underlying layers from the effects of traffic loads, weathering, and environmental factors. It also provides adequate friction for vehicle tires and contributes to road safety.

For the flexible pavement structure, the surface coarse is made up of *bituminous materials*. The thesis does not primarily focus on analyzing the overall structure and dimensioning of an entire pavement. Instead, it concentrates only on examining the surface layer composed of bituminous materials. Specifically, the research investigates the behaviors and damage caused by cracks in these layers under monotonic loading.

1.1.1 Composition of bituminous materials

Bituminous materials (also called '*asphalt*') used for the construction of road surfaces are complex mixtures primarily composed of bitumen (hydrocarbon binder), aggregates, and additives. The composition of bituminous materials can vary depending on the specific application and desired performance characteristics. Figure 1.2 displays the composition of the bituminous materials. Here's an elaboration on the components:

- Bitumen: Bitumen is the binder or glue-like material that holds the aggregates together in bituminous mixtures. It is a sticky, black, viscous substance derived from petroleum refining or natural deposits. Bitumen consists of hydrocarbon compounds, predominantly made up of complex chains of carbon and hydrogen atoms. It provides the waterproofing, adhesive, and cohesive properties necessary for the durability and strength of the pavement. These bitumens are grouped into two large families according to their chemical compositions, namely asphaltenes (a mixture of hydrogen and carbon) and maltenes (a mixture of resins and saturated oils)

- Aggregates: Aggregates are granular materials mixed with bitumen to form the bulk of the bituminous mixture. They include crushed stones, sand, gravel, and mineral fillers. Aggregates serve multiple functions, such as providing structural strength, improving load distribution, enhancing stability, and contributing to the overall texture and skid resistance

of the pavement. The size, shape, and gradation of aggregates influence the properties of the bituminous mixture.

- ✻ Additives: Various additives can be incorporated into bituminous materials to modify specific properties or improve performance. Common additives include fillers such as limestone powder and polymers to enhance their properties (increase resistance to aging, improve heat stability, increase elasticity, etc.)[1].

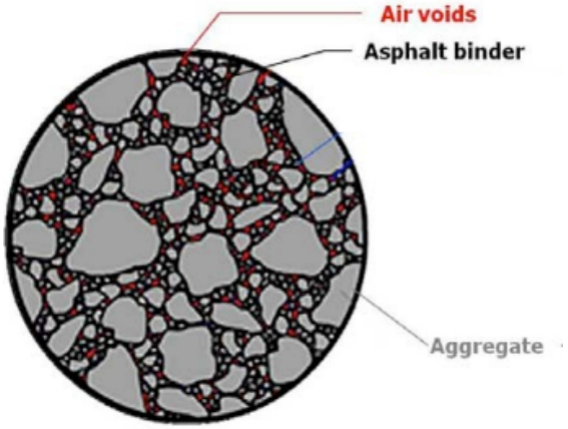

Figure 1.2 – Major composition of bituminous materials [2]

The precise composition and proportions of bituminous materials are determined through laboratory testing, mix design procedures, and consideration of project-specific requirements. The selection of appropriate components and additives aims to achieve the desired performance characteristics, such as strength, flexibility, durability, resistance to deformation and cracking, and suitability for specific climate conditions.

In the course of the thesis, our interest was limited to studying the fracture behavior in bituminous materials composed of fine aggregates (often referred to as Fine Aggregate Matrix (FAM) or matrix). For example, in [3], [4], the authors consider aggregates of size less than 0.6 mm as fine aggregates. In Figure 1.2, we can group the composition into FAM, air voids, and coarse aggregates, where the FAM is composed of asphalt binder and fine aggregates. Though the matrix (FAM) differs from conventional pavement mixtures used practically, its study is pivotal for multiple reasons as highlighted in [4].

1. First, the matrix is one of three primary phases of a surface layer of pavement structure along with the coarse aggregates and air voids. Moreover, in most cases (particularly at intermediate temperatures without moisture damage) the fracture occurs in matrix phase [4], while the coarse aggregate exhibits a relatively rigid behavior (tending to interlock and slide). Therefore, it is the matrix phase that needs to be properly examined for understanding the fracture behavior of conventional pavement structures.

2. Secondly, the testing of the matrix phase offers significantly improved repeatability and efficiency compared to the testing of extensively heterogeneous bituminous composites as used in pavement structures.

3. Finally, the model developed for the matrix phase can be employed in a highly heterogeneous bituminous composite mixture, by accounting for the behavior of individual components of the mixture [5], [6].

1.1.2 Mechanical behavior of bituminous materials

As previously mentioned, bitumen possesses a high viscosity. The behavior of bitumen is strongly influenced by temperature and loading due to its viscous nature. Figure 1.3 summarizes the various mechanical behavior of bitumen as a function of temperature T and strain ε.

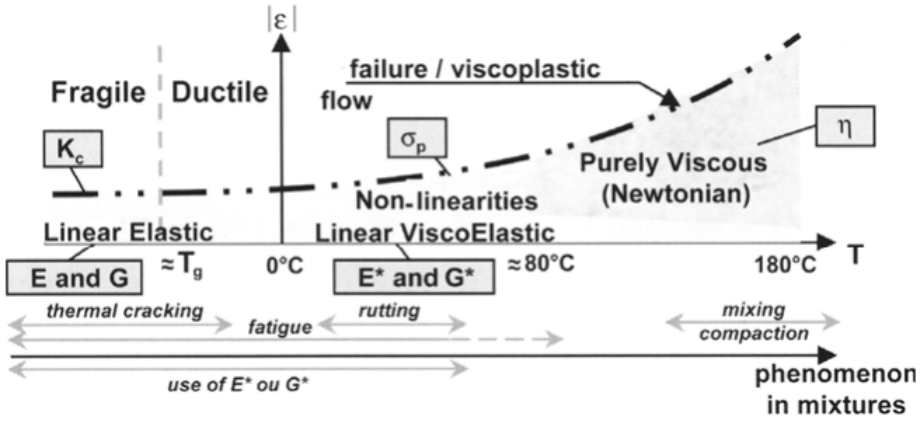

Figure 1.3 – Typical behaviour of bitumen at different temperatures T[7]

For small deformations, it can be seen from Figure 1.3 that the bitumen exhibits linear elastic behavior at low temperatures and behaves like a Newtonian fluid at elevated temperatures. In the intermediate temperatures, a viscoelastic behavior is observed.

The combination of aggregates and bitumen imparts the viscoelastic characteristics of asphalt (or bituminous materials). Figure 1.4 displays the different behavior of asphalt as a function of the number of loading cycles N and the amplitude of the strain ε.

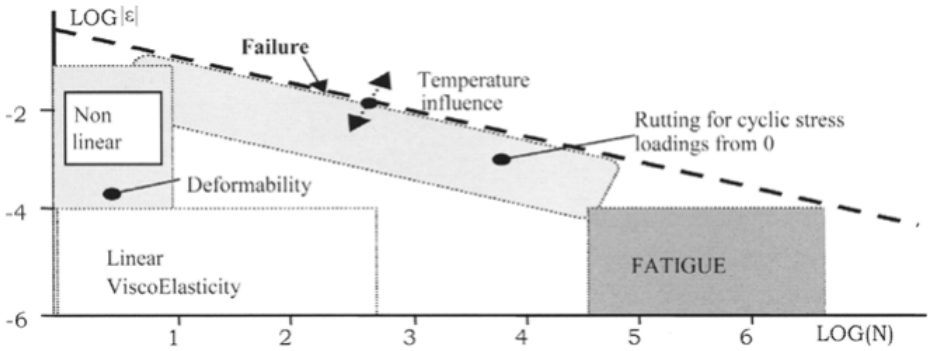

Figure 1.4 – Mechanical behavior of asphalt as a function of the number of loading cycles N [8]

The behavior of asphalt can be classified into 4 major classes as follows [8]:

Linear viscoelastic behavior This behavior is observed when the number of loading cycles is low (less than 300) and the deformation level is considered small (less than 10^{-4}). Linear viscoelasticity refers to the ability of a material to exhibit both elastic and viscous responses under loading. In the case of asphalt mixes, this behavior class is often associated with the bituminous component. The properties of linear viscoelasticity can be characterized using specific laboratory tests.

Nonlinear behavior This behavior class is characterized by a deformation level of a few percent, which is higher compared to the weak deformation observed in the linear viscoelastic behavior. However, the nonlinear behavior is observed for a very low number of loading cycles. In this case, the material exhibits a non-proportional response, meaning the stress and strain relationship is not linear. The underlying mechanisms causing this behavior can vary, and it can have implications for the performance and durability of asphalt mixes.

Fatigue behavior Fatigue is observed when the material experiences failure under repeated loading cycles, typically around 10^4 cycles. Despite the deformation being relatively weak, the accumulated cyclic loading leads to progressive damage and eventually failure. Fatigue behavior is a significant concern in asphalt pavements as it can result in cracking and reduced structural integrity over time. Understanding the fatigue properties of asphalt mixes is crucial for designing long-lasting and resilient pavements [9].

Rutting behavior This behavior class is associated with the appearance of deformations that accumulate over time, leading to the phenomenon of rutting. Rutting refers to the permanent deformation or depression in the surface of a pavement caused by the repetitive load of traffic.

The thesis focuses in particular on modeling the fracture behavior of asphalt in the small strain region from low to intermediate temperature (Figure 1.3) and for monotonous loading conditions

(Figure 1.4). In the considered region, the asphalt behavior can be adequately modeled by a *linear viscoelastic response*. In the subsequent sections, the discussion will focus on the linear viscoelastic behavior of asphalt mixes and the laboratory tests used to characterize this particular behavior. These tests are essential for understanding the mechanical properties of asphalt mixes and informing their design and performance in various applications.

1.2 Linear viscoelastic behavior

In this section, we aim to present a concise overview of linear viscoelastic behavior and the methodologies employed to assess it. The reader may refer to [10] for a comprehensive review of the content covered here.

1.2.1 Creep compliance and Relaxation modulus

Creep compliance Consider the response of a linear viscoelastic material subjected to constant stress σ_0 loaded from time $t = 0$ as represented in Figure 1.5a. The loading history is then represented as follows:

$$\sigma(t) = \sigma_0 \, H_s(t) \tag{1.1}$$

where $H_s(t)$ is the unit or Heaviside step function and its expression is given by

$$H_s(t) = \begin{cases} 0, & \text{if } t < 0 \\ 1, & \text{if } t \geq 0 \end{cases} \tag{1.2}$$

The response of the material can then be given by

$$\varepsilon(t) = D_c(t) \, \sigma_0 \tag{1.3}$$

where $D_c(t)$ is the creep compliance function. Creep compliance measures the ability of a material to deform or creep under a constant or sustained applied stress over time. It quantifies the strain response of a material to constant stress as a function of time. Creep compliance is commonly measured in experiments such as the bending beam rheometer (BBR) test [11].

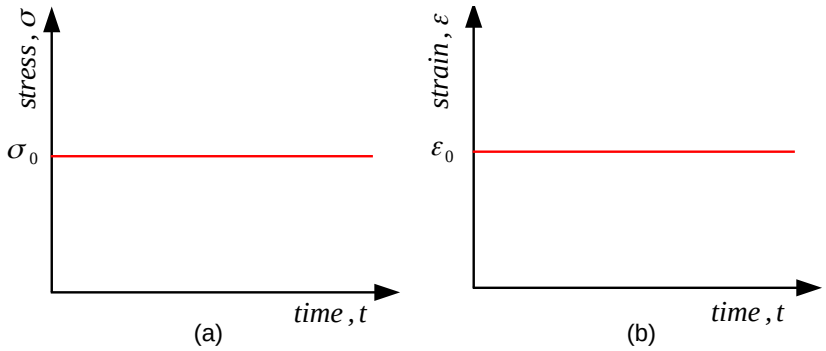

Figure 1.5 – (a) Constant stress input and (b) constant strain input

Relaxation modulus When the material is subjected to the following constant strain (see Figure 1.5b)

$$\varepsilon = \varepsilon_0 \, H_s(t) \tag{1.4}$$

the stress is then given by

$$\sigma = E(t) \, \varepsilon_0 \tag{1.5}$$

where $E(t)$ is the relaxation modulus. Relaxation modulus measures the ability of a material to relax or recover from a given strain. It quantifies the stress response of a material to a constant strain as a function of time. Relaxation modulus is commonly measured in experiments such as the dynamic shear rheometer (DSR) test [12].

1.2.2 Boltzmann Superposition Principle

In the previous section, creep compliance and relaxation modulus are used to find the strain and stresses only for the constant values of applied stresses and strains. Boltzmann superposition integral [13] provides the relation between stress and strain for variable input functions of stresses and strain.

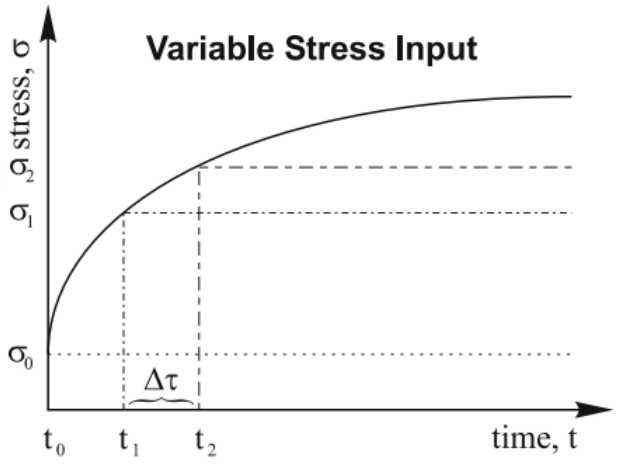

Figure 1.6 – A variable stress input as a function of time [10]

Consider a variable stress input $\sigma(t)$ as shown in Figure 1.6. The variable stress input $\sigma(t)$ can be approximated as a series of step functions as follows:

$$\sigma(t) = \sigma_0 H_s(t) + (\sigma_1 - \sigma_0)H_s(t - t_1) + ... + (\sigma_n - \sigma_{n-1})H_s(t_n - t_{n-1}) \tag{1.6}$$

where $\Delta\tau = t_n - t_{n-1}$. Because the material is assumed to be linear viscoelastic, the strain response can then be written as a series of step outputs for each step input (by using Eq. (1.3)) as follows

$$\varepsilon(t) = \sigma_0 D_c(t)H_s(t) + \sum_{i=1}^{n}(\sigma_i - \sigma_{i-1})D_c(t_i - t_{i-1})H_s(t_i - t_{i-1}) \tag{1.7}$$

For the limit $\Delta\tau \to 0$, the strain response can be written in the following integral form [10]

$$\varepsilon(t) = \sigma_0 D_c(t)H_s(t) + \int_{0^+}^{t} D_c(t - \tau)\frac{d\sigma(\tau)}{d\tau}d\tau = \int_{0}^{t} D_c(t - \tau)\frac{d\sigma(\tau)}{d\tau}d\tau \tag{1.8}$$

where $t = 0$ implies that the lower limit starts from time $t = 0^-$, thus allowing for the inclusion of any initial discontinuities. Similarly, for a variable strain input, the stress is given by

$$\sigma(t) = \int_{0}^{t} E(t - \tau)\frac{d\varepsilon(\tau)}{d\tau}d\tau \tag{1.9}$$

The relation between stress and strain given by the above expressions for integrals is also called the *Hereditary integral*. The above equations can also be written as the convolution of the creep

compliance function (or relaxation function) and stress rate (or strain rate) as follows:

$$\varepsilon(t) = (D_c * \dot{\sigma})(t) \tag{1.10a}$$

$$\sigma(t) = (E * \dot{\varepsilon})(t) \tag{1.10b}$$

where $*$ is the convolution of two functions. The above equations describe the constitutive law for a viscoelastic material.

As bituminous materials undergo the aging process, every event throughout their history contributes to the present state of stress and strain. Hence most often, the lower limit of the hereditary integral is taken as $t = -\infty$ as follows

$$\sigma(t) = \int_{-\infty}^{t} E(t-\tau)\frac{d\varepsilon(\tau)}{d\tau}d\tau \tag{1.11}$$

A material can be classified as non-aging if its mechanical properties do not evolve over time in the absence of mechanical stress. This means that the material's behavior remains time-invariant or unchanged when there is a translation on the time axis as shown in Figure 1.7.

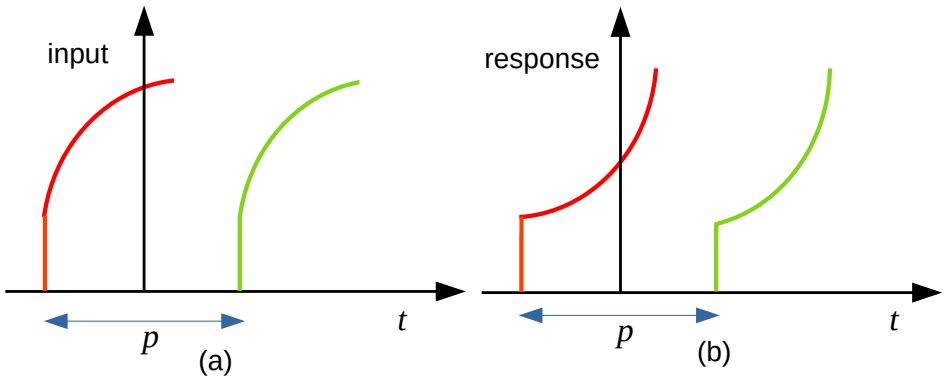

Figure 1.7 – Non-ageing viscoelastic material. (a) same inputs applied at time gap p produce (b) same response separated by time gap p

1.2.3 Relaxation and creep functions in frequency domain

Due to the occurrence of convolution integral (in Eq. (1.10)) in viscoelastic constitutive law, the Laplace transform can be used to convert the integrals (in the time domain) into multiplication (in the frequency domain). The Laplace transform of a function $f(t)$ is defined as follows:

$$\mathcal{L}\{f(t)\} = \overline{f}(s) = \int_0^{\infty} f(t)e^{-st}dt \tag{1.12}$$

where s is a complex variable (in the complex frequency domain). The Laplace transform of the time t, the time derivative of $f(t)$ (indicated as $f'(t)$) and the convolution of two functions $f(t)$ and $g(t)$ (indicated as $f * g$) can be derived using the Laplace transform definition provided above to yield the following results:

$$\mathcal{L}\{t\} = \frac{1}{s^2} \tag{1.13a}$$

$$\mathcal{L}\{f'(t)\} = s\overline{f}(s) - f(0) \tag{1.13b}$$

$$\mathcal{L}\{(f * g)(t)\} = \overline{f}(s)\overline{g}(s) \tag{1.13c}$$

By using Eq. (1.13), the Laplace transform of Eq. (1.10) can be written as follows

$$\overline{\varepsilon}(s) = s\overline{D}_c(s)\overline{\sigma}(s) = \overline{D}_c^*(s)\overline{\sigma}(s) \tag{1.14a}$$

$$\overline{\sigma}(s) = s\overline{E}(s)\overline{\varepsilon}(s) \quad = \overline{E}^*(s)\overline{\varepsilon}(s) \tag{1.14b}$$

where $\overline{E}(s)$ and $\overline{D}_c(s)$ are the Laplace transform of the relaxation modulus and creep compliance respectively, while $\overline{E}^*(s)$ and $\overline{D}_c^*(s)$ represents the *transformed relaxation modulus* and *transformed creep compliance*:

$$\overline{E}^*(s) = s\overline{E}(s) \tag{1.15a}$$

$$\overline{D}_c^*(s) = s\overline{D}_c(s) \tag{1.15b}$$

Note that the following holds from Eq. (1.14)

$$\overline{E}^*(s)\overline{D}_c^*(s) = 1 \tag{1.16}$$

On application of the inverse Laplace transform (using Eq. (1.13)) to the above equation yields

$$\int_0^t E(t)D_c(t-\tau)d\tau = \int_0^t E(t-\tau)D_c(t)d\tau = t \tag{1.17}$$

The above equation shows that the relaxation modulus and creep compliance are not reciprocals of each other (unlike elastic material). However, in the frequency domain (see Eq. (1.16)), the reciprocity holds. Moreover, the relation between stress and strain in the frequency domain (Eq. (1.14)) is similar to the relation in elasticity. Alfrey's correspondence principle makes use of this to find the solution to the linear viscoelastic problem by solving an equivalent elastic problem in the frequency domain, and inverting back the solution to the time domain [14], [10].

The relationship between time-dependent modulus and complex modulus is obtained by substi-

tuting $\varepsilon(t) = \varepsilon^* = \varepsilon_0 e^{i\omega t}$ in Eq. (1.11).

$$\sigma^* = i\omega\varepsilon_0 \left(\int_{-\infty}^{t} E(t-\tau) e^{i\omega\tau} d\tau \right) \tag{1.18}$$

where $i = \sqrt{-1}$ and ω denotes the frequency. By applying the change of variables $z = t - \tau$ in the above equation, we obtain the following

$$\sigma^* = \varepsilon_0 e^{i\omega t} \left(i\omega \int_0^{\infty} E(z) e^{-i\omega z} dz \right) \tag{1.19}$$

$$= \varepsilon^* \qquad (E^*(i\omega)) \tag{1.20}$$

where

$$E^*(i\omega) = i\omega \int_0^{\infty} E(t) e^{-i\omega t} dt \tag{1.21}$$

In a similar way, the expression of complex compliance is given by

$$D_c^*(i\omega) = i\omega \int_0^{\infty} D_c(t) e^{-i\omega t} dt \tag{1.22}$$

Thus if relaxation modulus $E(t)$ (or creep compliance $D_c(t)$) is known for a long period of time ($t \in [0, \infty)$), the complex modulus $E^*(i\omega)$ (or complex compliance $D_c^*(i\omega)$) could be found using the above expression. However, such long-term testing (in the interval of decades) to determine the relaxation modulus is impractical and it will be seen in the next section (Section 1.2.4) that the Time-Temperature-Superposition-Principle (TTSP) will be used to overcome this issue by performing the test only for a shorter duration but for different temperatures followed by a frequency sweep.

The complex compliance can also be written as follows:

$$E^*(i\omega) = \frac{\sigma^*}{\varepsilon^*} = \frac{\sigma_0}{\varepsilon_0} e^{i\delta} = E'(\omega) + iE"(\omega) = |E^*(i\omega)| e^{i\delta} \tag{1.23}$$

where the real part $E'(\omega)$ is the *storage modulus* and the imaginary part $E"(\omega)$ is the *loss modulus*. The terms 'storage' and 'loss' used for real and imaginary parts can be explained as follows: the energy stored is proportional to the real part and the viscous dissipated energy is proportional to the imaginary part [10]. $|E^*(i\omega)|$ and $\delta = tan^{-1}(E"/E')$ represent the absolute value of the complex modulus and the phase angle between stress and strain (see Figure 1.8).

As in elasticity, the following relations hold in the frequency domain for the complex shear

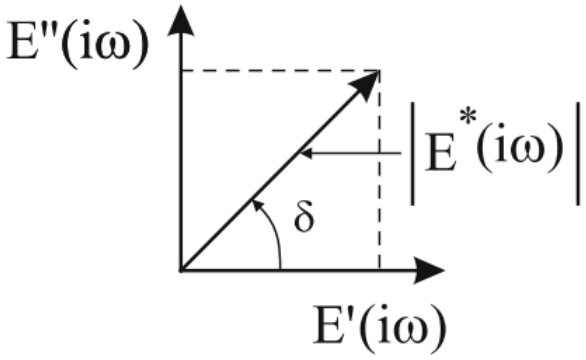

Figure 1.8 – Complex modulus E^* in complex plane [10]

modulus G^* and complex bulk modulus K^*

$$G^* = \frac{E^*}{2(1+\nu^*)} \quad , \quad K^* = \frac{E^*}{3(1-2\nu^*)} \tag{1.24}$$

where $\nu^* = \nu' + i\nu$" is the complex Poisson's ratio. However, in certain studies, the imaginary part of Poisson's ratio is assumed to be small (due to the increased difficulty in determining complex Poisson's ratio [15]) and is neglected [16, 17, 9]. In this thesis, we will also make a similar assumption: $\nu^* = \nu' = \nu$.

1.2.4 Time-Temperature-Superposition-Principle (TTSP)

The Time-Temperature-Superposition-Principle (TTSP) is based on the idea that the response of a material to external forces, such as stress or strain, can be shifted or scaled by applying a time-temperature shift factor. By applying the Time-Temperature-Superposition-Principle (TTSP), it is possible to extend the range of experimental data available for a material. This is particularly useful when studying materials under extreme conditions that are difficult to reproduce or measure directly.

Leaderman in the early 1940s [18] graphed several existing creep-temperature curves on a logarithmic scale, which served to validate his observation that *an increase in temperature has the effect of contracting the time scale*. Later it was demonstrated that data collected over a short time for various temperatures can be shifted to form a reduced curve (also called a *master curve*) [19]. This master curve is plotted for a reference temperature scaling over longer time periods (in log scale) by use of a calibration parameter α_T. The linear viscoelastic solids for which such change of temperature is completely equivalent to a shift of the logarithmic time scale is termed *'thermo-rheologically simple'* materials [19]. For thermo-rheologically simple solids, the following

holds

$$E^*(\omega, T) = E^*(\alpha_T \omega, T_{ref}) \quad ; \quad \alpha_T(T_{ref}) = 1 \tag{1.25}$$

where α_T is the *shift factor* that accounts for the change in temperature. T and T_{ref} are the actual and reference temperatures. The shift factor α_T can be found using Williams– Landel–Ferry (WLF) formula [20] given below

$$log(\alpha_T) = \frac{-C_1(T - T_{ref})}{C_2 + (T - T_{ref})} \tag{1.26}$$

where C_1 and C_2 are the parameters that depend on the reference temperature and

$$\omega_r = \alpha_T \times \omega \tag{1.27}$$

where ω_r is the reduced frequency at reference temperature. The importance of the TTSP principle is that it makes it possible to widen frequencies for a given set of temperatures towards new reduced frequencies which cannot be reached experimentally (using Eqs. (1.25), (1.26) and (1.27)).

1.2.5 Experiments to characterize viscoelastic materials

As discussed earlier, the behavior of viscoelastic materials in the laboratory is described mainly in two domains (a) time domain and (b) frequency domain. It should be noted that the deformation for both tests should be kept minimum so that the material behavior remains linear and viscoelastic. In the time domain, linear viscoelastic properties can be characterized by experiments such as creep recovery test, stress relaxation test, SHRP (Strategic Highway Research Program) direct tension specification test [21], Bending Beam Rheometer (BBR) test [11], etc. For example, the Bending Beam Rheometer (BBR) test is a widely used experimental method to characterize the linear viscoelastic behavior of bituminous materials, specifically their low-temperature bending creep properties and their ability to resist low-temperature cracking. It is particularly relevant for assessing the performance of asphalt binders in pavement applications.

In the frequency domain, several experimental tests can be conducted to obtain linear viscoelastic properties. These tests involve subjecting the material to cyclic or sinusoidal loading at various frequencies and temperatures and measuring the resulting response. Some of the common experimental tests used to obtain linear viscoelastic properties in the frequency domain include Dynamic Shear Rheometer (DSR) and tensile-compression test. Both these tests are generally referred to as Dynamic Mechanical Analysis (DMA) tests. DMA involves applying a sinusoidal strain to the sample, which generates sinusoidal stress (see Figure 1.9). Complex modulus can

then be calculated by measuring the amplitude of deformation at the peak of the sine wave and the phase lag between the stress and strain sine waves using Eq. (1.23) (see Figure 1.9b). For e.g., in [3], the linear viscoelastic behavior is obtained using a rheometer, by applying a small torsional sinusoidal strain (of the order of magnitude of .0060%) on cylindrical specimens

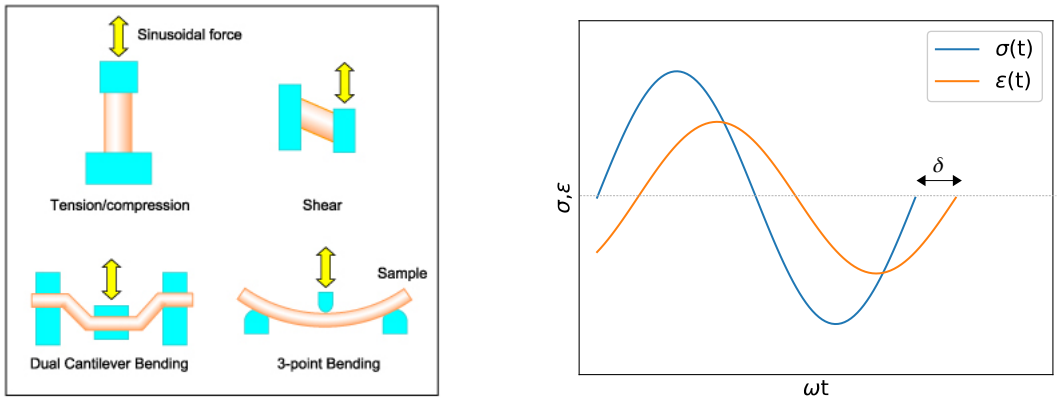

Figure 1.9 – (a) Schematic for Dynamic Mechanical Analysis (DMA) tests (Image source) (b) Stress response for applied strain input

In general, the hypotheses of isotropy and homogeneity are adopted in the procedure for characterizing the properties of bituminous materials. Several standards exist for performing the DMA. Here, we report the experimental results obtained in a previous thesis performed at Université Gustave Eiffel (ex-IFSTTAR) [9]. This includes performing DMA on sand bitumen 0/2 (see Figure 1.10) on a trapezoidal cantilever beam according to the standard EN 12697-26 [22]. The sand bitumen 0/2 has a maximum grain size of 6.3 mm.

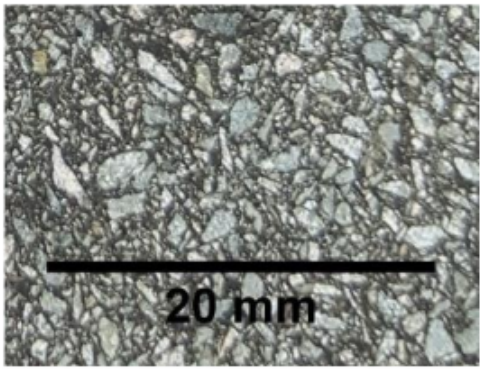

Figure 1.10 – Sand bitumen 0/2 [9]

Although sand bitumen 0/2 is little used in pavement structures, this material has the advantage of being more homogeneous at the specimen scale due to the smaller size of the aggregates.

Moreover, it was reported in [9] that sand bitumen is a good compromise to facilitate modeling in a homogeneous environment while preserving the specific characteristics of bituminous materials (viscoelasticity, granular structure, etc.). Furthermore, this reference material aids in establishing the assumptions of isotropy.

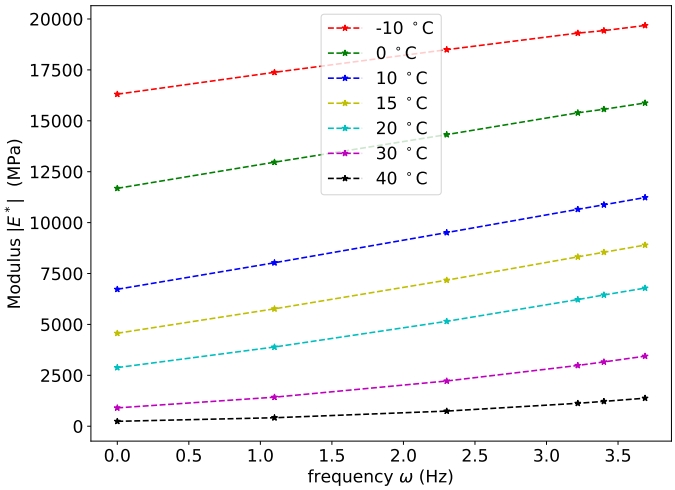

Figure 1.11 – Isothermal curves for the complex modulus as a function of frequency ω

The results obtained from experiments (DMA test) for the aforementioned sand bitumen 0/2 can be represented in different curves. Figure 1.11 displays the isothermal curves of the modulus $|E^*|$ as a function of frequency at different temperatures obtained using experiments. The curve in the *Black space* is constructed by plotting the phase angle δ as a function of modulus $|E^*|$ on a semi-logarithmic scale (see Figure 1.12a). On the other hand, the curve in the complex plane (also called the *Cole-Cole plane*) as shown in Figure 1.12b is constructed by plotting the storage modulus E' and loss modulus E".

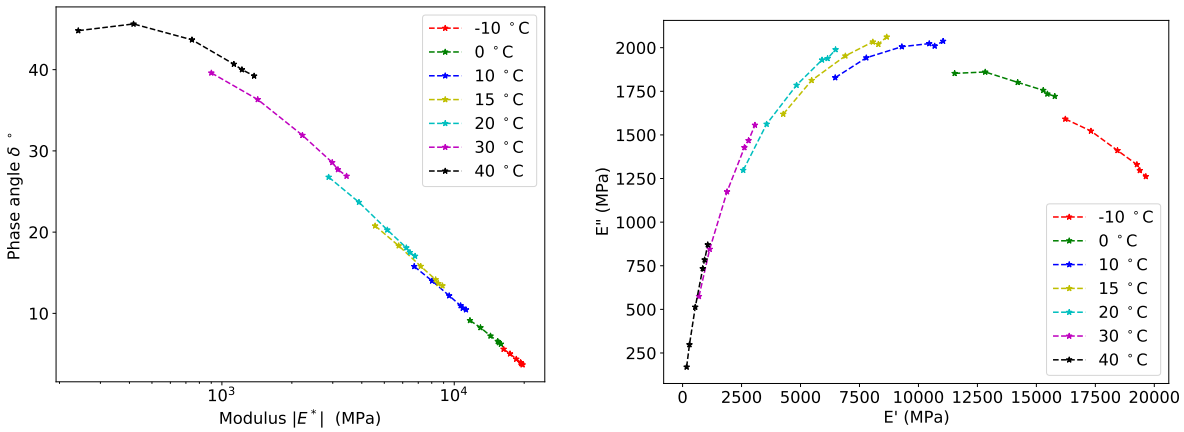

(a) curve in the Black-space

(b) curve in the complex plane

Figure 1.12 – Experimental characterization of sand bitumen 0/2

Once the isothermal curves for different temperatures as a function of frequency are obtained (see Figure 1.11), a frequency sweep can be done by using TTSP to produce the master curve for a reference temperature T_{ref}. The frequency sweep is done using the relation $\omega_r = \alpha_T \omega$ (Eq. (1.27), where the shift factor α_T is found using the WLF equation (Eq. (1.26)). The parameters used for the WLF equation for the considered sand bitumen are as follows [9]: $C1 = 32.6331; C2 = 214.5203$ for $T_{ref} = 15^oC$. The master curve is then plotted on a semi-logarithmic scale as shown in Figure 1.13. Notice that $\alpha_T > 1$ for $T < T_{ref}$ and $\alpha_T < 1$ for $T > T_{ref}$.

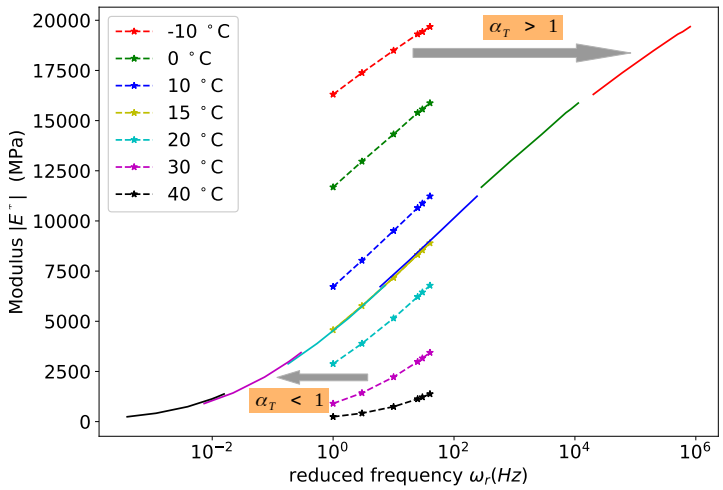

Figure 1.13 – Master curve for $T_r = 15^oC$

1.2.6 Rheological models

Rheological models are models which make it possible to describe the constitutive behavior of non-aging linear viscoelastic materials. These models consist of combinations of elementary components, such as springs representing elastic behavior (characterized by elastic modulus E) and dampers representing viscous behavior (characterized by viscosity η). In the literature, these rheological models are broadly categorized into two main groups:

1. Continuous relaxation spectrum models
2. Models with a discrete relaxation spectrum

In the first case, the relaxation behavior is described by a continuous distribution of relaxation times. The material's viscoelastic response is obtained by considering the hereditary integral or convolution (Eq. (1.10)) of the relaxation function with the applied loading function. Continuous relaxation spectrum models provide a more detailed description of the viscoelastic behavior, particularly for materials with a wide range of relaxation times. Examples of continuous relaxation spectrum models include the Huet model [23], the Huet-Sayeigh model [24, 25], the 2S2P1D model [26], etc. These models possess the advantage that they are able to very well represent the behavior of linear viscoelastic materials like bituminous materials while using fewer parameters than models with discrete relaxation spectrum. However, the disadvantage is that the direct integration of convolution integral to find stresses is computationally inefficient because strains at all previous time histories are involved [27, 28]. Moreover, splitting the integral based on a recursive formula to overcome the above issue is possible only for certain relaxation functions of exponential type [27, 28]. Hence, continuous relaxation spectrum models are often approximated by discrete relaxation spectrum models, since in the latter, the relaxation function (or creep function) is of exponential type.

In discrete relaxation spectrum models, the relaxation behavior is represented by a discrete (or finite) set of relaxation modes or processes. Each relaxation mode is associated with a specific relaxation time and a corresponding modulus. The material's overall viscoelastic response is obtained by considering the contributions of all the individual relaxation modes in a series and/or parallel arrangement. Examples of models with a discrete relaxation spectrum include the Pointing-Thompson (PT) model, the Maxwell model, the Kelvin-Voigt (KV) model, etc. [10, 27, 25].

In the forthcoming sections, we limit our discussion to the models with discrete relaxation spectra due to the aforementioned computational issue associated with continuous relaxation spectrum models.

1.2.6.1 Generalized Kelvin-Voigt (GKV) model

A Kelvin-Voigt model is a parallel connection of spring and dashpot whereas the Generalized Kelvin-Voigt (GKV) model (Figure 1.14) consists of a spring connected in series with a finite number (n) of such Kelvin-Voigt units.

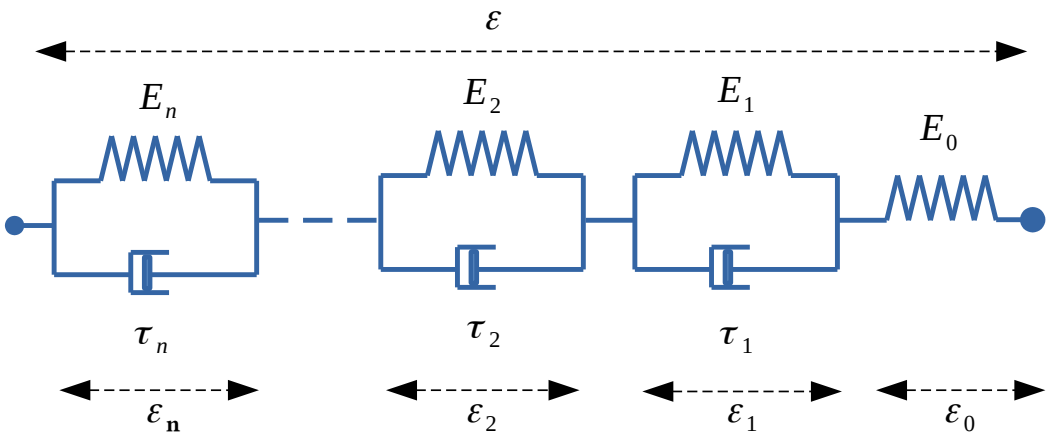

Figure 1.14 – Schematic of Generalized Kelvin-Voigt (GKV) model

$E_0, E_1, .., E_n$ are the relaxation modulus of the springs and $\tau_1, \tau_2, .., \tau_n$ are the *retardation times* of the dashpots. Since the individual KV units are connected in series, the stress σ in each unit is the same. The total strain ε is the sum of the internal strains $(\varepsilon_0, \varepsilon_1, ..., \varepsilon_n)$ of each unit :

$$\varepsilon = \sum_{k=0}^{n} \varepsilon_k \tag{1.28}$$

The creep function of the Generalized Kelvin-Voigt model is given as

$$D_c(t) = \frac{1}{E_0} + \sum_{k=1}^{n} \frac{1}{E_k}(1 - e^{-t/\tau_k}) \tag{1.29}$$

and the complex modulus is given by

$$E^*(i\omega) = \left[\frac{1}{E_0} + \sum_{k=1}^{n} \frac{1}{E_k + i\eta_k\omega}\right]^{-1} \tag{1.30}$$

where $\eta_k = \tau_k E_k$ is the viscosity of the dashpot k. The parameters for the GKV model can be found by fitting the experimental data. For example, in the Cole-Cole plane, we use the least

square minimization of the following objective function to find the model parameters,

$$\chi = (E'_{exp} - E'_{model})^2 + (E"_{exp} - E"_{model})^2 \tag{1.31}$$

Figure 1.15 shows the fit obtained for the aforementioned sand bitumen 0/2 (in Section 1.2.5) by employing 9 Kelvin-Voigt (KV) units. The parameters of the fit are given in Table 1.1. Note that the choice of parameters is not unique and one can have a different set of parameters leading to a similar mechanical behavior.

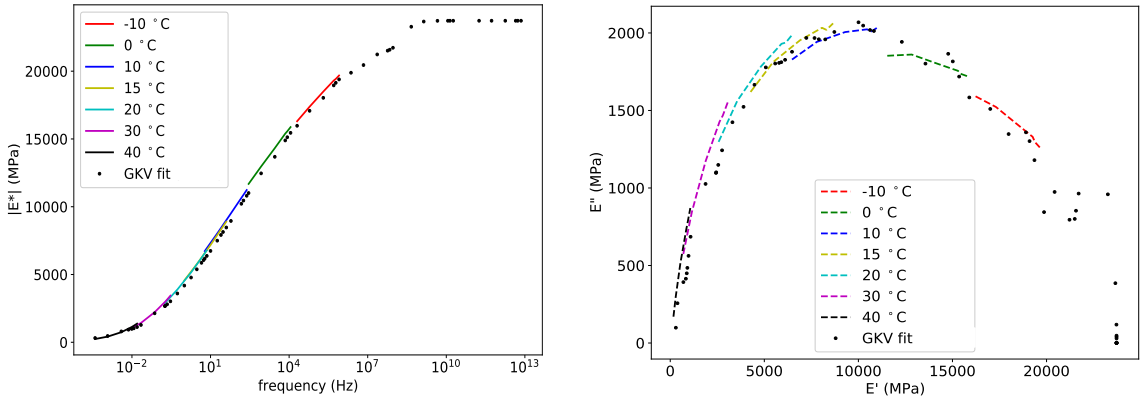

Figure 1.15 – Fit obtained for sand bitumen 0/2 using GKV model: (a) fit for the master curve (b) fit in Cole-Cole plane

KV unit (i)	0	1	2	3	4	5	6	7	8	9
E_i (MPa)	20.55e3	135.37e3	84.5e3	11.1e3	56.3e3	3.19e3	181.14e3	.327e3	21.95e3	34.6e3
$\tau_{i,ref}$ (s)	N/A	1.98e-5	2.35e-4	1.12	2.59e-3	13.49	1.76e-6	5.36e2	1.59e-1	2.09e-2

Table 1.1 – GKV model parameters for sand bitumen 0/2

1.2.6.2 Generalized Maxwell (GM) model

The Generalized Maxwell (GM) model (Figure 1.16) is made up of a parallel assembly of a spring and a finite number of Maxwell units (a spring in series with a linear damper). $E_0, E_1, .., E_n$ are the relaxation modulus of the springs and $\tau_1, \tau_2, .., \tau_n$ are the *relaxation times* of the dashpots. The total strain ε is constant across each unit. $(\varepsilon_1, ..., \varepsilon_n)$ denote the internal or viscous strain in each dashpot. Since the Maxwell units are connected in parallel, the total stress σ is equal to the summation of the stress in each unit.

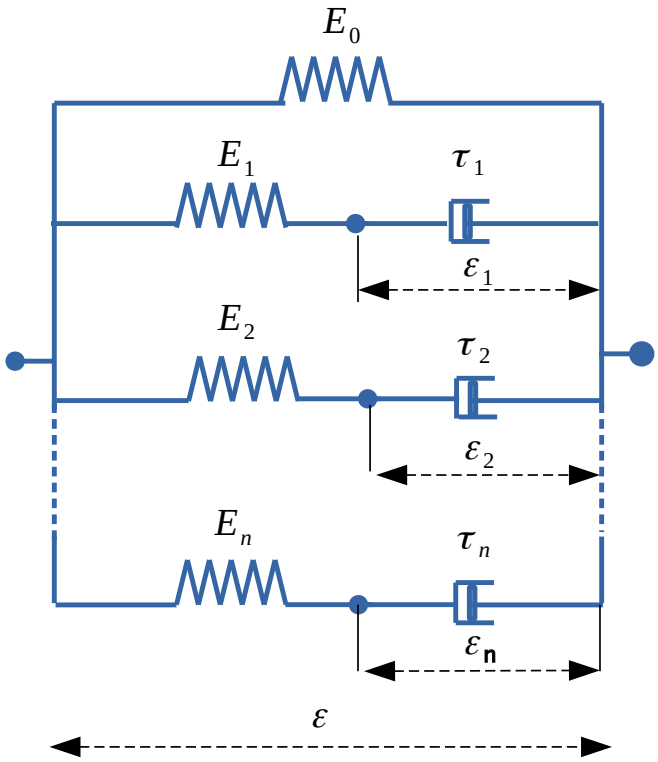

Figure 1.16 – Schematic of Generalized Maxwell (GM) model

The relaxation function of this model is given by the Prony series as follows

$$E(t) = E_\infty + \sum_{k=1}^{n} E_k e^{-t/\tau_k} \tag{1.32}$$

and the respective complex modulus by

$$E^*(i\omega) = E_\infty + \sum_{k=1}^{n} \frac{E_k \omega^2 \eta_k^2 + i E_k^2 \omega \eta_k}{E_k^2 + \omega^2 \eta_k^2} \tag{1.33}$$

The model parameters are fit by using a least square optimization as mentioned before (see Eq. (1.31)). Figure 1.17 illustrates the obtained fitting for sand bitumen 0/2 by employing 9 Maxwell units. The parameters of the fit are given in Table 1.2.

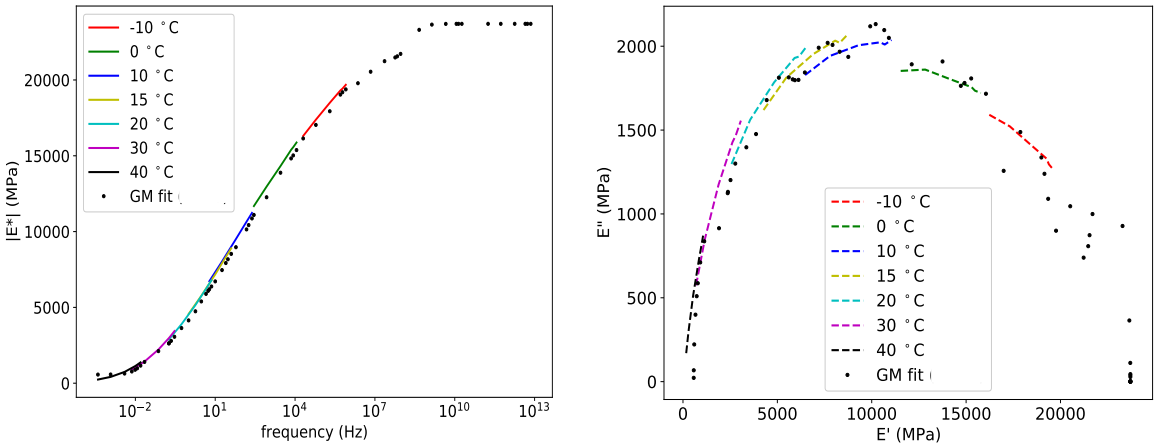

Figure 1.17 – Fit obtained for sand bitumen 0/2 using GM model: (a) fit for the master curve (b) fit in Cole-Cole plane

GM unit (i)	0	1	2	3	4	5	6	7	8	9
E_i (MPa)	275.85	2.152e3	2.243e3	2.384e3	2.711e3	2.673e3	2.769e3	2.1e3	1.224e3	2.02e3
$\tau_{i,ref}$ (s)	N/A	1.58e-6	1.75e-5	1.14e-1	1.57e-2	1.97e-4	2.07e-3	7.16e-1	90.88	5.91

Table 1.2 – GM model parameters for sand bitumen 0/2

It's worth noting that the difference in constitutive equations between the GKV and the GM models results in variations in their numerical implementation within a finite element code. Nevertheless, it's important to note that both models produce comparable outcomes when applied to a specific viscoelastic material. As will be seen in later chapters, we rely on the GKV model to describe the viscoelastic behavior.

1.3 Fracture in bituminous materials

Fracture in asphalt pavements is a common distress phenomenon that can occur due to various factors, including traffic loads, environmental conditions, material properties, and construction practices. Understanding the types of cracking in asphalt concrete is crucial for effective pavement design, maintenance, and rehabilitation strategies. The two most common types of cracking in asphalt concrete are fatigue cracking and thermal cracking.

Fatigue cracking is one of the most prevalent types of cracking in asphalt pavements. It is caused by repeated traffic loading, which leads to the progressive development of cracks due to the cyclic stresses induced in the asphalt layers. Figure 1.18 shows the two distinct types

of fatigue cracking: alligator cracks (a series of interconnected cracks resembling the pattern of alligator scales) and longitudinal cracks (cracks occurring in the direction of traffic flow)

(a) (b)

Figure 1.18 – (a) alligator cracks (image source) (b) longitudinal cracks (image source)

Thermal cracking occurs as a result of temperature fluctuations in the asphalt pavement. When the temperature drops, the asphalt contracts, and if the contraction is restricted, it can lead to tensile stresses and subsequent cracking. Similarly, during hot weather, asphalt expands, and if the expansion is constrained, it can result in compressive stresses and cracking. However, during hot weather, the relaxation properties of asphalt are increased, thereby reducing the likelihood of cracking. Figure 1.19 displays the two different types of thermal cracking: Block cracking (cracking in the form of blocks) and transversal cracking (cracks perpendicular to the pavement center line).

(a) (b)

Figure 1.19 – (a) block cracking (image source), (b) transversal cracking (image source)

In addition to the above cracking types, various other forms of deterioration (or distress) can

occur in pavements. For instance, rutting, which is primarily caused by the application of heavy loads on hot pavement, and the formation of potholes, which is attributed mainly to repeated freezing and thawing cycles (moisture-induced damage) [29]. The distress identification manual [30] of the Strategic Highway Research Program (SHRP) details various types of distress (including cracks) and the measures adopted to rate the severity of distress.

However, in the present thesis, the focus was limited to the cracking of bituminous materials in a laboratory setting subjected to monotonous loading rates. The tools developed herein can then serve as a foundation for future research aimed at investigating pavement cracking.

1.3.1 Experimental tests to characterize fracture in bituminous materials:

While Section 1.2.5 briefed about the experimental tests to obtain the viscoelastic properties of the bituminous materials, this section focuses on the laboratory tests to obtain the fracture properties associated with the bituminous materials. In particular, our interest lies only in the fracture tests under monotonous loading at low and intermediate temperatures. Figure 1.20 shows the schematics of the most commonly employed laboratory tests for bituminous materials to characterize fracture. It can be noted that all these tests employ specimens with a pre-existing notch to initiate and propagate cracks more predictably. Most of the common laboratory tests often explore the mode-I fracture behavior, as is the case shown in Figure 1.20.

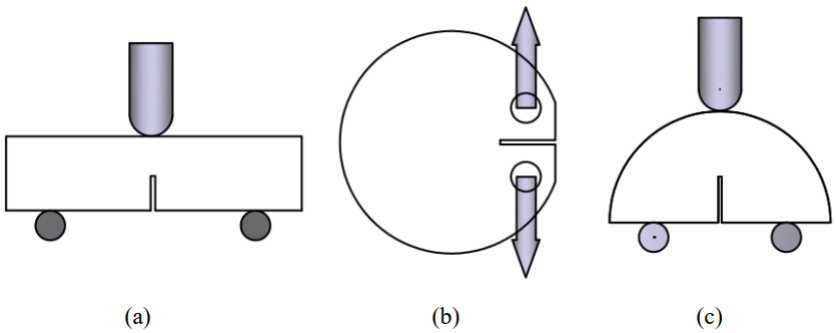

Figure 1.20 – (a) Single Edge Notched Beam (SE(N)B) test (b) Disc-shaped Compact Tension (DCT) test (c) Semi-Circular Beam (SCB) test [31]

The Single Edge Notched Beam (SE(N)B) test is a conventional 3-point bending beam test with a notch located at the center. Though this test has the advantage that a mixed-mode fracture can be easily considered by just changing the position of the loading line (or the position of the notch), it is less often used for bituminous materials as it has the disadvantage of a complex and dedicated fabrication process for bituminous materials (In particular, this test is not suitable for circular specimens obtained from the drilling of field cores from the actual pavement structure). Despite these limitations, this test has still been used to study fracture behavior and it was

reported in [32] that this test is more promising for studying *reflective cracking* (propagation of existing cracks through the new overlay). In the latter, SE(N)B tests were used to study the fracture characteristics at different temperatures (low), and the possibility of mixed-mode fracture was also explored.

A different test called the Disk-shaped Compact Tension test (DCT), makes it possible to use the specimens obtained from the drilling of field cores, as the specimen is circular in shape. This test is standardized as per the norms ASTM E399 (particularly for metallic materials) and ASTM D7313-07a (particularly for asphalt concrete). Moreover, to overcome the failure at the loading holes (due to stress concentration near the holes), new dimensions for the specimen were proposed complying with the standard ASTM E399 in [33]. Furthermore, this method has the advantage of a longer crack path due to its geometry, which provides enough time to analyze the fracture process at low-temperature settings [34]. However, making and preparing the specimen for the DCT test is a bit challenging because it involves using special accessories to position the specimen correctly in the testing setup to ensure a precise occurrence of the mode-I fracture.

An SCB test method is essentially a 3-point bending beam test on a semi-circular beam with a notch. It overcomes the major difficulty of the classical 3-point bending test for bituminous material, that the specimens of the test can be directly obtained from field cores. This test is thus often used due to simpler specimen preparation. For example, in [31], the repeatability and sensitivity of SCB tests were examined to evaluate the fracture characteristics of asphalt concrete mixtures.

In [35], the authors provide a detailed review of the above different laboratory testing methods including their advantages and limitations. The authors also reported a low Coefficient Of Variation (COV) in test results for fracture energy for the DCT test, indicating better repeatability and consistency. However, it was also reported that the SCB test is more practical due to the simplicity of specimen preparation and considering the sensitivity of the results under various test parameters. Other tests that were also found in the literature to study the fracture behavior of bituminous materials include the uniaxial tensile test and the indirect tensile test [36].

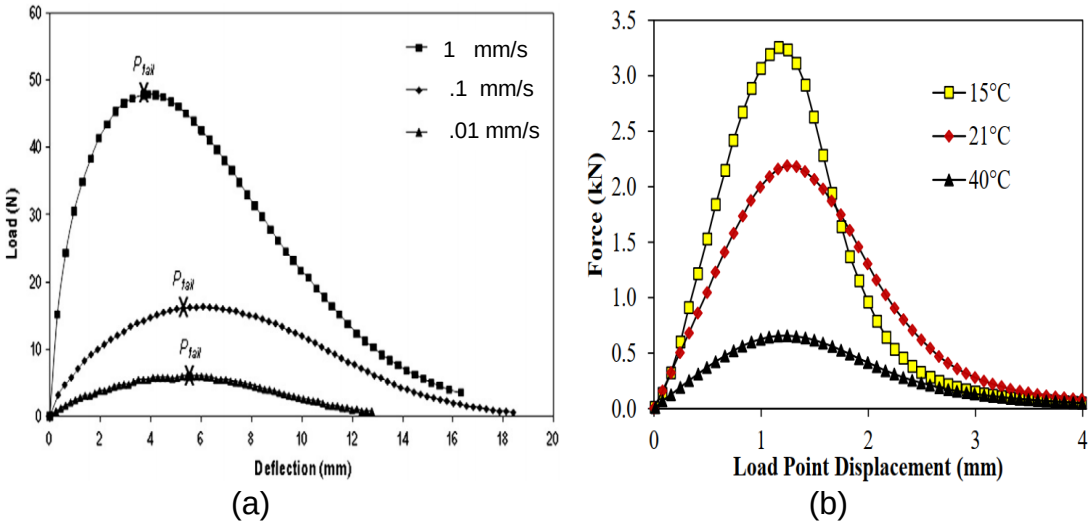

Figure 1.21 – Force displacement curves for (a) SE(N)B test at different displacement rates (fixed temperature) [36] and (b) SCB test at different temperatures (fixed displacement rate) [31]

Figure 1.21a displays the load-displacement plots obtained for SE(N)B test by varying the imposed displacement rates at constant temperature ($T = 20^oC$), while Figure 1.21(b) plots the same for the SCB test by varying the temperature at constant imposed displacement rate (5 mm/min). The difference in behavior is attributed to the rate and temperature sensitivity of the bituminous materials. Moreover, it can be seen that the maximum load increases with an increase in applied displacement rate (or decrease in temperature). In other words, an increase in temperature has a qualitatively similar effect as of decrease in loading rate.

1.3.1.1 Measure of fracture energy

The fracture mechanics approach has been widely accepted to be an essential tool in characterizing crack initiation and propagation in quasi-brittle materials and it is reported to have several advantages over the other classical failure theories based on strength or yield criteria [37]. The material failure in fracture mechanics is determined by the energy criterion (as will be seen in Eq. (1.35)). In particular, the interest lies in characterizing the fracture energy from the laboratory experiments discussed before. Fracture energy is an important material property and is a measure of materials resistant to fracture.

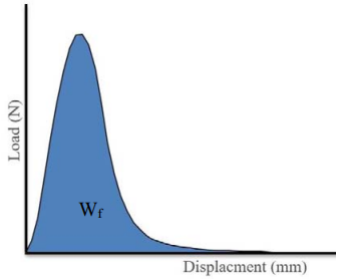

Figure 1.22 – Dissipation due to fracture W_f ([35])

According to RILEM TC 50-FMC (Technical Committee 50-Fracture Mechanics of Concrete) [38], the fracture energy is calculated from the global load-displacement plot (see Figure 1.22) obtained from experiments as follows:

$$G_c = \frac{W_f}{A_{lig}} \tag{1.34}$$

where G_c $[J/m^2]$ is the fracture energy (or fracture toughness), W_f $[J]$ is the area under the force-displacement plot (see Figure 1.22) and A_{lig} $[m^2]$ is the ligament area (the cross-sectional area that underwent fracture).

However, such characterization of fracture energy is only applicable for bituminous materials at low temperatures (see Figure 1.3), where the material behavior is elastic, and the only form of energy dissipation is due to fracture. The effect of an increase in temperature to intermediate temperatures ($\sim$ 10^oC *to* 35^oC) is that the material behavior in the bulk starts to exhibit viscoelastic behavior.

Since the bituminous material behaves in a viscoelastic manner at intermediate temperatures (leading to added viscous dissipation in the bulk apart from the dissipation due to fracture), Eq. (1.34) overestimates the value of fracture energy at intermediate temperatures. To overcome this issue, Aragão et al [4] used an integrated approach combining experimental (on SCB specimen) and numerical simulations (using Cohesive Zone Model CZM). In particular, the Digital Image Correlation (DIC) technique was used to extract the fracture properties at the notch tip (NMOD and NTOD [1]) for different loading rates at intermediate temperatures. This data at the notch tip was then used to calibrate the fracture parameters of the CZM. This helps to distinguish between the energy dissipated due to the viscous effect and the fracture. Figure 1.23(a) shows the fit obtained for the force-displacement plot using the CZM, while Figure 1.23(b) and 1.23(c) shows the fit for the NMOD and NTOD and the CZM fracture parameters for different loading rates.

1. Notch mouth Opening Displacement and Notch Tip Opening Displacement

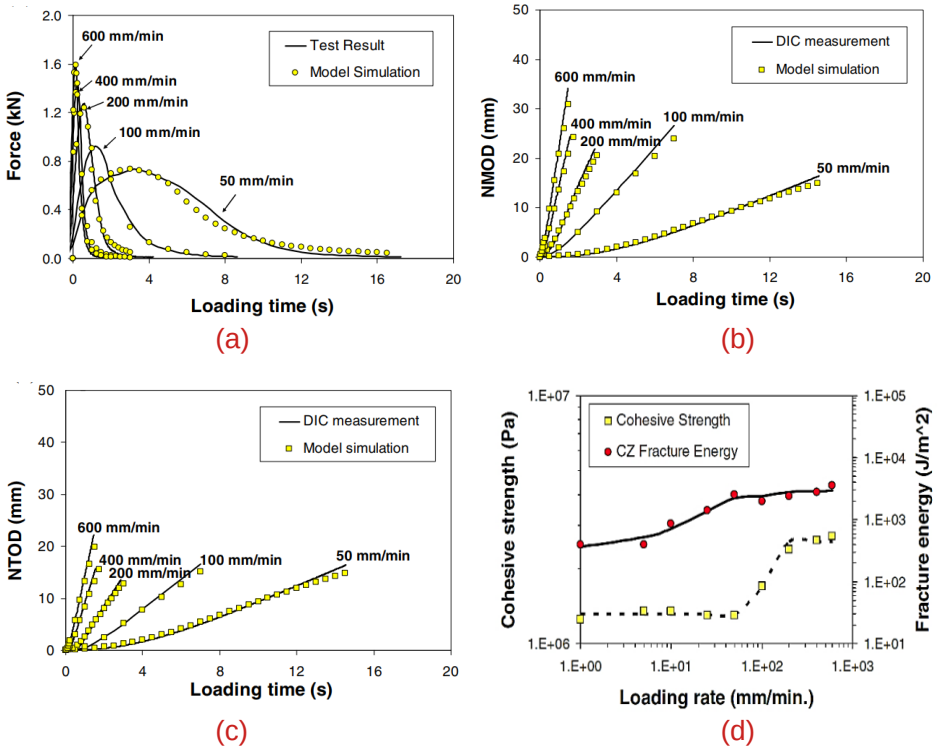

Figure 1.23 – Fracture energy estimation using integrated experimental-numerical (CZM) technique. Fit obtained using CZM for (a) force-displacement plot (b) NMOD (c) NTOP and (d) CZM model parameters as a function of loading rate [4]

Figure 1.23(d) plots the fracture parameters (for the CZM) as a function of applied displacement rates. It clearly indicates the *rate dependency of the fracture parameters*. Hence, it can be concluded that the *rate dependency due to the viscoelastic nature of the bulk is alone not sufficient to model the rate-dependent fracture behavior of bituminous materials*. In other words, rate-dependent (and temperature-dependent) fracture parameters have to be considered to accurately model the bituminous materials at different loading rates (and temperatures).

1.3.1.2 Brittle-ductile transition

Brittle-ductile transition is an important phenomenon that is commonly observed in bituminous materials undergoing fracture. Viscoelastic materials exhibit both elastic and viscous behavior, meaning they can return to their original shape after deformation but also flow and deform over time. The brittle-ductile transition in viscoelastic materials is characterized by changes in their deformation and fracture mechanisms under different conditions. Figure 1.24(a) shows the schematic for the Direct tensile test (DTT) and Figure 1.24(b) shows the typical results of the stress-strain curve obtained for bituminous material using the tensile test at varying loading

rates (or varying temperatures) [39]

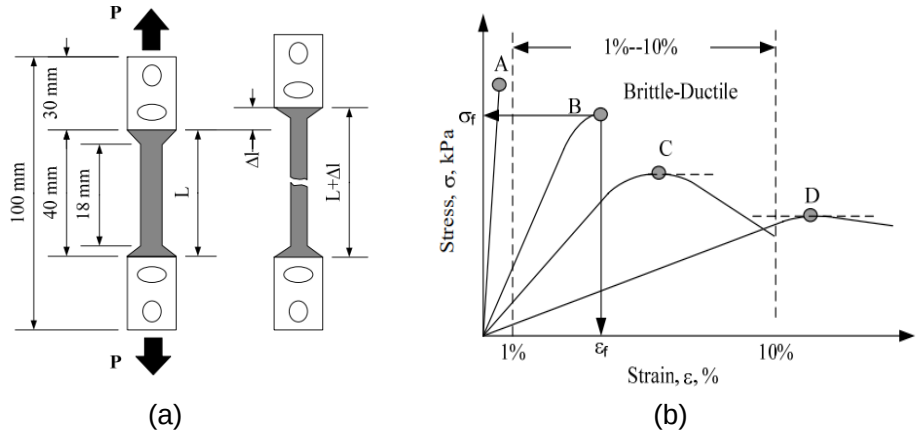

Figure 1.24 – (a) Schematic of Direct Tensile Test and (b) brittle-ductile transition [39]

The peak stress is denoted as σ_f and the corresponding strain associated with peak stress is denoted as ε_f. The characterization of brittle-ductile transition is usually defined by the percentage of strain. For example, in Figure 1.24b the brittle-ductile transition region is considered as the region where the ε_f lies between 1% and 10%. Hence for curve A, the failure is of brittle nature, while for curves B and C the failure starts to transition from brittle to ductile, and for curve D, the failure is ductile, where the specimen continues to stretch without fracture after attaining the maximum load.

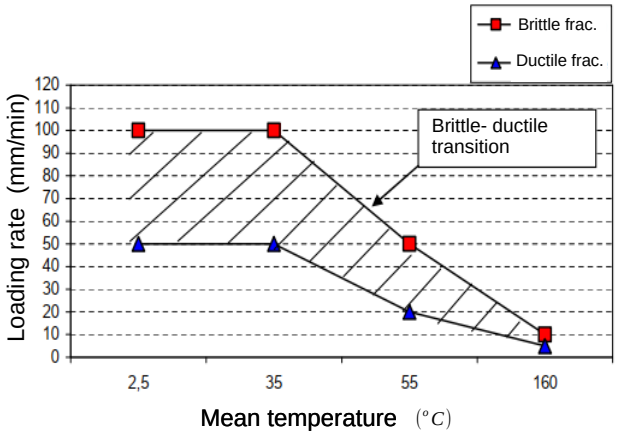

Figure 1.25 – Brittle-ductile transition zone [40]

Figure 1.25 plots the brittle-ductile transition region as a function of loading rates and temper-

atures [40]. It can be seen that at intermediate service temperatures, the transition from brittle to ductile behavior is observed to encompass a broader range of loading rates. The above results indicate the importance of a developed model to consider this brittle-ductile transition into account to simulate the fracture response of bituminous materials for a wide variety of loading rates and temperature conditions.

1.4 Fracture and damage mechanics

1.4.1 Fracture mechanics

Fracture mechanics started with the earlier work of Griffith [41]. Based on this theory, the stress becomes infinite at the crack tip. Fracture mechanics is employed to characterize the loads acting on a crack, typically through the use of a single parameter. Over time, various parameters have been developed and employed for this purpose. When the nonlinear zone around the crack tip, also called the Fracture Process Zone (FPZ) (which involves cavity formation, stringing, chain pull-outs for polymers, and bond breaking) is relatively small compared to the crack size, the cracking can then be described by the elastic forces within the bulk of the material and is termed as Linear Elastic Fracture Mechanics (LEFM). The stress state at the crack tip can then be characterized by the Stress Intensity Factor (SIF). The analytical expression for SIF for several configurations is available in the literature [42]. In this case, the crack is considered to grow rapidly when the SIF reaches the critical SIF (or fracture toughness), which is usually determined from experiments. However, due to the presence of finite width of the Fracture Process Zones (FPZ) in all natural materials, the SIF approach is often impractical as crack growth is heavily influenced by nonlinear processes near the crack tip. Therefore, an alternative parameter used for characterizing crack growth is based on the energy, called the energy release rate G. This approach is called the energy approach and the crack is considered to grow when the energy available for crack growth is sufficient to overcome the fracture resistance of the material G_c (Eq. (1.35)). Griffith was the first to propose the energy criterion for fracture [41]. The criterion for crack propagation for an increase in crack length da is given by the following energy balance equation :

$$G \geq G_c \tag{1.35}$$

G_c is the critical energy release rate (or fracture toughness). The expression for G is given in the case of linear elastic fracture by

$$G = -\frac{\partial \Pi}{\partial a} \tag{1.36}$$

where II is the potential of the system and a is the crack length. Figure 1.26 shows the different modes of fracture and the crack tip fields for the linear elastic fracture case are given by Eqs. (1.37, 1.38). These fields are defined by some magnitudes K_I, K_{II}, and K_{III} for each mode and they are called Stress Intensity Factors (SIF).

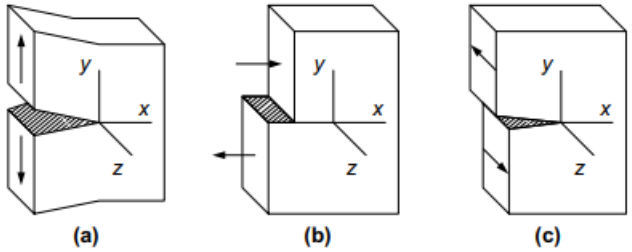

Figure 1.26 – Different modes of fracture (a) crack opening mode, mode-I (b) in-plane shear mode, mode-II and (c) out of plane shear mode, mode-III [43]

The stresses near the crack tip are given by

$$\sigma_{11} = \frac{K_I}{\sqrt{2\pi r}} \cos\frac{\theta}{2}\left(1 - \sin\frac{\theta}{2}\sin\frac{3\theta}{2}\right) - \frac{K_{II}}{\sqrt{2\pi r}} \sin\frac{\theta}{2}\left(2 + \cos\frac{\theta}{2}\cos\frac{3\theta}{2}\right) \tag{1.37a}$$

$$\sigma_{22} = \frac{K_I}{\sqrt{2\pi r}} \cos\frac{\theta}{2}\left(1 + \sin\frac{\theta}{2}\sin\frac{3\theta}{2}\right) + \frac{K_{II}}{\sqrt{2\pi r}} \cos\frac{\theta}{2}\sin\frac{\theta}{2}\cos\frac{3\theta}{2} \tag{1.37b}$$

$$\sigma_{12} = \frac{K_I}{\sqrt{2\pi r}} \cos\frac{\theta}{2}\sin\frac{\theta}{2}\cos\frac{3\theta}{2} + \frac{K_{II}}{\sqrt{2\pi r}} \cos\frac{\theta}{2}\left(1 - \sin\frac{\theta}{2}\sin\frac{3\theta}{2}\right) \tag{1.37c}$$

$$\sigma_{31} = -\frac{K_{III}}{\sqrt{2\pi r}} \sin\frac{\theta}{2} \quad \sigma_{32} = \frac{K_{III}}{\sqrt{2\pi r}} \cos\frac{\theta}{2} \tag{1.37d}$$

while the displacements near the crack tip are given by

$$u_1 = \frac{K_I}{\mu}\sqrt{\frac{r}{2\pi}}\left[1 - 2\boldsymbol{v} + \sin^2\frac{\theta}{2}\right]\cos\frac{\theta}{2} + \frac{K_{II}}{\mu}\sqrt{\frac{r}{2\pi}}\left[2 - 2\boldsymbol{v} + \cos^2\frac{\theta}{2}\right]\sin\frac{\theta}{2} \tag{1.38a}$$

$$u_2 = \frac{K_I}{\mu}\sqrt{\frac{r}{2\pi}}\left[2 - 2\boldsymbol{v} - \cos^2\frac{\theta}{2}\right]\sin\frac{\theta}{2} + \frac{K_{II}}{\mu}\sqrt{\frac{r}{2\pi}}\left[-1 + 2\boldsymbol{v} + \sin^2\frac{\theta}{2}\right]\cos\frac{\theta}{2} \tag{1.38b}$$

$$u_3 = \frac{K_{III}}{\mu}\sqrt{\frac{2r}{\pi}}\sin\frac{\theta}{2} \tag{1.38c}$$

where the origin of the polar coordinate system (r, θ) is located at the crack tip. In the above, u_1 and u_2 are provided for plane strain cases. For the linear elastic fracture case, the following relation holds,

$$G = \frac{K_I^2}{E'} + \frac{K_{II}^2}{E'} + \frac{K_{III}^2}{2\mu} \tag{1.39}$$

where each term corresponds to the energy release rates in 3 different modes. The expression for E' is given in terms of Young's modulus E and Poisson's ratio ν. For plane strain, $E' = E/(1-\nu^2)$ and $\mu = E/2(1+\nu)$.

The energy criterion mentioned above (Eq. (1.35)) was ignored for an extended duration until the early 1950s, mainly because Griffith's derivation of the analytical expression for G was limited to the linear elastic fracture scenario (or brittle fracture). The transformation of this approach into its current version was pioneered by Irwin, who introduced modifications accounting for non-linear FPZ effects, typically involving the inclusion of another term for dissipation (often plastic) [44]. Since then, various methods have been introduced to calculate the energy release rate. The J-integral is the commonly used numerical approach for this purpose [45], and in two-dimensional cases (Figure 1.27), it is defined as follows

$$J = \int_{\Gamma} \left(\boldsymbol{\sigma} : \boldsymbol{\varepsilon} dx_2 - \boldsymbol{\sigma}.\mathbf{n}.\frac{\partial \mathbf{u}}{\partial x_1}\, ds \right) \tag{1.40}$$

where $W = \boldsymbol{\sigma} : \boldsymbol{\varepsilon}$ is the strain energy density, x_1, x_2 are the coordinate directions, $\mathbf{t} = \boldsymbol{\sigma}.\mathbf{n}$ is the surface traction vector and $\mathbf{u}$ is the displacement vector. J-integral is path independent as demonstrated by Rice [45].

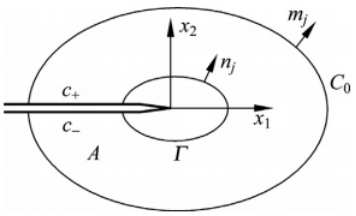

Figure 1.27 – J-integral around a crack tip in 2-dimensions[46]

For fracture in non-linear viscoelastic materials under large strain, Schapery utilizes the correspondence principle to define a time-dependent J-integral that is analogous to the approach for non-linear elastic scenarios [47] [48]. Building upon this, a novel model for studying viscoelastic fracture under creep loading is presented in [49]. This model extends the Griffith energy balance, initially designed for linear elastic materials, to encompass viscoelasticity by adding a viscous dissipation term. In this approach, crack growth is solely driven by free energy. Concurrently, the X-FEM approach [50, 51] has gathered significant attention. In [52, 53], X-FEM is employed to address linear viscoelasticity issues involving inclusions and cracks. However, the Griffith-type models possess certain limitations: a) they are unable to predict crack initiation unless pre-existing cracks are considered, and b) they cannot predict crack branching. Subsequently,

damage mechanics-based approaches were incorporated to enhance the Griffith-type models. This can be generally classified into two categories: the Cohesive Zone Model (CZM) [54, 55] and Continuum Damage Mechanics (CDM) [56, 57].

Methods developed for the linear elastic and elastic-plastic fracture cannot be used for the time-dependent viscoelastic fracture mainly due to the viscous dissipation in the bulk causing time-dependent fracture. Moreover, the critical energy release rate (G_c) for bituminous materials is not (material) constant and is influenced by factors such as specimen size (size effect), loading history, temperature, and speed [37] [4], [3]. Additionally, when conducting cracking tests on these materials, the crack tip stress singularity is often not observed. As a result, the conventional theory of fracture mechanics alone is insufficient to fully comprehend cracking phenomena in bituminous materials. To address this issue, researchers often have turned to the cohesive zone model (CZM). Both damage mechanics-based approaches (CZM and CDM) introduce a length scale into the model accounting for the micro-damage before fracture that can be associated with the nucleation, coalescence, and growth of voids to form macro-cracks.

1.4.2 Cohesive Zone model

The failure is of a quasi-brittle nature in the case of bituminous materials [58]. Such failure is shown in Figure 1.28. The Fracture Process Zone (FPZ) indicates the nonlinear zone ahead of the crack tip, characterized by several phenomena, including plastic deformation, microcracking, and energy dissipation. In the case of failure of quasi-brittle type, the FPZ is large (the ratio of nonlinear zone size to structure size is not small) and is not negligible. Moreover, for the quasi-brittle materials, a substantial non-linearity exists before reaching the maximum stress (see Figure 1.28b). After the proportional limit, micro-cracks start to appear and at some point before the peak stress, the micro-cracks tend to localize to form macro-cracks. Therefore, the use of Linear Elastic Fracture Mechanics LEFM is not suitable. For example, Li and Marasteanu (2010) [59] utilized the acoustic emissions method to assess the size of the fracture process zone (FPZ) in various types of asphalt mixtures under low-temperature conditions. Their study revealed that the FPZ for asphalt mixtures ranged from 40 mm or larger.

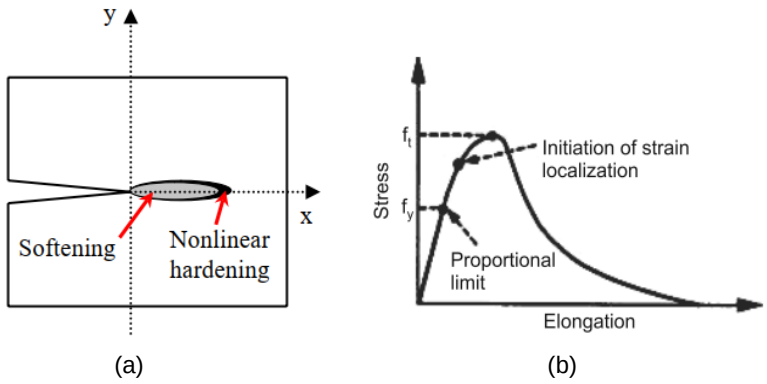

Figure 1.28 – (a) Typical Fracture Process Zone (FPZ) [60] and (b) typical stress-strain curve [61] for quasi-brittle fracture

The CZ or cohesive crack model [62], offers a framework to simulate the nonlinear fracture process. It is a phenomenological model that views fracture as a gradual phenomenon occurring across an extended crack tip or fracture process zone (CZ). Within this model, the fracture is resisted by cohesive tractions, and separation takes place gradually. The schematic of the CZ model is shown in Figure 1.29. t_n, δ_n, σ_c and δ_{cr} denote the normal traction, the normal opening displacement, the material strength, and the critical displacement (displacement corresponding to zero traction), respectively.

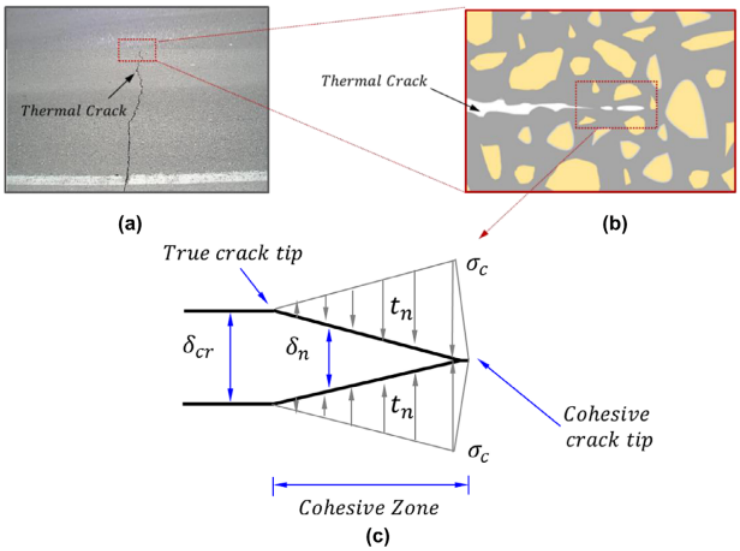

Figure 1.29 – Schematic of CZM [58]

This model was initially introduced in the early 1960s by Dugdale [63] and Barenblatt [64]. Since then, cohesive cracks have been employed by numerous researchers to describe the nonlinear zone near the crack tip in various engineering materials.

In comparison to the classical Linear Elastic Fracture Mechanics (LEFM) approach and other existing fracture models, the cohesive crack model (CZM) offers several advantages. It allows for spontaneous crack nucleation, crack branching, and fragmentation. Furthermore, it enables the simulation of mode-I and mixed-mode crack propagation without relying on an external fracture criterion.

These models introduce cohesive elements along crack lines or regions to represent the fracture process zone. The cohesive elements are governed by a traction-separation law that describes the relationship between cohesive traction (forces resisting separation) and separation displacements (relative displacement between the crack surfaces). Depending on whether an artificial initial stiffness is included in this law or not, cohesive crack (CZ) models can be categorized as intrinsic or extrinsic models (see Figure 1.30). t_n and δ_n are the traction stresses and displacement jump (separation) in the normal direction (for mode-I fracture) while σ_c is the cohesive strength and δ_{cr} is the critical displacement jump at which the traction t_n attains zero. The fracture energy G_c of the cohesive zone can be computed by the area under the traction-separation curve $G_c = \int_0^{\delta_{cr}} t_n(x)\delta_n(x)dx$.

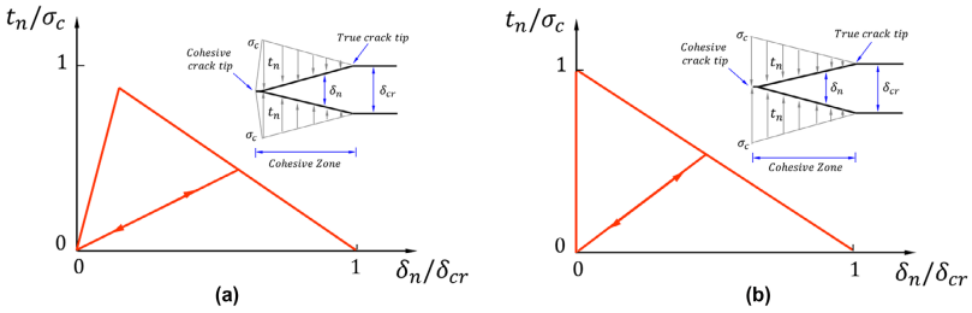

Figure 1.30 – Traction-separation law for (a) Intrinsic CZM and (b) extrinsic CZM[58]

Intrinsic models (Figure 1.30a) refer to those where an artificial initial stiffness is incorporated into the traction-separation law. On the other hand, extrinsic models (Figure 1.30b) assume an initial rigidity for the cohesive zone (CZ) in the traction-separation law.

However, in the case of intrinsic CZ models, the initial slope of the cohesive law, before reaching the peak load, can result in excessive compliance, leading to unrealistic predictions. To mitigate this issue, researchers have proposed various approaches. One common approach is the use of

a bilinear CZ model [65] with relatively high initial stiffness (or very high cohesive strength) of the traction-separation law. However, the use of 'too stiff' initial cohesive stiffness can generate problems with stability and severely restrict the simulation time steps for the dynamic problems [60].

Figure 1.31 compares different traction-separation laws of the CZ models. The power law and exponential softening CZ models allow for controlling the softening shape (important for quasi-brittle materials [58]), through the use of the parameters α and β.

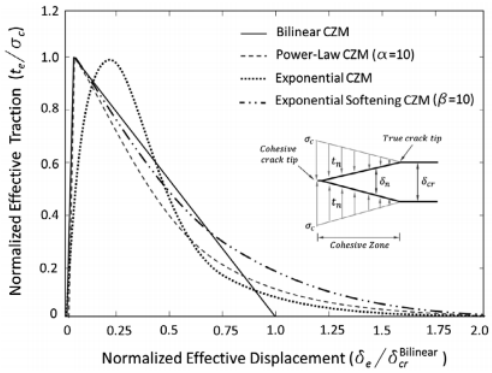

Figure 1.31 – Different traction-separation laws for CZM[58]

The implementation of an intrinsic model in a finite element analysis (FEA) necessitates embedding all cohesive elements within the discretized structure at the start of the simulation. Throughout the simulation process, there are no changes in the mesh connectivity. On the other hand, the implementation of extrinsic cohesive zone modeling (CZM) involves adaptively inserting cohesive elements into the mesh which requires node duplication and node renumbering, whenever a damage initiation criterion is reached. The continuous update of node numbering remains a challenge for the implementation of the extrinsic CZ models.

Cohesive models introduce a length scale (generally called cohesive zone length) due to cohesive softening behavior. The cohesive zone length is defined as the distance from the crack tip to the position where the maximum cohesive traction is attained.

In 2003, Soares et al. [66] utilized cohesive zone modeling (CZM) to simulate the propagation of mode I crack in asphalt concrete within the indirect tension test (IDT). To reduce compliance and improve accuracy, several works have also been carried out to implement a bilinear CZM specifically for asphalt concrete [67, 68, 58]. In the latter, both bilinear and exponential CZM are used to fit the experimental results for the fracture in the Disc-shaped Compact Tension test (DCT). Another notable work in this area is by Dave and Buttlar (2010a) [69], who employed a

temperature-dependent cohesive zone model for simulating low-temperature cracking in asphalt pavements. In [3], the authors used a rate-dependent cohesive zone model. In particular, the rate dependency of cohesive zone fracture parameters was accounted for by the use of a rate-dependent function inspired from [65].

One main drawback of the CZM is that crack patterns are highly sensitive to mesh orientation unless extensive adaptive re-meshing is used [70, 71]. The main reason why the CZM fails to produce mesh-independent results is that the cohesive elements are inserted only at the element interfaces and this results in the crack path being limited to the element edges causing these models to be dependent on mesh orientation. Another consequence of this is the difficulty of modeling crack branching and other complex crack patterns.

1.5 Continuum Damage mechanics

In the context of continuum damage mechanics [72, 73], the approach involves initially characterizing the state of damage in a material using appropriately defined damage variables. In the case of isotropic damage (assumption followed in the thesis), a scalar damage variable D (or d) is used to characterize the internal state of damage in a material. The value of D ranges from 0 (undamaged state) to 1 (complete failure or total loss of load-carrying capacity).

Consider the damage of a cylindrical bar shown in Figure 1.32 with cross-section area dA subjected to a tensile load dF.

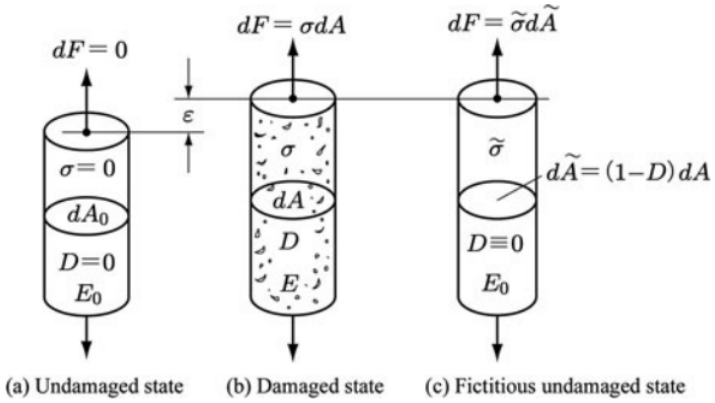

Figure 1.32 – Schematic representation of damage in a cylindrical bar [74]

Due to the presence of damage, the effective cross-sectional area over which the load is distributed

is $d\tilde{A}$ and its expression is given by

$$d\tilde{A} = (1 - D)dA \tag{1.41}$$

The stress in the damaged bar is then given by

$$\tilde{\sigma} = \frac{dF}{d\tilde{A}} = \frac{\sigma}{(1 - D)} \tag{1.42}$$

The stress $\tilde{\sigma}$ is called effective stress. In other words, for a damaged bar shown in Figure 1.32b, one can postulate an equivalent fictitious undamaged bar with cross-section area $d\tilde{A}$ (as shown in Figure 1.32c) subjected to stress $\tilde{\sigma}$ and undergoing the same strain ε as the damaged bar. If the behavior of the material is linear elastic in the undamaged phase with stiffness E_0, then

$$\tilde{\sigma} = E_0\varepsilon \tag{1.43}$$

which upon substitution in Eq. (1.42) yields

$$\sigma = (1 - D)E_0\varepsilon = E(D)\varepsilon \tag{1.44}$$

where

$$E(D) = (1 - D)E_0 \implies D = 1 - \frac{E(D)}{E_0} \tag{1.45}$$

Hence, damage can also be characterized by a reduction in stiffness (elastic modulus) of the material due to the development of micro-voids in the material [75].

1.5.1 Strain localisation

Strain localization during fracture refers to the phenomenon where deformation and strain concentrate in a localized region (high strain gradient in a narrow area) within a material as it approaches failure or fracture. In the case of quasi-brittle materials, as the material softens, strain tends to localize in regions of lower resistance, resulting in fracture initiation and propagation. At the onset of strain localization, which precedes macro-crack, the initially smooth distribution of the strain changes into a highly localized one. Usually, the strain increments tend to localize within narrow bands, while the majority of the structure undergoes unloading. The necessary condition for strain localization for rate-independent materials in the quasi-static case is given as [76]

$$det(\mathbf{Q}) = \mathbf{n}.\mathbf{C_e}.\mathbf{n} = 0 \tag{1.46}$$

where $\mathbf{Q}$ is called the localization tensor (or acoustic tensor) and $\mathbf{C_e}$ is the localization stiffness tensor. $\mathbf{n}$ is the unit vector normal to the localization plane. In the case of rate-dependent materials, the necessary condition for strain localization can be determined from the stability analysis [77].

1.5.2 Localisation limiters

From a mathematical point of view, the singularity of the localization tensor leads to the loss of ellipticity of the governing differential equation. The boundary values problem then remains ill-posed (doesn't have a unique solution). From a physical point of view, this results in localization happening on a plane of zero thickness, which results in zero energy dissipation during the failure process. From a numerical point of view, the ill-posedness results in pathological sensitivity of the results to the size of finite elements. As the mesh is refined and the size of the finite element approaches zero, the energy dissipated due to the failure process approaches zero. CZM (Section 1.4.2), crack band model [78, 79], micromorphic continuum [77], and non-local (or regularized) damage models [80] can be used as a remedy to the above problem.

Several works have also been performed in the past to study the mathematical nature of strain localization in rate-dependent materials [81, 82, 83]. In particular, the interest was to see if the rate dependency was able to regularize the problem and prevent strain localization from occurring on a plane of zero thickness. For example, in [83], the authors demonstrated through both theoretical and numerical approaches that viscosity and inertia do not regularize strain localization and can lead to mesh-dependent results.

Crack band model [84, 85] in its basic form assumes that a single localization band (or crack) appears inside each finite element when the crack fully develops. Since the width of the numerically resolved band is controlled by the size of finite elements, the constitutive formulation of the softening part of the stress-strain law must be adjusted according to the element size to recover the correct crack opening law.

Regularized models are based on generalized continuum theories that incorporate a characteristic length and prevent strain localization on a plan of zero thickness. Since the characteristic length scale enforces a certain minimum width of the numerically resolved process zone, they are called localization limiters. Examples include non-local integral type models, differential (gradient-enriched) models, Thick Level Set (TLS) approach, Phase-Field (PF) approach, Lip-Field (LF) approach, etc.

Here we limit our focus to the regularized models. First, a brief on such different models is provided followed by a discussion on lip-field formulation, which is the interest of the present thesis. In particular, we rely on the lip-field approach to prevent strain localization from occurring

on a plane of zero thickness (and thus to have mesh-independent results).

In *integral-type non-local damage models*[86, 87], the damage variable is not only dependent on the local state variables but also on their distribution throughout the material or within a defined region. This means that the damage at a specific point is influenced not only by the state variables at that particular point but also by the distribution of state variables in its surrounding region.

These models typically involve the integration of certain kernel functions or weight functions over the material domain Ω or the finite neighborhood. These functions govern the non-local interaction between different points and determine the contribution of damage at different locations to the overall damage evolution. For a given local field f (a function of state variables, usually strain [88]), the non-local field $\overline{f}$ in the integral form is given as follows

$$\overline{f}(\mathbf{x}) = \int_{\Omega} \alpha \left(\frac{\|\mathbf{x} - \mathbf{y}\|}{l_c} \right) f(\mathbf{y}) \, d\Omega \tag{1.47}$$

where α is the non-local weight function. The non-local field is then used as a thermodynamic force to drive damage. One of the simplest forms for f is the scaled energy norm [88]

$$f = \left(\frac{\boldsymbol{\varepsilon} : \mathbf{C_e} : \boldsymbol{\varepsilon}}{E} \right)^{\frac{1}{2}} \tag{1.48}$$

For *explicit gradient type regularization* [88, 89], the damage is assumed to be driven not only by the local driving force f but also by its Laplacian $\nabla^2 f$. In the simplest case, one can consider the following driving force

$$\overline{f} = f + l_c^2 \nabla^2 f \tag{1.49}$$

Here $\overline{f}$ is the non-local driving force in a weaker sense as the non-local quantity is computed from the local quantities only in an arbitrarily small neighborhood (rather than a finite neighborhood of a point like in integral damage models). The numerical implementation of explicit gradient models poses challenges due to the involvement of second derivatives.

In the case of *implicit gradient formulation* [88, 89], the non-local driving force is given as a solution to the following differential equation

$$\overline{f} - l_c^2 \nabla^2 \overline{f} = f \;\; in \;\; \Omega \tag{1.50}$$

$$\boldsymbol{\nabla} \overline{f} . \mathbf{n} = 0 \;\; on \;\; \partial\Omega \tag{1.51}$$

It can be shown that the implicit gradient type regularization is similar to the integral type

regularization, with a special kernel function of exponential type [88]. However, the numerical implementation of both these regularization methods is quite different [90].

Phase field approach is yet another regularization approach that was initially developed by the physics community and then later used for application in mechanics [91, 92, 93, 94]. In the phase field approach, the crack is represented by an auxiliary phase-field variable d (similar to the scalar damage variable D). In this case, the problem is recast into an energy minimization problem, giving the so-called variational approach to fracture. The regularization is by making the energy potential depend on the damage gradient term. Consider a body occupying a domain Ω with boundary $\Gamma = \Gamma_u \cup \Gamma_N$, where displacement boundary conditions $\mathbf{u_d}(t)$ are applied on Γ_u and zero traction forces are applied on Γ_N. For the case of fracture in linear elastic solids under a quasi-static setting (with the assumption of small strain and negligible body force), the mechanical fields at time $t_{m+1} = t$ is then given by the solution of the following optimization problem [2]

$$\{\mathbf{u}, d\} = \arg \min_{\substack{\mathbf{u}' \in \mathcal{U}_m \\ d' \in \mathcal{A}_m}} F(\mathbf{u}', d', \nabla d') \tag{1.52}$$

where $\mathcal{U}_m$ and $\mathcal{A}_m$ represent the admissible spaces for displacement and damage fields and they are as follows:

$$\mathcal{U}_m = \{\mathbf{u} \in H^1(\Omega) : \mathbf{u} = \mathbf{u_d}(t) \ \ on \ \ \Gamma_u\} \tag{1.53}$$

$$\mathcal{A}_m = \{d \in L^\infty(\Omega) : d_m \leq d \leq 1\} \tag{1.54}$$

where the space $\mathcal{A}_m$ ensures the irreversibility of the damage field (d_m represents the damage field at the previous time step t_m). The incremental potential F in Eq. (1.52) is given by

$$F = \int_\Omega \frac{1}{2}\boldsymbol{\varepsilon} : g(d)\mathbb{C} : \boldsymbol{\varepsilon} + G_c\gamma(d, \nabla d)\, d\Omega \tag{1.55}$$

In the above equation, $\mathbb{C}$ is the elastic tensor, $g(d)$ is the energy degradation function, and $\gamma(d, \nabla d)$ is the crack surface density function. Notice the dependency of the crack surface density function on the damage gradient term, thus aiding in the regularization of the damage field. Some works on the use of a phase-field approach to model damage in viscoelasticity can be found in [95, 96, 97].

It is also worth mentioning the Thick Level Set (TLS) approach [98] and higher-order kinematic models for regularization [99]. The thick level set approach extends the capabilities of the traditional level set method by incorporating thickness information into the representation (length

2. to simplify notations, we disregard the time step indices $m + 1$ for all state variables

scale), allowing for a more accurate representation of the damaged zone. Moreover, this model offers an automatic transition from damage to fracture by use of X-FEM [50, 51]. The use of the TLS approach to model strain softening in bituminous materials can be found in [100]. In particular, in the latter, the authors were able to fit the experimental results corresponding to different temperatures for the uni-axial Direct Tensile Test (DTT) using a viscoelastic damage model regularized through the TLS approach.

In the following section, we look briefly into the lip-field approach to introduce regularization.

1.5.3 Lip-field approach

The lip-field approach is a new approach for introducing length scale into the model. This approach was first introduced for the quasi-static fracture (1D and 2D) in [101, 102] and then extended to dynamic fragmentation (1D) in [103]. The lip-field approach is similar to the phase-field approach in the sense that they are both variational in nature. However, in the lip-field approach, the energy functional to be minimized is a local one (non-regularized) while a non-local (regularized) energy functional is considered for the phase-field approach (see Eq. (1.55)). The regularization in the lip-field approach is then through the use of Lipschtiz constraints that the damage gradient should be bounded by a critical value. This ensures Lipschitz's regularity on the damage field. For example, in the case of fracture in an elastic body Ω (quasi-static, small strain, no body force), with displacements applied on Γ_u of the boundary and traction-free boundary conditions on the remaining portion of the boundary Γ_N, the mechanical fields are given by the solution of the following optimization problem

$$\{\mathbf{u}, d\} = \arg \min_{\substack{\mathbf{u}' \in \mathcal{U}_m \\ d' \in \mathcal{A}_m \cap \mathcal{L}_\Omega}} F(\mathbf{u}', d') \tag{1.56}$$

where the incremental potential F is given by

$$F = \int_\Omega \frac{1}{2} \boldsymbol{\varepsilon} : g(d)\mathbb{C} : \boldsymbol{\varepsilon} + Y_c h(d) \, d\Omega \tag{1.57}$$

where Y_c is the critical energy release rate per unit volume $[J/m^3]$ and $h(d)$ is the damage softening function. In contrast to the potential for the phase-field (Eq. (1.55)), the potential used in the lip-field approach doesn't depend on the damage gradient term. In other words, a purely local potential is used and the regularization is by enforcing the damage field to lie in the Lipschitz space $\mathcal{L}_\Omega$ defined as follows [101, 102].

$$\mathcal{L}_\Omega = \left\{ d \in L^\infty(\Omega) : |d(\mathbf{x}) - d(\mathbf{y})| \leq \frac{1}{l_c} dist(\mathbf{x}, \mathbf{y}) \;\; \forall \mathbf{x}, \mathbf{y} \in \Omega \right\} \tag{1.58}$$

where $dist(\mathbf{x}, \mathbf{y})$ is the minimum distance between $\mathbf{x}$ and $\mathbf{y}$ inside Ω and l_c is the regularizing length scale parameter. The spaces $\mathcal{U}_m$ and $\mathcal{A}_m$ in Eq. (1.56) are given by Eqs. (1.53, 1.54). A major advantage of this approach is that the minimization process to find the damage field can be greatly simplified by performing a local-non-local split, thanks to the bounds estimate proved in [101].

1.5.3.1 Bounds estimate and its properties

Herein, we list the properties of the bounds, which will simplify the process of Lipschitz projection of any given Lipschitz-discontinuous damage field. Consider the problem of finding only the damage field for a given displacement field u as follows (from Eq. (1.56))

$$d = \arg \min_{d' \in \mathcal{A}_m \cap \mathcal{L}_\Omega} F(\mathbf{u}, d') \tag{1.59}$$

Let us also consider a non-regularized version of the above equation

$$\overline{d} = \arg \min_{d' \in \mathcal{A}_m} F(\mathbf{u}, d') \tag{1.60}$$

Notice that d is enforced to lie in the Lipschitz space $\mathcal{L}_\Omega$ while it is not the case for $\overline{d}$. In other words, $\overline{d}$ is a local damage field. The following properties then holds for d and $\overline{d}$ [101]

$$d_m(\mathbf{x}) \leq \pi^l \overline{d}(\mathbf{x}) \leq \overline{d}(\mathbf{x}) \leq \pi^u \overline{d}(\mathbf{x}) \leq 1 \tag{1.61a}$$

$$\pi^l \overline{d}(\mathbf{x}) \leq d(\mathbf{x}) \leq \pi^u \overline{d}(\mathbf{x}) \leq 1 \tag{1.61b}$$

$$\pi^l \overline{d}(\mathbf{x}) = \pi^u \overline{d}(\mathbf{x}) \implies \overline{d}(\mathbf{x}) = d(\mathbf{x}) \in \mathcal{L}_\Omega \tag{1.61c}$$

It is evident that Eq. (1.61c) naturally follows from Eq. (1.59) in conjunction with Eqs. (1.61a, 1.61b). Here, $\pi^u \overline{d}$ and $\pi^l \overline{d}$ are upper and lower bounds, and they are defined as follows: [101]

$$\pi^u \overline{d}(\mathbf{x}) = \max_{\mathbf{y} \in \Omega} (\overline{d}(\mathbf{y}) - \frac{1}{l_c} dist(\mathbf{x}, \mathbf{y})) \qquad \forall \mathbf{x} \in \Omega \tag{1.62a}$$

$$\pi^l \overline{d}(\mathbf{x}) = \min_{\mathbf{y} \in \Omega} (\overline{d}(\mathbf{y}) + \frac{1}{l_c} dist(\mathbf{x}, \mathbf{y})) \qquad \forall \mathbf{x} \in \Omega \tag{1.62b}$$

where π^u and π^l are the upper and lower projection operators. Furthermore, we define the active zone $\overline{\Omega}$ as the region where the bounds are unequal.

$$\overline{\Omega} := \{\mathbf{x} \in \Omega : \pi^l(\overline{d}) \neq \pi^u(\overline{d})\} \tag{1.63}$$

Figure 1.33 shows the sketch of the bounds for the 1D case and the region enclosed by $[a, b]$ where the bounds are unequal indicate the active zone $\overline{\Omega}$.

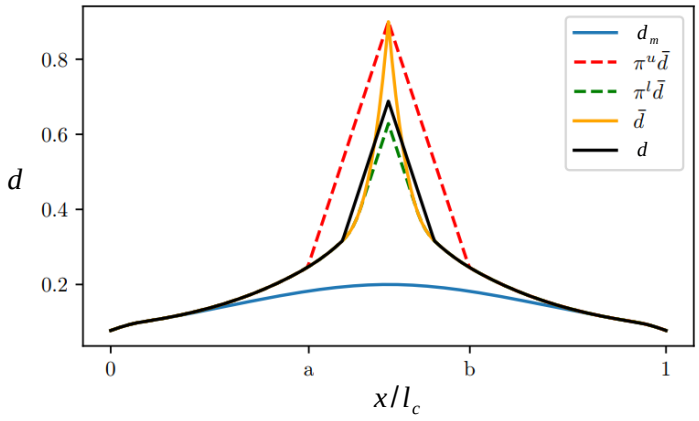

Figure 1.33 – Schematic diagram showing the bounds estimate $\pi^u \overline{d}$ and $\pi^l \overline{d}$ and its properties listed in Eq. (1.61) . The region lying inside $[a, b]$ indicate the active zone $\overline{\Omega}$ (bounds are not equal) [101]

1.5.3.2 Lipschitz projection using bounds

Here, we demonstrate the use of bounds discussed in the previous section to efficiently project any given damage field into the Lipschitz space $\mathcal{L}_\Omega$. This will be used to efficiently compute Lipschitz's continuous damage field (for equations of type Eq. (1.59)) in Chapters 4 and 5.

Let us consider the following problem,

$$d = \arg \min_{d' \in \mathcal{L}_\Omega} \int_\Omega |d' - \overline{d}|^2 \, d\Omega \tag{1.64}$$

which involves projection of any given damage field $\overline{d}$ defined over a domain Ω into a Lipschitz space $\mathcal{L}_\Omega$ using the L^2 norm. The simple strategy is to solve the above problem over the entire domain Ω using an existing optimization solver (like Matlab's optimization toolbox), which is computationally expensive. Alternatively, for an efficient implementation of a Lipschitz projection, we can make use of the properties of bounds listed in Eq. (1.61). In this case, the initial step involves computing the projection of $\overline{d}$ using Eq. (1.62), followed by the utilization of the properties detailed in Eq. (1.61) to address the following alternate problem:

$$d = \left\{ \begin{array}{ll} \overline{d} & \forall \, \mathbf{x} \in \Omega / \overline{\Omega} \\ \arg \min\limits_{d' \in \mathcal{L}_{\overline{\Omega}}} \int_{\overline{\Omega}} |d' - \overline{d}|^2 \, d\overline{\Omega} & \forall \, \mathbf{x} \in \overline{\Omega} \end{array} \right\} \tag{1.65}$$

where $\overline{\Omega}$ is the active zone as defined in Eq. (1.63). It is important to observe that the minimization task is confined to a specific subsection of the domain, denoted as $\overline{\Omega}$, in contrast to

the entirety of the domain Ω as depicted in Eq. (1.64). The above projection relatively requires less computational effort, provided some efficient algorithms are used for computing the upper and lower bounds (and thus the active zone $\overline{\Omega}$). In this thesis, a Dijkstra-based fast marching algorithm detailed in [102] has been used to compute the aforementioned bounds. It requires $O(Nlog(N))$ computations, where N is the number of nodes.

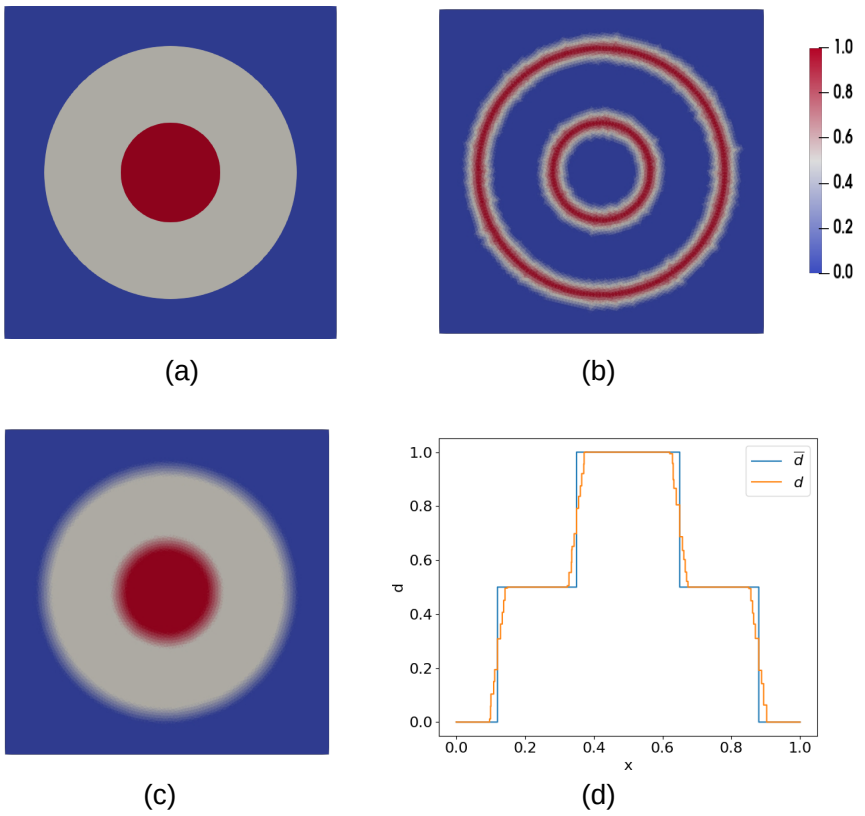

Figure 1.34 – Lipschitz projection of a Lipschitz discontinuous damage field $\overline{d}$. (a) Lipschitz discontinuous damage field $\overline{d}$ (b) difference in bounds $\pi^u\overline{d} - \pi^l\overline{d}$, with values greater than 0 indicating active zone $\overline{\Omega}$ (c) Lipschitz projection d of $\overline{d}$ and (d) $\overline{d}$ and d along the mid section

Figure 1.34, which is composed of a square domain with a unit length, illustrates the Lipschitz projection of $\overline{d}$ with a regularization length of $l_c = .1$ units using Eq. (1.65). Clearly, from Figure 1.34a, $\overline{d}$ is Lipschitz discontinuous due to the discontinuity in the normal direction along the two circles. Figure 1.34b plots the difference in bounds $\pi^u\overline{d} - \pi^l\overline{d}$, where the region marked by values greater than zero indicates the active zone $\overline{\Omega}$. In the region outside the active zone, $d = \overline{d}$ as per Eq. (1.65). Hence, the actual minimization has to be performed only in the active zone $\overline{\Omega}$. Moreover, it can be noticed from Figure 1.34b that the active zone is situated in the vicinity

of regions where there is a sharp jump in the $\overline{d}$. Figure 1.34c depicts the Lipschitz projected damage field d, while Figure 1.34d plots both $\overline{d}$ and d along the midsection of the domain. It can be seen that the regularizing length has the effect of smoothing the damage field.

1.6 Summary

This chapter outlines the key components required to fulfill the goals of the thesis concerning the modeling of cracking in viscoelastic bituminous mixtures. Initially, we introduced the structure of a road and the various issues that impact the lifespan and performance of these constructions. Following that, we discussed techniques for evaluating the properties of bituminous mixtures in both the time and frequency domains. We also presented the discrete rheological models which allow us to simulate the behavior of bituminous materials. The various laboratory tests studying cracking in bituminous materials were then discussed. Our interest was limited to the monotonous loading rates and this will be the case in subsequent chapters of the thesis. The rate and temperature dependency of the fracture in bituminous materials were also briefed. In particular, the material is likely to undergo a rupture of the ductile or brittle type, depending on the speeds and test temperatures. In the last part of this chapter, we presented the approaches to fracture mechanics and damage mechanics. Following that, we informed on the different regularization approaches to overcome the mesh dependency of the finite element solution at the onset of strain localization. Specifically, the recently developed lip-field approach was briefed, which will serve as a base for the work carried out in this thesis.

Chapter 2

Development of viscoelastic damage model: Thermodynamic framework and variational formulation

In Chapter 1, a general overview of modeling fracture in bituminous materials using different methods has been briefed. This lays the foundation for the present chapter. In this chapter, a thermodynamically consistent variational formulation to describe the damage in viscoelastic materials is developed. This model will be studied later and attempts to model fracture in bituminous materials under uni- and multi-dimensional cases will be discussed in detail in the forthcoming chapters. Chapter 2 consists of three parts: The initial section of this chapter revisits the fundamental principles of thermodynamics, delves into the Clausius-Duhem inequality, and introduces the concept of generalized standard materials as a means to fulfill the aforementioned inequality. This will allow us to ensure the thermodynamic consistency of the developed model. In the second part, the thermodynamically consistent constitutive formulation is developed, thanks to the notion of internal variables and the concept of generalized standard materials. In the third part, the mechanical governing equations and the developed constitutive equations are embedded into a variational framework, by use of an implicit time discretization. This allows us to reformulate the problem of finding the state variables as an optimization problem. Finally, to avoid ill-conditioning and pathological mesh dependence (as discussed in Section 1.5.2), the introduction of length scale through lip-field regularization will also be discussed.

2.1 Thermodynamic framework

In this section, we will provide a review of the initial two principles of thermodynamics, focusing on energy conservation, dissipation, entropy, and the Clausius-Duhem inequality. This

thermodynamic framework provides the basis for the consistent constitutive formulation.

2.1.1 First law of thermodynamics

The first law of thermodynamics states that the total energy in a system should be conserved. In other words, the combined rate of change of internal energy and kinetic energy within a thermodynamic system is equivalent to the rate of external mechanical work being done on the system, as well as the rate of heat supplied to the system through heat flux and a heat source. Mathematically, for a thermodynamic system B (with boundary ∂B), it can be expressed as

$$\dot{E} + \dot{K} = \dot{W} + \dot{Q} \tag{2.1}$$

where E and K represents the internal energy and kinetic energy of B, and W and Q represents the external mechanical work and heat supplied to B. The corresponding expression for energies, when B is assumed to be a continuum, is given below

$$E = \int_B \rho e dV \tag{2.2}$$

$$K = \int_B \frac{1}{2}\rho \mathbf{v} \,.\mathbf{v} dV \tag{2.3}$$

$$\dot{W} = \int_B \rho \mathbf{f} \,.\boldsymbol{v} dV + \int_{\partial B} \mathbf{t} \,.\mathbf{v} dS \tag{2.4}$$

$$\dot{Q} = \int_B r dV + \int_{\partial B} \mathbf{q} \,.\mathbf{n} dS \tag{2.5}$$

The variables ρ, e, and $\mathbf{v}$ correspond to the mass density, specific internal energy, and velocity, respectively. On the other hand, $\mathbf{f}$ and $\mathbf{t}$ represent the body force per unit mass acting on the region B and the traction forces on its boundary ∂B. Additionally, r, $\mathbf{q}$, and $\mathbf{n}$ signify the volumetric rate of internal heat generation within B, the outward heat flux vector on the boundary ∂B, and the outward unit normal vector on ∂B. Here, $\dot{A} = DA/Dt$ indicates the material time derivative [74].

After the application of Reynold's transport theorem to Eq. (2.1), followed by the use of conservation of mass and divergence theorem, the following expression for energy conservation in local form can be obtained [104, 74]

$$\rho \dot{e} = \boldsymbol{\sigma} : \nabla \mathbf{v} - \nabla \,.\mathbf{q} + r \tag{2.6}$$

where $\nabla \mathbf{v}$ and $\nabla \,.\mathbf{q}$ indicates the gradient of velocity and the divergence of heat flux.

2.1.2 Second law of thermodynamics

While the first law discusses only energy conservation, the second law describes the permissible direction for a non-equilibrium thermodynamic process by use of two thermodynamic variables: entropy per unit mass (s) and the absolute temperature (T). The second law states that the rate at which the entropy of a system increases is always greater than or equal to the rate at which entropy increases due to the heat source and heat flux. Mathematically, it can be expressed as

$$\frac{D}{Dt}\int_B \rho s dV \geq \int_B \frac{r}{T} dV - \int_B \frac{\mathbf{q}\,.\mathbf{n}}{T} dV \tag{2.7}$$

On the right-hand side of the equation, the terms r/T and $\mathbf{q}/T$ represent the increase in entropy resulting from heat generation and heat flow, respectively. These terms are referred to as the entropy source and entropy flux. The equality in this equation is valid for the reversible process.

By utilizing the divergence theorem together with the Reynolds transport theorem and incorporating the principle of energy conservation (Eq. (2.6)), the above inequality can be rewritten in the following local form [104, 74]

$$\boldsymbol{\sigma} : \nabla \mathbf{v} + \rho(T\dot{s} - \dot{e}) - \mathbf{q}.\frac{\nabla T}{T} \geq 0 \tag{2.8}$$

By using the following definition of Helhmohtz free energy per unit mass Ψ

$$\Psi = e - Ts \tag{2.9}$$

to eliminate internal energy in Eq. (2.8) results in the following inequality

$$\boldsymbol{\sigma} : \nabla \mathbf{v} - \rho(\dot{\Psi} + \dot{T}s) - \mathbf{q}.\frac{\nabla T}{T} \geq 0 \tag{2.10}$$

The equation mentioned above is referred to as the *Clausius-Duhem inequality* and must be fulfilled for all possible processes[105, 104, 74]. Hence, this inequality establishes crucial limitations on constitutive equations and serves as the basis for the thermodynamic constitutive theory governing the dissipative behavior of a continuum.

Remark 1 *In our case (for the thesis), the focus lies within the small strain region with no heat fluxes and no internal heat generation. Moreover, we limit ourselves to the isothermal ($\dot{T} = 0$) and uniform temperature ($\nabla T = \vec{0}$) setting. In this case, Eq. (2.6) and Eq. (2.10) yields the following*

$$\rho\dot{e} = \boldsymbol{\sigma} : \dot{\boldsymbol{\varepsilon}} \tag{2.11}$$

$$\Phi = \boldsymbol{\sigma} : \dot{\boldsymbol{\varepsilon}} - \rho\dot{\Psi} \geq 0 \tag{2.12}$$

where Φ *denotes the dissipation per unit volume.*

2.1.3 Generalized Standard Materials

An advanced method for constructing constitutive models for dissipative systems is presented by the generalized standard materials framework put forth by Halphen and Nguyen (1975) [106]. This approach facilitates the creation of evolutionary models that can be designed to inherently satisfy the Clausius-Duhem inequality.

Let $\boldsymbol{\alpha}$ be the finite set of internal variables (apart from the external state variable $\boldsymbol{\varepsilon}$) and $\boldsymbol{\mathcal{A}}$ be the driving forces associated with the internal variables. Let $\psi(\boldsymbol{\varepsilon}, \boldsymbol{\alpha})$ indicate the free energy per unit volume of the system (material). The thermodynamic forces associated with the state variables can be described by the derivative of free energy $\psi(\boldsymbol{\varepsilon}, \boldsymbol{\alpha})$ with respect to the state variables

$$\boldsymbol{\sigma} = \frac{\partial \psi}{\partial \varepsilon} \qquad \boldsymbol{\mathcal{A}} = -\frac{\partial \psi}{\partial \boldsymbol{\alpha}} \tag{2.13}$$

The evolution of internal variables $\boldsymbol{\alpha}$ can be given by considering a dissipation potential $\phi^*(\boldsymbol{\mathcal{A}})$

$$\dot{\boldsymbol{\alpha}} = \frac{\partial \phi^*}{\partial \boldsymbol{\mathcal{A}}} \qquad (or) \qquad \boldsymbol{\mathcal{A}} = \frac{\partial \phi}{\partial \dot{\boldsymbol{\alpha}}} \tag{2.14}$$

where $\phi(\boldsymbol{\mathcal{A}})$ and $\phi^*(\dot{\boldsymbol{\alpha}})$ are Legendre-Fenchel transforms of each other and are given by

$$\phi(\dot{\boldsymbol{\alpha}}) = \sup_{\boldsymbol{\mathcal{A}}}(\boldsymbol{\mathcal{A}}\dot{\boldsymbol{\alpha}} - \phi^*(\boldsymbol{\mathcal{A}})) \qquad \phi^*(\boldsymbol{\mathcal{A}}) = \sup_{\dot{\boldsymbol{\alpha}}}(\boldsymbol{\mathcal{A}}\dot{\boldsymbol{\alpha}} - \phi(\dot{\boldsymbol{\alpha}})) \tag{2.15}$$

We also consider ψ and ϕ to be convex functions such that

$$\phi(\dot{\boldsymbol{\alpha}}) \geq 0, \qquad \phi(\mathbf{0}) = 0 \tag{2.16}$$

When ψ and ϕ are convex functions of their arguments ($(\boldsymbol{\varepsilon}, \boldsymbol{\alpha})$ and $\dot{\boldsymbol{\alpha}}$) satisfying Eq. (2.16), then the material governed by Eq. (2.13) and Eq. (2.14) is said to be Generalized Standard Materials [106, 107, 108]. If ϕ is differentiable, Eq. (2.14b) holds. For a non-differentiable function, since ϕ is convex, the notion of gradients can be replaced by the more general notion of sub-gradients (or sub-differentials) $\partial\phi$. In this case, $\boldsymbol{\mathcal{A}} \in \partial\phi$ (or equivalently $\dot{\boldsymbol{\alpha}} \in \partial\phi^*$). For ϕ convex, the sub-differential is defined as follows:

$$\partial\phi(\dot{\boldsymbol{\alpha}}) = \{\boldsymbol{\beta} : \phi(\boldsymbol{\alpha}^*) - \phi(\dot{\boldsymbol{\alpha}}) \geq \boldsymbol{\beta}.(\boldsymbol{\alpha}^* - \dot{\boldsymbol{\alpha}}) \ \forall \ \text{admissible} \ \ \boldsymbol{\alpha}^*\} \tag{2.17}$$

$\boldsymbol{\mathcal{A}} \in \partial\phi(\dot{\boldsymbol{\alpha}})$ ensures that the dissipation $\boldsymbol{\mathcal{A}}.\dot{\boldsymbol{\alpha}}$ is positive. In particular, this can be verified by

substituting $\boldsymbol{\alpha}^* = \mathbf{0}$ in Eq. (2.17) and by making use of Eq. (2.16)

$$\boldsymbol{\beta}.\dot{\boldsymbol{\alpha}} \geq 0 \tag{2.18}$$

This framework, thus ensures the positivity of dissipation, leading to an irreversible change in behavior for dissipative systems.

2.2 Thermodynamic Constitutive Theory of Viscoelasticity with Internal Variables

In this section, the consistent constitutive theories for viscoelastic materials subjected to damage will be discussed on the basis of the thermodynamic potential functions and the Clausius-Duhem inequality.

We recall the assumption that the deformation is small. As seen in Section 1.2.6, it is often convenient to characterize the mechanical response of a viscoelastic material using a discrete spectral approach through the incorporation of several internal variables (viscous strains).

$$\{\boldsymbol{\varepsilon}_i;\ i = 1, 2, ..., n\}. \tag{2.19}$$

where $\boldsymbol{\varepsilon}_i$ are the viscous strains in tensor form. Hereafter, $\boldsymbol{\varepsilon}_i$ will be used to represent the set of all viscous strains.

In addition to the standard internal variables (viscous strains), an internal scalar damage variable d (or D) is used to represent locally the state of damage in the system (see Section 1.5). Hence the following set denotes the set of state variables [1]

$$\{\boldsymbol{\varepsilon}, \boldsymbol{\varepsilon}_i, d\} \tag{2.20}$$

where $\boldsymbol{\varepsilon}$ (small strain tensor) is the only external variable (observable). We postulate that the Helmholtz free energy per unit mass (or specific free energy [2]) Ψ of the considered viscoelastic material can be expressed as a function of the above set of state variables.

$$\Psi = \Psi(\boldsymbol{\varepsilon}, \boldsymbol{\varepsilon}_i, d) \tag{2.21}$$

1. Temperature T ignored from the set of state variables for isothermal and uniform temperature setting
2. Ψ and ψ are used to indicate specific free energy and free energy per unit volume respectively.

The time derivative of the above potential yields the following

$$\dot{\Psi} = \frac{\partial \Psi}{\partial \boldsymbol{\varepsilon}} : \dot{\boldsymbol{\varepsilon}} + \frac{\partial \Psi}{\partial \boldsymbol{\varepsilon}_i} : \dot{\boldsymbol{\varepsilon}}_i + \frac{\partial \Psi}{\partial d}\dot{d} \tag{2.22}$$

On substitution of the above equation into Claussis-Duhem inequality (Eq. (2.12)) yields the following

$$\Phi = (\boldsymbol{\sigma} - \rho\frac{\partial \Psi}{\partial \boldsymbol{\varepsilon}}) : \dot{\boldsymbol{\varepsilon}} - \rho\frac{\partial \Psi}{\partial \boldsymbol{\varepsilon}_i} : \dot{\boldsymbol{\varepsilon}}_i - \rho\frac{\partial \Psi}{\partial d}\dot{d} \geq 0 \tag{2.23}$$

The above relation should hold for every thermodynamic process described by the free energy potential Ψ. Hence, for the special case of elastic deformation without damage, the above inequality becomes

$$\Phi = (\boldsymbol{\sigma} - \rho\frac{\partial \Psi}{\partial \boldsymbol{\varepsilon}}) : \dot{\boldsymbol{\varepsilon}} \geq 0 \tag{2.24}$$

The preceding inequality should be satisfied for any choice of $\dot{\boldsymbol{\varepsilon}}$. Hence, the following equation (state or constitutive equation) should hold

$$\boldsymbol{\sigma} = \rho\frac{\partial \Psi}{\partial \boldsymbol{\varepsilon}} \tag{2.25}$$

When the constitutive equation mentioned above is substituted back into Eq. (2.23), it leads to the subsequent inequality.

$$\Phi = -\rho\frac{\partial \Psi}{\partial \boldsymbol{\varepsilon}_i} : \dot{\boldsymbol{\varepsilon}}_i - \rho\frac{\partial \Psi}{\partial d}\dot{d} \geq 0 \tag{2.26}$$

By defining the thermodynamic forces $(\boldsymbol{\sigma}_i, Y)$ conjugate to state variables $(\boldsymbol{\varepsilon}_i, d)$ in the following way

$$\boldsymbol{\sigma}_i = -\rho\frac{\partial \Psi}{\partial \boldsymbol{\varepsilon}_i} = -\frac{\partial \psi}{\partial \boldsymbol{\varepsilon}_i} \tag{2.27}$$

$$Y = -\rho\frac{\partial \Psi}{\partial d} = -\frac{\partial \psi}{\partial d} \tag{2.28}$$

and replacing them in Eq. (2.26), the equation can be simplified to

$$\Phi = \boldsymbol{\sigma}_i : \dot{\boldsymbol{\varepsilon}}_i + Y\dot{d} \geq 0 \tag{2.29}$$

The above equation is referred to as the dissipation inequality (Φ is the intrinsic dissipation), which asserts that the dissipation resulting from the alteration of the internal state is always

non-negative.

It was shown that the constitutive equation associated with the external state variable $\boldsymbol{\varepsilon}$ is given by the free energy potential Ψ and Eq. (2.25). However, the description of the evolution of internal state variables necessitates the constitutive equation associated with them. Moreover, for these equations to be consistent, they should also satisfy the dissipation inequality given by Eq. (2.29). For this, we make the assumption of generalized standard materials (see Section 2.1.3). This allows us to define a free energy potential per unit mass Ψ and a dissipation potential ϕ, both being convex. We make an additional assumption that the dissipation potential can be additively decomposed into a viscous dissipation potential (associated with viscous strains) and a damage dissipation potential (associated with damage), such that both are convex [3] while also satisfying Eq. (2.16).

$$\phi(\dot{\boldsymbol{\varepsilon}}_i, d, \dot{d}) = \phi_v(\dot{\boldsymbol{\varepsilon}}_i) + \phi_d(\dot{d}) \tag{2.30}$$

Notice that, ϕ_v is not a function of damage d. More comments on this will be made in the subsequent sections. We can then write the following relation between thermodynamic forces and dissipation potentials [108]

$$\boldsymbol{\sigma}_i = \frac{\partial \phi}{\partial \dot{\boldsymbol{\varepsilon}}_i} = \frac{\partial \phi_v}{\partial \dot{\boldsymbol{\varepsilon}}_i} \tag{2.31}$$

$$Y = \frac{\partial \phi}{\partial \dot{d}} = \frac{\partial \phi_d}{\partial \dot{d}} \tag{2.32}$$

Equating Eq. (2.27-2.28) and Eq. (2.31-2.32) results in the following set of constitutive equations associated with the internal variables $\boldsymbol{\varepsilon}_i$ and d

$$\frac{\partial \psi}{\partial \boldsymbol{\varepsilon}_i} + \frac{\partial \phi_v}{\partial \dot{\boldsymbol{\varepsilon}}_i} = 0 \tag{2.33}$$

$$\frac{\partial \psi}{\partial d} + \frac{\partial \phi_d}{\partial \dot{d}} = 0 \tag{2.34}$$

Furthermore, the dissipation related to internal variables can be reformulated by utilizing Eq. (2.31 - 2.32) in the following manner:

$$\Phi = \boldsymbol{\sigma}_i : \dot{\boldsymbol{\varepsilon}}_i + Y\dot{d} = \frac{\partial \phi_v}{\partial \dot{\boldsymbol{\varepsilon}}_i} : \dot{\boldsymbol{\varepsilon}}_i + \frac{\partial \phi_d}{\partial \dot{d}}\dot{d} \tag{2.35}$$

In reference to the Section 2.1.3 on generalized standard materials, here $\dot{\boldsymbol{\alpha}} = \{\dot{\boldsymbol{\varepsilon}}_i, \dot{d}\}$ and $\boldsymbol{\mathcal{A}} = \{\boldsymbol{\sigma}_i, Y\}$. Since $\boldsymbol{\mathcal{A}} \in \partial\phi(\dot{\boldsymbol{\alpha}})$ (from Eq. (2.31) and Eq. (2.32)), the positivity of dissipation is ensured as per the arguments made in Section 2.1.3.

3. ϕ_v convex w.r.t $\dot{\varepsilon}_i$ and ϕ_d convex w..r.t $\dot{d}$

2.3 Variational framework

In this section, the mechanical problem of finding the state variables is written in a variational framework. By variational, we imply that an incremental potential will be proposed (in line with the works of [109, 110, 108] on variationally consistent incremental principles for dissipative systems) such that the minimization of this incremental potential at every time instant provides the solution to the mechanical problem. This incremental formalism inherently incorporates a fully implicit time discretization. These methods also exhibit appealing characteristics as they provide possibilities for extensive mathematical and numerical analysis [111].

Let's examine the deformation of a body that initially occupies a domain Ω and undergoes deformation via a displacement field $\mathbf{u}$. In this analysis, we assume small, isotropic, and quasi-static deformations occurring under isothermal conditions. The Cauchy stress and small strain tensor are represented by $\boldsymbol{\sigma}$ and $\boldsymbol{\varepsilon}$, respectively.

$$\boldsymbol{\varepsilon(u)} = \frac{1}{2}(\nabla \mathbf{u} + \nabla^T \mathbf{u}) \tag{2.36}$$

Concerning the boundary conditions, we impose displacement on a specific section of the boundary denoted as Γ_u. Additionally, we assume that the remaining portion of the boundary (denoted as Γ_N) experiences zero traction forces, and there are no body forces present (without loss of generality). In order to ensure kinematic admissibility at any given time t, the displacement field $\mathbf{u}$ must belong to $\mathcal{U}(t)$.

$$\mathcal{U}(t) = \{\mathbf{u} \in H^1(\Omega) : \mathbf{u} = \mathbf{u_d}(t) \;\; on \;\; \Gamma_u\} \tag{2.37}$$

The equilibrium condition then reads

$$\int_\Omega \boldsymbol{\sigma} : \varepsilon(\mathbf{u}^*)\, d\Omega = 0, \quad \forall\, \mathbf{u}^* \in \mathcal{U}^* \tag{2.38}$$

where

$$\mathcal{U}^* = \{\mathbf{u} \in H^1(\Omega) : \mathbf{u} = 0 \;\; on \;\; \Gamma_u\} \tag{2.39}$$

The equilibrium and the kinematic equations must be complemented by the constitutive equations (Eqs. (2.21, 2.25) and Eqs. (2.30, 2.33, 2.34)).

The time domain under investigation, denoted as $[0, T_e]$, is divided into time intervals $t_0, t_1, ..., t_m, t_{m+1}, ..., t_M = T_e$. Here, $t_{m+1} - t_m = t - t_m = \Delta t$, with the index $m+1$ dropped for simplicity. This convention will be adopted for all state variables throughout the remainder of the thesis. Therefore, $\boldsymbol{\varepsilon_m}, \boldsymbol{\varepsilon_{i,m}}, d$ and $\boldsymbol{\varepsilon}, \boldsymbol{\varepsilon_i}, d$ are employed to represent the material state at time steps t_m

and $t_{m+1} = t$ respectively. An implicit Euler time discretization method has been utilized to discretize the time derivative of internal strains.

$$\dot{\boldsymbol{\varepsilon}}_{\boldsymbol{i,m+1}} = \dot{\boldsymbol{\varepsilon}}_{\boldsymbol{i}} = \frac{(\boldsymbol{\varepsilon_i} - \boldsymbol{\varepsilon_{i,m}})}{\Delta t} \tag{2.40}$$

The above equation can be used to rewrite the evolution equation (or constitutive equation) for the internal strain (or viscous strain) $\boldsymbol{\varepsilon}_i$ (given by Eq. (2.33)) in time discretized form (or incremental form) as follows:

$$\frac{\partial \psi}{\partial \boldsymbol{\varepsilon}_i} + \frac{\partial \phi_v}{\partial \dot{\boldsymbol{\varepsilon}}_i} \approx \frac{\partial \psi}{\partial \boldsymbol{\varepsilon}_i} + \frac{\partial \phi_v}{\partial \varepsilon_i}\frac{\partial \boldsymbol{\varepsilon}_i}{\partial \dot{\boldsymbol{\varepsilon}}_i} \approx \frac{\partial \psi}{\partial \boldsymbol{\varepsilon}_i} + \Delta t \frac{\partial \phi_v}{\partial \varepsilon_i} = 0 \tag{2.41}$$

As Δt becomes sufficiently small, the discretized evolution equation for the internal strain converges to the time-continuous evolution equation.

Up to this point, no specific limitation has been imposed on the rate of damage evolution, $\dot{d}$. This lack of restriction permits the consideration of self-healing mechanisms. However, in our particular case, we confine ourselves to scenarios where no self-healing mechanism exists. Consequently, we introduce the constraint of damage irreversibility, expressed as $\dot{d} \geq 0$. The evolution laws governing damage are subsequently selected in the following manner (as opposed to Eq. (2.34)):

$$\dot{d} \geq 0, \qquad -\frac{\partial \psi}{\partial d} - \frac{\partial \phi_d}{\partial \dot{d}} \leq 0, \qquad \left(-\frac{\partial \psi}{\partial d} - \frac{\partial \phi_d}{\partial \dot{d}}\right)\dot{d} = 0 \tag{2.42}$$

In the aforementioned scenario, the evolution of damage is solely driven by the free energy. However, it is possible to consider alternative evolution laws where a portion of viscous dissipation also contributes to driving the damage (e.g., as seen in [97] for modeling creep-induced damage). However, this prohibits the energy conservation of the model. By defining the damage dissipation potential ϕ_d in the following manner

$$\phi_d = Y_c H(d)\dot{d} \tag{2.43}$$

the damage evolution laws (Eq. (2.42)) can be rewritten in the following manner (using Eq. (2.28))

$$\dot{d} \geq 0, \qquad Y - Y_c H(d) \leq 0, \qquad (Y - Y_c H(d))\dot{d} = 0 \tag{2.44}$$

where Y_c (> 0) is the critical energy release rate per unit volume (a material parameter) and $H(d)$ is the softening function (an increasing function) that governs the damage evolution behavior. The dependence of Y_c on an increasing function $H(d)$ is to avoid catastrophic failure. Moreover,

the choice of $H(d)$ dictates the softening shape of the stress-strain curve. Hence, an appropriate choice of $H(d)$ holds considerable importance particularly for quasi-brittle fracture (as is the case in bituminous materials), where the size of the fracture process zone is relatively large compared to the structure size.

ϕ_d being convex w.r.t $\dot{d}$ (from Eq. (2.43)), it is necessary for ϕ_d to satisfy Eq. (2.16) in order to align with the assumption of generalized standard materials. This condition implies that $H(d) \geq 0$ (in Eq. (2.43)) due to the constraint that $\dot{d} \geq 0$. In particular, we make the following choice to have a non-zero material resistance to damage

$$H(d) > 0 \tag{2.45}$$

Assuming all the state variables are known at time t_m, the mechanical problem to find state variables at time $t_{m+1} = t$ can now be rewritten as the following optimization problem

$$(\mathbf{u}, \boldsymbol{\varepsilon_i}, d) = \arg \min_{\substack{\mathbf{u}' \in \mathcal{U}_m \\ \boldsymbol{\varepsilon}'_i \in \mathcal{P} \\ d' \in \mathcal{A}_m}} F(\mathbf{u}', \boldsymbol{\varepsilon}'_i, d' \ ; \ \mathbf{u_m}, \boldsymbol{\varepsilon_{i,m}}, d_m, \Delta t) \tag{2.46}$$

$$F = \int_\Omega f \ d\Omega = \int_\Omega \psi(\boldsymbol{\varepsilon}, \boldsymbol{\varepsilon_i}, d) + \Delta t \phi_v(\boldsymbol{\varepsilon}_i; \Delta t) + Y_c h(d) d\Omega \tag{2.47}$$

where

$$h(d) = \int_0^d H(\tilde{d}) d\tilde{d} \tag{2.48}$$

and $\psi = \rho\Psi$ is the Helmholtz free energy per unit volume. The admissible spaces for the kinematic and damage fields are given as follows

$$\mathcal{U}_m = \mathcal{U}(t_{m+1}) = \mathcal{U}(t) \tag{2.49}$$

$$\mathcal{P} = \{\mathbf{q} : \mathbf{q}_{ij} = \mathbf{q}_{ji}, \ \mathbf{q}_{ij} \in L^\infty(\Omega)\} \tag{2.50}$$

$$\mathcal{A}_m = \{d \in L^\infty(\Omega) : d_m \leq d \leq 1\} \tag{2.51}$$

The minimization problem given by Eq. (2.46) [4] results in the equilibrium equation (Eq. (2.38)) and the evolution equation for the internal variables (Eqs. (2.41, 2.44)) (see Appendix A).

4. In the case where ϕ_v is also a function of damage, the minimization of F w.r.t d would result in the following evolution equation for d

$$\dot{d} \geq 0, \qquad -\frac{\partial \psi}{\partial d} - \Delta t \frac{\partial \phi_v}{\partial d} - Y_c H(d) \leq 0, \qquad \left(-\frac{\partial \psi}{\partial d} - \Delta t \frac{\partial \phi_v}{\partial d} - Y_c H(d)\right) \dot{d} = 0 \tag{2.52}$$

which also results in a part of the viscous dissipation driving the damage, thereby violating the principle of energy conservation. Hence, such a scenario is not considered in this work.

Note that F is not convex leading to several local minima and also non-uniqueness to the global minimum (several solutions leading to same global minima) [101]. However, the formalism of generalized standard materials ensures that the incremental potential is convex with respect to each state variable separately (provided $h(d)$ is convex). On the other hand, the admissible spaces (Eq. (2.49-2.51)) are also convex. As will be seen in the subsequent chapters, this will enable us to use the alternate minimization at each time step where the (convex) minimization with respect to each variable is performed separately in a repeated manner until convergence [101, 102].

Lip-field regularization

The minimization problem given by Eq. (2.46) is an ill-posed problem for $d \in \mathcal{A}_m$, leading to pathological mesh-dependent results (Section 1.5.2). To overcome this issue, we rely on the Lip-field approach to introduce length scale into the model. This approach solves for the following different problem by enforcing $d \in \mathcal{A}_m \cap \mathcal{L}_\Omega$.

$$\{\mathbf{u}, \boldsymbol{\varepsilon_i}, d\} = \arg \min_{\substack{\mathbf{u}' \in \mathcal{U}_m \\ \boldsymbol{\varepsilon}'_{\boldsymbol{i}} \in \mathcal{P} \\ d' \in \mathcal{A}_m \cap \mathcal{L}_\Omega}} F(\mathbf{u}', \boldsymbol{\varepsilon}'_{\boldsymbol{i}}, d' \ ; \ \mathbf{u_m}, \boldsymbol{\varepsilon_{i,m}}, d_m, \Delta t) \tag{2.53}$$

where F is given by Eq. (2.53). The space $\mathcal{L}_\Omega$ is called the Lipschitz space and is defined as follows [101, 102]

$$\mathcal{L}_\Omega = \left\{ d \in L^\infty(\Omega) : |d(\mathbf{x}) - d(\mathbf{y})| \leq \frac{1}{l_c} dist(\mathbf{x}, \mathbf{y}) \ \ \forall \ \mathbf{x}, \mathbf{y} \in \Omega \right\} \tag{2.54}$$

where $dist(\mathbf{x}, \mathbf{y})$ is the minimum distance between $\mathbf{x}$ and $\mathbf{y}$ inside Ω and l_c is the regularizing length scale parameter. The optimization problem given by Eq. (2.46) is the same as Eq. (2.52), except that the gradient of damage is bounded by a critical value. The constant $1/l_c$ is called the Lipschitz constant. It should be noted that the space $\mathcal{L}_\Omega$ is also convex. Hence, the aforementioned alternate minimization could still be employed.

2.4 Summary

The present chapter deals with the development of a thermodynamically consistent viscoelastic damage model, where the viscoelastic behavior is represented by the use of discrete spectrum models (through the use of internal variables). This model thus ensures energy conservation and the positivity of dissipation. Subsequently, the mechanical problem has been reformulated as an optimization problem, through the definition of an appropriate incremental potential. Finally, to overcome the pathological mesh-dependent issues, lip-field regularization has been

used to regularize the problem. In the following chapters, the focus will lie on the numerical implementation and studying the behavior of the developed model in uni- and multi-dimensional cases.

Chapter 3

Formulation of a 1D Viscoelastic Damage Model

In Chapter 2, we developed a thermodynamically consistent mechanical model to represent damage in viscoelastic materials. Moreover, a variational framework was also presented. The variational framework embodies in itself the equilibrium and the constitutive equations. Moreover, it also allows us to rewrite the mechanical problem of finding the state variables as an optimization problem. To avoid spurious mesh dependency, we have seen that the damage field can be forced to lie in the Lipschitz space (lip-field regularization). In the present chapter, we consider the numerical implementation and then study the model behavior for the 1D homogeneous bar under applied monotonous displacement rates. In particular, we consider two different viscoelastic damage models: one associated with the Generalized Kelvin-Voigt (GKV) model and the other associated with the Generalized Maxwell (GM) model.

Chapter 3 consists of five parts: In the first part, the governing and the constitutive equations for the viscoelastic damage model using the GKV model are presented, followed by the numerical implementation and validation with the analytical solution. The simulation results are then presented for different applied displacement rates. Unlike in softening elasticity [101], a homogeneous evolution of damage is observed for a time period before the damage localizes. To understand such behavior, in part 2, we perform Lyapunov's stability analysis, which reveals the presence of intrinsic time scale associated with damage for the viscoelastic damage models in the 1D homogeneous case. In part 3, we consider a different viscoelastic damage model, the one associated with the GM model. It will also be seen from numerical experiments that both damage models (GKV and GM models) exhibit the same mechanical behavior. In part 4, we consider the case of a 1D non-homogeneous bar (with different notch sizes) to study the influence of non-homogeneity on the aforementioned intrinsic time scale. Finally, we conclude this chapter with a summary and a general discussion of the results obtained using the developed model.

3.1 Softening Generalized Kelvin-Voigt (GKV) model

In this section, we consider the softening Generalized Kelvin-Voigt model (GKV) to describe the viscoelastic behavior with damage. The schematic of the GKV model with damage is shown in Figure 3.1. Here, $E_0, E_1, .., E_n$ and $\tau_1, \tau_2 ..., \tau_n$ represent the relaxation modulus (of the springs) and the retardation times (of the dashpots) of the GKV model. The notion of viscosity η_i of the dashpot i can also be used in place for the retardation times τ_i and they are related as follows:

$$\eta_i = \tau_i \, . \, E_i \tag{3.1}$$

The damage d is then introduced by the use of a degradation function $g(d)$ (as indicated in Figure 3.1) that affects the material's capability to store free energy.

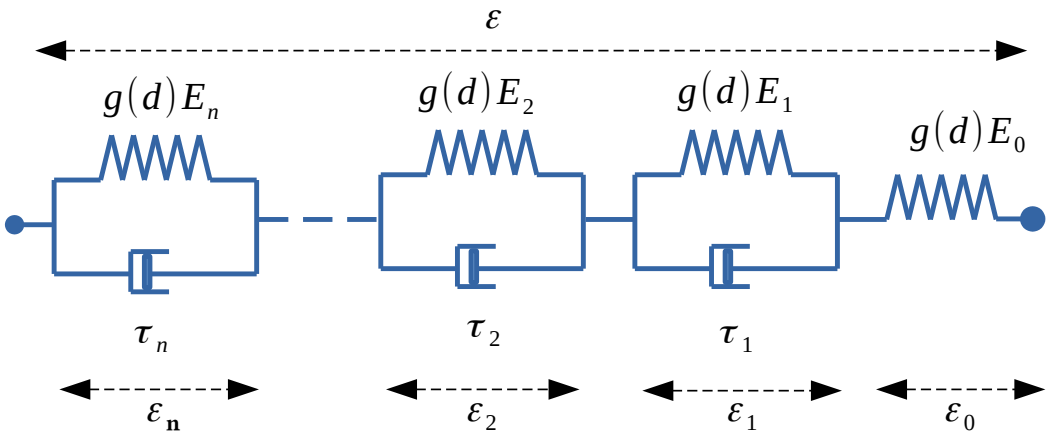

Figure 3.1 – Generalized Kelvin-Voigt (GKV) model with damage

The free energy per unit volume of the GKV model with damage is given by

$$\psi = g(d) \left[\frac{1}{2} E_0 (\varepsilon - \sum_{i=1}^{n} \varepsilon_i)^2 + \sum_{i=1}^{n} \frac{1}{2} E_i \varepsilon_i^2 \right] = g(d) \psi_0 \tag{3.2}$$

where ψ_0 is the undamaged free energy. $g(d)$ is such that

$$g(d=0) = 1, \qquad g(d=1) = 0, \qquad g''(d) \geq 0 \;\; \forall \;\; d \; \in \; [0,1] \tag{3.3}$$

The last condition that the second derivative of the degradation function should be positive ensures that $g(d)$ is convex and thus the convexity of the free energy potential. The viscous

dissipation potential for the respective model is given by

$$\phi_v = \sum_{i=1}^{n} \frac{1}{2}\eta_i \dot{\varepsilon}_i^2 \approx \sum_{i=1}^{n} \frac{1}{2}\eta_i \left(\frac{\varepsilon_{i,m+1} - \varepsilon_{i,m}}{\Delta t}\right)^2 = \sum_{i=1}^{n} \frac{1}{2}\eta_i \left(\frac{\varepsilon_i - \varepsilon_{i,m}}{\Delta t}\right)^2 \tag{3.4}$$

where m and $m+1$ are the time step indices at the previous and current time step and the $m+1$ indices are neglected for simplicity as explained in Section 2.3. Recall from Chapter 2 that the viscous dissipation potential is not directly a function of the damage to ensure energy conservation (Eq. (2.52)). This is reflected in Figure 3.1 where the damage only affects the springs and not the dashpots. Moreover, it is the variational consistency that puts the restriction on viscous dissipation not being a function of damage. This is not the case in [100] where the Thick Level Set (TLS) approach is used to model damage in viscoelasticity. In the latter, despite the damage being driven only by free energy, the viscous dissipation potential was considered still a function of damage. However, such models are not variationally consistent (inability to reformulate the problem as a minimization of a single incremental potential).

Herein, we recall the expression for the damage dissipation potential. (using Eqs. (2.43, 2.48))

$$\phi_d = Y_c H(d)\dot{d} = Y_c h'(d)\dot{d} \tag{3.5}$$

The thermodynamic forces conjugate to the state variables are given as follows (utilizing the Eqs (2.25,2.27,2.28)):

$$\sigma = \frac{\partial \psi}{\partial \varepsilon} = g(d)E_0(\varepsilon - \sum_{i=1}^{n} \varepsilon_i) \tag{3.6}$$

$$\sigma_i = -\frac{\partial \psi}{\partial \varepsilon_i} = \sigma - g(d)E_i\varepsilon_i \tag{3.7}$$

$$Y = -\frac{\partial \psi}{\partial d} = -g'(d)\left[\frac{1}{2}E_0(\varepsilon - \sum_{i=1}^{n} \varepsilon_i)^2 + \sum_{i=1}^{n} \frac{1}{2}E_i\varepsilon_i^2\right] \tag{3.8}$$

where σ is the stress in each Kelvin-Voigt (KV) unit [1] (Cauchy stress), σ_i is the viscous stress in the dashpot with viscosity η_i and Y is the local energy release rate associated with damage. The thermodynamic forces conjugate to viscous strains can also be written as follows (from Eq. (2.31))

$$\sigma_i = \frac{\partial \phi_v}{\partial \dot{\varepsilon}} = \eta_i \dot{\varepsilon}_i \tag{3.9}$$

1. For the GKV model shown in Figure 3.1, the stress in each Kelvin-Voigt (KV) is the same as the stress in the free spring (indicated by E_0), since all the units are connected in series.

The damage evolution laws can be rewritten using Eq. (2.44) and Eq. (2.48)

$$\dot{d} \geq 0, \qquad Y - Y_c h'(d) \leq 0, \qquad (Y - Y_c h'(d))\dot{d} = 0 \tag{3.10}$$

Eq. (3.8) and Eq. (3.10) form the constitutive equations describing the damage evolution in the viscoelastic material using the Generalized Kelvin-Voigt (GKV) model.

Consider a 1D homogeneous bar occupying the domain $\Omega := [0, L]$, where L is the length of the bar. The considered bar is fixed at one end, and the displacements are applied (monotonous displacement rate) at the other end as shown in Figure 3.2.

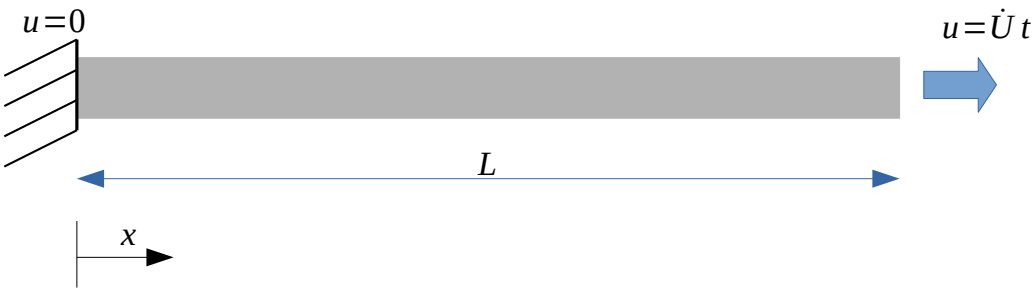

Figure 3.2 – 1D homogeneous bar with displacement applied at right end and fixed at the other end

The applied displacement rate $\dot{U} = \dot{a}L$, where a is used to indicate the total strain in the bar. The problem to find the mechanical fields at time $t_{m+1} = t$ is then reduced to the following optimization problem (from Eq. (2.53))

$$(u, \varepsilon_i, d) = \arg \min_{\substack{u' \in \mathcal{U}_m \\ \varepsilon_i{}' \in \mathcal{P} \\ d' \in \mathcal{A}_m \cap \mathcal{L}_\Omega}} F(u', \varepsilon_i{}', d' \ ; \ u_m, \varepsilon_{i,m}, d_m, \Delta t) \tag{3.11}$$

$$F = \int_0^L f \ dx = \int_0^L \psi(\varepsilon, \varepsilon_i, d) + \Delta t \phi_v(\varepsilon_i; \Delta t) + Y_c h(d) \ dx \tag{3.12}$$

The admissible spaces for the kinematic and damage fields are given as follows (see Eq. (2.49-2.51) and Eq. (2.54)):

$$\mathcal{U}_m = \mathcal{U}(t) = \{u \in H^1(\Omega) : u(x = 0, t) = 0, \ u(x = L, t) = \dot{U}t\} \tag{3.13}$$

$$\mathcal{P} = \{q : q \in L^\infty(\Omega)\} \tag{3.14}$$

$$\mathcal{A}_m = \{d \in L^\infty(\Omega) : d_m \leq d \leq 1\} \tag{3.15}$$

$$\mathcal{L}_\Omega = \left\{ d \in L^\infty(\Omega) : |d(x) - d(y)| \leq \frac{1}{l_c} dist(x, y) \ \ \forall x, y \in \Omega \right\} \tag{3.16}$$

Recall that the equilibrium equation and the constitutive equations associated with the internal variables are embedded naturally in the minimization problem given by Eq. (3.11) (as shown in Appendix A).

3.1.1 Numerical implementation

As discussed earlier in Section 2.3, F is not convex but F is convex with respect to the sets $\{u, \varepsilon_i\}$ and $\{d\}$ separately. Moreover, the admissible spaces for state variables are also convex. Hence an alternate minimization strategy can be used at each time step to solve for $\{u, \varepsilon_i\}$ by fixing d, followed by solving for $\{d\}$ by fixing $\{u, \varepsilon_i\}$. This process has to be repeated until convergence. The k^{th} iteration of the alternate minimization for a given time step $t_{m+1} = t$ can be expressed as follows [2]

$$(u^{k+1}, \varepsilon_i^{k+1}) = \arg \min_{\substack{u' \in \mathcal{U}_m \\ \varepsilon_i{}' \in \mathcal{P}}} F(u', \varepsilon_i{}', d^k) \tag{3.17}$$

$$(d^{k+1}) = \arg \min_{d' \in \mathcal{A}_m \cap \mathcal{L}_\Omega} F(u^{k+1}, \varepsilon_i{}^{k+1}, d') \tag{3.18}$$

Both problems are convex. Hence, it leads to a series of convex optimization problems. However, it should be noted that the converged solution of the alternate minimization does not necessarily lead to the global minimum. Moreover, since only the first-order optimality conditions are used for the alternate minimization (as will be seen shortly), the converged solution could also be a non-stable solution (local maximum). This could be a limitation of the alternate minimization. For example, in [112], to overcome the limitation of alternate minimization, second-order stability criteria have been used to filter out the unstable modes for the phase-field fracture in the quasi-static case. Nevertheless, exploring such approaches falls beyond the scope of the present research, and thus, we adhere to the conventional method of alternate minimization.

3.1.1.1 Finding displacements and internal strains

We now look into the first problem given by Eq. (3.17) [3]. The minimization of F with respect to u results in the equilibrium equation

$$\int_0^L \sigma\varepsilon(u^*)dx = 0 \tag{3.19}$$

2. Here, we distinguish between the indices of internal (or viscous) strains, time steps and iterations. The indices of internal strains (i) and time steps (m) are annotated as subscripts separated by a comma (eg: $\varepsilon_{i,m}$), and the indices of iterations (k) are annotated by superscripts (e.g. ε^k).

3. Since F is convex w.r.t $\{u, \varepsilon_i\}$, first-order optimality conditions are sufficient to solve Eq. (3.17).

where $u^* \in \mathcal{U}^*$ (given by Eq. (2.39)). On the other hand, the minimization with respect to ε_i results in the following

$$\int_0^L \frac{\partial \psi}{\partial \varepsilon_i} + \Delta t \frac{\partial \phi_v}{\partial \varepsilon_i} dx = 0 \tag{3.20}$$

Since the above equation is true for a bar of arbitrary length L, it has to be valid for all $x \in [0, L]$. Hence, the above equation reduces to the following local form

$$\frac{\partial \psi}{\partial \varepsilon_i} + \Delta t \frac{\partial \phi_v}{\partial \varepsilon_i} = 0 \tag{3.21}$$

Using Eq. (3.2) and Eq. (3.4) in the above equation to replace the free energy and viscous dissipation potential lead to the following

$$-g(d)E_0(\varepsilon - \sum_{i=1}^{n} \varepsilon_i) + g(d)E_i\varepsilon_i + \eta_i \frac{(\varepsilon_i - \varepsilon_{i,m})}{\Delta t} = 0 \tag{3.22}$$

The preceding equation can be rewritten to get the subsequent expression for the viscous strain (or internal strain) ε_i

$$\varepsilon_i = \frac{\Delta t}{g(d)\Delta t + \tau_i} \left(\frac{\sigma}{E_i} + \frac{\tau_i \varepsilon_{i,m}}{\Delta t} \right) \tag{3.23}$$

which upon substitution in Eq. (3.6) and rearranging leads to the following expression for σ

$$\sigma = p(d) \left(\varepsilon - \sum_{i=1}^{n} \frac{\tau_i}{g(d)\Delta t + \tau_i} \varepsilon_{i,m} \right) \tag{3.24}$$

where $p(d)$ is the modified stiffness and its expression is given by

$$p(d) = \left(1 + g(d) \sum_{i=1}^{n} \frac{E_0}{E_i} \frac{\Delta t}{g(d)\Delta t + \tau_i} \right)^{-1} g(d)E_0 \tag{3.25}$$

On back substitution of above equation into the equilibrium equation Eq. (3.19), we obtain the following

$$\int_0^L p(d)\varepsilon(u)\varepsilon(u^*)dx = \int_0^L \sigma_{int}\varepsilon(u^*)dx \qquad \forall \ u^* \in U^* \tag{3.26}$$

where σ_{int} is given as

$$\sigma_{int} = p(d) \sum_{i=1}^{n} \frac{\tau_i}{g(d)\Delta t + \tau_i} \varepsilon_{i,m} \tag{3.27}$$

It should be noted that the weak form given by Eq. (3.26) is similar to the weak form in elasticity except for the body force like term σ_{int} to account for the viscoelastic effect. The finite element discretization is done using linear 2-node bar elements with element size h_e. The displacement fields are stored at the nodes and the internal variables are stored at the element centers (Figure 3.3). Hence, the displacement fields are continuous and linear over each element and the internal variables are piecewise constant over each element.

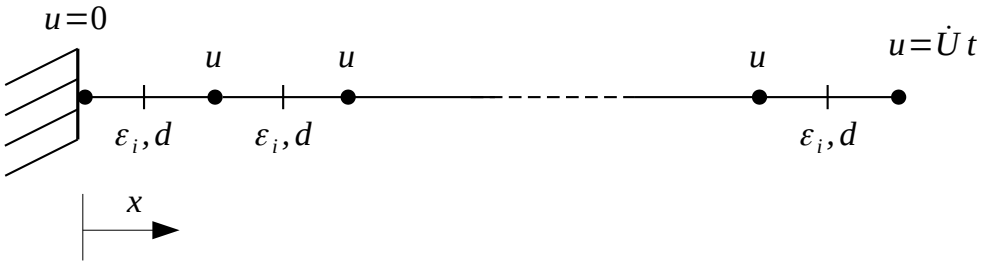

Figure 3.3 – Discretization of a 1D bar: displacements stored at nodes and internal variables stored at element centers

The displacement field is given by

$$u(x,t) = \sum_{i \in \mathcal{N}} u_i(t) N_i(x) \tag{3.28}$$

where $\mathcal{N} = \{1, 2, .., N\}$ is the set of finite element nodes, and $N_i(x)$ are the interpolation (or shape) functions associated with each node. Eq. (3.26) then leads to the following discretized form of the equilibrium equation

$$[\mathbf{K}(d)][\mathbf{U}] = [\mathbf{F}(d)] \tag{3.29}$$

where

$$K_{ij} = \int_0^L p(d) N_{i,x} N_{j,x} dx \qquad \forall\, (i,j) \in \mathcal{N} \times \mathcal{N} \tag{3.30}$$

$$F_i = \int_0^L \sigma_{int} N_{i,x} dx \qquad \forall\, i \in \mathcal{N} \tag{3.31}$$

In Eq. (3.29), the terms $[\mathbf{K}(d)]$ and $[\mathbf{F}(d)]$ represent the global stiffness matrix and the global force vector, respectively.

3.1.1.2 Finding damage

For the minimization problem with respect to d given by Eq. (3.18), a direct minimization is performed. To enforce $d \in \mathcal{A}_m \cap \mathcal{L}_\Omega$, we arrive at the following discrete spaces $\mathcal{A}_m^h$ and $\mathcal{L}_\Omega^h$ analogous to the continuous spaces $\mathcal{A}_m$ and $\mathcal{L}_\Omega$ [101, 103]

$$A_m^h := \{d_i : d_{i,m} \leq d_i \leq 1 \ \ \forall\, i \in \{1, 2.., N_e\}\} \tag{3.32}$$

$$\mathcal{L}_\Omega^h := \left\{ d_i : \begin{array}{l} d_{i+1} - d_i \leq h_e/l_c \ \ \forall\, i \in \{1, 2.., N_e - 1\} \\ d_i - d_{i-1} \leq h_e/l_c \ \ \forall\, i \in \{2, 3, ..N_e\} \end{array} \right\}. \tag{3.33}$$

where $N_e = N - 1$ is the number of finite elements. The discretized form of Eq. (3.18) can now be written as follows

$$(d^{k+1}) = \arg \min_{d' \in \mathcal{A}_m^h \cap \mathcal{L}_\Omega^h} F^h \quad \text{with} \quad F^h = \sum_{i \in \mathcal{N}_e} f_i h_e \tag{3.34}$$

where f is the local incremental potential as given by Eq. (3.12) and $\mathcal{N}_e$ is the set of all finite elements.

The algorithm for alternate minimization is shown in Algorithm 1. The algorithm has been implemented in Python. For the damage solver, the Sequential Least Square Programming (SLSQP) method is used, thanks to the *scipy* package of Python [113].

Algorithm 1 1D softening GKV model

Initialize $m = 0$, $\varepsilon_{i,m}, [\mathbf{U}_m], d_m, \Delta t$
while $m \leq M$ **do**
  $k = 0$, $d^k = d_m$, $\varepsilon_i^k = \boldsymbol{\varepsilon}_{i,m}$, $err_u = err_d = +\infty$
  while $k < k_{max}$ **and** $err_u > tol_u$ **and** $err_d > tol_d$ **do**
    Assemble stiffness matrices $[\mathbf{K}(d^k)]$ ▷ using Eq. (3.30)
    Assemble forces vectors $[\mathbf{F}(d^k)]$ ▷ using Eq. (3.31)
    Find the nodal displacement vector $[\mathbf{U}^{k+1}]$ ▷ using Eq. (3.29)
    Compute elemental stress vector with d^k ▷ using Eq. (3.24)
    Update the internal strains ε_i^{k+1} ▷ using Eq. (3.23)
    Find the damage field vector d^{k+1} ▷ using Eq. (3.34)
    Compute errors

$$err_u = |\mathbf{U}^{k+1} - \mathbf{U}^k|, \quad err_d = |d^{k+1} - d^k| \tag{3.35}$$

    $k \leftarrow k + 1$
  end while
  $m \leftarrow m + 1$
end while

3.1.2 Numerical results

Consider a homogeneous bar of length $L = 1\ m$ and uniform cross-section area $S = 1\ m^2$. For all the cases considered in this chapter, we apply a monotonous displacement rate $\dot{U} = \dot{a}L$ at one end of the bar while the other end is fixed as shown in Figure 3.2. $a = \varepsilon_{mean}$ is the total strain (or mean strain) in the bar. For the viscoelastic parameters related to the GKV model, we use the values corresponding to the sand bitumen 0/2 [9] from Table 1.1. The critical energy release rate $Y_c = 500\ J/m^3$ is used for all the tests performed in this section. The above value has been fixed, independent of the applied displacement rate $\dot{U}$. Recall, as discussed in Chapter 1 (Section 1.3.1.1 and Figure 1.23), that Y_c exhibits rate dependency in the case of bituminous materials. However, since our interest in this chapter lies only in studying the developed model (and not fitting the experimental results), we assume a constant value for Y_c.

Unless explicitly specified, the degradation function $g(d)$ and the softening function $h(d)$ mentioned below are utilized in all cases for the present chapter.

$$g(d) = (1-d)^2 \tag{3.36}$$

$$h(d) = 2d + 3d^2 \tag{3.37}$$

The above choice is based on the motivation from [101], [102] on the Lip-field approach for softening elasticity. Both functions are convex. The choice of the above functions is also such that the damage initiates when $\psi_0 = Y_c$ (from Eq. (3.10)) followed by strain softening behavior. It should be noted that the above functions $g(d)$ and $h(d)$ may not necessarily represent the softening behavior exhibited for a chosen bituminous material. In other words, more importance has to be given to the choice of these functions and more details on this will be discussed in the subsequent chapters while fitting experimental results. Since the aim here is to study the behavior of the developed model in the 1D case, we are selecting one of the simplest options (as denoted in Eqs. (3.36, 3.37)) for both $g(d)$ and $h(d)$. Concerning discretization, we set $N = 40$ nodes. The tolerance for the convergence of the alternate minimization is chosen as follows: $tol_u = tol_d = 1e-10$ (l^2-norm is used for the error measurement in Eq. (3.35)).

3.1.2.1 Local (or homogeneous) solution

First, we validate the numerical implementation for the considered 1D case with the local (semi-) analytical solution. This also helps to understand the local behavior of the model. One strategy to replicate the local behavior (or obtain a homogeneous solution) is to adopt a very high l_c, so that the Lipschitz constant $1/l_c \to 0$ (thus imposing a constant d over the bar). The (semi-) analytical solution in local form for the case of the GKV model with damage is given in Appendix B. We employ two different strain rates $\dot{\varepsilon}_{mean} = (1e-5, 1e-3)\ s$ and the corresponding time

steps $\Delta t = (1e-1, 1e-3)\ s$.

Figure 3.4 compares the homogeneous (or local) solution obtained using the numerical implementation (detailed in the last section) and the (semi-) analytical solution. It can be seen that the results are in good agreement with each other, thus validating the numerical implementation (indicated in Algorithm 1). Furthermore, it is observed that with the selected $h(d)$, the stress-strain curve displays softening behavior after the initiation of damage. Moreover, due to the viscous effects, some rate effects can be observed in the model. For instance, the stress at the damage initiation increases with an increase in applied strain rate, and the strain at damage initiation decreases with an increase in applied strain rate.

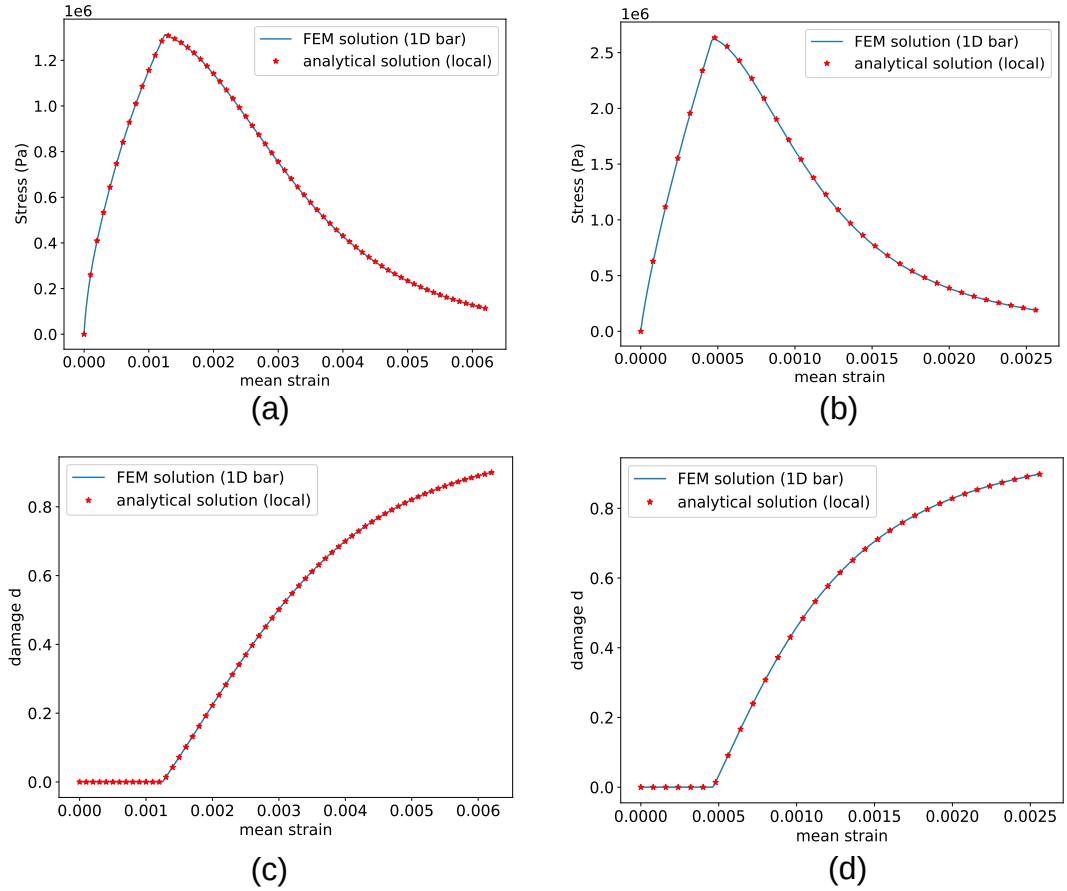

Figure 3.4 – Validation of numerical implementation: Local (or homogeneous) stress-strain plots (top row) and damage evolution plots (bottom row) for $\dot{\varepsilon}_{mean} = 1e-5\ /s$ (left column) and $\dot{\varepsilon}_{mean} = 1e-3\ /s$ (right column)

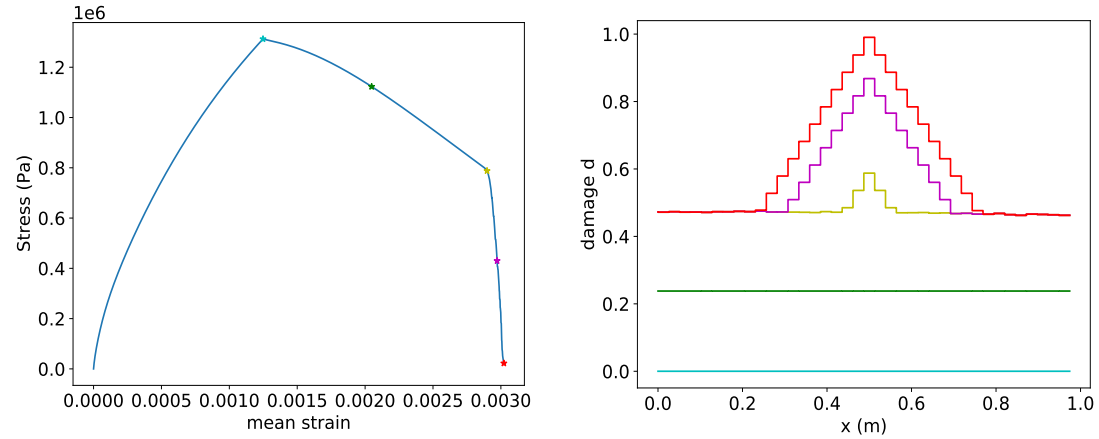

(a)

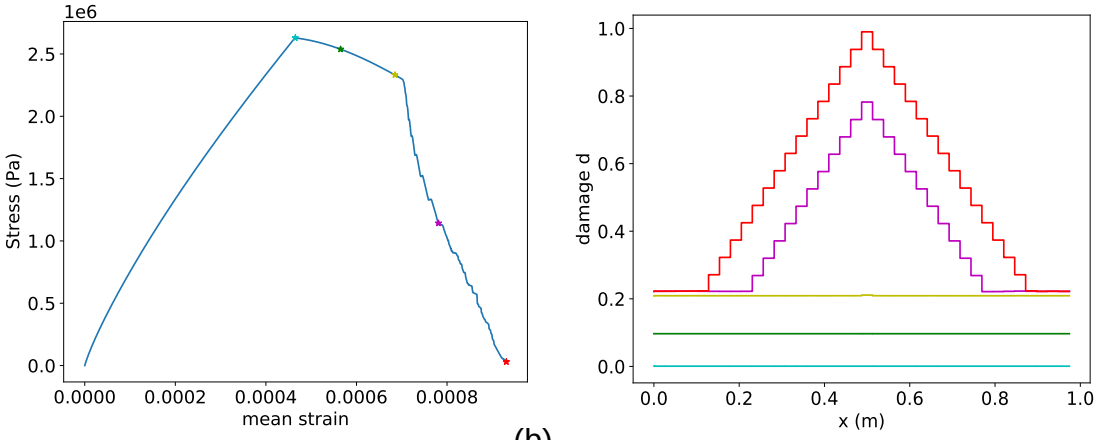

(b)

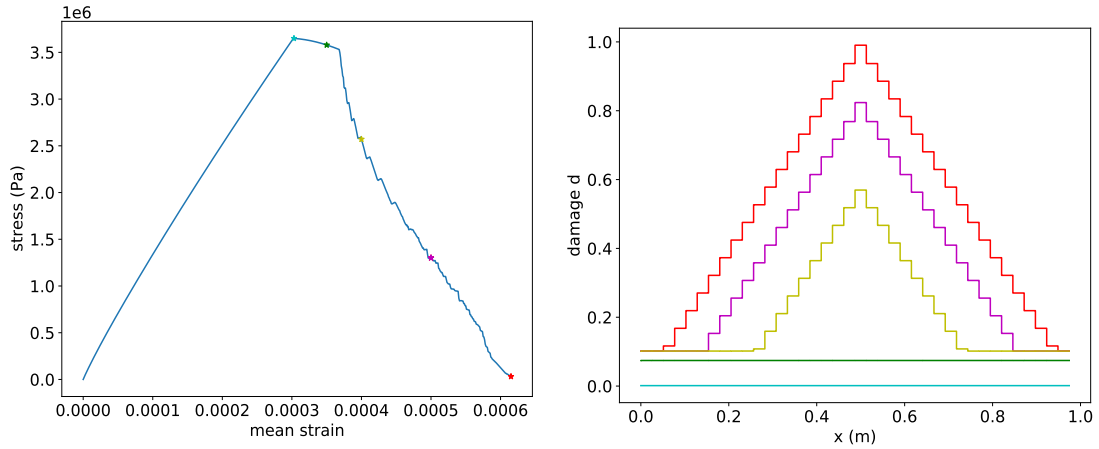

(c)

Figure 3.5 – Stress-strain plots and the damage evolution plots for $\dot{U} = \{1e-5,\ 1e-3,\ 1e-1\}\ m/s$ (from top to bottom). The damage profile along the bar is plotted at different time instants indicated by colored bullets in stress-strain plots

3.1.2.2 Localization behaviour

Next, we are interested in studying the localization behavior of the model for the case of the 1D homogeneous bar. Since the bar is homogeneous, to trigger damage (or strain) localization, a small perturbation is applied to the damage field ($1e-3$) at the beginning of each time step (initial guess of the damage field). In our case, we apply the perturbation at the center of the bar $x = L/2$ to trigger the localization at the center. In this case, we consider three different imposed displacement rates $\dot{U} = (1e-5,\ 1e-3,\ 1e-1)\ m/s$ and the corresponding time steps $\Delta t = (1e-1,\ 1e-3,\ 1e-5)\ s$. The characteristic length scale l_c is set to $0.5\ m$.

Figure 3.5 plots the stress-strain curve and the corresponding damage evolution at different time instants (indicated by a bold circle in the stress-strain curve) for the considered imposed displacement rates. The stair-like shape of the stress-strain curve during the localization is an artifact of the discretization of d and the Lipschitz constraint, which actually smooths out while the mesh is refined. The stress-strain curve can be characterized into three different phases based on the observed behavior. In the beginning, when $Y < Y_c$, the damage along the bar is zero, resulting in the solution being identical to the local solution (homogeneous solution). For $Y \geq Y_c$, initially, the damage evolves in a homogeneous fashion followed by damage localization at the center. The homogeneous evolution of damage observed initially is not the case in softening elasticity and is only observed in softening elastoplastic models with hardening [101]. For the 1D case, in softening elasticity with hardening plasticity, the hardening phase leads to a homogeneous evolution of damage, and the localization is triggered only during the softening phase [101]. In contrast, for the softening viscoelastic damage model considered here, despite the absence of any hardening, a homogeneous evolution of damage is observed initially after the onset of damage. Moreover, for the considered case, the damage threshold after which the damage localizes decreases with an increase in the applied displacement rate (see Figure 3.5). Such homogeneous evolution of damage might indicate the presence of an intrinsic time scale in the model associated with damage. This intrinsic time scale (if it exists) might act as a resistance to the damage growth rate, leading to a homogeneous damage evolution initially.

Figure 3.6 compares the stress-strain curve and the damage field at rupture for the considered displacement rates. Again the rate effects can be observed: the maximum stress increases with increasing loading speed and the elongation at rupture decreases with increasing loading speed. This can indicate that the developed model is consistent (in a qualitative sense) with the classical response of bituminous materials obtained during the laboratory tensile tests (see Figures 1.23a and 1.24b). Moreover, it can be seen that the model is able to qualitatively represent the brittle-ductile transition (as discussed in Figure 1.24b) when the loading rate is decreased. Furthermore, such homogeneous evolution of damage doesn't occur in the classical Thick Level Set (TLS) approach [98] [100], since the TLS approach artificially rules out the homogeneous evolution by

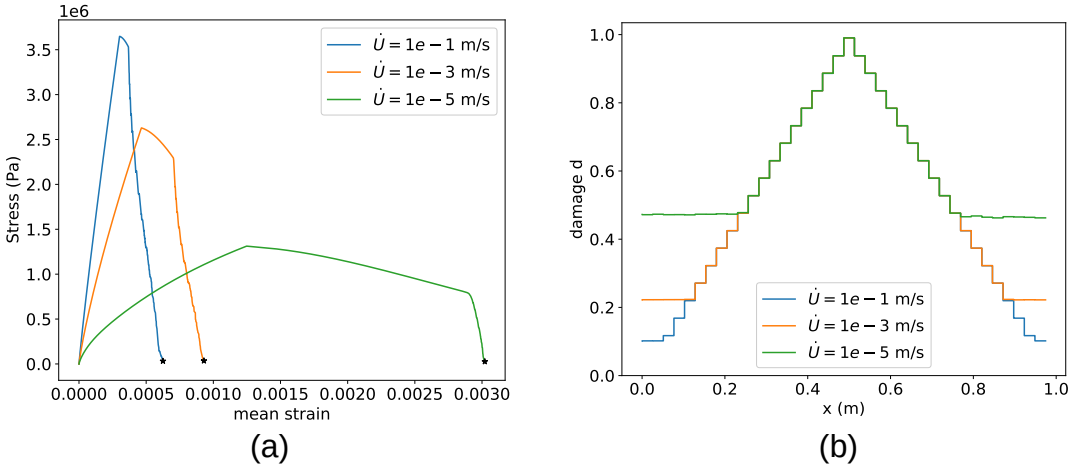

Figure 3.6 – (a) Stress-strain plot and (b) damage at rupture for different applied displacement rates

introducing strong kinematic constraint on the damage field d. However, the Lip-field approach, due to the relaxed constraint on d, is able to obtain homogeneous evolution of damage and thus preserve the information available in the local solution.

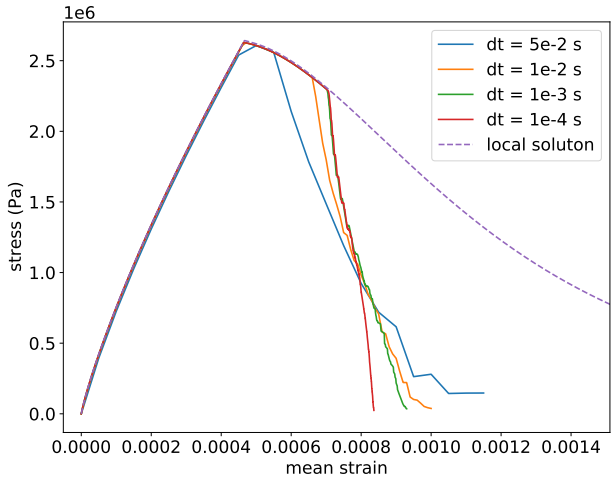

Figure 3.7 – Influence of time step dt for $\dot{U} = 1e-3\ m/s$

To study the influence of the time step Δt (or dt), the simulations were run for different dt for the case of $\dot{U} = 1e-3\ m/s$. Figure 3.7 compares the stress-strain curves obtained for different time steps and the local solution. Initially, a convergence in dt is very obvious from the

figure. Moreover, it should be noted that for the undamaged phase, dt doesn't have a significant influence (due to the implicit time discretization), and the stress-strain curves match very well. However, for the damage phase, dt does have some influence. In particular, as dt increases, the stress-strain curve soon deviates from the local (or homogeneous) solution. In other words, the higher the dt, the sooner the localization. This could again be attributed to the possibility of the presence of an intrinsic time scale associated with damage.

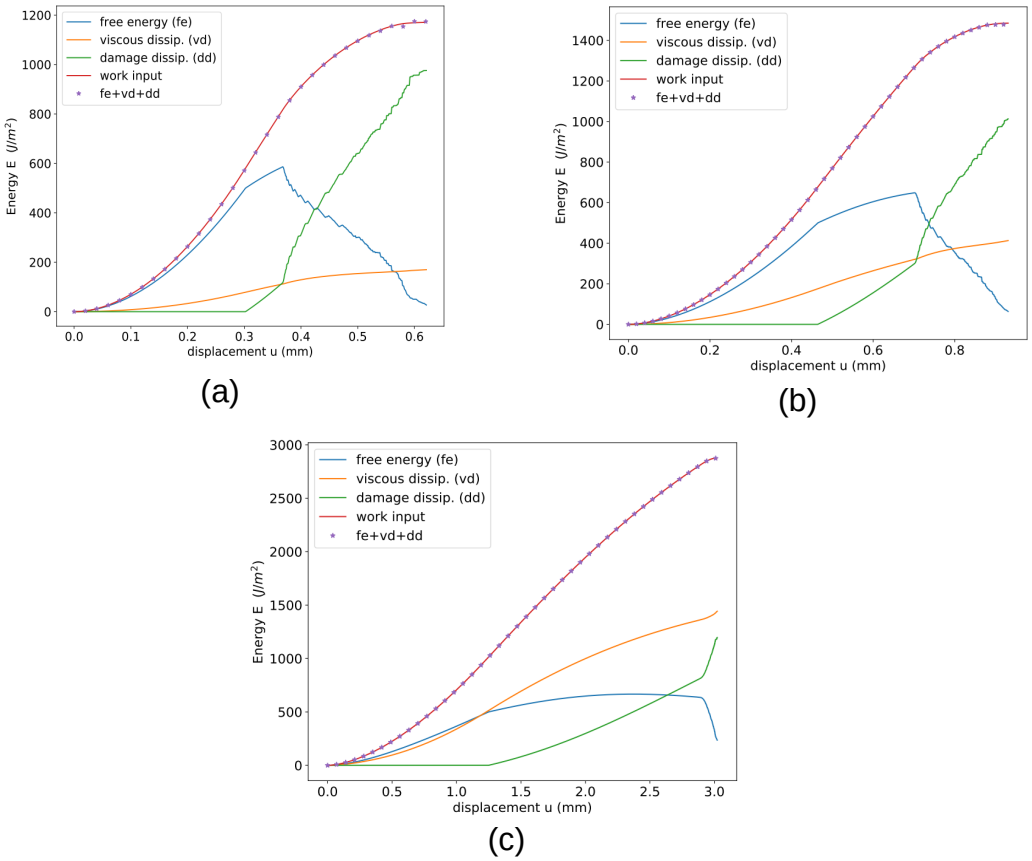

Figure 3.8 – Energy diagrams for (a) $\dot{U} = 1e{-}1\ m/s$, (b) $\dot{U} = 1e{-}3\ m/s$ and (c) $\dot{U} = 1e{-}5\ m/s$

Figure 3.8 plots the global energy as a function of displacements. The expressions for input work,

free energy, viscous dissipation, and damage energy are as follows:

$$\text{input work} = \int_0^t \sigma \dot{U} A \, dt \tag{3.38}$$

$$\text{free energy} = \int_0^L \psi(\varepsilon, \varepsilon_i, d) dx \tag{3.39}$$

$$\text{viscous dissipation} = \int_0^t \int_0^L \sum_{i=1}^{n} \sigma_i \dot{\varepsilon}_i dx dt \tag{3.40}$$

$$\text{damage dissipation} = \int_0^L Y_c h(d) dx \tag{3.41}$$

where A is the cross-sectional area of the bar. The energies at each time step are computed using the equations mentioned above. The thermodynamic consistency of the model we've developed can be readily assessed through Figure 3.8 as follows:

1. The work input aligns closely with the internal energy, which is the sum of free energy, viscous dissipation, and damage dissipation. This alignment suggests that the model upholds the principle of energy conservation.
2. The curves representing viscous dissipation and damage dissipation consistently rise, indicating the positive nature of dissipation at each time step.

Furthermore, it's evident that as the loading rate decreases, viscous dissipation begins to take precedence over damage dissipation, highlighting the predominantly viscous nature of the material under these conditions.

To understand in a quite abstract setting the reasons for the differing localization behavior in softening elasticity (immediate localization at the onset of damage initiation) and softening viscoelasticity (homogeneous evolution of damage precedes localization), stability analysis is performed for the 1D case in the following section.

3.2 Lyapunov stability analysis

Stability analysis is a mathematical tool that can be used to determine the qualitative and quantitative nature of the mathematical problem under consideration without the need to solve it explicitly. Consider the problem of a homogeneously deformed bar under some applied external displacement. Bifurcation and stability analysis can provide useful information on the existence of other solutions (solutions with deformation bands over a localized zone apart from homogeneous solutions) under a given load and their stability behavior [114]. For example, in the case of a 1D homogeneous bar, a small perturbation of the reference homogeneous solution that grows in time indicates *instability* of the reference homogeneous solution and formation of the deformation band over a localized zone. On the other hand, if the perturbation decays or

doesn't grow with time, it indicates *stability* of the reference homogeneous solution.

The problem of strain localization has been addressed mathematically already in the literature [115], [99], [114] for some of the classical strain softening plasticity models and the presence of intrinsic characteristic time or length scale was investigated. However, to our knowledge, such analysis has not been done for viscoelastic softening damage models. In particular, we use Lyapunov's first method (based on motivation from [99], [114] and references therein) to perform the Linear Stability Analysis(LSA) of damage softening models to investigate their localization behavior (and the presence of intrinsic time scale). It should also be noted that both the LSA and the classical bifurcation analysis lead to the same condition for strain localization in the case of rate-independent materials – that the determinant of the acoustic tensor has to be zero (Eq. (1.46)) [99], [114]. Our interest in the study is limited to the 1D case of a homogeneous bar with the formation of *dilatation bands* (outward normal vector to the band and the direction of the discontinuity of strain are in the same direction) [99]. Moreover, we limit ourselves to the *quasi-static case* (at the limit density tends to zero) and *monotonously applied strain rates*.

3.2.1 Definition of stability

We use the notion of stability that has been well established from the work of Lyapunov ([114] and references from therein). It should be noted that in time-independent quasi-static systems (such as quasi-static softening elasticity), although time is neglected, the transition from the homogeneous reference solution to the localized solution occurs over a certain time scale. Hence, time is central in stability theory [114].

Consider an autonomous (f not an explicit function of time t) non-linear dynamical system [114]

$$\dot{y} = f(y(t)) \qquad y(0) = y_0 \tag{3.42}$$

where $y \in \mathcal{D} \subseteq \mathbb{R}^n$, $\mathcal{D}$ is an open set containing origin and $f : \mathcal{D} \to \mathbb{R}^n$ is a continuous vector field on $\mathcal{D}$. Suppose f has an equilibrium at y_e indicating $f(y_e) = 0$, then,

1. The equilibrium is *Lyapunov stable* if for every $\epsilon > 0$, there exists a $\delta > 0$ such that, if $|y(0) - y_e| < \delta$, then for every $t \geq 0$ we have $|y(t) - y_e| < \epsilon$.
2. The equilibrium is *asymptotically stable* if it is Lyapunov stable and there exists $\delta > 0$ such that if $|y(0) - y_e| < \delta$, then $\lim_{t\to\infty} |y(t) - y_e| = 0$

The conditions for stability for a linear and non-linear system are given in Appendix C.

We will now analyze classical damage models, specifically those without external regularization, in the 1D case of a homogeneous bar at the onset of damage initiation($\psi_0 = Y_c,\ \dot{d} \neq 0$ and $d = 0$).

Before the onset of localization, the solution is uniform (state variables are homogeneous) and stable. Let $\sigma^*, u^*, \varepsilon^*$ *and* d^* indicate the equilibrium solution of the homogeneously deformed bar at any given instance (could be a stable or unstable equilibrium). LSA involves applying small perturbations around this equilibrium solution as follows and studying the evolution of the perturbation

$$u = u^* + \tilde{u} \tag{3.43a}$$

$$\varepsilon = \varepsilon^* + \tilde{\varepsilon} \tag{3.43b}$$

$$\sigma = \sigma^* + \tilde{\sigma} \tag{3.43c}$$

$$d = d^* + \tilde{d} \tag{3.43d}$$

where $\tilde{}$ on top of the variables represents small perturbations around them respectively. For the kinematics of the formation of the deformation band considered here (pure dilation band), the following form of perturbation can be considered [114], [99] (see Appendix D for brief justification on the following choice):

$$\tilde{u} = ge^{st+ikx} \tag{3.44a}$$

$$\tilde{d} = he^{st+ikx} \tag{3.44b}$$

$$\tilde{\varepsilon} = \tilde{u}_{,x} = gike^{st+ikx} \tag{3.44c}$$

where $i = \sqrt{-1}$, $k = \frac{2\pi}{\lambda}$ is the wave number with λ being the wavelength of the perturbation and s is the Lyapunov coefficient [4] that determines the stability of the system. The stability condition for the eigenvalues (indicated in Appendix C) also applies to this Lyapunov exponent. (In fact, when the partial differential equations (PDE's) are written as a system of ordinary differential equations (ODE's), the eigenvalues and the Lyapunov exponents are the same [114]).

Remark 2

1. *For the perturbations to respect the boundary conditions for a given bar of length L, it is enough to consider the set of wavelengths λ such that the perturbations are zero at the boundary. However, for some arbitrary length of the bar L, without loss of generality, all wavelengths could be considered.*

2. *g and h in Eq. (3.44) are the amplitudes of the perturbations and not to be confused with $g(d)$ and $h(d)$ used in the damage evolution equation.*

4. The Lyapunov coefficient has the unit of sec^{-1}.

For the rest of the work in this section, we consider the following choices for $g(d)$ and $h(d)$:

$$g(d) = (1-d)^2 \tag{3.45}$$

$$h(d) = 2d \tag{3.46}$$

3.2.2 softening elasticity

The rheological model for this case is shown in Figure 3.9.

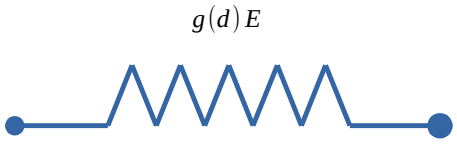

Figure 3.9 – Softening elasticity model

The governing equations in local form for the softening elasticity, in this case, are given as follows:

$$\sigma_{,x} = \rho\ddot{u} \qquad (Momentum\ balance) \tag{3.47a}$$

$$g'(d)\psi_0 + Y_c h'(d) = 0 \ \text{ when } \ Y \geq Y_c \qquad (damage\ evolution) \tag{3.47b}$$

$$\sigma = g(d)E\varepsilon \qquad (Constitutive\ equation) \tag{3.47c}$$

$$\varepsilon = u_{,x} \qquad (Kinematic\ compatibility\ equation) \tag{3.47d}$$

where $\psi = g(d)\psi_0$, $\psi_0 = 0.5E\varepsilon^2$ and $Y = -\partial\psi/\partial d = -g'(d)\psi_0$. Since $\sigma^*, u^*, \varepsilon^*$ *and* d^* are the equilibrium solution of the homogeneously deformed bar at any given instance for the externally applied loading, the following holds:

$$\sigma^*{}_{,x} = 0 \tag{3.48a}$$

$$g'(d^*)\frac{1}{2}E\varepsilon^{*2} + Y_c h'(d^*) = 0 \ \text{ when } \ Y^* \geq Y_c \tag{3.48b}$$

$$\sigma^* = g(d^*)E\varepsilon^* \tag{3.48c}$$

$$\varepsilon^* = u^*_{,x} \tag{3.48d}$$

Now, substitution of the Eqs. (3.43) in Eqs. (3.47) and making use of Eqs. (3.48) results in the

following equations in the linearized form (for small perturbations)

$$\tilde{\sigma}_{,x} = \rho\ddot{\tilde{u}} \tag{3.49a}$$

$$g''(d)\tilde{d}\psi + g'(d)\tilde{\psi} + Y_c h''(d)\tilde{d} = 0 \;\text{ when }\; Y \geq Y_c \tag{3.49b}$$

$$\tilde{\sigma} = g'(d)\tilde{d}E\varepsilon + g(d)E\tilde{\varepsilon} \tag{3.49c}$$

$$\tilde{\varepsilon} = \tilde{u}_{,x} \tag{3.49d}$$

By substituting Eqs. (3.44) into Eqs. (3.49), we obtain the following linearized form of perturbation equations associated with the momentum balance and damage evolution equation for $\psi = Y_c$.:

$$\begin{bmatrix} -k^2E - \rho s^2 & -2ikE\varepsilon \\ ikE\dot{\varepsilon} - iksE\varepsilon & \frac{1}{2}E\varepsilon^2 s \end{bmatrix} \begin{bmatrix} g \\ h \end{bmatrix} = \begin{bmatrix} 0 \\ 0 \end{bmatrix} \tag{3.50}$$

The Lyapunov exponent can be found by making the determinant of the system to be zero (resulting in a cubic equation for the Lyapunov exponent). To understand the stability behavior of the system in this case, we consider the following parameters for the calculation. Note that

ρ	E	ε	$\dot{\varepsilon}$	$Y_c(=\psi)$
$1e-14\ Kg/m^3$	$2\ Pa$	1	$1e-3\ /s$	$1\ Pa$

Table 3.1 – Elasticity parameters for calculation

ρ takes the limit of zero in Table 3.1 so that we stay in the quasi-static case (and the inertial effects can be neglected). For the considered material parameters, the Lyapunov exponent (found using the Sympy module [116] of Python) is shown for various wavelengths in Figure 3.10 Since one of the Lyapunov coefficients ($s3$) is positive, the system is unstable (as per the conditions for stability of non-linear systems discussed in Appendix C). Here, the term 'unstable' signifies the instability of the homogeneous solution at the onset of damage. Moreover, it can be noted that $s3 \to \infty$ as $\lambda \to 0$. In other words, at the onset of damage initiation, strain localization happens in the mathematical plane (localization zone of zero thickness). This is similar to the behavior of the Lyapunov exponent obtained for softening plasticity models using the Cauchy continuum (no intrinsic regularization) in [77]. Moreover, if we make the following definition for characteristic time scale (T_{char}) present in the system:

$$T_{char} = \frac{1}{max(Re(s))} \tag{3.51}$$

then $T_{char} \to 0$ in this case as $max(Re(s)) \to \infty$. Hence for the softening elasticity with no external regularization, there exists no intrinsic characteristic length and time scale and the

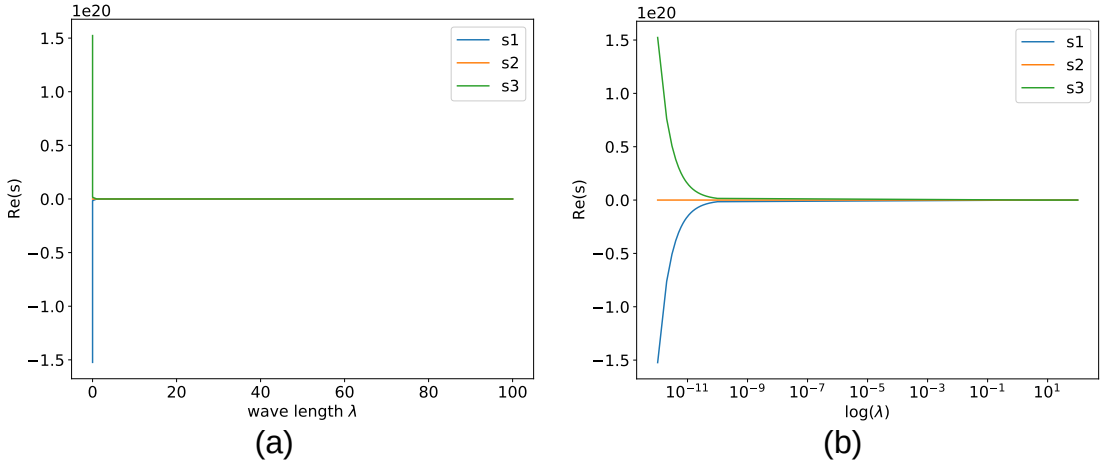

Figure 3.10 – Real part of the Lyapunov coefficients s at $\psi = Y_c$ for softening elasticity with no external regularization (figure (b) is the same as figure (a) but plotted in a semi-logarithmic scale).

strain localization occurs in a mathematical plane. The pathological mesh size dependency at strain softening (localization zone same as the mesh size) can also be justified if we associate the size of the mesh with the wavelength of perturbation. In other words, the smaller the size of the finite elements (which can be associated with smaller wavelengths), the faster the damage reaches 1.

Now we assess the case for rate-dependent softening elasticity. In this case, we consider again the equations associated with softening elasticity (given by Eq. (3.47)), except for the damage evolution equation (Eq. (3.47b)). In particular, we make the damage resistance (in the damage evolution equation) dependent on the rate of damage as follows:

$$g'(d)\psi_0 + Y_c(h'(d) + \tau_{vd}\dot{d}) = 0 \;\text{ when }\; Y \geq Y_c \qquad (\textit{damage evolution}) \tag{3.52}$$

where τ_{vd} represents a viscosity-like parameter related to damage evolution. This parameter acts as a resistance to the damage rate (and thus introduces a time scale into the model).

Following a similar procedure as explained earlier, we obtain the following set of equations corresponding to the linearized form of perturbations for momentum balance and damage evolution at $\psi = Y_c$.

$$\begin{bmatrix} -k^2E - \rho s^2 & -2ikE\varepsilon \\ ikE\varepsilon & -sY_c\tau_{vd} \end{bmatrix} \begin{bmatrix} g \\ h \end{bmatrix} = \begin{bmatrix} 0 \\ 0 \end{bmatrix} \tag{3.53}$$

The parameters listed in Table 3.1 are again used here. In addition, we use the following two

different choices for τ_{vd}: $\tau_{vd} = \{1, 2\}$.

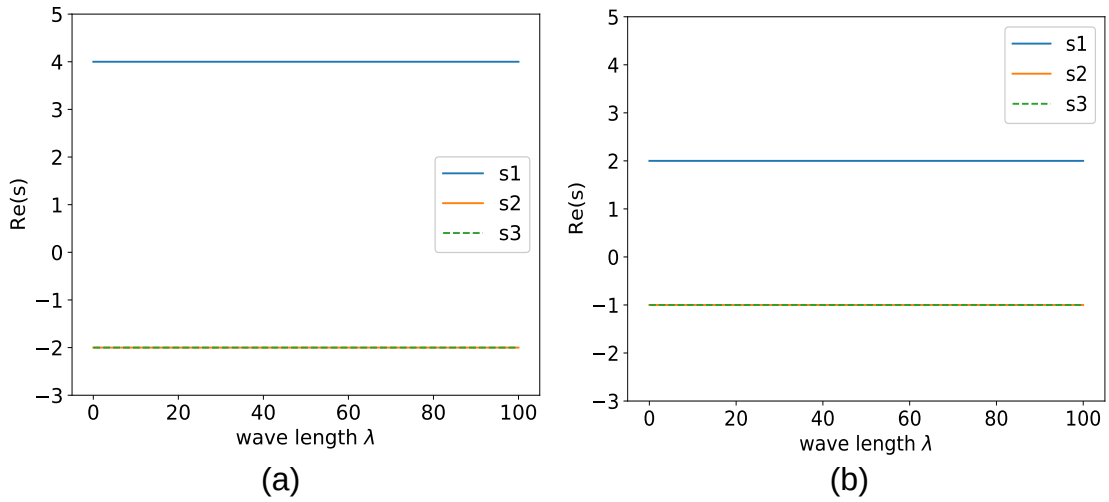

Figure 3.11 – Real part of the Lyapunov coefficients s at $\psi = Y_c$ for rate-dependent softening elasticity with no external regularization for (a) $\tau_{vd} = 1$ and (b) $\tau_{vd} = 2$

Figure 3.11 plots the real part of the Lyapunov coefficient (by solving Eq. (3.53)) for the considered different values of τ_{vd}. It can be observed from the figure that the positive part of the Lyapunov exponent stays finite (unlike the previous case in Figure 3.10 where $\tau_{vd} = 0$). Hence, $\tau_{vd} > 0$ introduces a characteristic time scale into the model (as per Eq. (3.51)). Moreover, the positive part of the Lyponov coefficient ($s1$) decreases with an increase in τ_{vd}, which is expected (higher the τ_{vd}, higher the resistance on damage rate as per Eq. (3.52) and hence higher the T_{char} and hence lower the Lyapunov coefficient.).

Despite the real part of the Lyapunov coefficient being finite for both cases, since one of them is positive, the system (homogeneous solution) is unstable. The only difference with the previous case ($\tau_{vd} = 0$) is that here the instability propagates in finite time (as $T_{char} > 0$). However, as $\lambda \to 0$, $Re(s3) > 0$. This indicates the possibility of localization still occurring on a mathematical plane (localization zone of zero thickness). Moreover, it can be observed that the Lyapunov coefficient stays constant for all the wavelengths. This signifies the mesh independence at the onset of damage initiation for the 1D homogeneous bar. The finite element simulation for the present model is reported in Appendix E. It is observed from Figure E.1 that the introduction of τ_{vd} only delays the localization process but doesn't prevent localization from occurring on a plane (instability propagating in finite time).

3.2.3 softening viscoelasticity

In this case, we consider the softening Kelvin-Voigt (KV) model (Figure 3.12). Despite being the simplest viscoelastic model, it could shed some light on the homogeneous evolution of damage observed before localization in the softening GKV model (Figure 3.5).

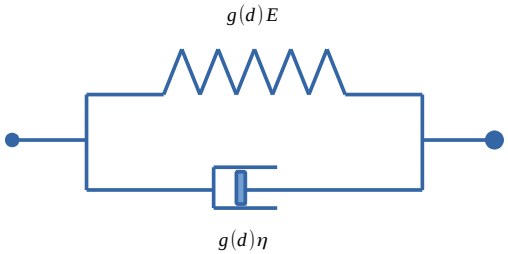

Figure 3.12 – Softening Kelvin-Voigt(KV) model

The governing equations for the softening KV model are given as follows:

$$\sigma_{,x} = \rho\ddot{u} \qquad (Momentum\ balance) \tag{3.54a}$$

$$g'(d)\psi_0 + Y_c h'(d) = 0 \ \text{ when } \ Y \geq Y_c \qquad (damage\ evolution) \tag{3.54b}$$

$$\sigma = g(d)(E\varepsilon + \eta\dot{\varepsilon}) \qquad (Constitutive\ equation) \tag{3.54c}$$

$$\varepsilon = u_{,x} \qquad (Kinematic\ compatibility\ equation) \tag{3.54d}$$

By following a similar procedure as adopted in softening elasticity (Section 3.2.2), after the introduction of the perturbations (from Eqs. (3.43)) in the above set of equations, and making use of the equilibrium solutions ($u^*, \varepsilon^*, \sigma^*$ *and* d^*), we obtain the following linearized form of the perturbation equations

$$\tilde{\sigma}_{,x} = \rho\ddot{\tilde{u}} \tag{3.55a}$$

$$g''(d)\tilde{d}\psi_0 + g'(d)\tilde{\psi} + Y_c h''(d)\tilde{d} = 0 \ \text{ when } \ Y \geq Y_c \tag{3.55b}$$

$$\tilde{\sigma} = g'(d)\tilde{d}(E\varepsilon + \eta\dot{\varepsilon}) + g(d)(E\tilde{\varepsilon} + \eta\dot{\tilde{\varepsilon}}) \tag{3.55c}$$

$$\tilde{\varepsilon} = \tilde{u}_{,x} \tag{3.55d}$$

On using Eqs. (3.44), (3.45) and (3.46) in the above set of equations, the following equation for perturbations associated with momentum balance and damage evolution are obtained.

$$\begin{bmatrix} -g(d)(k^2E + k^2\eta s) - \rho s^2 & g'(d)ik(E\varepsilon + \eta\dot{\varepsilon}) \\ c_1 ik + c_2 iks & \psi^2 s \end{bmatrix} \begin{bmatrix} g \\ h \end{bmatrix} = \begin{bmatrix} 0 \\ 0 \end{bmatrix} \tag{3.56}$$

where

$$c_1 = \dot{d}E^2\varepsilon^3 - 0.5E^2\varepsilon^2\dot{\varepsilon} + (\psi - Y_c)E\dot{\varepsilon} \tag{3.57}$$

$$c_2 = -\frac{1}{2}E^2\varepsilon^3 + (\psi - Y_c)E\varepsilon \tag{3.58}$$

The following table (Table 3.2) lists the parameters used for the stability analysis. Notice $\rho \to 0$ as we stick to the quasi-static case. We force the determinant to be zero to find the Lyapunov exponent.

ρ	E	η	ε	$\dot{\varepsilon}$	$Y_c(=\psi)$
$1e-14\ Kg/m^3$	$2\ Pa$	$1\ Pa\ s$	1	$1e-3\ /s$	$1\ Pa$

Table 3.2 – Viscoelasticity parameters for calculation

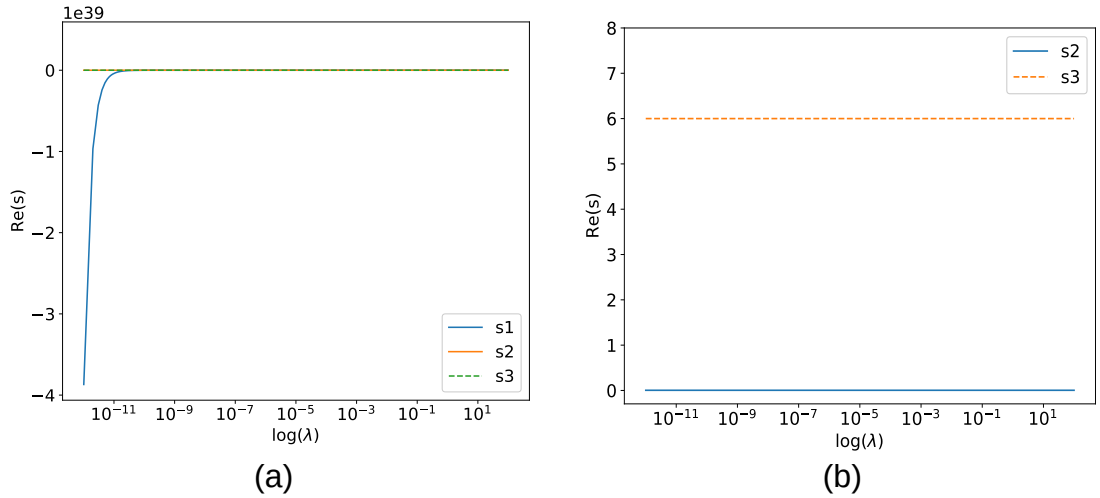

Figure 3.13 – Real part of Lyapunov coefficients s at $\psi = Y_c$ for softening Kelvin-Voigt (KV) model with no external regularization. (a) indicates all the Lyapunov coefficients while (b) indicates only the positive ones.

Figure 3.13a displays the Lyapunov exponents for $\psi = Y_c$, while Figure 3.13b displays only the positive Lyapunov exponents. As the real part of $s2$ is positive, the homogenous solution is unstable. However, since the psoitive part of the Lyapunov exponent is finite, the instability propagates in finite time. This behavior is similar to the rate-dependent softening elasticity model ($\tau_{vd} > 0$) discussed in the previous section. Hence, it can be said that the softening KV model possesses a characteristic time scale associated with damage (intrinsic to the model). This characteristic time scale acts as a resistance to damage growth and this explains the homogeneous

evolution of damage prior to localization in softening GKV model (Section 3.1 and Figure 3.5).

Remark 3 *The stability behavior obtained in this section is only applicable to the 1D case of a homogeneous bar and the results obtained can't be directly generalized to the 2D case. In other words, stability analysis has to be performed separately for the 2D case to understand their localization behavior. In fact, for a more general case, the geometry, type of loading, any initial defects, etc. could act as external perturbations and the stability results obtained for the 1D homogeneous case are no longer valid. It is demonstrated with an example of a 1D homogeneous bar with an initial notch (external perturbations) in the later section (Section 3.4).*

3.3 Softening Generalized-Maxwell (GM) model

In this section, we consider the softening Generalized Maxwell (GM) model to describe the viscoelastic behavior with damage. Despite it being well known that the behavior of the GKV model and GM model is the same without damage (when the respective model parameters are calibrated), their behavior under damage is not well understood. For example, in a dynamic setting, the arrangement of springs and dashpots (series or parallel) was reported to produce different results under localization [115]. Since in our case, both rheological models have different schematics, numerical simulation has to be performed to comment on their localization behavior. In particular, the interest lies in comparing the localization behavior of the softening GM model with the softening GKV model. The schematic of the GM model with damage is shown in Figure 3.14 The free energy per unit volume ψ and viscous dissipation potential for the considered model is given below

$$\psi = g(d)\left[\frac{1}{2}E_0\varepsilon^2 + \sum_{i=1}^{n}\frac{1}{2}E_i(\varepsilon-\varepsilon_i)^2\right] = g(d)\psi_0 \tag{3.59}$$

$$\phi_v = \sum_{i=1}^{n}\frac{1}{2}\eta_i\dot{\varepsilon}_i^2 \approx \sum_{i=1}^{n}\frac{1}{2}\eta_i\left(\frac{\varepsilon_i-\varepsilon_{i,m}}{\Delta t}\right)^2 \tag{3.60}$$

where ψ_0 is the undamaged free energy and $g(d)$ is the degradation function that satisfies the conditions given in Eq. (3.3). The viscosity η_i and relaxation times τ_i are again related by Eq. (3.1). The viscous dissipation potential is again not a function of damage as is the case in Section 3.1 for the softening GKV model.

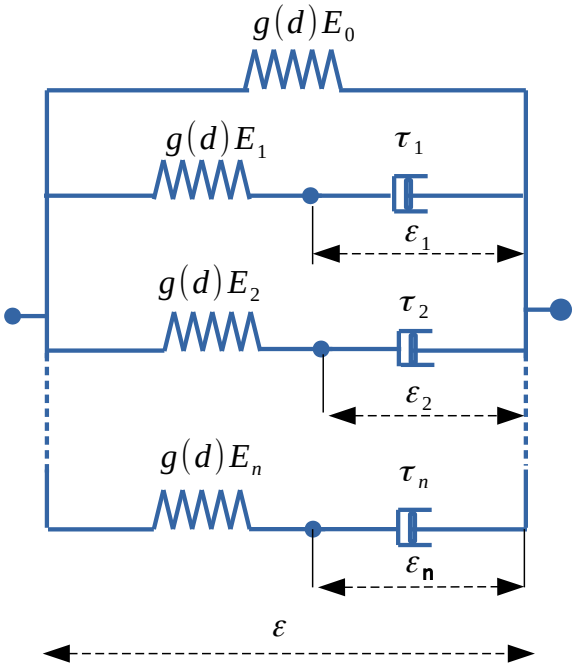

Figure 3.14 – softening Generalized Maxwell (GM) model

The thermodynamic forces conjugate to the state variables are then given as

$$\sigma = \frac{\partial \psi}{\partial \varepsilon} = g(d)\left(E_0\varepsilon + \sum_{i=1}^{n} E_i(\varepsilon - \varepsilon_i)\right) \tag{3.61}$$

$$\sigma_i = -\frac{\partial \psi}{\partial \varepsilon_i} = g(d)E_i(\varepsilon - \varepsilon_i) \tag{3.62}$$

$$Y = -\frac{\partial \psi}{\partial d} = g'(d)\left(E_0\varepsilon + \sum_{i=1}^{n} E_i(\varepsilon - \varepsilon_i)\right) \tag{3.63}$$

where σ is the stress, σ_i is the stress in the dashpot i and Y is the local energy release rate. The viscous stress can also be written as the derivative of the viscous dissipation potential as follows:

$$\sigma_i = \frac{\partial \phi_v}{\partial \dot{\varepsilon}_i} = \eta \dot{\varepsilon}_i \tag{3.64}$$

The damage evolution laws are then given by Eq. (3.10). The mechanical problem to find the state variables remains the same as in Section 3.1 for the softening GKV model and is given by Eq. (3.11) and Eq. (3.12), except for the free energies and viscous dissipation potential in Eq. (3.12) replaced by Eq. (3.59) and Eq. (3.60).

3.3.1 Numerical implementation

For finding displacements and internal strains, one looks for solving the minimization problem given by Eq. (3.17). Recall that the minimization w.r.t u, results in the equilibrium equation (Eq. (3.19)), while the minimization w.r.t ε_i resulted in the time discretized evolution equation of the viscous strain (Eq. (3.21)).

On substitution of Eq. (3.59) and Eq. (3.60) in Eq. (3.21), and rearranging leads to the following expression for the viscous strain in incremental form

$$\varepsilon_i = \frac{\Delta t}{g(d)\Delta t + \tau_i}\left(g(d)\varepsilon + \frac{\tau_i}{\Delta t}\varepsilon_{i,m}\right) \tag{3.65}$$

which when swapped in Eq. (3.61) results in the following

$$\sigma = p(d)\varepsilon - \sigma_{int} \tag{3.66}$$

where

$$p(d) = g(d)\left(E_0 + \sum_{i=1}^{n} E_i - \sum_{i=1}^{n} g(d)E_i\frac{\Delta t}{g(d)\Delta t + \tau_i}\right) \tag{3.67}$$

$$\sigma_{int} = g(d)\sum_{i=1}^{n} E_i\frac{\tau_i}{g(d)\Delta t + \tau_i}\varepsilon_{i,m} \tag{3.68}$$

On substitution of Eq. (3.66) in the equilibrium equation (Eq. (3.19)) and discretizing using 2 noded bar element (see Figure 3.3) leads to the following

$$[\mathbf{K}(d)][\mathbf{U}] = [\mathbf{F}(d)] \tag{3.69}$$

where

$$K_{ij} = \int_0^L p(d)N_{i,x}N_{j,x}dx \qquad \forall\,(i,j)\ \in\ \mathcal{N}\times\mathcal{N} \tag{3.70}$$

$$F_i = \int_0^L \sigma_{int}N_{i,x}dx \qquad \forall\, i\ \in\ \mathcal{N} \tag{3.71}$$

where $\mathcal{N} = \{1, 2, .., N\}$ is the set of finite element nodes. For the minimization w.r.t damage, the problem is again given by Eq. (3.34).

3.3.2 Numerical results

We consider the 1D homogeneous bar of length $L = 1\ m$ as shown in Figure 3.2. The viscoelastic parameters for the GM model are provided in Table 1.2. Note that for the considered viscoelastic

Algorithm 2 1D softening GM model

Initialize $m = 0$, $\varepsilon_{i,m}, [\mathbf{U}_m], d_m, \Delta t$
while $m \leq M$ **do**
  $k = 0$, $d^k = d_m$, $\varepsilon_i^k = \varepsilon_{i,m}$, $err_u = err_d = +\infty$
  while $k < k_{max}$ **and** $err_u > tol_u$ **and** $err_d > tol_d$ **do**
    Assemble stiffness matrices $[\mathbf{K}(d^k)]$ ▷ using Eq. (3.70)
    Assemble forces vectors $[\mathbf{F}(d^k)]$ ▷ using Eq. (3.71)
    Find the nodal displacement vector $[\mathbf{U}^{k+1}]$ ▷ using Eq. (3.69)
    Compute elemental stress vector with d^k ▷ using Eq. (3.66)
    Update the internal strains ε_i^{k+1} ▷ using Eq. (3.65)
    Find the damage field vector d^{k+1} ▷ using Eq. (3.34)
    Compute errors

$$err_u = |\mathbf{U}^{k+1} - \mathbf{U}^k|, \quad err_d = |d^{k+1} - d^k| \tag{3.72}$$

    $k \leftarrow k + 1$
  end while
  $m \leftarrow m + 1$
end while

parameters in Section 3.1 and in this section, the undamaged behavior ($\psi_0 < Y_c$) of the GKV and GM model are the same (since both model parameters are calibrated from the same experimental data obtained on sand bitumen 0/2 [9]). Concerning the fracture parameters, we use the same values used in the softening GKV model with damage (Section 3.1) to aid the comparison of both models: $Y_c = 500\ J/m^3$ and $g(d)$ and $h(d)$ are given by Eq. (3.36) and Eq. (3.37).

3.3.2.1 Local (or homogeneous) evolution

Initially, we validate the numerical implementation by comparing the numerical results with the (semi-) analytical results in local form. The (semi-) analytical results for the GM model with damage are presented in Appendix B. To obtain a homogeneous evolution of damage in the numerical simulations, we set l_c high enough such that $1/l_c \to 0$. We employ two different strain rates $\dot{\varepsilon}_{mean} = (1e-5, 1e-3)\ s$ and the corresponding time steps $\Delta t = (1e-1, 1e-3)\ s$.

Figure 3.15 compares the results in the local form obtained for the GM model with the (semi-) analytical solution and the GKV model. Here, it is evident that the numerical results of the GM model with damage coincide well with the (semi-) analytical solution, thus validating the numerical implementation. Moreover, it can also be observed that the numerical results of the GM and GKV models are in good agreement with each other.

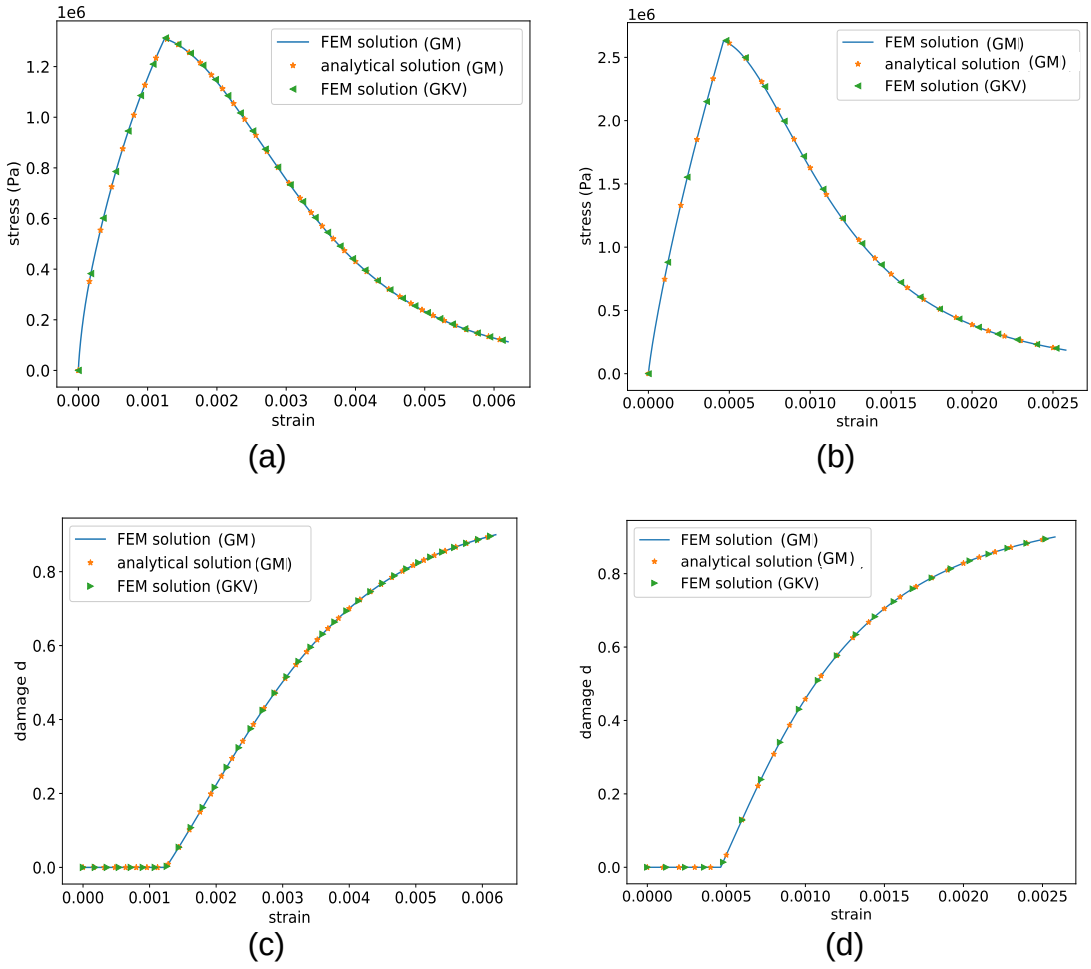

Figure 3.15 – Validation of numerical implementation: Local (or homogeneous) stress-strain plots (top row) and damage evolution plots (bottom row) for $\dot{\varepsilon}_{\text{mean}} = 1e-5\,\text{s}^{-1}$ (left column) and $\dot{\varepsilon}_{\text{mean}} = 1e-3\,\text{s}^{-1}$ (right column)

3.3.2.2 Localisation behavior

In this section, we are interested in studying the localization behavior of the considered model, and then comparing its results to the softening GKV model (Figure 3.6). Since the bar is homogeneous, a small perturbation is applied to the damage field ($1e-3$) at the beginning of each time step to initiate localization. In our case, we apply the perturbation at the center of the bar $x = L/2$ to trigger the localization at the center. Here, we consider three different imposed displacement rates $\dot{U} = (1e-5,\ 1e-3,\ 1e-1)\ m/s$ and the corresponding time steps $\Delta t = (1e-1,\ 1e-3,\ 1e-5)\ s$. The characteristic length scale l_c is again set to 0.5 m. Figure

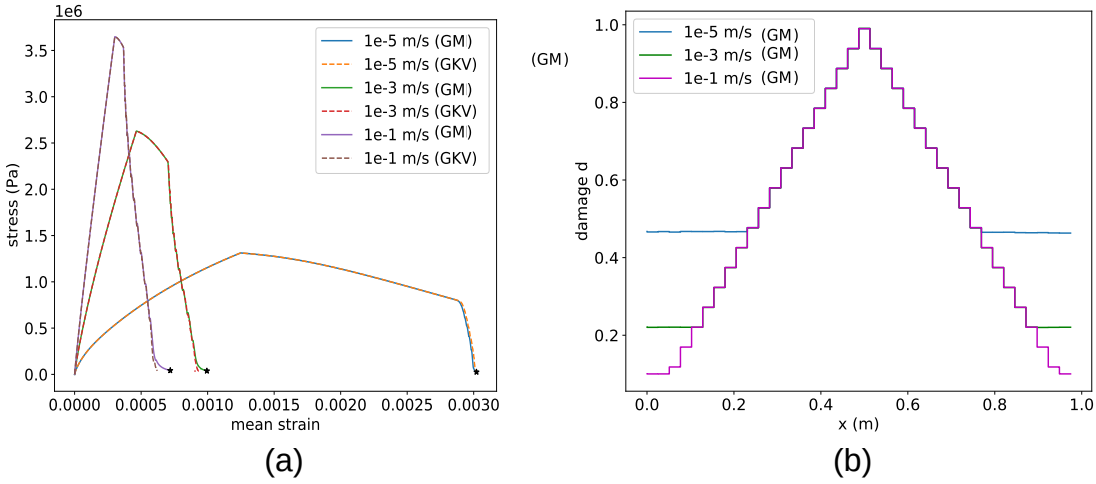

Figure 3.16 – Comparison of results for softening GM model and softening GKV model (a) stress-strain plot and (b) damage at rupture for softening GM model

3.16 compares the results of the softening GM model and the softening GKV model for different applied displacement rates. Overall, it is clear from the figure that both models exhibit similar behavior. In particular, one can observe the same rate effects for both models: The higher the applied displacement rate, the higher the stress at damage initiation and the lower the mean strain at rupture. Moreover, the localization behavior of both models is also similar. In particular, after the damage initiation, a homogeneous evolution of damage is observed initially as is the case in the softening GKV model, followed by localization. This indicates the presence of an intrinsic time scale (associated with damage) in the softening GM model as well. Furthermore, since the localization behavior is the same for both models, we can also conclude that the values of the intrinsic time scale are also the same. It should also be noted that the damage threshold, at which the damage localizes decreases with an increase in loading rate, signifying the diminishing effect of intrinsic time scale as the loading rate is increased.

3.4 Influence of external perturbation

In section 3.2, the stability analysis at the onset of damage initiation was performed by applying a perturbation to the homogeneous solution and seeing the evolution of the perturbation. The results obtained for the analysis hold only for the 1D case of a homogeneous bar. Such analysis revealed the presence of an intrinsic time scale present in the softening viscoelastic models (Section 3.2.3), which signifies that the instability propagates in finite time. This explains the homogeneous evolution of damage (in Sections 3.1 and 3.3) before the occurrence of localization.

In this section, we consider a non-homogeneous bar and analyze numerically the localization behavior of softening viscoelastic models. In particular, we consider a bar with an initial notch at the center as shown in Figure 3.17. To numerically represent the notch, the damage at the center is initialized as $d(x = L/2, t = 0) = d_c$ (as indicated in Figure 3.17). Specifically, we consider three different values for d_c: $\{0,\ 0.1,\ 0.25\}$, where $d_c = 0$ implies the case of a homogeneous bar without a notch.

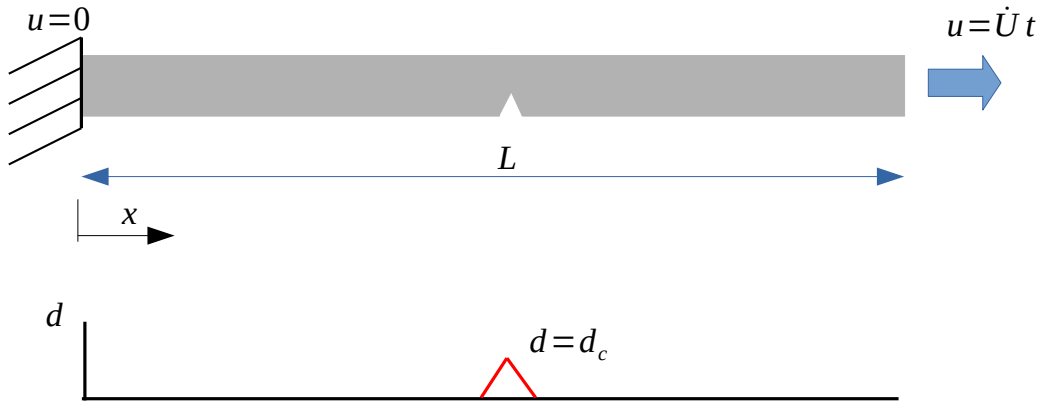

Figure 3.17 – 1D non-homogenous bar with a notch at the center (top); Numerical representation of the notch by setting $d = d_c > 0$

For the viscoelastic parameters, we use the softening GKV model (regularized through lip-field approach) with the same set of parameters used in Section 3.1 (one can also consider the softening GM model and expect a similar result based on the similarity of the results observed in Section 3.3).

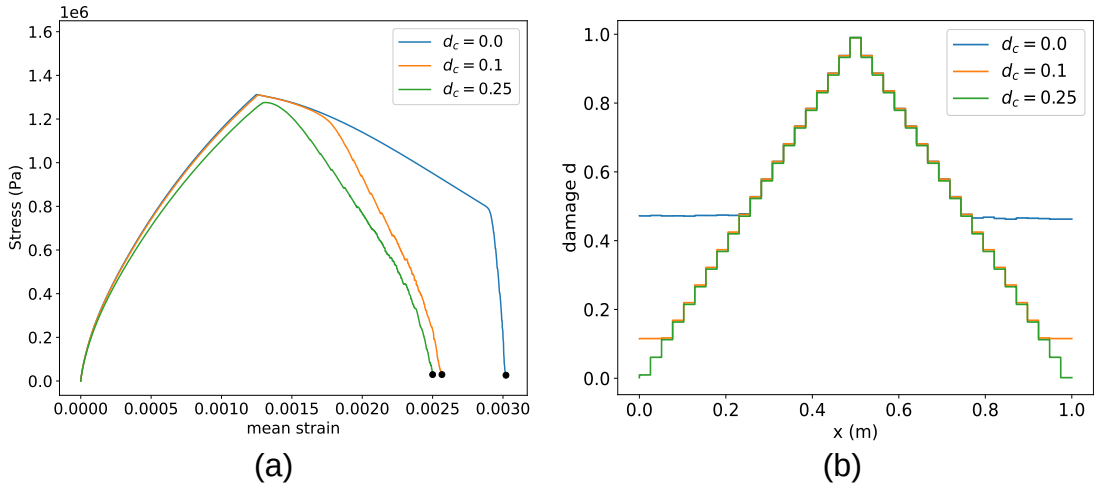

Figure 3.18 – (a) Stress-strain curves and (b) damage evolution curves for different values of d_c (notch sizes)

Figure 3.18 compares the stress-strain curve and the damage field at rupture for the considered different values of d_c. It can be seen that, as the value of d_c is increased, the sooner the occurrence of localization. In particular, for the case of $d_c = 0.25$, the localization seems to occur much sooner after damage initiation. This could indicate that as the size of the notch is increased (by increasing the values of d_c), the intrinsic time scale associated with damage diminishes. Hence, the initial perturbation applied at the center of the bar grows at a faster rate as the value of d_c is increased.

Hence, this section reveals that the intrinsic time scale effect present in the softening viscoelastic models is more pertinent to the 1D case of a homogeneous bar, and its effect may not be felt significantly in other cases, where external perturbations (like notches, non-homogeneous boundary conditions, etc) are present.

3.5 Summary and concluding remarks

This chapter focused on studying the behavior of the viscoelastic damage model (developed in Chapter 2) for the 1D case. In particular, both the softening generalized Kelvin-Voigt (GKV) model and the softening Generalized Maxwell (GM) model behavior were considered and it was observed that both models exhibit similar behavior (when the number of GKV and GM units are high enough to represent well the continuous spectrum of the material). Moreover, they were able to qualitatively represent the rate-dependent effects commonly observed in bituminous materials. However, both models experienced homogeneous evolution of damage before the onset of localization. To understand such homogeneous evolution of damage, stability analysis was

conducted for a 1D homogeneous bar at the onset of damage initiation (for the softening Kelvin-Voigt (KV) model), which revealed the presence of intrinsic time scale associated with damage in the softening viscoelastic models. The aforementioned intrinsic time scale was found to delay the damage localization process but doesn't prevent the localization from occurring on a plane of zero thickness. Hence, regularization is still required to yield mesh-independent results. It should also be noted that the homogeneous evolution of damage is also because of the ability of the lip-field approach to preserve local solutions (unlike the classical Thick-Level-Set TLS approach). Moreover, the effect of the intrinsic time scale was found to decrease with an increase in loading rate. Future research should involve conducting tensile tests on a 1D bar to investigate the potential homogeneous evolution of damage (stress-strain softening behavior without strain localization) in bituminous materials (due to the growth of micro-voids (damage) in a uniformly distributed fashion in the specimen).

Numerical tests were also conducted for the 1D case of a non-homogeneous bar with a notch at the center, which revealed the diminishing effect of intrinsic time scale as the size of the notch increases. This will also be observed later (in Chapter 5) in the case of 2D, due to the presence of external perturbations in terms of geometry, loading conditions, etc.

Chapter 4

Extension of the model to multi-dimensional case

Chapter 3 discussed the lip-field (LF) formulation for softening viscoelastic damage models in a one-dimensional setting. The current chapter, however, is dedicated to the extension of this approach to encompass multi-dimensional (2D) scenarios. This chapter can be divided into three sections: The initial section concerns the extension of the viscoelastic damage model to multi-dimensional contexts. In particular, we use the eigen split of internal strains to accommodate unilateral effects, wherein material behavior in tension is different from that in compression (bituminous materials like most materials are typically weaker in tension compared to compression). The second part of this chapter concentrates on the numerical implementation of the developed model in the 2D case. This involves computational aspects related to the equilibrium solver and the lip-field damage solver. In the concluding section, our focus shifts to validating the numerical implementation. This involves a comparison of the results obtained for the 2D simulations with both analytical solutions and the 1D finite element solution (presented in Chapter 3). This validation process serves as a pivotal step in calibrating the developed model to align with laboratory fracture tests on bituminous materials, which will be discussed in the next chapter.

Most of the subjects explored in this chapter have already been presented in our recent publication [117] and at the conferences [118] [119].

4.1 Viscoelastic damage model: LF formulation

Consider the quasi-static deformation of a body initially occupying a domain Ω (with boundary Γ) and undergoes deformation via a displacement field $\mathbf{u}$, where the Cauchy stress and small strain tensor are denoted by $\boldsymbol{\sigma}$ and $\boldsymbol{\varepsilon}$ (Eq. (2.36)), respectively. Displacement boundary conditions are applied on the portion Γ_u of the boundary, while zero traction forces are applied on the remaining portion Γ_N and we also assume that there are no body forces (without loss of gen-

erality). The temporal discretization follows the methodology outlined in Section 2.3, utilizing $\Delta t = t_{m+1} - t_m = t - t_m$, whereby, for the sake of simplicity, the $m+1$ indices will be omitted for all variables, as previously indicated. Our objective involves determining the state variables at the time instant $t_{m+1} = t$, given the state variables at time t_m, as per the following equation (as seen in Eq. (2.53)):

$$\{\mathbf{u}, \boldsymbol{\varepsilon_i}, d\} = \arg \min_{\substack{\mathbf{u}' \in \mathcal{U}_m \\ \boldsymbol{\varepsilon}'_{\boldsymbol{i}} \in \mathcal{P} \\ d' \in \mathcal{A}_m \cap \mathcal{L}_\Omega}} F(\mathbf{u}', \boldsymbol{\varepsilon}'_{\boldsymbol{i}}, d' \ ; \ \boldsymbol{\varepsilon_{i,m}}, \Delta t) \tag{4.1}$$

where the incremental potential F is given below (from Eq. (2.47))

$$F = \int_\Omega f \ d\Omega = \int_\Omega \psi(\boldsymbol{\varepsilon}, \boldsymbol{\varepsilon_i}, d) + \Delta t \phi_v(\boldsymbol{\varepsilon}_i; \boldsymbol{\varepsilon_{i,m}}, \Delta t) + Y_c h(d) d\Omega \tag{4.2}$$

We reiterate that, in the above equation, $\boldsymbol{\varepsilon}_i$ ($\forall \ i \in \{1, 2, .., n\}$) and d represents the internal (or viscous) strain tensor and the scalar damage field, while ψ, ϕ_v, and $h(d)$ denote the free energy per unit volume, viscous dissipation potential per unit volume, and the damage softening function. The admissible spaces for displacement, internal strains, and damage field are as follows:

$$\mathcal{U}_m = \mathcal{U}(t) = \{\mathbf{u} \in H^1(\Omega) : \mathbf{u} = \mathbf{u_d}(t) \ \ on \ \ \Gamma_u\} \tag{4.3}$$

$$\mathcal{P} = \{\mathbf{q} : \mathbf{q}_{ij} = \mathbf{q}_{ji}, \ \mathbf{q}_{ij} \in L^\infty(\Omega)\} \tag{4.4}$$

$$\mathcal{A}_m = \{d \in L^\infty(\Omega) : d_m \leq d \leq 1\} \tag{4.5}$$

$$\mathcal{L}_\Omega = \left\{ d \in L^\infty(\Omega) : |d(\mathbf{x}) - d(\mathbf{y})| \leq \frac{1}{l_c} dist(\mathbf{x}, \mathbf{y}) \ \ \forall \mathbf{x}, \mathbf{y} \in \Omega \right\} \tag{4.6}$$

The space $\mathcal{A}_m$ ensures the irreversibility of the damage field (no healing), while the space $\mathcal{L}_\Omega$ (Lipschitz space) introduces the length scale to prevent the pathological mesh-dependent results.

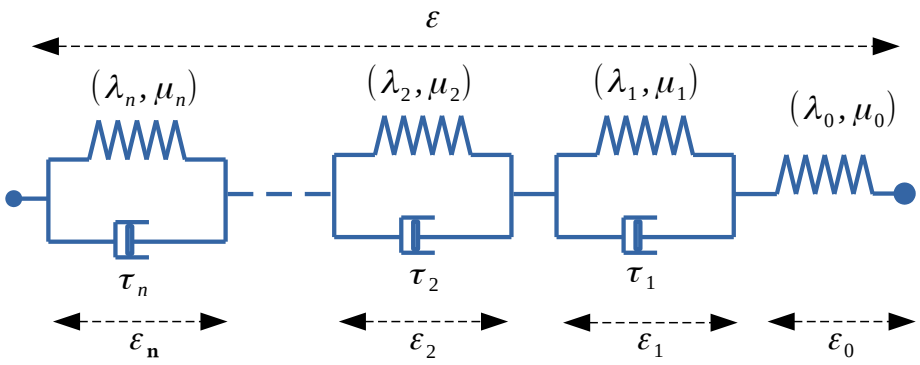

Figure 4.1 – Schematic of Generalized Kelvin-Voigt (GKV) model

Eq. (4.1) can be closed by defining the free energy potential ψ, viscous dissipation potential ϕ_v, and the softening function $h(d)$. In particular, we consider the softening Generalized Kelvin-Voigt (GKV) model to define the viscoelastic behavior [1]. The schematic of the GKV model is shown in Figure 4.1. $\{(\lambda_0, \mu_0), ..., (\lambda_1, \mu_1)\}$ and $\{\tau_1, ..., \tau_n\}$ denote the Lamé's constants and the retardation times of each unit attached to the GKV model. The small strain tensor in this case is given as follows:

$$\boldsymbol{\varepsilon} = \sum_{i=0}^{n} \boldsymbol{\varepsilon_i} \tag{4.7}$$

It is also assumed that Poisson's ratio ν is constant and time-independent for all KV units (as discussed in Section 1.2.3). The free energy and viscous dissipation potential are then given as follows: (analogous to the 1D case provided in Eqs. (3.2, 3.4))

$$\psi = g(d) \sum_{i=0}^{n} \left(\mu_i \boldsymbol{\varepsilon_i} : \boldsymbol{\varepsilon_i} + \frac{\lambda_i}{2} Tr(\boldsymbol{\varepsilon_i})^2 \right) \tag{4.8}$$

$$\phi_v = \sum_{i=1}^{n} \tau_i \left(\mu_i \dot{\boldsymbol{\varepsilon}}_{\boldsymbol{i}} : \dot{\boldsymbol{\varepsilon}}_{\boldsymbol{i}} + \frac{\lambda_i}{2} Tr(\dot{\boldsymbol{\varepsilon}}_{\boldsymbol{i}})^2 \right) \tag{4.9}$$

where $g(d)$ is the energy degradation function (satisfying the conditions specified in Eq. (3.3)) and $Tr(.)$ denotes the trace operator. $\dot{\boldsymbol{\varepsilon}}_i \quad \forall\ i \ \in \{1, 2, ..., n\}$ denotes the time derivative of the viscous strain and is approximated by an implicit Euler time discretization as indicated in Eq. (2.40). Replacing the expression for $\boldsymbol{\varepsilon}_0$ in Eq. (4.8) using Eq. (4.7), the stress $\boldsymbol{\sigma}$ and energy

1. Alternatively, a softening Generalized Maxwell (GM) model could be chosen and expect similar results, as observed in the 1D case (Figure 3.16)

release rate Y can then be derived using Eqs. (2.25, 2.28)

$$\boldsymbol{\sigma} = g(d)\left[2\mu_0\left(\boldsymbol{\varepsilon} - \sum_{i=1}^{n}\boldsymbol{\varepsilon_i}\right) + \lambda_0 Tr\left(\boldsymbol{\varepsilon} - \sum_{i=1}^{n}\boldsymbol{\varepsilon_i}\right)\mathbb{I}\right] \tag{4.10}$$

$$Y = -g'(d)\sum_{i=0}^{n}\left(\mu_i\boldsymbol{\varepsilon_i}{:}\boldsymbol{\varepsilon_i} + \frac{\lambda_i}{2}Tr(\boldsymbol{\varepsilon_i})^2\right) \tag{4.11}$$

It can be observed that the material exhibits identical characteristics under both tensile and compressive states. In simpler terms, the energy release rate, denoted as Y, remains unaffected by the signs of the eigenvalues of the strains. This implies that the growth of damage persists even if the affected area encounters only compression. In most situations, this behavior might lack realism and could result in solutions that deviate significantly from actual observations (bituminous materials, like most materials, are typically weaker in tension compared to compression, and the failure is often due to tension). Hence, in order to address this, it is common in softening elasticity models to introduce a slightly non-linear free energy function [93, 94] that induces asymmetric behavior in tension and compression. We adopt a similar procedure, where the damage affects the tensile and compressive parts of the free energy in a different manner (asymmetry) as follows:

$$\begin{aligned}\psi = \sum_{i=0}^{n}\Bigg[&g(d)\left(\mu_i < \boldsymbol{\varepsilon_i} >_+ : < \boldsymbol{\varepsilon_i} >_+ + \frac{\lambda_i}{2}Tr(< \boldsymbol{\varepsilon_i} >_+)^2\right) + \\ &g(\theta d)\left(\mu_i < \boldsymbol{\varepsilon_i} >_- : < \boldsymbol{\varepsilon_i} >_- + \frac{\lambda_i}{2}Tr(< \boldsymbol{\varepsilon_i} >_-)^2\right)\Bigg]\end{aligned} \tag{4.12}$$

where, $< \boldsymbol{\varepsilon} >_+$ and $< \boldsymbol{\varepsilon} >_-$ denote the eigen decomposition of $\boldsymbol{\varepsilon}$ as follows:

$$\boldsymbol{\varepsilon} = < \boldsymbol{\varepsilon} >_+ + < \boldsymbol{\varepsilon} >_- \tag{4.13}$$

such that

$$< \boldsymbol{\varepsilon} >_+ = \sum_{a=1}^{b} < \varepsilon^a >_+ \mathbf{n}^a \otimes \mathbf{n}^a \qquad < \boldsymbol{\varepsilon} >_- = \sum_{a=1}^{b} < \varepsilon^a >_- \mathbf{n}^a \otimes \mathbf{n}^a \tag{4.14}$$

where $0 \leq \theta \leq 1$ offers user-defined control over the material's response to tensile and compressive forces. A value of $\theta = 1$ corresponds to the symmetric potential given by Eq. (4.8). Conversely, when $\theta < 1$, the material behavior becomes asymmetrical, and when $\theta = 0$ ($g(0) = 1$ as per Eq. (3.3)), the energy degradation due to damage affects only the tensile part of free energy (Eq. (4.12)). It should be noted that $(\{\varepsilon^a\}_{a=1,2,..,b})$ indicate the eigen values and $(\{\mathbf{n}^a\}_{a=1,2,..,b})$ denote the eigen vectors of $\boldsymbol{\varepsilon}$. b takes the values 2 and 3 for two and three dimensions respectively.

The bracket operators $< q >_+$ and $< q >_-$ for any given scalar q are defined as follows:

$$< q >_+ = \frac{1}{2}(q + |q|) \qquad < q >_- = \frac{1}{2}(q - |q|) \tag{4.15}$$

For the case of $\theta = 1$, the stress $\boldsymbol{\sigma}$ and energy release rate Y are given by Eqs. (4.10, 4.11), while for the case of $\theta = 0$, they can be written as follows using Eqs. (4.7, 2.25, 2.28):

$$\begin{aligned} \boldsymbol{\sigma} = g(d) \left[2\mu_0 \left\langle \boldsymbol{\varepsilon} - \sum_{i=1}^{n} \boldsymbol{\varepsilon_i} \right\rangle_+ + \lambda_0 Tr \left(\left\langle \boldsymbol{\varepsilon} - \sum_{i=1}^{n} \boldsymbol{\varepsilon_i} \right\rangle_+ \right) \mathbb{I} \right] + \\ \left[2\mu_0 \left\langle \boldsymbol{\varepsilon} - \sum_{i=1}^{n} \boldsymbol{\varepsilon_i} \right\rangle_- + \lambda_0 Tr \left(\left\langle \boldsymbol{\varepsilon} - \sum_{i=1}^{n} \boldsymbol{\varepsilon_i} \right\rangle_- \right) \mathbb{I} \right] \end{aligned} \tag{4.16}$$

$$Y = -g'(d) \sum_{i=0}^{n} \left[\left(\mu_i < \boldsymbol{\varepsilon_i} >_+ : < \boldsymbol{\varepsilon_i} >_+ + \frac{\lambda_i}{2} Tr(< \boldsymbol{\varepsilon_i} >_+)^2 \right) \right] \tag{4.17}$$

Notice from Eq. (4.16) that even when the material is completely damaged ($d = 1$ and $g(1) = 0$), it will still be able to withstand stresses under compression. Moreover, only the tensile modes of the free energy contribute to damage driving force Y, as per Eq. (4.17). Hence, the damage growth is only due to the tensile part of the free energy for $\theta = 0$. The contribution of damage growth under compression can be controlled by θ. For example, the Indirect Tensile Test (ITT) results reported for bituminous materials in [36] indicate that the failure occurs in the plane that undergoes tension, despite the loading being compressive in nature. Hence, a damage model with damage growth driven primarily by the tensile part of free energy is more suitable for modeling such failure.

Remark 4 *The above choice of split is model-dependent and one could also consider a different form of split of free energy specific to an application. We list the other forms of splits considered during the thesis in Appendix F.*

4.2 Computational aspects

This focus now lies on the computational aspects and the numerical implementation for solving the minimization problem given by Eq. (4.1). In particular, the focus will be on extending the numerical implementation discussed for the 1D case to the 2D case. Besides, the lip-field damage solver will also be detailed, thanks to the bounds estimation provided in [101] (1D) and [102] (2D), as discussed in Section 1.5.3.

Recall from the discussion made in Section 3.1.1 (1D case) that the function F (given by Eq.

(4.2)) is not convex. However, F is convex w.r.t $\{\mathbf{u}, \boldsymbol{\varepsilon}_i\}$ and d separately (provided $g(d)$ and $h(d)$ are convex). Hence, an alternate minimization strategy could be used to solve for $\{\mathbf{u}, \boldsymbol{\varepsilon}_i\}$ by fixing d, and then solving for d by fixing the remaining variables. In particular, at time step $t_{m+1} = t$, alternate minimization involves performing the following iterations until convergence

$$(\mathbf{u}^{k+1}, \boldsymbol{\varepsilon}_i^{k+1}) = \arg \min_{\substack{\mathbf{u}' \in \mathcal{U}_m \\ \boldsymbol{\varepsilon}_i{}' \in \mathcal{P}}} F(u', \boldsymbol{\varepsilon}_i{}', d^k) \tag{4.18}$$

$$(d^{k+1}) = \arg \min_{d' \in \mathcal{A}_m \cap \mathcal{L}_\Omega} F(\mathbf{u}^{k+1}, \boldsymbol{\varepsilon}_i{}^{k+1}, d') \tag{4.19}$$

where k represents the iteration corresponding to the alternate minimization. Notice that both problems are convex.

4.2.1 Spatial discretization

The spatial discretization of domain Ω, denoted as Ω^h, is done using linear triangular elements (2D) with the help of the *gmsh* software [120]. This will be the case for all the 2D simulations reported in this thesis. Subsequently, the displacement field is discretized using classical linear finite element discrete space defined over Ω^h. In this context, the displacement field exhibits continuity across Ω^h while maintaining linearity within each individual element. Consequently, the strain field becomes a piecewise constant across each element. The internal strains $\boldsymbol{\varepsilon}_i$ and damage field d are stored at the centroids of the elements and remain piecewise constant throughout each element. The discretized displacement field and strain field are given by

$$\mathbf{u}(\mathbf{x}) = [N]\{\mathbf{U}\} \tag{4.20a}$$

$$\boldsymbol{\varepsilon}(\mathbf{x}) = [\nabla \mathbf{N}]\{\mathbf{U}\} = [\mathbf{B}]\{\mathbf{U}\} \tag{4.20b}$$

where $[\mathbf{N}]$ is the matrix of shape functions obtained by the global assembly of shape functions associated with each element. $\{\mathbf{U}\}$ is the nodal displacement vector and $[\mathbf{B}] = [\nabla \mathbf{N}]$ is the operator that transforms displacements into strains.

In the subsequent sections, the focus is on solving the minimization problems given by Eq. (4.18) and Eq. (4.19).

4.2.2 Finding displacement and internal strains

In this section, our attention is limited to solving Eq. (4.18) to find displacement and internal strains. Specifically, we consider the two different cases for θ as per Eq. (4.12) and detail their numerical implementation separately.

Case (A): $\theta = 1$ (symmetrical behavior in tension and compression)

Case (B): $0 \leq \theta \leq 1$ (asymmetrical behavior in tension and compression for $\theta \neq 1$)

Certainly, the numerical implementation for case (B) is more general and can accommodate case (A). However, it will be seen in the following sections that Case (A) requires less computational effort relative to Case (B), owing to the non-linearity induced due to the eigen split in Case (B). Hence, for the case of $\theta = 1$, the numerical implementation discussed in case (A) can be preferred to save computational time.

4.2.2.1 Case (A)

For this case ($\theta = 1$), we recover a symmetrical behavior of the model in tension and compression as per Eq. (4.8). Considering $\mathbb{C}_i$ ($\forall\, i \ \in \{0, 1, 2.., n\}$) as the set of fourth-order elasticity tensors associated to i^{th} unit of the GKV model (Figure 4.1), we can express the following for a material that is both homogeneous and isotropic:

$$\mathbb{C}_i = 2\mu_i \mathbb{I} + \lambda_i \mathbf{1} \otimes \mathbf{1} \quad \forall\, i \ \in \ \{0, 1, 2, .., n\} \tag{4.21}$$

where $\mathbb{I}$ and $\mathbf{1}$ are the fourth and second-order identity tensors respectively. The relations between Lamé's constants and Young's modulus are given as follows:

$$\lambda_i = \frac{\nu E_i}{(1+\nu)(1-2\nu)} \quad \text{for plane strain} \tag{4.22a}$$

$$\lambda_i = \frac{\nu E_i}{1-\nu^2} \quad \text{for plane stress} \tag{4.22b}$$

$$\mu_i = \frac{E_i}{2(1+\nu)} \tag{4.22c}$$

The free energy potential ψ (Eq. (4.8)) and viscous dissipation ϕ_v (Eq. (4.9)) can now be rewritten as follows

$$\psi = \frac{1}{2}\left(\boldsymbol{\varepsilon} - \sum_{i=1}^{n} \boldsymbol{\varepsilon_i}\right) : g(d)\mathbb{C}_0 : \left(\boldsymbol{\varepsilon} - \sum_{i=1}^{n} \boldsymbol{\varepsilon_i}\right) \ + \ \sum_{i=1}^{n} \frac{1}{2}\boldsymbol{\varepsilon_i} : g(d)\mathbb{C}_i : \boldsymbol{\varepsilon_i} \tag{4.23}$$

$$\phi_v = \sum_{i=1}^{n} \frac{1}{2}\dot{\boldsymbol{\varepsilon_i}} : \tau_i \mathbb{C}_i : \dot{\boldsymbol{\varepsilon_i}} \tag{4.24}$$

The expression for stress $\boldsymbol{\sigma}$ is then given as follows:

$$\boldsymbol{\sigma} = \frac{\partial \psi}{\partial \boldsymbol{\varepsilon}} = g(d)\mathbb{C}_0 : \left(\boldsymbol{\varepsilon} - \sum_{i=1}^{n} \boldsymbol{\varepsilon_i}\right) \tag{4.25}$$

Since all the units in the GKV model are connected in series (Figure 4.1), the stress in each unit should be the same. Hence, the stress $\boldsymbol{\sigma}$ can also be written as follows:

$$\boldsymbol{\sigma} = g(d)\mathbb{C}_{\mathbf{i}} : \boldsymbol{\varepsilon_i} + \tau_i \mathbb{C}_{\mathbf{i}} : \dot{\boldsymbol{\varepsilon}}_{\boldsymbol{i}} \;\approx\; g(d)\mathbb{C}_{\mathbf{i}} : \boldsymbol{\varepsilon_i} + \tau_i \mathbb{C}_{\mathbf{i}} : \left(\frac{\boldsymbol{\varepsilon_i} - \boldsymbol{\varepsilon_{i,m}}}{\Delta t}\right) \quad \forall\, i \;\in\; \{1, 2, .., n\} \tag{4.26}$$

Equating the expression for stresses provided in Eq. (4.25) and Eq. (4.26) and rearranging leads to the following expression for viscous strain in incremental form:

$$\boldsymbol{\varepsilon_i} = \frac{\Delta t}{g(d)\Delta t + \tau_i}\mathbb{C}_i^{-1} : \left(\boldsymbol{\sigma} + \frac{\tau_i}{\Delta t}\mathbb{C}_i : \boldsymbol{\varepsilon_{i,m}}\right) \quad \forall\, i \;\in\; \{1, 2, .., n\} \tag{4.27}$$

Substituting the above equation for $\boldsymbol{\varepsilon}_i$ in Eq. (4.25) leads to the subsequent expression for stress

$$\boldsymbol{\sigma} = \mathbb{P} : \left(\boldsymbol{\varepsilon} - \sum_{i=1}^{n} \frac{\tau_i}{g(d)\Delta t + \tau_i}\boldsymbol{\varepsilon_{i,m}}\right) = \mathbb{P} : \boldsymbol{\varepsilon} - \boldsymbol{\sigma_{int}} \tag{4.28}$$

where $\mathbb{P}$ and $\boldsymbol{\sigma_{int}}$ are given as follows

$$\mathbb{P} = g(d)\left[\mathbb{I} + \sum_{i=1}^{n} \frac{g(d)\Delta t}{g(d)\Delta t + \tau_i}\mathbb{C}_0 : \mathbb{C}_i^{-1}\right]^{-1} : \mathbb{C}_0 \tag{4.29}$$

$$\boldsymbol{\sigma_{int}} = \mathbb{P} : \left(\sum_{i=1}^{n} \frac{\tau_i}{g(d)\Delta t + \tau_i}\boldsymbol{\varepsilon_{i,m}}\right) \tag{4.30}$$

Remark 5 *Furthermore, it can be confirmed that the stress σ in the 1D scenario (as defined in Eq. (3.24)) can be retrieved as a particular instance of the stress tensor $\boldsymbol{\sigma}$ outlined in Eq. (4.28).*

The directional derivative of F in the direction of $[\mathbf{u}^*, \varepsilon_i^*] \in [\mathcal{U}^*, \mathcal{P}]$, denoted as δF is given as follows:

$$\delta F(\mathbf{u}, \boldsymbol{\varepsilon}_i, d)[\mathbf{u}^*, \boldsymbol{\varepsilon}_i^*] = \int_\Omega \boldsymbol{\sigma} : \boldsymbol{\varepsilon}(\mathbf{u}^*) d\Omega + \int_\Omega \sum_{i=1}^{n} \left(\frac{\partial \psi}{\partial \boldsymbol{\varepsilon}_i}\varepsilon_i^* + \Delta t \frac{\partial \phi_v}{\partial \boldsymbol{\varepsilon}_i}\varepsilon_i^*\right) d\Omega \tag{4.31}$$

where δF is also called the functional (or variational) derivative.

Since F is convex w.r.t $\{\mathbf{u}, \boldsymbol{\varepsilon}_i\}$, the minimization of F w.r.t $\{\mathbf{u}, \boldsymbol{\varepsilon}_i\}$ can be written as stationarity of the functional derivative δF as follows:

$$\delta F(\mathbf{u}, \varepsilon_i, d)[\mathbf{u}^*, \varepsilon_i^*] = 0 \tag{4.32}$$

Zeroing the directional derivative w.r.t $[\mathbf{u}^*, 0]$ results in the equilibrium equation:

$$\int_\Omega \boldsymbol{\sigma} : \boldsymbol{\varepsilon}(\mathbf{u}^*)\ d\Omega = 0, \quad \forall\ \mathbf{u}^* \in \mathcal{U}^* \tag{4.33}$$

while zeroing the directional derivative w.r.t $[0, \varepsilon_i^*]$ and using Eqs. (4.23, 4.24) results in the incremental equation for the internal strains $\boldsymbol{\varepsilon}_i$ as given in Eq. (4.27).

Replacing the expression for stress $\boldsymbol{\sigma}$ in the equilibrium equation given by Eq. (4.33) using Eq. (4.28) results in the following weak form

$$\int_\Omega \boldsymbol{\varepsilon}(\mathbf{u}^*) : \mathbb{P}(d) : \boldsymbol{\varepsilon}(\mathbf{u})\ d\Omega = \int_\Omega \boldsymbol{\sigma_{int}} : \boldsymbol{\varepsilon}(\mathbf{u}^*)\ d\Omega \quad \forall\ \mathbf{u}^* \in \mathcal{U}^*\ , \mathbf{u} \in \mathcal{U}_m \tag{4.34}$$

The discretized form of the above equations can be obtained using Eq. (4.20) as follows:

$$[\mathbf{K}(d)]\{\mathbf{U}\} = [\mathbf{R}] \tag{4.35}$$

where

$$[\mathbf{K}(d)] = \int_\Omega [\mathbf{B}]^T \mathbb{P}(d) [\mathbf{B}]\ d\Omega, \quad [\mathbf{R}] = \int_\Omega [\mathbf{B}]^T \boldsymbol{\sigma_{int}}\ d\Omega \tag{4.36}$$

The procedure for solving the minimization problem given by Eq. (4.18) then involves solving the Eq. (4.35) to find the displacement field $\mathbf{u}(\mathbf{x})$ (using the latest available damage field d^k) and then updating the internal strain $\boldsymbol{\varepsilon}_i$ using Eq. (4.27). It should be noted that the equations for finding displacements and internal strains remain linear in this case.

4.2.2.2 Case (B)

This is a more general case with $0 \leq \theta \leq 1$. Recall that, for $\theta = 0$, the damage growth is driven only by free energy associated with the tensile modes of each unit of the GKV model (as per Eq. (4.17)). Contrary to Case (A), a linear equation for finding the displacements and internal strains is not possible due to the eigen split of the strain tensors. Hence, a Newton-based method will be used to find the displacements and internal strains.

Solving the minimization problem as defined in Eq. (4.18) leads to the stationarity condition presented in Eq. (4.32). Setting the directional derivatives along $\mathbf{u}^*$ and $\boldsymbol{\varepsilon}_i^*$ to zero separately yields the following

$$f_0 = \int_\Omega \boldsymbol{\sigma}(\boldsymbol{\varepsilon}(\mathbf{u}), \boldsymbol{\varepsilon}_i, d) : \boldsymbol{\varepsilon}(\mathbf{u}^*)\ d\Omega = 0 \quad \forall \mathbf{u}^* \in \mathcal{U}^* \tag{4.37}$$

$$f_i = \int_\Omega \frac{\partial \psi}{\partial \boldsymbol{\varepsilon_i}}(\boldsymbol{\varepsilon}(\mathbf{u}), \boldsymbol{\varepsilon_i}, d) + \Delta t \frac{\partial \phi_v}{\partial \boldsymbol{\varepsilon_i}}(\boldsymbol{\varepsilon_i}, \boldsymbol{\varepsilon_{i,m}})\ d\Omega = 0 \quad \forall i \in \{1, 2, .., n\} \tag{4.38}$$

where $\mathbf{u}^* \in \mathcal{U}^*, \mathbf{u} \in \mathcal{U}_m$ and $\boldsymbol{\varepsilon_i} \in \mathcal{P}(\Omega)$. Newton-Raphson method will be used to solve these $n+1$ non-linear equations, which involves solving the below linear equation iteratively until convergence.

$$[\mathbf{K}^j]\,\{\boldsymbol{\Delta\alpha}^j\} = [\mathbf{r}^j] \tag{4.39}$$

where the superscript j is associated with Newton's iteration. Here, $\mathbf{K}^j$, $\boldsymbol{\alpha}^j$ and $\mathbf{r}^j$ are the Hessian (or tangent) matrix (Hessian of F), the vector of unknowns and the vector of residuals at iteration j and their expression is given as follows:

$$[\mathbf{K}^j] = \begin{pmatrix} \frac{\partial f_0^j}{\partial \mathbf{u}} & \frac{\partial f_0^j}{\partial \boldsymbol{\varepsilon_1}} & \dots & \frac{\partial f_0^j}{\partial \boldsymbol{\varepsilon_n}} \\ \frac{\partial f_1^j}{\partial \mathbf{u}} & \frac{\partial f_1^j}{\partial \boldsymbol{\varepsilon_1}} & \dots & \frac{\partial f_1^j}{\partial \boldsymbol{\varepsilon_n}} \\ \vdots & \vdots & \ddots & \vdots \\ \frac{\partial f_n^j}{\partial \mathbf{u}} & \frac{\partial f_n^j}{\partial \boldsymbol{\varepsilon_1}} & \dots & \frac{\partial f_n^j}{\partial \boldsymbol{\varepsilon_n}} \end{pmatrix}, \qquad \{\boldsymbol{\alpha}^j\} = \begin{Bmatrix} \{\mathbf{U}^j\} \\ \{\boldsymbol{\varepsilon_1^j}\} \\ \vdots \\ \{\boldsymbol{\varepsilon_n^j}\} \end{Bmatrix}, \qquad [\mathbf{r}^j] = \begin{Bmatrix} -f_0^j \\ -f_1^j \\ \vdots \\ -f_n^j \end{Bmatrix} \tag{4.40}$$

At each iteration j of the Newton method, one solves for $\boldsymbol{\Delta\alpha}^j$ using Eq. (4.39). The displacements and internal strain at each iteration are then updated using the following relation

$$\{\boldsymbol{\Delta\alpha}^j\} = \{\boldsymbol{\alpha}^{j+1}\} - \{\boldsymbol{\alpha}^j\} \tag{4.41}$$

In this case, the Hessian matrix $[\mathbf{K}^j]$ has to be computed at each Newton's iteration (j). Moreover, solving $n+1$ non-linear equations requires relatively high computational effort as opposed to Case (A) (the more the number of units in the GKV model, the more the computational complexity). The computational effort can also be reduced by approximating the Hessian matrix using a quasi-Newton method. However such implementation has not been considered in this thesis.

The elements of the Hessian matrix $[\mathbf{K}^j]$ are given as follows upon discretization using Eq (4.20).

$$\frac{\partial f_0^j}{\partial \mathbf{u}} = \int_\Omega [\mathbf{B}]^T \frac{\partial \boldsymbol{\sigma}^j}{\partial \boldsymbol{\varepsilon}} [\mathbf{B}]\, d\Omega \tag{4.42a}$$

$$\frac{\partial f_0^j}{\partial \boldsymbol{\varepsilon}_i} = \int_\Omega [\mathbf{B}]^T \frac{\partial \boldsymbol{\sigma}^j}{\partial \boldsymbol{\varepsilon}_i}\, d\Omega \qquad \forall\, i \in \{1, 2, .., n\} \tag{4.42b}$$

$$\frac{\partial f_i^j}{\partial \mathbf{u}} = \int_\Omega \frac{\partial \boldsymbol{\sigma}^j}{\partial \boldsymbol{\varepsilon}_i} [\mathbf{B}]\, d\Omega \qquad \forall\, i \in \{1, 2, .., n\} \tag{4.42c}$$

$$\frac{\partial f_k^j}{\partial \boldsymbol{\varepsilon}_i} = \int_\Omega \frac{\partial^2 \psi^j}{\partial \boldsymbol{\varepsilon}_i \partial \boldsymbol{\varepsilon}_k} + \Delta t \frac{\partial^2 \phi_v^j}{\partial \boldsymbol{\varepsilon}_i \partial \boldsymbol{\varepsilon}_k}\, d\Omega \qquad \forall\, i, k \in \{1, 2, .., n\} \tag{4.42d}$$

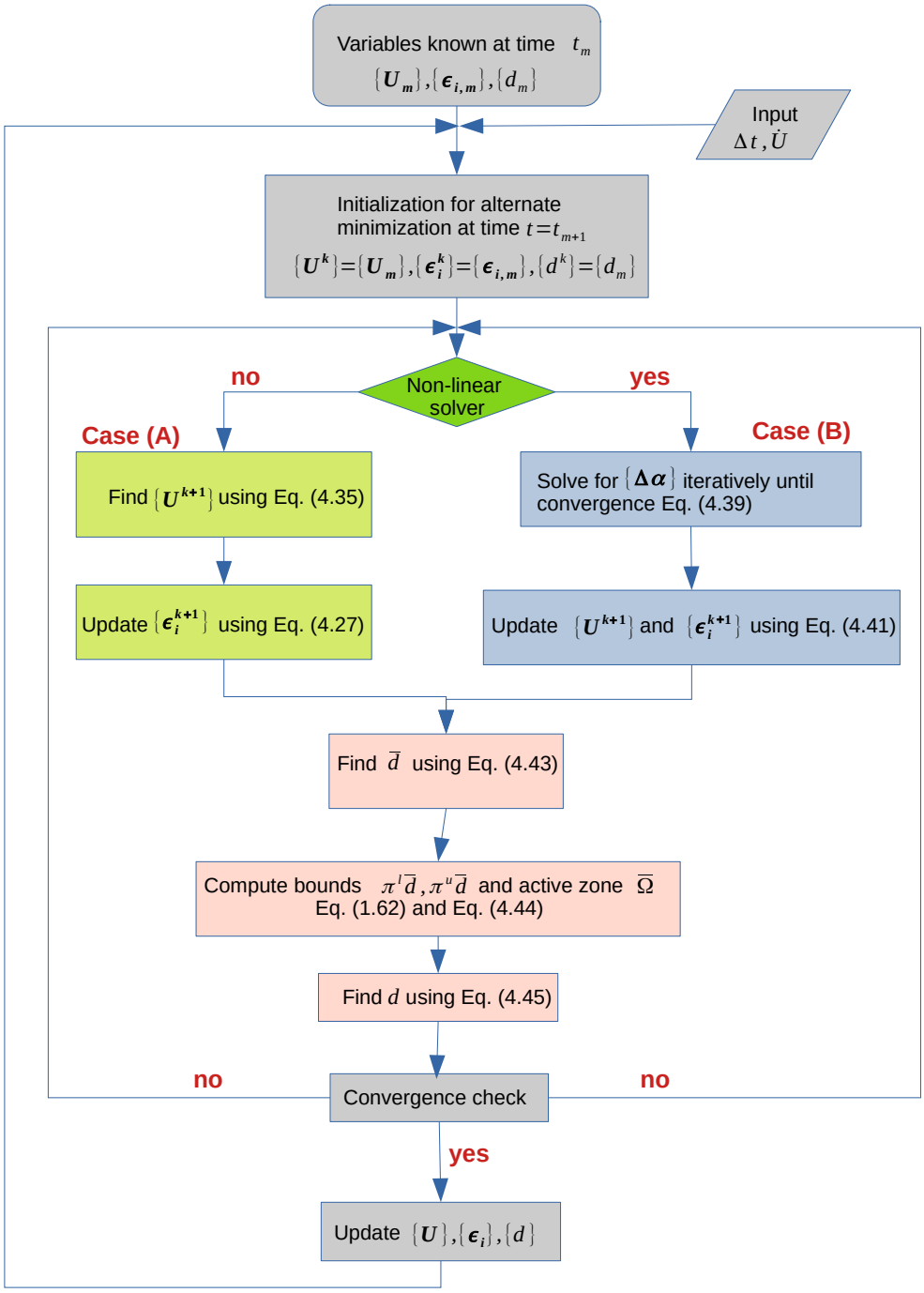

Figure 4.2 – Algorithm for 2D viscoelastic simulation with damage

4.2.3 Lip-field damage solver

This section focuses on solving the minimization problem given by Eq. (4.19) to find the damage field. The most straightforward method involves employing a brute-force strategy to solve for damage field d by performing the minimization over the entire domain Ω. However, this would be computationally very expensive, considering the high number of finite elements required to capture the damage zone accurately. Hence, we use the bounds estimation and its properties discussed in Chapter 1 (Section 1.5.3) to solve the problem in a relatively efficient manner. This consists of the following steps:

Step 1: Solve for the non-regularized version of the Eq. (4.19)

$$\overline{d}(\mathbf{x}) = arg \min_{d' \in \mathcal{A}_m} F(\mathbf{u}, \boldsymbol{\varepsilon_i}, d') \quad \forall\, \mathbf{x} \in \Omega \tag{4.43}$$

where $\overline{d}$ is the local damage field.

Step 2: Project $\overline{d}$ into the upper and lower bounds (denoted as $\pi^u \overline{d}$ and $\pi^l \overline{d}$) using Eq. (1.62) and define the active zone $\bar{\Omega}$ as follows:

$$\bar{\Omega} := \{\mathbf{x} \in \Omega : \pi^u \overline{d}(\mathbf{x}) \neq \pi^l \overline{d}(\mathbf{x})\} \tag{4.44}$$

Step 3: Find the Lipschitz continuous damage field d satisfying Eq. (4.19) as follows (using the properties listed in Eq. (1.61)):

$$d = \left\{ \begin{array}{ll} \overline{d} & \forall\, \mathbf{x} \in \Omega / \overline{\Omega} \\ \arg \min\limits_{d' \in \overline{\mathcal{A}}_m \cap \mathcal{L}_{\overline{\Omega}}} F(\mathbf{u}^{k+1}, {\boldsymbol{\varepsilon}_i}^{k+1}, d') & \forall\, \mathbf{x} \in \overline{\Omega} \end{array} \right\} \tag{4.45}$$

where the admissible spaces are as follows:

$$\overline{\mathcal{A}}_m = \{d \in L^\infty(\overline{\Omega}) : \pi^l \overline{d} \leq d \leq \pi^u \overline{d}\} \tag{4.46}$$

$$\mathcal{L}_{\overline{\Omega}} = \left\{ d \in L^\infty(\overline{\Omega}) : |d(\mathbf{x}) - d(\mathbf{y})| \leq \frac{1}{l_c} dist(\mathbf{x}, \mathbf{y}) \;\; \forall \mathbf{x}, \mathbf{y} \in \overline{\Omega} \right\} \tag{4.47}$$

It should be noted that the local minimization in step 1 (relatively less expensive and easily parallelizable) is performed over the entire domain while the non-local minimization in step 3 (relatively more expensive) is performed only over a portion of the domain $\overline{\Omega}$ (active zone). As seen in Section 1.5.3.2 (Figure 1.34), the active zone lies in the vicinity of regions enclosing sharp discontinuities in the damage field and hence this zone surrounds only the regions close to the crack tip. Therefore, for the case of damage in elastic solids with a relatively smaller damage area compared to the size of the specimen, this could result in very little computational effort (provided step 2 is performed in an efficient manner), as opposed to the phase-field approach

where the non-local minimization has to be performed over the entire domain Ω to preserve the variational structure [91, 121, 122].

Imposing Lipschitz constraints in discretized space [102]

The admissible space for the damage field in discretized space is as follows

$$d^h(t) \in \mathcal{W}^h(\Delta^h) = \mathcal{L}^h(\Delta^h) \cap \mathcal{A}^h_m(\Delta^h) \tag{4.48}$$

where $\mathcal{L}^h(\Delta^h)$ and $\mathcal{A}^h_m(\Delta^h)$ are the discrete approximation to the function spaces $\mathcal{L}_\Omega$ and $\mathcal{A}_m$. Here, Δ^h represents a dual (or lip) mesh that is constructed by connecting the centroids of the base mesh Ω^h. Figure 4.3 visually illustrates the base mesh Ω^h in blue and its corresponding lip-mesh Δ^h in red, which is designed for a circular plate with a central hole. Notably, the vertices of the lip-mesh coincide with the centroids of the base mesh's elements. The primary purpose of the lip-mesh is to define Lipschitz constraints within the computational domain. The lip-mesh is generated using the *triangle* package of Python [123].

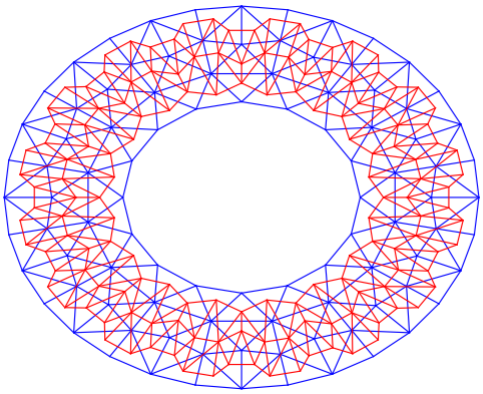

Figure 4.3 – Base mesh Ω^h in red and lip-mesh (dual mesh) Δ^h in blue colour [117]

Consequently, the damage field exhibits a piecewise constant behavior over Ω^h while maintaining linearity over Δ^h. Let $\mathcal{S}^h(\Delta^h)$ denote the finite-dimensional space defined over Δ^h using linear basis function. The function spaces $\mathcal{L}^h(\Delta^h)$ and $\mathcal{A}^h_m(\Delta^h)$ can then be defined as follows:

$$\mathcal{L}^h(\Delta^h) = \{d \in \mathcal{S}^h(\Delta^h) \ : \ \|(\nabla d)_t\| \leq \frac{1}{l_c}, \ \ \forall\, t \in \mathcal{T}(\Delta^h)\} \tag{4.49}$$

$$\mathcal{A}^h_m(\Delta^h) = \{d \in \mathcal{S}^h(\Delta^h) : \pi^l \overline{d} \leq d \leq \pi^u \overline{d}\} \tag{4.50}$$

where $\mathcal{T}(\Delta^h)$ is set of all elements in Δ^h. If $\mathbf{B}_t$ and $\mathbf{d}_e$ denote the elemental gradient operator and the nodal damage field in the lip-mesh Δ^h, then the gradient of damage field is given by

$(\nabla d)_t = \mathbf{B}_t \mathbf{d}_e$. In addition to $\mathcal{L}^h(\Delta^h)$, alternative spaces were explored in [102] to enforce the Lipschitz constraint within a discrete framework. However, it was reported in the latter that the space defined by Eq. (4.49) exhibited relatively lower susceptibility to mesh orientation issues. Furthermore, this space offered the advantage of requiring the least number of discrete Lipschitz constraints, equating to the number of elements in the lip-mesh.

The first step in determining the local damage field $\overline{d}^h$ over the vertices of the lip-mesh Δ^h, as defined in Eq. (4.43), is performed using the open-source Python package *scipy* [113]. To estimate the bounds $\pi^u\overline{d}$ and $\pi^l\overline{d}$, specified in Eq. (1.62), we use a *Dijkstra-based fast marching algorithm* outlined in [102]. This approach enables the computation of bounds with a computational complexity of approximately $O(r\ \log(r))$, where r represents the number of vertices in the lip-mesh Δ^h. The active zone can then be defined over the lip-mesh as per Eq. (4.44).

The remaining challenge (step 3) is to determine $d^h \in \mathcal{W}^h(\overline{\Delta^h})$ by minimizing the incremental potential specifically over the active zone, $\overline{\Delta^h}$. For this purpose, we opt for a direct minimization approach utilizing the *cp* solver from the open-source *cvxopt* [124] Python package. This particular package facilitates the imposition of discrete constraints, specifically $d^h \in \mathcal{W}^h(\overline{\Delta^h})$, through the utilization of first and second-order cone constraints, while simultaneously minimizing the incremental potential.

The algorithm for the alternate minimization is shown in Figure 4.2.

Remark 6 *Convergence criteria:*

- *The maximum number of iterations for the Newton-Raphson method is set to* 20 *and the method has been considered to converge when* $\| \int_{\Omega/\Gamma_u} [B]^T \boldsymbol{\sigma} d\Omega \| \leq 1e{-}8$ *(force equilibrium) and* $\Delta F^j = F^{j+1} - F^j \leq 1e-8$ *(stationarity of incremental potential* F *w.r.t* $\mathbf{u}$ *and* $\boldsymbol{\varepsilon}_i$*).*
- *For the damage solver using cvxopt package of Python,* $\Delta F \leq 1e-7$ *(stationarity of incremental potential* F *w.r.t* d*) was used as a convergence condition.*
- *For the Alternate Minimization (AM), we adopt the following conditions: maximum iterations* $= 5$*,* $max(d^{k+1} - d^k) \leq 1e-2$ *and* $\Delta F^k = F^{k+1} - F^k \leq 1e-3$ *(stationarity of incremental potential* F *w.r.t* $\mathbf{u}$*,* $\boldsymbol{\varepsilon}_i$ *and* d*)*
- *Indices* j *and* k *refer to Newton-Raphson and AM iterations respectively.*
- *To reduce the number of AM iterations and, consequently, computational time, a relatively higher convergence tolerance for the 2D case has been employed compared to the 1D case.*

4.3 Validation of numerical implementation

In this section, we validate the numerical implementation of the algorithm presented in Figure 4.2. We employ a step-by-step validation approach. Initially, we perform unit tests to validate

the displacement and internal strain solvers (Section 4.2.2), without considering damage effects. Subsequently, we perform integrated validation that includes damage scenarios, confirming that these distinct solver units work together as a whole.

For the case without damage, the validation is performed by comparing the 2D Finite Element (FE) results against the available analytical solutions for a three-point bending beam. The geometry of three-point bending is shown in Figure 4.4. We make the assumption of plane strain and zero Poisson's ratio ($\nu = 0$). The beam is considered slender enough (L/h is large) so that the Euler-Bernoulli beam theory is valid. This theory simplifies the analysis and makes it easier to find the relation between forces and deflections. For the material parameters associated with the GKV model, we use the values listed in Table 1.1. As the damage evolution is not considered here, a relatively coarse mesh (with linear triangular elements) is used.

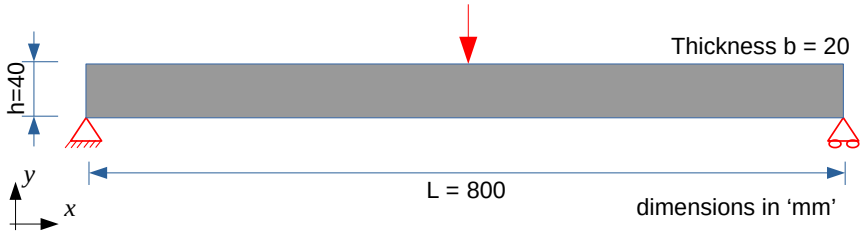

Figure 4.4 – Geometry of 3-point bending beam as a means to validate the numerical implementation of the displacement and internal strain solver (excluding damage evolution)

Now, the analytical solution relating forces and displacements under the assumption of the Euler-Bernoulli beam will be derived for linear viscoelastic material (excluding damage). The analytical relation between forces F and load line displacement δ for linear elasticity is given as follows:

$$F = g_1 E \delta \tag{4.51}$$

where $g_1 = \frac{4bh^3}{L^3}$ is a geometric constant. Recall from Eq. (1.14b) that the relation between stress and strain for a linear viscoelastic material in $s-$domain (or complex frequency domain) is similar to the relation in elasticity, with E replaced by $\overline{E}^*(s)$. Hence, analogous to Eq. (4.51), the following holds for linear viscoelastic material in the $s-$domain

$$\overline{F}(s) = g_1 \overline{E}^*(s) \overline{\delta}(s) \tag{4.52}$$

where $\overline{E}^*(s)$ for the GKV model is given by Eq. (1.30). The imposed displacement rate $\dot{\delta}(t) = c$

is held constant and hence the following holds

$$\delta(t) = ct \tag{4.53}$$

The Laplace transform of the above equation using Eq. (1.13a) yields the following:

$$\overline{\delta}(s) = \frac{c}{s^2} \tag{4.54}$$

Upon substitution of Eq. (1.30) and Eq. (4.54) into Eq. (4.52), the following expression is obtained for a linear viscoelastic material characterized by the GKV model

$$\overline{F}(s) = g_1 \left[\frac{1}{E_0} + \sum_{k=1}^{n} \frac{1}{E_k + \eta_k s} \right]^{-1} \frac{c}{s^2} \tag{4.55}$$

where $\eta_k = \tau_k E_k$. The force in time domain $F(t)$ is then given by the inverse Laplace transform of $\overline{F}(s)$

$$F(t) = \mathcal{L}^{-1}[\overline{F}(s)] \tag{4.56}$$

The inverse Laplace transform is computed numerically using the *mpmath* [125] library of Python.

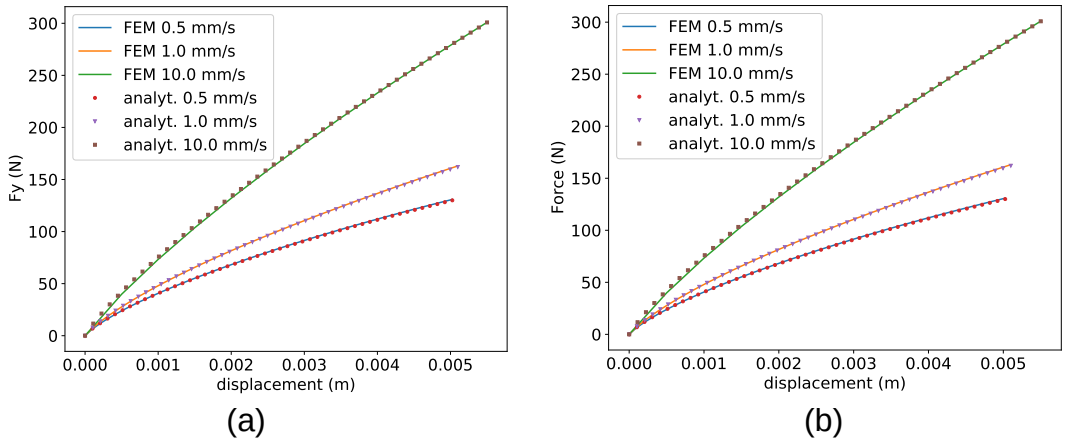

Figure 4.5 – Validation excluding damage. Comparison of the analytical solution (Eq. (4.56)) and the 2D Finite Element (FE) solution for (a) Case A using linear solver ($\theta = 1$) and (b) Case B using non-linear solver ($\theta = 0$)

Figure 4.5(a) and Figure 4.5(b) compare the FE simulations obtained for linear (Case A) and non-linear solvers (Case B) discussed in Section 4.2.2 with the analytical solution given by Eq. (4.56). It can be seen that the results of both linear and non-linear solvers compare well with the

analytical solution for different imposed displacement rates. This validates the implementation of solvers used for finding the displacements and internal strains.

Now, we perform an integrated test (along with damage) to validate the alternate minimization algorithm listed in Figure 4.2. For this case, we use a 1D homogeneous bar (see Figure 4.6). The results for the considered bar in the 1D case have already been provided in Section 3.1.2. Since

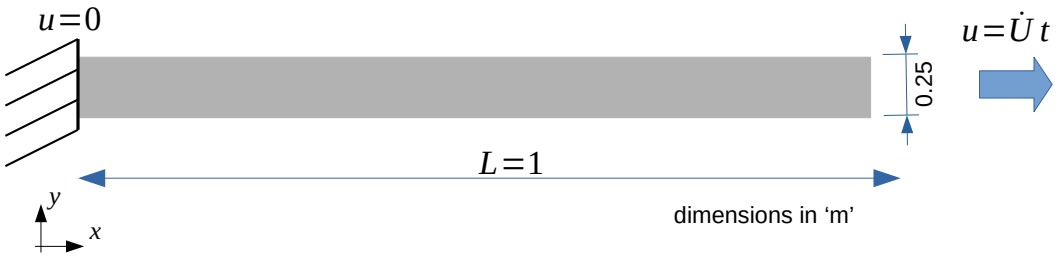

Figure 4.6 – Geometry of a homogeneous bar for validation of numerical implementation of algorithm listed in Figure 4.2

our interest lies in comparing the 2D FE results with 1D results for the softening GKV model, we use the same set of material parameters used in Section 3.1.2: The GKV model parameters are listed in Table 1.1 with $\nu = 0$. The energy degradation function $g(d)$ and the softening function $h(d)$ are provided in Eq. (3.36) and Eq. (3.37). The energy release rate, denoted as Y_c, and the regularization length scale are configured to match the values used in the 1D simulation, which are 500 J/m^3 and 0.5 m respectively. We apply a displacement rate of $\dot{U} = 1e-1\ m/s$ to the right end of the bar as shown in Figure 4.6. The 2D bar is discretized using linear triangular elements of size dx such that $L/dx = 40$. For this case, since the bar is subjected only to tension, we use $\theta = 1$ and the non-linear solver discussed in Section 4.2.2.2 is employed to find displacements and internal strains.

Figure 4.7a compares the homogeneous solution obtained for 2D FE simulation with the local (semi-) analytical solution (presented in Appendix B), while Figure 4.7b compares the localized solution obtained for 2D FE simulation with 1D FE simulation (Figure 3.5c). The homogeneous solution for the 2D case is obtained by setting a very high l_c s.t. $L/l_c = 1e-12$. For the localized solution ($l_c = 0.5\ m$) in Figure 4.7b, to trigger localization at the center of the bar, a small perturbation ($1e-3$) is applied to the center of the bar at the start of each time iteration. It can be seen that the 2D finite element results compare well with the reference results, thus validating the numerical implementation for the 2D case. In the case of Figure 4.5b, after damage initiation, the stress-strain curve follows a homogeneous evolution before localization (as is the case in 1D) due to the effect of intrinsic time scale associated with damage. The small discrepancies between

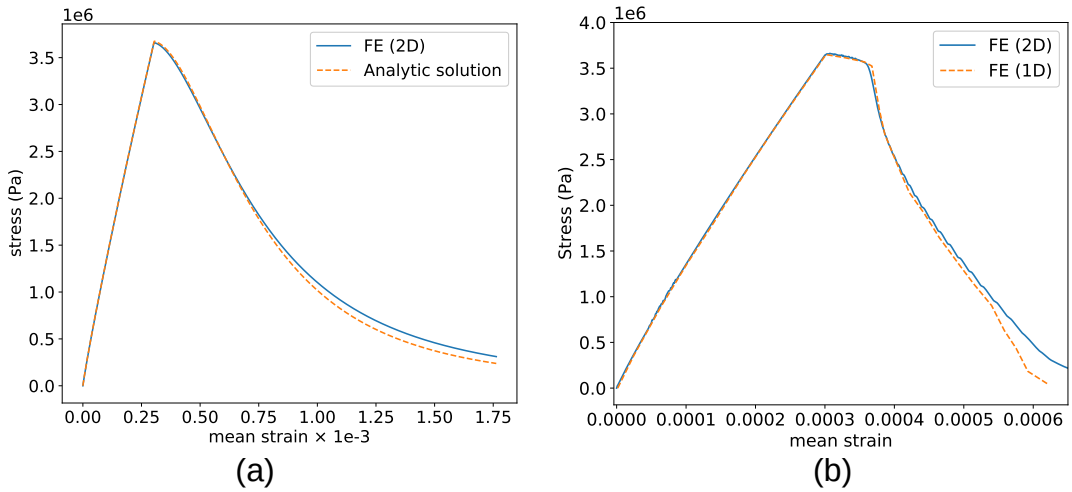

Figure 4.7 – Validation including damage: Comparison of 2D finite element (FE) results with the 1D case for (a) homogeneous evolution (or local solution) and (b) for localized solution

the reference and 2D FE results at the failure phase can be attributed to the larger tolerance used for the convergence of Alternate Minimization (AM) in the 2D case (as discussed in Remark 6). Figure 4.8 shows that such discrepancy is not found when a smaller tolerance has been used for AM. However, a relatively larger tolerance has been chosen for all upcoming simulations. This choice aims to reduce the number of iterations required for AM to converge, thus accelerating computational time.

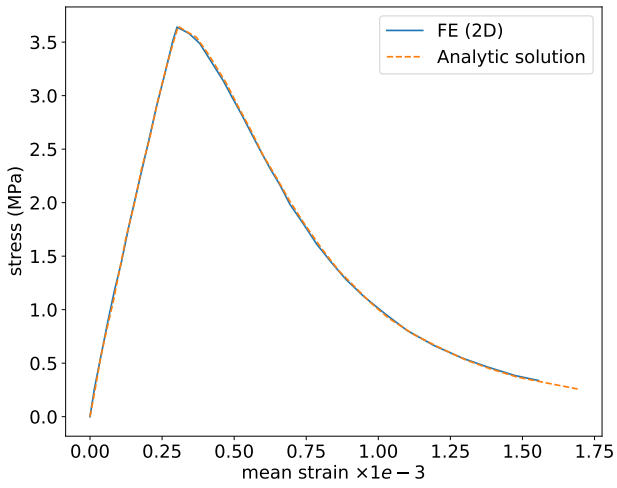

Figure 4.8 – Validation including damage: Comparison of 2D FE results with the local analytical solution (a smaller tolerance has been used for the convergence of alternate minimization)

4.4 Summary

This chapter primarily focused on expanding the numerical implementation of the softening viscoelastic damage model in the 1D scenario, as discussed in Chapter 3, to a 2D context. Initially, we extended the viscoelastic damage model based on the GKV model, introduced in Chapter 3, to encompass multi-dimensional scenarios. Additionally, we accounted for unilateral effects by introducing an asymmetric split of the free energy. This will favor damage growth under tension compared to compression, a behavior frequently observed in most materials.

Subsequently, our attention shifted towards the numerical implementation of the model within the lip-field formulation. We provided detailed explanations of the solvers employed to compute displacements, viscous strains, and damage. Furthermore, we applied bounds estimates, as discussed in Chapter 1, to efficiently solve for the damage field.

To validate the numerical implementation, we compared the results of 2D simulations with analytical solutions and results from 1D simulations. With the implementation now validated, the model is set for practical application in the context of bituminous materials, which will be the central focus of the forthcoming chapter (Chapter 5).

Chapter 5

Application to bituminous materials

In Chapter 4, we implemented the viscoelastic damage model within a multi-dimensional (2D) framework and validated it against established reference solutions. This chapter is dedicated to its application for simulating fracture behavior in bituminous materials, comprising three key sections:

In the initial part, we adopt a softening function equivalent to one proposed for the Thick-Level-Set (TLS) approach. This choice is driven by the capacity of the aforementioned softening function to effectively represent experimental data for bituminous materials.

In the second part, the focus is on modeling fracture within a Single Edge Notch bending Beam (SENB) test, subject to monotonously applied loading rates. The objective is to fit the model against the available experimental results (from the literature) for bituminous mortar mix. The viscoelastic parameters are calibrated using the initial phase of the force-displacement curve, assuming an undamaged state initially. We then investigate the influence of fracture-related parameters by conducting a parametric study and fine-tuning them to match the force-displacement curves through iterative adjustments. The simulated force-deflection curves are then compared to their experimental counterparts.

In the final section, we explore the efficacy of two different types of split employed for free energy in capturing crack propagation in mixed-mode fracture scenarios, specifically in the SENB test with the notch position offset from the center.

5.1 Choice of softening function

As discussed in Chapter 1, the softening behavior of the constitutive law plays a crucial role in simulating the fracture behavior of bituminous materials. Hence, initially, we focus on studying the softening behavior for a given $g(d)$ (energy degradation function) and $h(d)$ (softening func-

tion). For this section, we limit ourselves to the elastic case. The local stress and the damage evolution equations (after the onset of damage initiation) in the 1D case are then given by

$$\sigma = g(d)E\varepsilon \tag{5.1}$$

$$g'(d)\psi_0 + Y_c h'(d) = 0 \tag{5.2}$$

where $\psi_0 = .5E\varepsilon^2$. Taking the time derivative of the above equations yields the following

$$\dot{\sigma} = g'(d)\dot{d}E\varepsilon + g(d)E\dot{\varepsilon} \tag{5.3}$$

$$g''(d)\dot{d}\psi_0 + g'(d)E\varepsilon\dot{\varepsilon} + Y_c h''(d)\dot{d} = 0 \tag{5.4}$$

Subsequently, the last equation can be rewritten as

$$\dot{d} = \frac{-g'(d)E\varepsilon\dot{\varepsilon}}{g''(d)\psi_0 + Y_c h''(d)} = \frac{-g'(d)E\varepsilon\dot{\varepsilon}}{z(d,\varepsilon)} \tag{5.5}$$

where $z(d,\varepsilon)$ is given by

$$z(d,\varepsilon) = g''(d)\psi_0 + Y_c h''(d) \tag{5.6}$$

$$= g''(d)\psi_0 - \left(\frac{g'(d)\psi_0}{h'(d)}\right) h''(d) \qquad \text{(using Eq. (5.2))} \tag{5.7}$$

$$z(d,\varepsilon) = \left[\frac{g''(d)h'(d) - g'(d)h''(d)}{h'(d)}\right] \psi_0 \tag{5.8}$$

When substituting the above expression into Eq. (5.5), the resulting damage rate is as follows:

$$\dot{d} = \frac{g'(d)h'(d)E\varepsilon\dot{\varepsilon}}{r(d)\psi_0} \tag{5.9}$$

where $r(d)$ is given by

$$r(d) = g'(d)h''(d) - g''(d)h'(d) \tag{5.10}$$

On back substitution of $\dot{d}$ (Eq. (5.9)) in Eq. (5.3), the resulting constitutive equation in rate form is as follows:

$$\dot{\sigma} = \left[\frac{2(g'(d))^2 h'(d)}{r(d)} + g(d)\right] E\dot{\varepsilon} = K(d)E\dot{\varepsilon} \tag{5.11}$$

Depending on $K(d) > 0$ or $K(d) < 0$, one obtains a hardening or softening behavior. For the choice of $g(d)$ and $h(d)$ used in Chapters 3 and 4 (Eqs. (3.36), (3.37)), it can be verified that $K(d)$ is always negative for $d \in [0,1]$, indicating that only softening behavior can be obtained.

This is also evident from the curves plotted in Figure 3.4 for a 1D homogeneous bar.

However, a simple quadratic function for $h(d)$ used before might not be the optimal choice for modeling bituminous materials. For example, in [100], the softening function of the following type (within the Thick Level Set TLS approach) has been used to fit simulation results with experimental results of bituminous material for the uni-axial tension test.

$$H(d) = h'(d) = (1 - \beta d)^{-\alpha} \tag{5.12}$$

where α and β are the fracture parameters that control the softening behavior. As this softening function has already proven its ability to effectively match experimental data for bituminous materials, we utilize a comparable softening function in the following manner:

$$h'(d) = c(1 - \beta d)^{-\alpha} \tag{5.13}$$

where the constant c is such that the damage initiates when $\psi_0 = Y_c$ (see Eqs. (3.2),(3.8) and (3.10)).

$$c = g'(0) \tag{5.14}$$

The energy degradation function $g(d)$ then can also be written as follows:

$$g(d) = (1 - d)^c \tag{5.15}$$

Eq. (3.3) then provides the condition on c:

$$c \geq 1 \tag{5.16}$$

On the integration of Eq. (5.13), and applying the condition that $h(0) = 0$ (since $Y_c h(d)$ is a measure of damage energy), we obtain the following

$$h(d) = \frac{c}{\beta(\alpha - 1)}[(1 - \beta d)^{1-\alpha} - 1] \tag{5.17}$$

We limit ourselves to $\alpha > 1$ and $0 \leq \beta \leq 1$. In this case, it can be verified that $h(d)$ is convex for $d \in [0, 1]$.

To analyze the softening characteristics of the function $h(d)$ given by Eq. (5.17), we apply it to Eq. (5.11). Figure 5.1a illustrates the behavior of $K(d)$ as a function of damage for various combinations of α and β. Notably, when $c = 2$, the function conforms to a quadratic degradation pattern as indicated in Eq. (3.36). It is evident that altering the values of α and β leads to

variations in the behavior of $K(d)$ and, consequently, the nature of softening. For instance, with $(c, \alpha, \beta) = (2, 6, 0.6)$, $K(d)$ transitions from positive to negative as d increases. This implies an initial hardening phase followed by a softening phase. Figure 5.1b displays the corresponding local (or homogeneous) stress-strain curves for the specified combinations of α and β. The aforementioned hardening softening behavior for $(c, \alpha, \beta) = (2, 6, 0.6)$ is also clearly visible here.

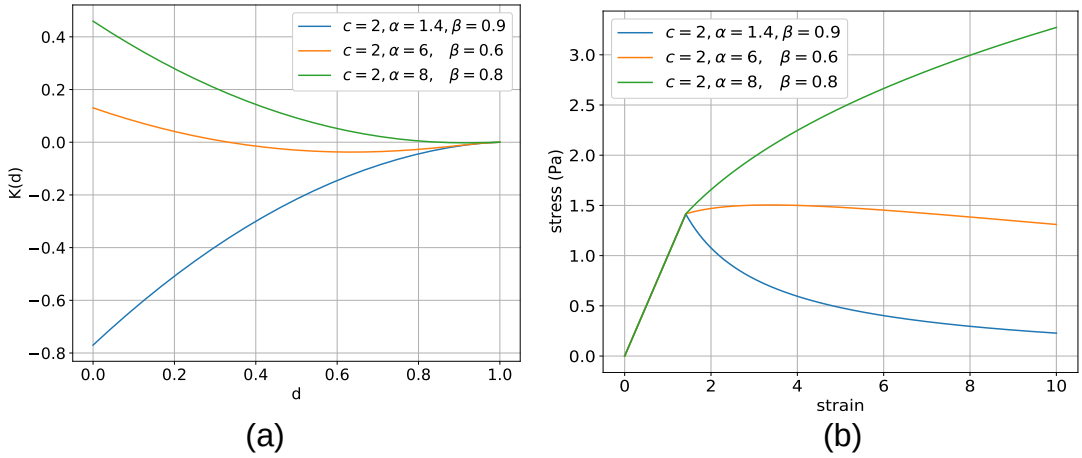

Figure 5.1 – Softening characteristics of $h(d)$ given by Eq. (5.17) for elasticity ($E = 1, Y_c = 1$). (a) $K(d)$ as a function of damage d for different values of (α, β) and (b) the respective local stress-strain plots

5.2 Mode-I fracture

This section focuses on modeling the response of a bituminous material subjected to mode-I fracture. Specifically, we examine experimental data provided in [36] for a Single Edge Notch Bending Beam (SENB) test, with the notch positioned at the center, conducted on bituminous mortar mix at room temperature 20^oC under monotonic loading rates. The geometry of the specimen and the loading are shown in Figure 5.2. The experimental forces displacement curves were reported in [36] for three different imposed displacement rates: ($1mm/s$, $0.1mm/s$, $0.01mm/s$). The corresponding experimental curves are plotted in Figure 5.4 using continuous lines. The rate sensitivity is clearly evident indicating the viscoelastic nature of the bituminous mortar mix. For the simulations performed in this case, four different meshes are considered for the study. The meshes are generated using *gmsh* software [120] and the post-processing is done using *paraview* software [126]. The domain under consideration is discretized using linear triangular elements with fine elements in the potential damage zone (or critical zone). In this case, the critical zone lies in the regions close to the vertical midsection. Table 5.1 lists the meshes used for the simulation with dx being the element size in the critical zone. To illustrate, Figure 5.3 depicts

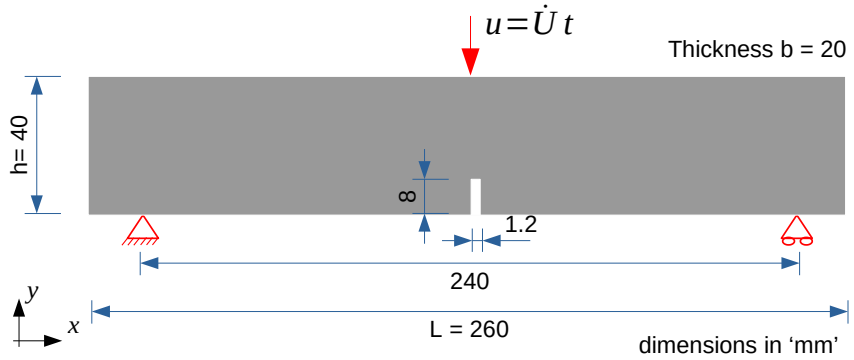

Figure 5.2 – Geometry of Single Edge Notch Beam (SENB) test

Mesh 1, characterized by a finer element size along the potential crack path (critical zone). In

Mesh	nb. of elements	size of elements in critical zone dx (mm)	l_c/dx
mesh 1	5116	1.0	5
mesh 2	13506	0.7	7.142
mesh 3	20876	0.5	10
mesh 4	29065	0.4	12.5

Table 5.1 – Meshes used for the mode-I fracture

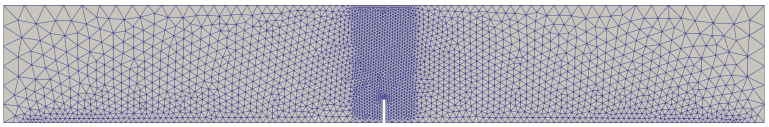

Figure 5.3 – Mesh 1 (smaller elements inside critical zone)

order to prevent damage growth close to the position of the boundary conditions, the boundary conditions are applied over a small length rather than a point. For all the simulations carried out in this section, the free energy based on eigen decomposition with $\theta = 0$ is being used (in Eq. (4.12)) to completely arrest damage growth under compression. The respective time steps for the imposed displacement rates $\dot{U} = (1mm/s\ 0.1mm/s\ 0.01mm/s)$ were chosen as $\Delta t = (0.05s, 0.5s, 5s)$. The softening function $h(d)$ is given by Eq. (5.17) for all the simulations performed in this section. The regularizing length scale is set as $l_c = 5\ mm$.

5.2.1 GKV model parameters

The first step to fit the damage model with the experimental results is to find the model parameters associated with viscoelasticity. However, it's worth noting that in [36], only the experimental force-displacement curves were documented, and no data regarding the dynamic modulus curves for the bituminous mortar mix were provided. Therefore, we focus solely on the initial portion of the experimental force-displacement curves and proceed to estimate the parameters of the Generalized Kelvin-Voigt (GKV) model under the assumption of the absence of damage during this initial phase. This is possible, thanks to the analytical solution for the three-point bending beam given by Eq. (4.56). Specifically, the GKV model parameters are obtained by the least square minimization, where the objective function to be minimized is given as follows

$$q = \sum_j \sum_i \left[F_{exp}(u_i, a_j) - F_{analytic}(u_i, a_j)\right]^2 \tag{5.18}$$

where $F_{exp}(u_i, a_j)$ and $F_{analytic}(u_i, a_j)$ are the forces corresponding to experimental and analytical values at applied displacement u_i for the imposed displacement rate a_j. The expression for $F_{analytic}$ is given by the Euler-Bernoulli beam theory (Eq. (4.56)). It is also to be noted that the analytical solution used is for the case of a three-point bending beam without a notch and supported at the ends (in contrast to the SENB experiment displayed in Figure 5.2). However, the simulation results shown later (Figure 5.10) indicate that the fit obtained could still be used for the case with a notch at the center. Figure 5.4 compares the fit obtained using the GKV

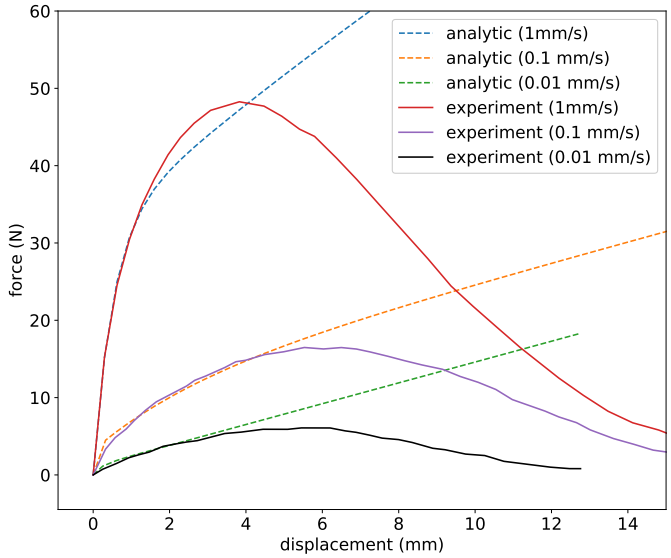

Figure 5.4 – Comparison of fit obtained using GKV model (n = 2) with experimental results from [36]

model against the experimental results. Notice that the fit obtained using GKV model parameters can be used only in the initial phase (undamaged phase) and the use of a damage model is necessary to obtain the fit after the initial phase. A thumb rule for deciding on the number of units of the GKV model required to fit is that it should not be greater than the number of logarithmic decades covered by the span of the test [39]. Hence, the number of KV units of the GKV model is chosen as $n = 2$ and the obtained model parameters are listed in Table 5.2.

KV unit (i)	0	1	2
E_i (MPa)	227.31	23.26	5.92
τ_i (s)	N/A	6.65	105.88

Table 5.2 – GKV model parameters used for the simulation

The fit displayed in Figure 5.4 is for the case of Poisson's ratio $\nu = 0$ (due to the assumption of Euler-Bernoulli beam theory). However, $\nu = 0.2$ will be assumed while performing simulations and it will be seen that the results for force-displacement curves don't change significantly.

5.2.2 Parametric study

In order to fit the parameters of the damage model to simulate the experimental force-displacement curves, the influence of different parameters is to be understood. Hence, this section focuses on performing a parametric study of different model parameters associated with damage and understanding their significance. This knowledge will then be used to fit the experimental results on a trial-and-error basis. For the parametric study, the displacements are applied through an imposed monotonous displacement rate of $\dot{U} = 1\ mm/s$. Mesh 1 is used to perform all the simulations for the parametric study.

5.2.2.1 Influence of $g(d)$

In this case, we consider both linear and quadratic degradation functions corresponding to $c = 1, 2$ (Eq. (5.15)). The following values have been used for the study: $\alpha = 1.8$, $\beta = 0.99$, $Y_c = 2000 J/m^3$. Figure 5.5 compares the force-displacement plots for the considered different energy degradation functions $g(d)$. It can be seen that the peak force is high for $c = 1$ (or $g(d) = 1 - d$). This can be explained by the changes in the softening function (Eq. (5.17)) for different values of c. Moreover, the magnitude of the post-peak slope for $c = 1$ is relatively higher. This can be attributed to the damage driving force Y being a function of the derivative of the degradation function (Eq. (4.17)). In other words, for $c = 1, 2$, the damage driving forces are given by $Y = \psi_0^+$ and $Y = 2(1 - d)\psi_0^+$. The multiplication of the tensile part of the free energy ψ_0^+ by $2(1 - d)$ in the latter case ($c = 2$) causes the damage driving force to decrease as damage grows, resulting in a relatively slower damage evolution and hence lower magnitude of softening

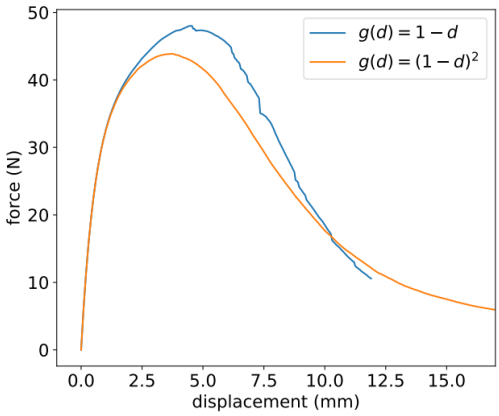

Figure 5.5 – Influence of $g(d)$

slope. Figure 5.6 plots the damage field close to rupture. It can be seen that the damage field

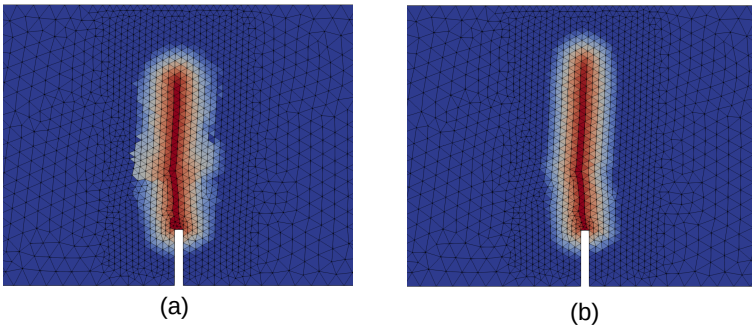

Figure 5.6 – Influence of $g(d)$ on damage profile (a) $g(d) = 1 - d$ and (b) $g(d) = (1 - d)^2$

is relatively wider and less smooth for $c = 1$. A similar issue is also being observed in [127] and this is caused when the damage driving force doesn't vanish as the damage approaches 1. Hence in the rest of the study, we adopt $g(d) = (1 - d)^2$ with $c = 2$.

5.2.2.2 Influence of α and β

In this section, our focus lies in examining how the parameters α and β of the softening function $h(d)$ exert their influence. Figure 5.7a plots $K(d)$ (Eq. (5.11)) as a function of damage for different values of α and β with $c = 2$. It can be seen that for all the considered values of α and β, $K(d)$ is negative indicating a purely softening behavior except for $(\alpha, \beta) = (4, 0.8)$. For the latter case, $K(d)$ changes from positive to negative value indicating a hardening-softening transition behavior as the damage growth occurs. Figure 5.7b plots the force-displacement curves obtained for the considered values of α and β. It is evident from Figure 5.7a and Figure 5.7b, that the lower the values of $K(d)$ the sharper the softening that occurs after attaining peak force.

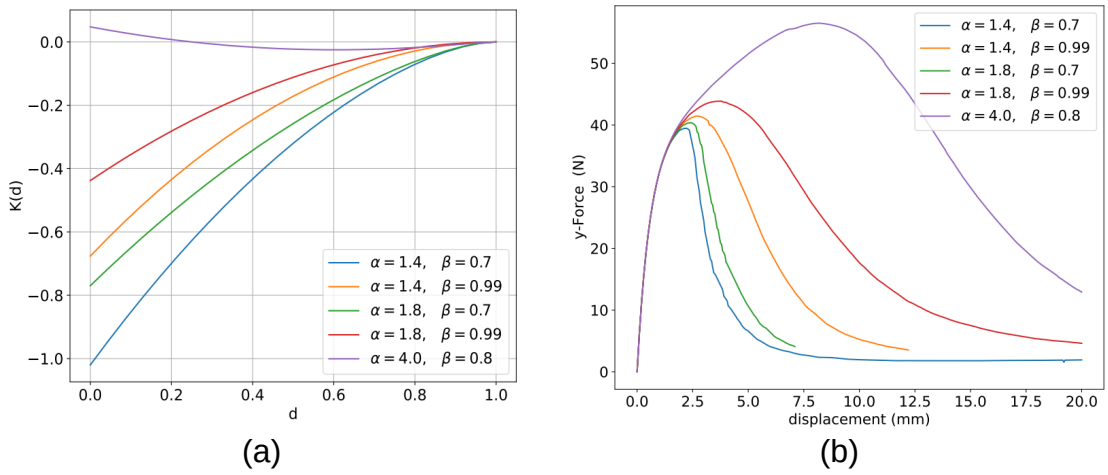

Figure 5.7 – Influence of α and β for $c = 2$: (a) $K(d)$ as a function of d and (b) force-displacement plots for SENB test

5.2.2.3 Influence of Y_c and l_c

In this case, we study the influence of critical energy release rate Y_c and the regularizing length scale l_c. The softening function parameters are kept fixed and are given as follows: $(\alpha, \beta) = (1.8, 0.99)$. These values correspond to a pure softening behavior (see Figure 5.7a). Figure 5.8a

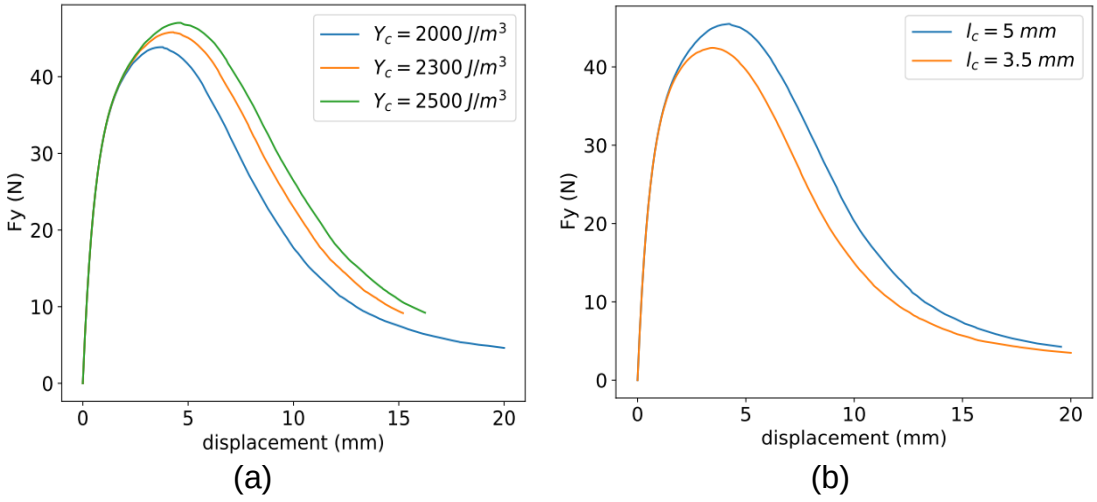

Figure 5.8 – Influence of Y_c and l_c on force-displacement curves

compares the force-displacement plots for different values of Y_c with $l_c = 5\ mm$. It can be seen that the higher the value of Y_c, the higher the peak force and the higher the displacement at which the peak force is attained. This is rather expected as the damage initiation is delayed when Y_c is increased.

Figure 5.8b compares the force-displacement plots for different values of l_c with $Y_c = 2300\ J/m^3$. It can be seen that the increase in l_c has a qualitatively similar effect as the increase in Y_c. This can be explained as follows: when l_c is larger, it results in a wider damage softening zone, which, in turn, necessitates a relatively higher amount of energy per unit length of crack growth. Consequently, this leads to a higher resistance to damage growth. In our case, the calibration of l_c is required to fit experimental force-displacement curves, and hence l_c will be considered as a material parameter.

5.2.3 Mesh and time step convergence study

In this section, the following parameters are used for the study: $\dot{U} = 1\ mm/s, c = 2, \alpha = 1.8, \beta = 0.99, Y_c = 2300 J/m^3$.

In the case of the mesh convergence study, the simulations are performed for 4 different meshes (Table 5.1) for $dt = 0.05s$. Figure 5.9a plots the force-displacement curves for the considered meshes. It can be noticed that the considered meshes didn't have any noticeable effect in the pre-peak force region. Besides, it is also evident that as the mesh is refined, the results after peak force start to converge. Mesh refinement ensures that there are enough elements within the softening zone to capture the damage zone accurately. Despite mesh 4 being the best choice, mesh 2 will be used for the rest of the study since the simulation results are not significantly affected by the choice of mesh. This choice is made in order to reduce computational time. Figure 5.9b illustrates

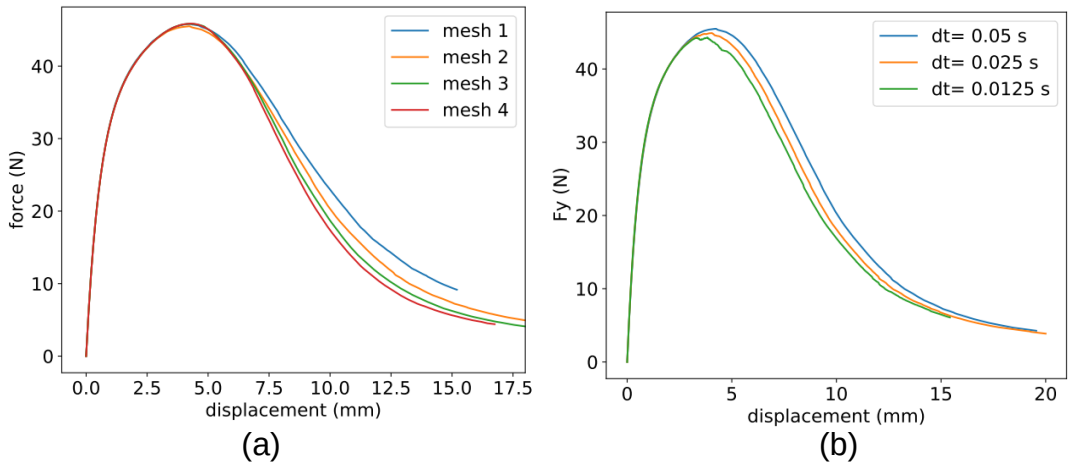

Figure 5.9 – (a)Mesh convergence and (b) time step convergence study

the outcomes of the time step convergence analysis conducted on mesh 2. It is important to highlight that an implicit time discretization method was employed in solving the equations. The examination reveals that the time step exhibited negligible impact before reaching the peak

force, but a subtle influence became noticeable after surpassing the peak force. The effect of the time step during the damage phase can be explained by the constraints placed on the number of allowable iterations and the relatively large error tolerance specified in the convergence criteria for alternate minimization (refer to Remark 6). This observed time step influence is anticipated to diminish as we increase the allowed number of alternate minimization iterations and decrease the error tolerance. However, to save computational time, the aforementioned conditions were used for convergence. Owing to the small influence of the time step, $\Delta t = 0.05s$ will be used for $\dot{U} = 1\ mm/s$ in the rest of the study to further reduce computational time.

5.2.4 Model calibration to fit experimental data

With the viscoelastic parameters corresponding to the GKV model already being calibrated, the next phase involves calibrating the parameters associated with damage to fit the observed experimental results. Using the insights gained from the parametric study, the fitting process involves a systematic trial-and-error calibration of the parameters. As a reminder, mesh 2 will be employed throughout all calibration procedures. The time intervals have been selected as $\Delta t = (0.05s,\ 0.5s,\ 5s)$, corresponding to velocity values of $\dot{U} = (1mm/s,\ 0.1mm/s,\ 0.01mm/s)$. We have utilized the quadratic energy degradation function with $c = 2$, as defined in Eq. (5.15), along with the associated softening function outlined in Eq. (5.17). Figure 5.10 plots

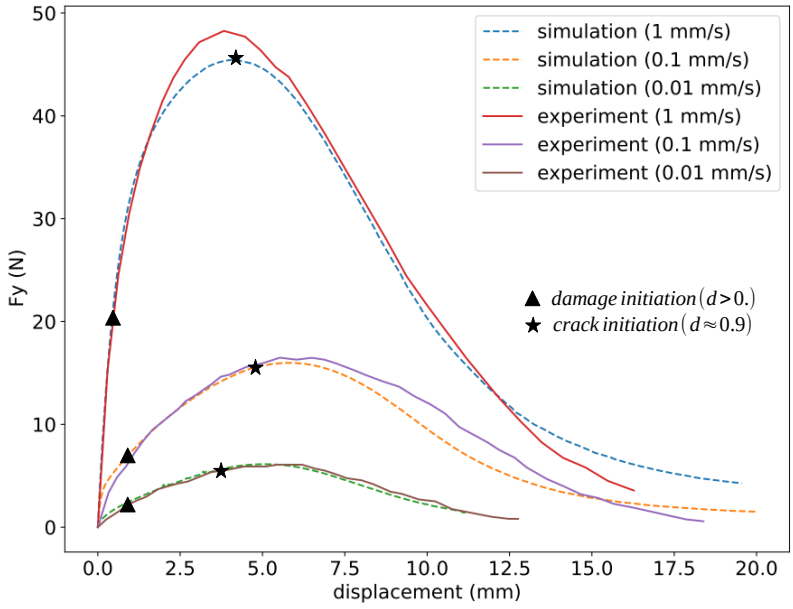

Figure 5.10 – Comparison of numerical and experimental results for SENB test

the force-displacement curves obtained using simulation and experiments, while Table 5.3 lists the parameters obtained after calibration. It is clear from Figure 5.10 that the results of the

simulation using calibrated parameters compare well with experiments. The damage initiation and crack initiation are also indicated in the figure. It can be observed that despite the (micro-) damage initiates at an early stage, the crack initiation occurs only close to the peak force. In other words, the force starts to drop following the crack initiation. The data presented in Table

$\dot{U}$ mm/s	Y_c J/m^3	c	α	β	l_c (mm)
1	2300	2	1.8	0.99	5
0.1	750				
0.01	220				

Table 5.3 – Fracture parameters associated with the model

5.3 reveals the rate dependency of the critical energy release rate, Y_c, as previously observed in [3] for bituminous materials (see Figure 1.23d). Notably, the softening function parameters and the internal length scale l_c remained constant across all considered rates. Moreover, it is also to be noted that the calibrated parameters for $g(d)$ and $h(d)$ don't include any hardening behavior in the homogeneous case (see Figure 5.7a).

Additionally, it's important to acknowledge that the choice of $g(d)$ and $h(d)$ are not unique, and alternative softening functions can be chosen to effectively fit the overall force-displacement curves. To achieve a more accurate representation of experimental findings, a broader data set from experiments at the local scale (in the vicinity of the crack tip) is necessary to facilitate a more informed choice of these functions and their associated parameters.

Figure 5.11 displays the damage evolution at the vertical mid-section of the beam for the considered displacement rates. In particular, the damage plots were shown at the load line displacements of 5 mm, 8 mm, and 11 mm respectively. It is apparent that damage initiation occurs exclusively at the bottom, where the material experiences tensile stresses, and progresses upward, mirroring what is observed in experiments. This behavior can be replicated thanks to the incorporation of unilateral effects in the model. Interestingly, despite the internal length scale l_c being kept constant for all the considered rates (Table 5.3), the width of the damage softening zone exhibits rate dependency. This aspect in particular can be attributed to the lip-field approach, which preserves the local solution (unlike the classical TLS approach [98] [100]). Moreover, the width of the damage zone increases with a decrease in the loading rate, which is a phenomenon commonly observed in bituminous materials. For instance, as the loading rate is decreased, the fracture behavior transitions from brittle to ductile with plastic deformations followed by fracture (as illustrated in Figure 1.25). The widening of the damage zone as the loading rate is decreased can be phenomenologically associated with the increase in size of the Fracture Process Zone (FPZ) as the material transitions from brittle to ductile fracture. Besides, it can also be observed from Figure 5.11 that the higher the imposed displacement rate,

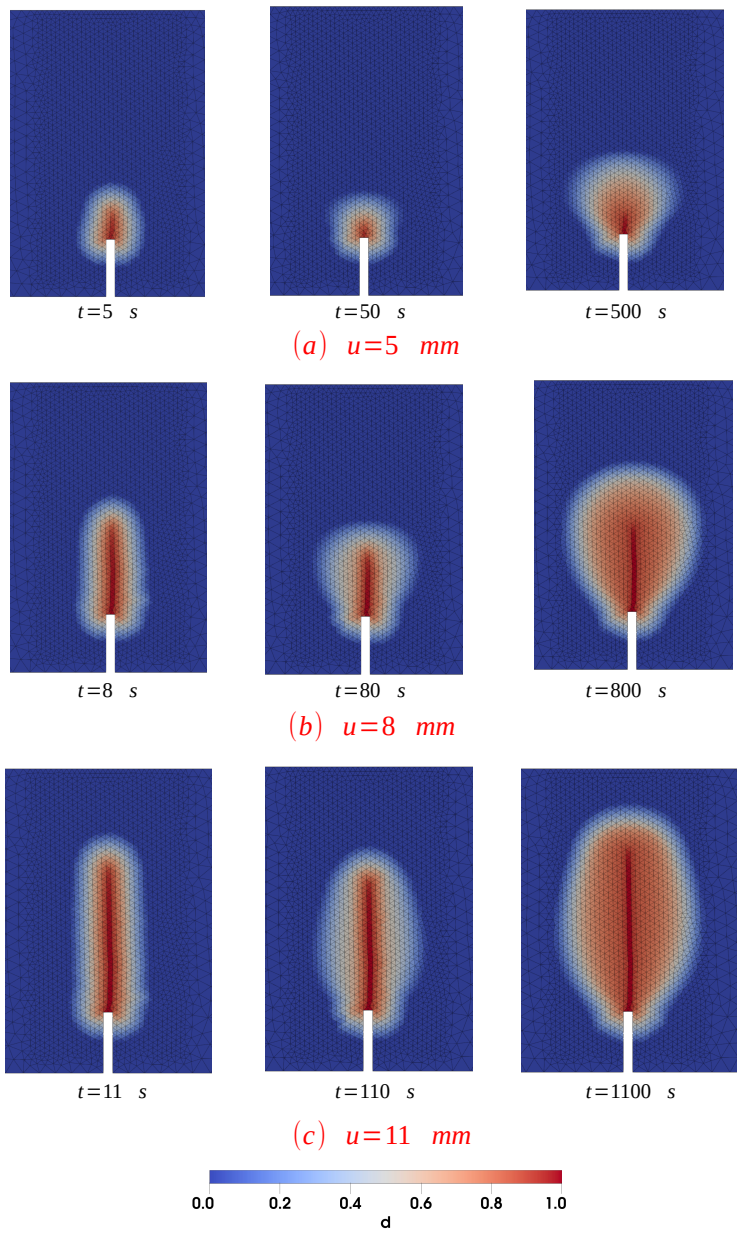

Figure 5.11 – Contour plots of damage at the mid-section for the considered imposed displacement rates 1 mm/s, 0.1 mm/s, and 0.01 mm/s (from left to right) at (a) u = 5 mm, (b) u = 8 mm, and (c) u = 11 mm

the faster the crack growth. Figure 5.12 plots the contour plot of stress in x-direction (σ_{xx}) for

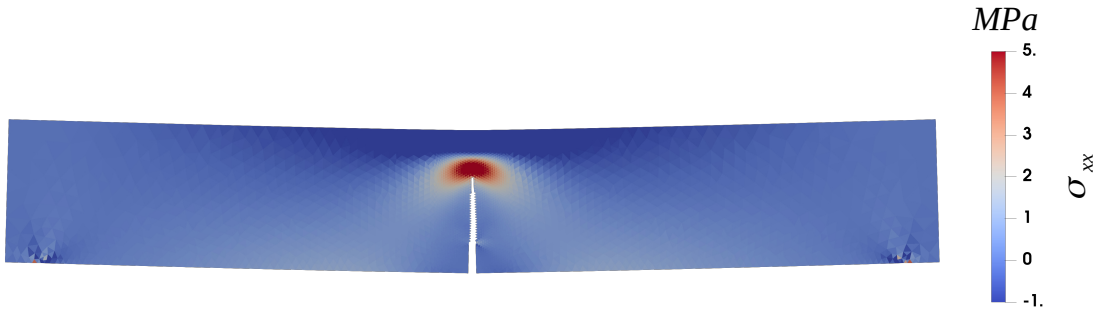

Figure 5.12 – Contour plot of stress in x-direction on a deformed mesh for $\dot{U} = 1\ mm/s$ at $u = 11\ mm$ (magnification factor = 250). Elements with $d > 0.9$ have been removed to show the crack

the imposed displacement rate of 1 mm/s corresponding to the load line displacement of 11 mm. The elements with $d > 0.9$ have been removed to show the crack. The stress concentration at the crack tip can be clearly observed. Figure 5.13 plots the different components of energy for the considered imposed displacement rates. The expressions for different components of energy are given as follows:

$$\text{input work} = \int_0^t F_y \dot{U} dt \tag{5.19}$$

$$\text{free energy} = \int_\Omega \psi(\boldsymbol{\varepsilon}, \boldsymbol{\varepsilon}_i, d) d\Omega \tag{5.20}$$

$$\text{viscous dissipation} = \int_0^t \int_\Omega \sum_{i=1}^{n} \dot{\varepsilon}_i : \tau_i \mathbb{C}_i : \dot{\varepsilon}_i d\Omega dt \tag{5.21}$$

$$\text{damage dissipation} = \int_\Omega Y_c h(d) d\Omega \tag{5.22}$$

where F_y is the reaction force at the point of loading and $\mathbb{C}_i$ is the elasticity tensor associated with i^{th} unit of the GKV model and its expression is given by Eq. (4.21). The energy diagram clearly suggests that the calculation of fracture energy based on the area under the force-displacement curve is not valid due to the significant portion of the viscous dissipation in the bulk (as highlighted in Section 1.3.1.1). The damage dissipation remains zero until a certain point (damage initiation point) after which it starts to increase. It can also be seen that after the onset of damage initiation, the free energy storing capacity of the specimen starts to drop. Moreover, it can also be noticed that as the imposed displacement rate is decreased, the material ruptures with less work input.

The plots for work input and internal energy (sum of free energy, viscous dissipation, and

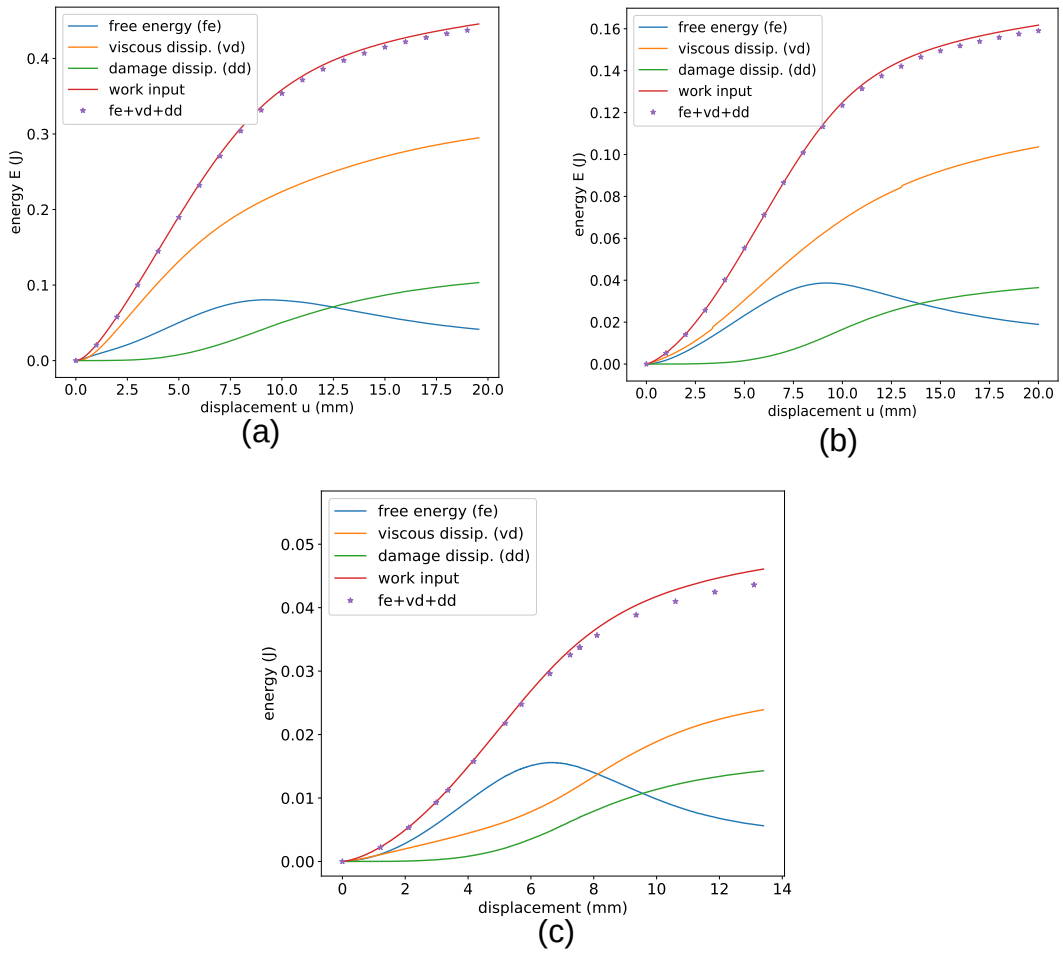

Figure 5.13 – Energy diagrams for (a) $\dot{U} = 1\ mm/s$, (b) $\dot{U} = 0.1\ mm/s$ and (c) $\dot{U} = 0.01\ mm/s$

damage dissipation) are also in good agreement with each other [1]. This demonstrates the energy conservation of the model. Moreover, the curves for viscous and damage dissipation continue to increase (positive slope) indicating that the dissipation is positive. These observations confirm the thermodynamic consistency of the developed model.

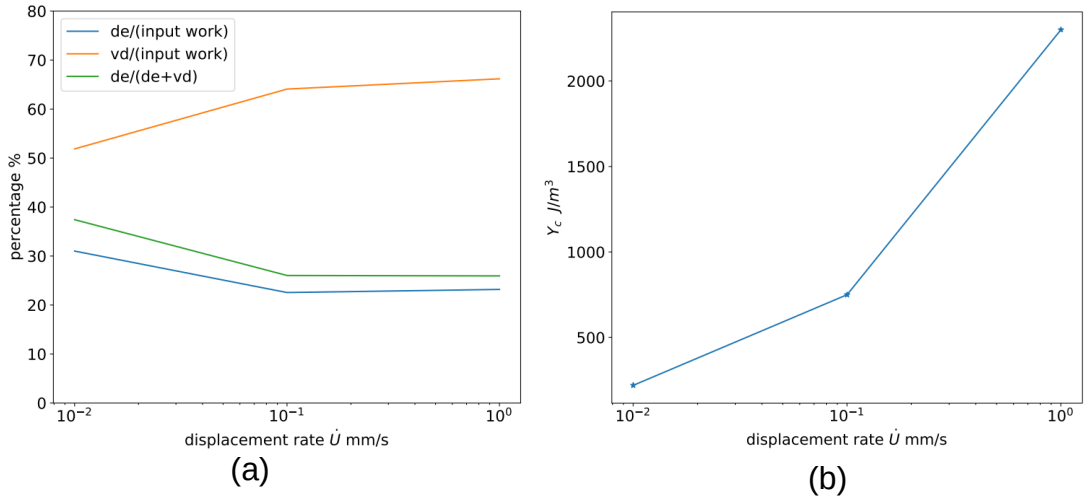

Figure 5.14 – (a) Percentage of dissipated energies relative to input work and total dissipation (b) dependence of Y_c on imposed displacement rate $\dot{U}$ (*de* and *vd* represents the damage and viscous dissipation respectively)

Figure 5.14a illustrates the percentages of dissipated energy relative to the input work, as well as the percentages of damage dissipation in relation to the total dissipation, for the considered imposed displacement rates (close to the rupture). It can be noticed that the contribution of viscous dissipation is higher for all the cases (as previously indicated in Figure 5.13). Though the percentages remain almost the same for $\dot{U} = 0.1\ mm/s$ and $\dot{U} = 1\ mm/s$, they are different for $\dot{U} = 0.01\ mm/s$. For instance, the percentage of damage dissipation relative to total dissipation is higher for $\dot{U} = 0.01\ mm/s$, despite Y_c being the lowest for this case (Figure 5.14b). This could be attributed to the damage widening observed in Figure 5.11 for $\dot{U} = 0.01\ mm/s$, which resulted in more damage energy dissipation.

$\dot{U}$	nb. of elements	nb. of time steps	CPU time for finding $\mathbf{u}$ and $\boldsymbol{\varepsilon}_i$	CPU time for finding d	Total CPU time
1 mm/s	7026	400	4656 s	1501 s	1.7 hours

Table 5.4 – CPU times for mesh 2 and $\dot{U} = 1\ mm/s$

Table 5.4 lists the CPU time observed for the imposed displacement rate of 1 mm/s with 400 time steps. The simulations were performed on a computer equipped with 32 GB of RAM and a

1. The little discrepancy close to the rupture can be attributed to accumulated errors stemming from the relaxed convergence criteria employed in alternate minimization (Remark 6).

6-core processor. It can be seen that most time is being spent in the Newton-Raphson solver used for finding displacements $\mathbf{u}$ and internal strains $\boldsymbol{\varepsilon}_i$, while the CPU time for the damage solver is quite minimal thanks to the bounds estimate and its properties used in lip-field regularization to reduce the computational time. It should also be noted that for the considered Newton-Raphson implementation, the more the number of units of the viscoelastic model (broader spectrum), the more the computational cost.

5.3 Mixed mode fracture

This section involves performing simulations to analyze the validity of the model to perform mixed-mode fracture. In experiments, it is common practice to induce mixed-mode fracture by offsetting the position of the initial notch from the center line of the beam. Hence, in this case, we use a bending beam with a notch offset and loading applied through monotonous displacement rates at the center as shown in Figure 5.15. Specifically, our interest lies in studying the capability

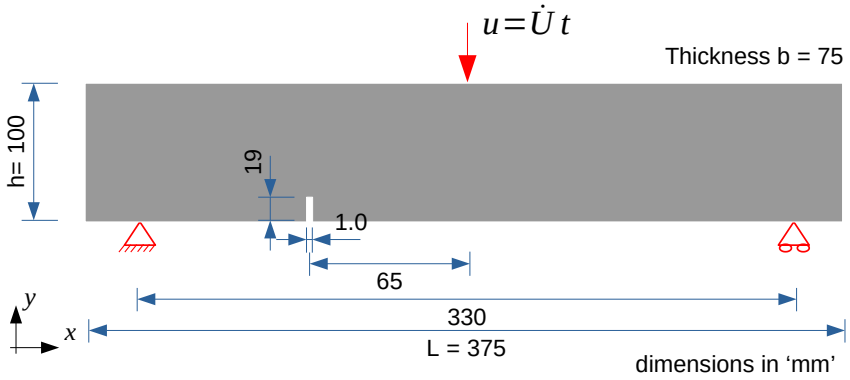

Figure 5.15 – Geometry and boundary conditions used of mixed mode fracture

of the model to predict the experimental crack path. Therefore in this case our interest doesn't lie in fitting experimental results for force-displacement curves. Plane strain assumption has been used and to describe the viscoelastic behavior, we retain the parameters of the GKV model used in Section 5.2 for mode-I fracture corresponding to bituminous mortar mix (Table 5.2). The Poisson's ratio was set as $\nu = 0.2$. Concerning the fracture parameters the following values were used: $Y_c = 2300\ J/m^3$ $\alpha = 1.8,\ \beta = 0.99,\ c = 2,\ l_c = 6\ mm$. For the free energy split, two different types of split were used: (a) split 1 and (b) split 2. Split 1 is based on the eigen decomposition split of the free energy given by Eq. (4.12) with $\theta = 0$, while split 2 is based on the volumetric-deviatoric split given by Eq. (F.3) (see Appendix F). Notice that while split 1 completely prevents damage growth under compression, split 2 offers only partial prevention of damage growth in such circumstances. The geometry is discretized using 25094 linear triangular elements. The mesh is made fine in the critical zone (potential crack path) with element size

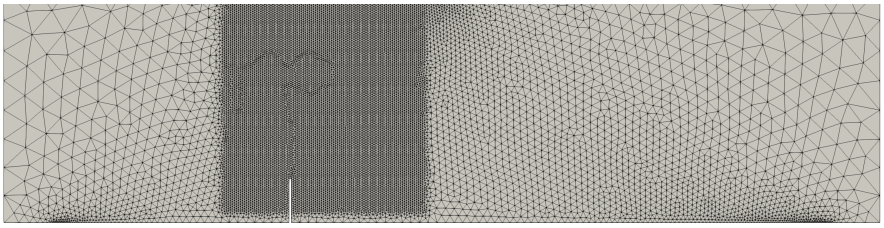

Figure 5.16 – Mesh used for mixed-mode fracture. Smaller element size used in the critical zone (potential crack path)

dx = 1 mm as shown in Figure 5.16. Figure 5.17 plots the force-displacement curves for the

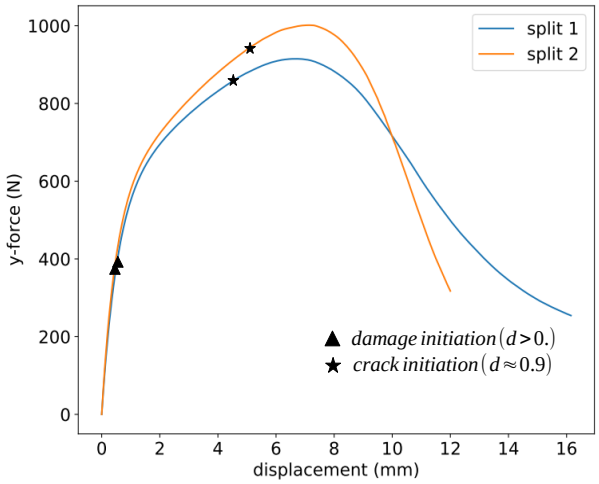

Figure 5.17 – Force-displacement plots for mixed mode fracture

considered splits. Despite damage initiated a little earlier for split 2, its first occurrence of crack is a little delayed. Moreover, it can also be seen that the peak force for split 1 is lesser than the split 2. However, after attaining peak force, the forces drop relatively at a faster rate for split 2 indicating faster crack growth. Figure 5.18 plots the damage profiles for the considered

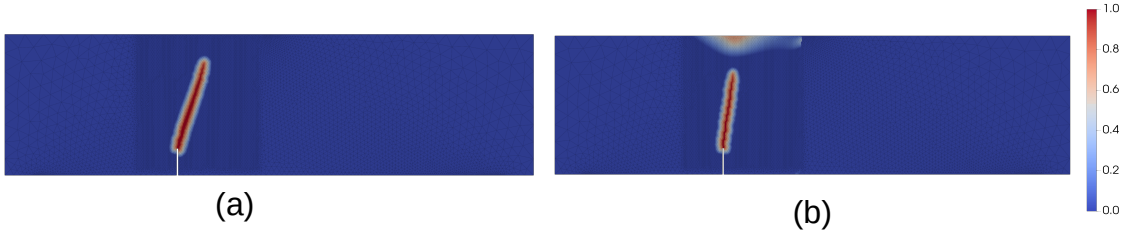

Figure 5.18 – Damage profile for mixed mode fracture using (a) split 1 and (b) split 2

splits. Clearly, the crack path is inclined for both the splits indicating mixed mode fracture.

Furthermore, it becomes evident that the crack angle (angle between the crack and the positive x-axis) in Split 2 is relatively greater than that in Split 1. This is due to the difference in crack driving forces for the considered splits. The presence of a small damage zone at the top of the beam in split 2, where the beam experiences compression, is also noticeable. In contrast, split 1 does not exhibit this feature, which aligns with our previous explanation that split 2 only partially prevents damage growth under compression, unlike split 1. Figure 5.19 compares the

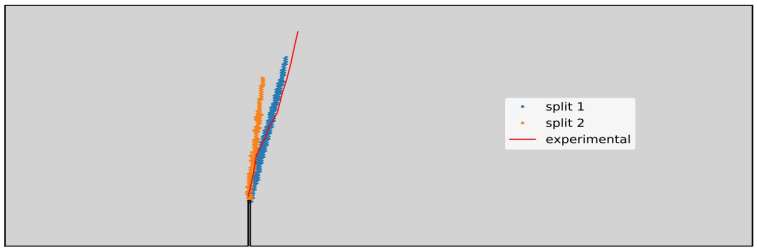

Figure 5.19 – Comparison of numerical crack path with experimental crack path from [32]

crack path obtained for splits 1 and 2 with the experimental crack path presented in [32] for asphalt concrete (bituminous material) at 0^oC. It can be seen that the crack path predicted by split 1 is relatively more accurate compared to split 2. For a different application, one can also calibrate the parameter θ in Eq. (4.12) to fit the experimental crack path.

5.4 Summary

Numerical studies were conducted in this chapter in a 2D setting for the Single Edge Notch Beam (SENB). In the initial phase of the analysis, we positioned the notch at the center to investigate mode-I fracture. Subsequently, to examine the model's response under mixed-mode fracture conditions, we intentionally offset the notch from the center. The parametric study was conducted to understand the influence of different fracture parameters. This knowledge was then used to fit the experimental results under mode-I fracture for a bituminous mortar mix under different loading rates. The simulation results compare well with the experimental results and the rate dependency of critical energy release rate was also observed. In the case of mixed-mode fracture, the simulations were conducted to study the capability of the model to predict the experimental crack path. Two different types of free energy split were considered to account for the unilateral effects. It was observed that the crack path predicted by a pure tension compression split based on eigen decomposition of strain compared well with the experimental results for asphalt concrete.

Conclusions and perspectives

This manuscript completes three years of thesis done at MAST-LAMES, Université Gustave Eiffel, Nantes in collaboration with GeM, École Centrale de Nantes. MAST-LAMES is a laboratory for modeling, experimentation, and survey of transport infrastructures. In this context, most of the work conducted in this lab deals with studying the pavement structure for their effective design. Bituminous materials are the primary constituent of the pavement structure and their fracture is the major cause of deterioration in pavements. The physics of cracking in bituminous materials is not yet fully understood particularly due to their complex rate and temperature-dependent behavior. In this context, the mechanism of fracture in bituminous materials must be satisfactorily modeled.

In addition to the characterization of material and developing relevant behavior models to describe the fracture, one of the major difficulties is the modeling of the numerical simulation of the localization phenomenon that precedes rupture. In order to characterize the localization phenomenon and to model rupture, the recently developed lip-field approach has been used. This approach introduces length scale into the model, thus alleviating the well-known problem of spurious mesh-dependent results associated with softening damage models. In this context, we summarize the following important points addressed during the thesis:

- The first chapter (Chapter 1) was proposed to clarify the context and define the general framework for the study. In particular, characterizing bituminous materials using linear viscoelastic behavior and the associated rheological models have been discussed along with the fracture behavior of bituminous materials. The fracture behavior of bituminous materials shows rate and temperature-dependent behavior. Specifically, they can exhibit both brittle and ductile fracture depending on the rate and temperature effects. Furthermore, it is also difficult to measure the fracture energy through the classical way of measuring the area under the force-displacement curve because of the added viscous dissipation in the bulk. Hence, it was also seen that an integrated experimental-numerical approach is often used to measure fracture energy in bituminous materials. Since in the present thesis, we rely on the lip-field approach to regularize the problem, this chapter concludes with a brief overview of the lip-field approach.
- In Chapter 2, after a brief on thermodynamic laws, we derive the formulation of the vis-

coelastic damage model, continuous and purely local, written in a thermodynamic framework. In particular, the concept of generalized standard materials has been used to ensure the thermodynamic consistency of the developed model. This chapter concludes with the presentation of a variational approach to model damage in viscoelastic materials. The variational approach leads to a minimization problem for the mechanical fields of interest.

- Chapter 3 primarily deals with solving the aforementioned variational problem for the 1D case of a homogeneous bar. Both the Generalized Kelvin-Voigt (GKV) model and the Generalized Maxwell (GM) model have been considered to describe the viscoelastic behavior and both these models were observed to yield the same localization behavior. The numerical results for both these models have also been validated using the respective analytical solutions in local form. Moreover, a homogeneous evolution of damage was also observed before localization. Elementary stability analysis revealed the presence of intrinsic time scale present in the model to be responsible for such homogeneous evolution of damage. The numerical studies conducted for the 1D case of a non-homogeneous bar with a notch revealed the diminishing effect of intrinsic time scale.
- Chapter 4 primarily focuses on extending the model to a more general case of 2D or 3D. Here, the unilateral effects (tension-compression asymmetry) were also incorporated into the model. The numerical implementation was then detailed for the 2D case, followed by validation of the numerical results obtained for 2D with analytical solution and 1D simulation results.
- In Chapter 5, the focus was laid on the application of the developed model to simulate fracture in a bituminous mortar mix. A parametric study was initially conducted to study the influence of different parameters, the knowledge of which was then used to fit the experimental force-displacement curves for mode-I fracture. This calibration revealed the rate dependency of the critical energy release rate Y_c (a parameter analogous to Griffith fracture energy G_c). In order to analyze the capability of the model to predict crack paths in mixed mode fracture, numerical simulations were conducted on a 3-point bending beam with a notch positioned at the offset. The simulation results for the crack path were also found to be in good agreement with experimental results.

This thesis made it possible to arrive at a variational approach to solve the problem of fracture in structures with viscoelastic behavior. The finite element codes for the viscoelastic damage model were also set up in Python (by extending the existing code available for the elastic damage model [102]). This constitutes an important and innovative aspect of the present work. However, there are certain limitations of the study that need to be addressed in the future:

- The cross-comparison of simulation results for different cracking tests (under monotonous loading rates and for different temperatures) and studying the ability of the model to

predict experimental force-displacement curves. This is important to analyze the possibility of having an intrinsic model to describe the behavior of damage in bituminous materials, irrespective of the laboratory tests.

- ✻ As for the behavior of the roadways, it would also be useful to study cracking under slow thermal stresses. Hence, the variational approach developed should be extended to account for temperature changes and thermal deformations (thermo-elastic- viscoelastic-damage model).
- ✻ The model could also be extended to consider variable temperatures by integrating the heat equation into the model. In this context, it's worth noting that the evolution equation for all state variables can still be expressed within a variational framework, as discussed in [128].
- ✻ The computational cost of the non-linear solver used for finding displacements and internal strains is relatively higher compared to the damage solver. Therefore, optimizing the solver is imperative to mitigate these computational challenges and make the model more practical for real-world applications.
- ✻ Extending the developed model to accommodate highly heterogeneous bituminous composite mixtures may require creating separate material models for the aggregates while using the model developed in this thesis to represent the matrix phase (fine aggregate matrix).

Appendix A

Minimization of incremental potential

The minimization of incremental potential (given by Eq. (2.46)) can be written as the following unilateral stationarity condition

$$\delta F(\mathbf{u}, \boldsymbol{\varepsilon}_i, d) \geq 0 \tag{A.1}$$

where the expression for F is given by Eq. (2.47). Here, δF is the variational (or functional) derivative of F and its expression is given as follows:

$$\delta F(\mathbf{u}, \boldsymbol{\varepsilon}_i, d) = \int_\Omega \left[\frac{\partial \psi}{\partial \boldsymbol{\varepsilon}} : \boldsymbol{\varepsilon}(\boldsymbol{\delta u}) \; + \sum_{i=1}^{n} \left(\frac{\partial \psi}{\partial \boldsymbol{\varepsilon}_i} + \Delta t \frac{\partial \phi_v}{\partial \boldsymbol{\varepsilon}_i} \right) \boldsymbol{\delta \varepsilon}_i \; + \left(\frac{\partial \psi}{\partial d} + Y_c h'(d) \right) \delta d \right] d\Omega \tag{A.2}$$

where $\boldsymbol{\delta u}$, $\boldsymbol{\delta \varepsilon}_i$ and δd are the admissible variations in $\mathbf{u}$, $\boldsymbol{\varepsilon}_i$ and d (such that $\boldsymbol{\delta u} = \mathbf{0}$ on Dirichlet boundary Γ_u and $\delta d \geq 0$). On utilizing Eqs. (2.25,2.28,2.48) and the application of the divergence theorem, the above equation can be rewritten as follows.

$$\delta F = \int_\Omega \left[-(\nabla . \boldsymbol{\sigma}) . \boldsymbol{\delta u} + \sum_{i=1}^{n} \left(\frac{\partial \psi}{\partial \boldsymbol{\varepsilon}_i} + \Delta t \frac{\partial \phi_v}{\partial \boldsymbol{\varepsilon}_i} \right) \boldsymbol{\delta \varepsilon}_i + \left(-Y + Y_c H(d) \right) \delta d \right] d\Omega + \int_{\Gamma_N} (\boldsymbol{\sigma} . \mathbf{n}) . \boldsymbol{\delta u} dS \tag{A.3}$$

The unilateral stationarity condition of F (Eq. (A.1)) i.e., $\delta F = 0$ for $\delta d > 0$ and $\delta F > 0$ for $\delta d = 0$, gives the following governing equations in strong form

$$\nabla . \boldsymbol{\sigma} = 0 \qquad in \quad \Omega \tag{A.4}$$

$$\boldsymbol{\sigma} . \mathbf{n} = \mathbf{0} \qquad on \quad \Gamma_N \tag{A.5}$$

$$\frac{\partial \psi}{\partial \boldsymbol{\varepsilon}_i} + \Delta t \frac{\partial \phi_v}{\partial \boldsymbol{\varepsilon}_i} = 0 \quad \forall \; i \in \{1, 2, .., n\} \qquad in \quad \Omega \tag{A.6}$$

as well as

$$Y - Y_c H(d) = 0 \quad for \;\; \dot{d} > 0 \;\; in \;\; \Omega \tag{A.7}$$

$$Y - Y_c H(d) < 0 \quad for \;\; \dot{d} = 0 \;\; in \;\; \Omega \tag{A.8}$$

which can be written as the Karush-Kuhn-Tucker conditions as follows:

$$\dot{d} \geq 0, \quad Y - Y_c H(d) \leq 0, \quad (Y - Y_c H(d))\dot{d} = 0 \tag{A.9}$$

In the above set of governing equations, Γ_N is the Neumann boundary, and $\mathbf{n}$ is the unit normal vector to the boundary $\Gamma = \Gamma_u \cup \Gamma_N$.

Thus the equilibrium equation and the evolution equation for internal variables are recovered as the solution of the optimization problem given by Eq. (2.46).

Appendix B

LOCAL ANALYTICAL SOLUTION

In this section, the equations to arrive at the (semi-) analytical solution in local form for the softening Generalized Kelvin-Voigt (GKV) model and the softening Generalized Maxwell (GM) model are derived. This helps to validate the finite element implementation for the case of a 1D homogeneous bar.

GKV model with damage

The stress and viscous strain (in incremental form) are given as follows (from Eqs. (3.6), (3.23)):

$$\sigma = g(d)E_0(\varepsilon - \sum_{i=1}^{n} \varepsilon_i) \tag{B.1}$$

$$\varepsilon_i = \frac{\Delta t}{g(d)\Delta t + \tau_i}\left(\frac{\sigma}{E_i} + \frac{\tau_i \varepsilon_{i,m}}{\Delta t}\right) \tag{B.2}$$

Substitution of Eq. (B.2) in Eq. (B.1) leads to the following equation for the stress

$$\sigma = p(d)\left(\varepsilon - \sum_{i=1}^{n} \frac{\tau_i \varepsilon_{i,m}}{g(d)\Delta t + \tau_i}\right) \tag{B.3}$$

where the expression for $p(d)$ is given in Eq. (3.25). The local damage is obtained by solving the below minimization problem

$$d = arg \min_{d_m \leq d \leq 1} g(d)\psi_0 + Y_c h(d) \tag{B.4}$$

The explicit scheme algorithm used is shown in Algorithm 3. At each time step, the stress σ is found by the latest available values for the strain ε and damage d (using Eq. (B.3)). Then the viscous strain ε_i is updated using Eq. (B.2), followed by the update of the damage variable d using Eq. (B.4).

GM model with damage

The stress and viscous strain (in incremental form) are given as follows (from Eqs. (3.61), 3.65):

$$\sigma = g(d)\left(E_0\varepsilon + \sum_{i=1}^{n} E_i(\varepsilon - \varepsilon_i)\right) \tag{B.5}$$

$$\varepsilon_i = \frac{\Delta t}{g(d)\Delta t + \tau_i}\left(g(d)\varepsilon + \frac{\tau_i \varepsilon_{i,m}}{\Delta t}\right) \tag{B.6}$$

Substitution of Eq. (B.6) in Eq. (B.5) leads to the following equation for the stress

$$\sigma = p(d)\varepsilon - \sigma_{int}(d) \tag{B.7}$$

where the expression for $p(d)$ and σ_{int} are given in Eq. (3.67, 3.68). The local damage is obtained by solving the below minimization problem

$$d = arg \min_{d_m \leq d \leq 1} g(d)\psi_0 + Y_c h(d) \tag{B.8}$$

The same explicit scheme algorithm is used here as in the previous case for the softening GKV model. The algorithm is shown in Algorithm 3. In both cases, Δt has to be chosen small enough for the explicit scheme to converge.

Algorithm 3 Local (semi-) analytical solution for softening GKV (or) GM model

1: Initialize $m = 0$, $\dot{\varepsilon}$, ε_m $\varepsilon_{i,m}, d_m, \Delta t$
2: **while** $m \leq M$ **do**
3: Find σ ▷ using Eq. (B.3) or Eq. (B.7)
4: Update ε_i ▷ using Eq. (B.2) or Eq. (B.6)
5: Find the damage d ▷ using Eq. (B.4) or Eq. (B.8)
6: Update $\varepsilon+ = \dot{\varepsilon} \times \Delta t$
7: $m \leftarrow m + 1$
8: **end while**

Appendix C

Conditions for stability

The condition for stability [114] is listed here separately for the linear and non-linear systems.

Linear system of ODE's

Consider the following linear time-invariant system of ODE's,

$$\dot{\mathbf{y}} = \mathbf{A}\mathbf{y} \tag{C.1}$$

where $\mathbf{A}$ is a real constant matrix of size $n \times n$, $y_0 = \mathbf{0}$ is the equilibrium solution. The stability of the above linear system can be given by the following conditions [114]

1. If all the eigen values of $\mathbf{A}$ has non-positive real parts and all the eigen values with zero real parts are simple (*distinct*), then the zero solution $y_0 = \mathbf{0}$ is Lyapunov stable.
2. If and only if all the eigen values of $\mathbf{A}$ has negative real parts, then $y_0 = \mathbf{0}$ is asymptotically stable.
3. If there exists atleast one eigen value of $\mathbf{A}$ with positive real part, $y_0 = \mathbf{0}$ is unstable.
4. If all the eigen values of $\mathbf{A}$ has non-positive real parts and atleast one of the eigen values with zero real parts is *not* simple (*not distinct* indicating multiplicity more than 1), then the zero solution $y_0 = \mathbf{0}$ is unstable.

Non-linear system of ODE's

The stability condition for the non-linear (autonomous) system is listed here [114]. Consider the following non-linear system of ODE's (f is a non-linear function of y)

$$\dot{y} = f(y) \tag{C.2}$$

If y_0 is an equilibrium solution of the above problem (then $\dot{y}_0 = f(y_0) = 0$), and $\tilde{y}$ is a small perturbation around $y = 0$, then the stability of the non-linear system can be understood by

studying the behaviour of $\underline{\psi} = y_0 + \tilde{y}$ (points close to equilibrium solution). Replacing y by $\underline{\psi}$ in Eq. (C.2), the following equation is obtained for the behavior of points close to the equilibrium solution

$$\dot{\underline{\psi}} = f(y_0 + \tilde{y}) \tag{C.3}$$

$$\implies \dot{\tilde{y}} = f(y_0 + \tilde{y}) - f(y_0) \tag{C.4}$$

If the above equation can be written in the following linearized form,

$$\dot{\tilde{y}} = A\tilde{y} + p(\tilde{y}) \tag{C.5}$$

where A is the *Jacobian matrix* of $f(y)$ at y_0, p is a continuous function with $p(0) = 0$ and $\lim_{\tilde{y}\to 0} \frac{\|p(\tilde{y})\|}{\|\tilde{y}\|} = 0$, then the following condition for stability can be obtained [114], [129],

1. If all the eigen values of A have negative real part, the equilibrium solution y_0 (or the zero solution $\tilde{y} = 0$) is stable
2. If atleast one of the eigen values of A have positive real parts, then the equilibrium solution is unstable (perturbation $\tilde{y}$ grows with time)
3. If all the eigen values of A have non positive real parts and atleast there exists one eigen value with zero real part, then no conclusion can be drawn (in this case, the dynamics of the linearized system doesn't represent the dynamics of non-linear system).
4. However for the special case of conservative systems (eg: conserved total energy) or the reversible systems (*with time reversal symmetry* s.t. $y(-t) = y(t)$), if all the eigen values of A have non positive real parts and all the eigen values with zero real part are simple (*distinct*), then the equilibrium point is stable (in Lyapunov sense but not asymptotically stable) [130]

Appendix D

Perturbation solution for softening elasticity

In this case, we consider the softening elasticity with no external regularization case and justify the choice of the perturbation for $\tilde{u}$ and $\tilde{d}$ used in Eq. (3.44). Consider the linearized equations associated with the perturbations from Eq. (3.49). $g(d)$ and $h(d)$ are given by the following equations (from Eq. (3.45), (3.46)).

$$g(d) = (1-d)^2 \tag{D.1}$$

$$h(d) = 2d \tag{D.2}$$

In this case, the rate of damage growth at the onset of damage initiation $\psi = Y_c$ (where $d = 0,\ \dot{d} \neq 0$) is given as follows (from Eq. (3.47b) and Eq. (D.1, D.2)).

$$\dot{d} = \frac{\dot{\psi}}{\psi} = \frac{E\varepsilon\dot{\varepsilon}}{\frac{1}{2}E\varepsilon^2} \tag{D.3}$$

The (linearized) perturbation equation associated with damage evolution is then given by

$$\dot{\tilde{d}}\psi + \dot{d}E\varepsilon\tilde{\varepsilon} - E\varepsilon\dot{\tilde{\varepsilon}} - E\tilde{\varepsilon}\dot{\varepsilon} = 0 \tag{D.4}$$

Substituting Eq. (3.49c) in Eq. (3.49a) and noting that $\varepsilon_{,x} = d_{,x} = 0$ for an elastic homogeneous bar at the onset of damage initiation, we obtain the following perturbation equation associated to the linear momentum balance

$$g'(d)\tilde{d}_{,x} + g(d)E\tilde{\varepsilon}_{,x} = \rho\ddot{\tilde{u}} \tag{D.5}$$

For the perturbation of u and d, we can consider the following separation of variables

$$\tilde{u}(x,t) = X(x)\hat{u}(t) \tag{D.6a}$$

$$\tilde{d}(x,t) = X(x)\hat{d}(t) \tag{D.6b}$$

$X(x)$ in the 1D homogeneous case where the dilation band occurs can be chosen as either $cos(kx - \frac{\pi}{2})$ or $sin(kx)$ (respects zero perturbation at $x = 0$ and k can be chosen such that zero perturbation is also attained at $x = L$). But to simplify the mathematics involved, we choose the following: $X(x) = e^{ikx}$, where $k = \frac{2\pi}{\lambda}$ is the wave number and λ is the wavelength of the perturbation. Substitution of Eq. (D.6) in Eq. (D.5) and Eq. (D.4) and introduction of change of variable $\dot{\hat{u}} = \hat{v}$, we obtain the following (linearized) first order (in time) ode's for the perturbations.

$$\frac{d}{dt}[\boldsymbol{Y}] = [\boldsymbol{A}][\boldsymbol{Y}] \tag{D.7}$$

where

$$\boldsymbol{Y} = \begin{bmatrix} \hat{v} \\ \hat{u} \\ \hat{d} \end{bmatrix} \; and \; \boldsymbol{A} = \begin{bmatrix} 0 & -\frac{g(d)Ek^2}{\rho} & \frac{g'(d)ikE\varepsilon}{\rho} \\ 1 & 0 & 0 \\ \frac{2ik}{\varepsilon} & \frac{-\dot{d}ik(\varepsilon+\dot{\varepsilon})}{\varepsilon^2} & 0 \end{bmatrix} \tag{D.8}$$

Trying $\boldsymbol{Y} = \boldsymbol{q}e^{st}$ as the solution of Eq. (D.7), results in the following eigen value problem:

$$(\boldsymbol{A} - s\boldsymbol{I})\boldsymbol{q} = 0 \tag{D.9}$$

with $\boldsymbol{q}$ being the eigen vector corresponding to the eigen value s. Now back substitution of $\boldsymbol{Y} = \boldsymbol{q}e^{st}$ in Eq. (D.6) results in the followin

$$\tilde{u}(x,t) = X(x)\hat{u}(t) = ge^{ikx}e^{st} \tag{D.10a}$$

$$\tilde{d}(x,t) = X(x)\hat{d}(t) = he^{ikx}e^{st} \tag{D.10b}$$

The last expression justifies the expression for perturbations (given by Eq. (3.44)) considered for the study.

The condition discussed for the stability can be justified by looking into the general solution of Eq. (D.7). The general solution can be given for the following three cases:

1. All eigen values s_i are real and distinct and $\boldsymbol{v_i}$ being the respective eigen vectors, then

$$\boldsymbol{Y}(t) = c_1\boldsymbol{v_1}e^{s_1t} + c_2\boldsymbol{v_2}e^{s_2t} + c_3\boldsymbol{v_3}e^{s_3t} \tag{D.11}$$

2. $s_1 = s_2$ and all eigen values are real,

$$\boldsymbol{Y}(t) = c_1\boldsymbol{v_1}e^{s_1 t} + c_2(t\ e^{s_2 t}\boldsymbol{v_1} + e^{s_2 t}\boldsymbol{p_1}) + c_3\boldsymbol{v_3}e^{s_3 t} \tag{D.12}$$

where $\boldsymbol{v_i}$ is the eigen vector corresponding to s_i, abd $\boldsymbol{p_1}$ is given as follows: $([\boldsymbol{A}]-s_1[\boldsymbol{I}])\boldsymbol{p_1} = \boldsymbol{v_1}$

3. s_1 and s_2 are complex ($\implies$ $s_1 = \bar{s}_2$ and $\boldsymbol{v_1} = \bar{\boldsymbol{v}}_{\boldsymbol{2}}$) and s_3 is real

$$\boldsymbol{Y}(t) = c_1\mathcal{R}e(\boldsymbol{v_1}e^{s_1 t}) + c_2\mathcal{I}m(\boldsymbol{v_1}e^{s_1 t}) + c_3\boldsymbol{v_3}e^{s_3 t} \tag{D.13}$$

The growth or decay of the perturbation ($\boldsymbol{Y}(t)$) over time determines the stability of the system and it is determined by the value that s_i takes as discussed in Section C.

Appendix E

Rate dependent softening elasticity

In this section, we present the finite element results for the rate-dependent softening elasticity for the case of a 1D homogeneous bar (Figure 3.2) with an applied monotonous displacement rate. In particular, we consider the minimization of the following incremental potential at each time step as the solution of the mechanical problem

$$(u, d) = \arg \min_{\substack{u' \in \mathcal{U}_m \\ d' \in \mathcal{A}_m}} F(u', d' \ ; \ u_m, d_m, \Delta t) \tag{E.1}$$

$$F = \int_\Omega g(d) \frac{1}{2} E \varepsilon^2 + Y_c (h(d) + (\tau_{vd} \dot{d})^2) dx \tag{E.2}$$

The admissible spaces for the displacement and damage field are given in Eqs. (3.13, 3.15). Here, τ_{vd} is the viscosity-like parameter associated with the damage evolution. This parameter acts as a resistance to the damage rate and thus introduces a time scale into the model. (The stability analysis of such models was performed in Section 3.2.2). Moreover, *here we haven't employed any external regularization* (notice from Eq. (E.1), the admissible spaces for the damage field doesn't include the Lipschitz space)

The choice of $g(d)$ and $h(d)$ are given in Eqs. (3.36, 3.37). The following parameters are used for the simulation: $L = 1\ m$, $\dot{U} = 1e-3\ m/s$, $E = 2\ Pa$, $Y_c = 1\ J/m^3$ and $\tau_{vd} = 10\ s$.

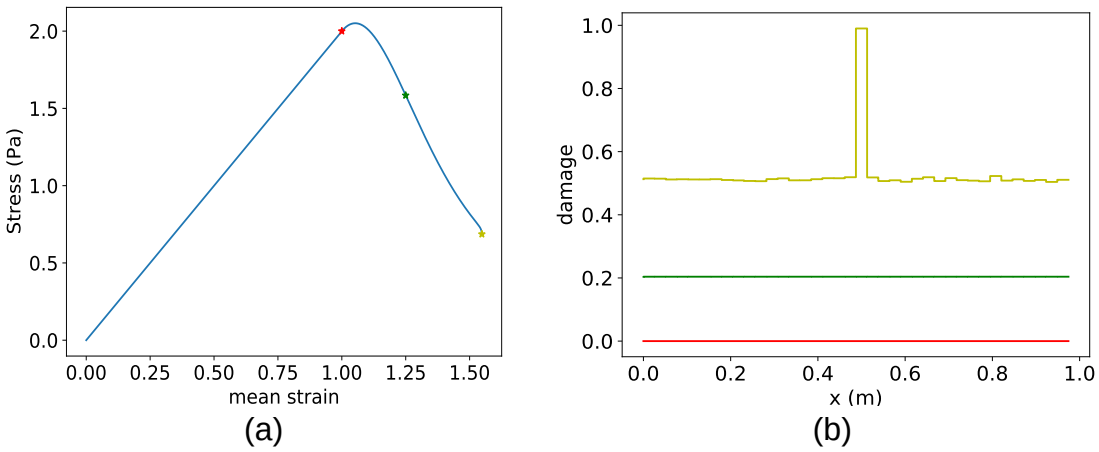

Figure E.1 – (a) Stress-strain curve and (b) damage evolution at different instants indicated by bullets in stress-strain curve

Figure E.1 plots the stress-strain curve and damage field at different instants of time. The introduction of time scale into the softening elasticity model results in a homogeneous evolution of damage initially after the onset of damage initiation, followed by localization. This is expected based on the results of the stability analysis performed for such models (in Section 3.2.2). The homogeneous evolution of damage for such models is due to the propagation of instability in finite time. This is due to the finite value of the Lyapunov exponent for rate-dependent softening elasticity (Figure 3.11) as opposed to the infinite value of Lyapunov exponent for rate-independent softening elasticity (Figure 3.10). However, as time progresses, the instability grows, and localization occurs. Due to the absence of any external regularization, the localization occurs on a single finite element.

Owing to the similarity of results (homogeneous evolution of damage preceding localization) in this case with the softening viscoelastic damage models (in Sections 3.1, 3.3), it confirms the presence of intrinsic time scale associated with damage in softening viscoelastic damage models.

Appendix F

Different forms of free energy split

In this section, we brief on the different types of split considered for free energy.

$$\psi = g(d)\psi_0^+ + \psi_0^- \tag{F.1}$$

where ψ_0^+ is the only portion of free energy affected by damage.

Apart from the pure eigen split of strains to express free energy (as discussed in Section 4.1), it is also common in the damage mechanics community to consider splits based on volumetric ($\boldsymbol{\varepsilon}_V$) and deviatoric part ($\boldsymbol{\varepsilon}_D$) of the strain tensor $\boldsymbol{\varepsilon}$.

$$\boldsymbol{\varepsilon} = \boldsymbol{\varepsilon}_V + \boldsymbol{\varepsilon}_D, \quad \boldsymbol{\varepsilon}_V = \frac{1}{b} Tr(\boldsymbol{\varepsilon})\mathbf{1} \tag{F.2}$$

where $\mathbf{1}$ is the identity matrix (second-order identity tensor) and b takes values 2 and 3 for two and three dimensions respectively.

Based on the split for free energy proposed in [91], we consider the following positive and negative parts of free energy

$$\psi_0^+ = \sum_{i=0}^{n} \frac{1}{2} K_i < Tr(\boldsymbol{\varepsilon}_i) >_+^2 + \mu_i \boldsymbol{\varepsilon}_D : \boldsymbol{\varepsilon}_D, \quad \psi_0^- = \sum_{i=0}^{n} \frac{1}{2} K_i < Tr(\boldsymbol{\varepsilon}_i) >_-^2 \tag{F.3}$$

where $K_i = \lambda_i + 2\frac{\mu_i}{b}$ is the bulk modulus and μ_i is the shear modulus corresponding to the i^{th} unit of the GKV model (Figure 4.1). The above split only partially prevents the creation of cracks in compression (contrary to the pure eigen split with $\theta = 0$ in Eq. (4.12)).

In [131], for the case of shear fracture, the authors used a form of split where only the deviatoric part contributes to the damage growth and the model was able to reproduce results for shear fracture (mode-II cracks) observed in the structural members of French Panthéon. Following in a

similar manner, we extend the split to the viscoelastic materials undergoing pure shear fracture as follows:

$$\psi_0^+ = \sum_{i=0}^{n} \mu_i \boldsymbol{\varepsilon}_D : \boldsymbol{\varepsilon}_D, \quad \psi_0^- = \sum_{i=0}^{n} \frac{1}{2} K_i Tr(\boldsymbol{\varepsilon}_i)^2 \tag{F.4}$$

Notice from Eq. (F.1) and Eq. (F.4) that the volumetric part of the free energy is not affected by damage.

BIBLIOGRAPHY

[1] E. Remišová and M. Holỳ, "Changes of properties of bitumen binders by additives application," in *IOP conference series: Materials science and engineering*, vol. 245, no. 3. IOP Publishing, 2017, p. 032003. [Online]. Available: https://dx.doi.org/10.1088/1757-899X/245/3/032003

[2] M. Tumpu, M. Tjaronge, and A. Djamaluddin, "Prediction of long-term volumetric parameters of asphalt concrete binder course mixture using artificial ageing test," in *IOP Conference Series: Earth and Environmental Science*, vol. 419, no. 1. IOP Publishing, 2020, p. 012058. [Online]. Available: https://dx.doi.org/10.1088/1755-1315/419/1/012058

[3] F. T. S. Aragão, Y.-R. Kim, and M. H. Javaherian, "Modeling rate-dependent fracture behavior of asphalt mixtures," in *Transportation Research Board 91st Annual Meeting*, 2012.

[4] F. Aragão and Y.-R. Kim, "Mode i fracture characterization of bituminous paving mixtures at intermediate service temperatures," *Experimental mechanics*, vol. 52, pp. 1423–1434, 2012. [Online]. Available: https://doi.org/10.1007/s11340-012-9594-4

[5] H. Kim and W. G. Buttlar, "Discrete fracture modeling of asphalt concrete," *International Journal of Solids and Structures*, vol. 46, no. 13, pp. 2593–2604, 2009. [Online]. Available: https://doi.org/10.1016/j.ijsolstr.2009.02.006

[6] F. T. S. Aragão, Y.-R. Kim, J. Lee, and D. H. Allen, "Micromechanical model for heterogeneous asphalt concrete mixtures subjected to fracture failure," *Journal of Materials in Civil Engineering*, vol. 23, no. 1, pp. 30–38, 2011. [Online]. Available: https://doi.org/10.1061/(ASCE)MT.1943-5533.0000004

[7] F. Olard, "COMPORTEMENT THERMOMÉCANIQUE DES ENROBÉS BITUMINEUX À BASSES TEMPÉRATURES. Relations entre les propriétés du liant et de l'enrobé," Theses, INSA de Lyon, 2003. [Online]. Available: https://theses.hal.science/tel-00006050

[8] H. Di Benedetto, "Nouvelle approche du comportement des enrobés bitumineux : résultats expérimentaux et formulation rhéologique," *'Mechanical Tests for Bituminous Mixes,*

Characterization, Design and Quality Control', Proceedings of the Fourth RILEM Symposium, 1990.

[9] I. Santos, "Modélisation intrinsèque de la fissuration par fatigue des enrobés bitumineux à partir de mesures de champs. : Application à la correspondance entre différents types d'essais de fatigue," Ph.D. dissertation, École centrale de Nantes, 2020. [Online]. Available: https://theses.hal.science/tel-03267849

[10] H. F. Brinson and L. C. Brinson, *Polymer Engineering Science and Viscoelasticity: An Introduction*. Springer US.

[11] P. Romero *et al.*, "Using the bending beam rheometer for low temperature testing of asphalt mixtures," Utah. Dept. of Transportation, Tech. Rep., 2016.

[12] Z. eng, B. S. Underwood, and C. Castorena, "Low-temperature performance grade characterisation of asphalt binder using the dynamic shear rheometer," *International Journal of Pavement Engineering*, vol. 23, no. 3, pp. 811–823, 2022. [Online]. Available: https://doi.org/10.1080/10298436.2020.1774766

[13] L. Boltzmann, ""zur theorie der elastischen nachwirkung."," *Annalen Der Physik Und Chemie*, p. 241(11):430–32, 1878.

[14] T. Alfrey, "Non-homogeneous stresses in visco-elastic media," *Quarterly of Applied Mathematics*, vol. 2, no. 2, pp. 113–119, 1944.

[15] N. Tschoegl, W. Knauss, and I. Emri, "Poisson's ratio in linear viscoelasticity – a critical review," *Mechanics of Time-Dependent Materials*, pp. 6, 3–51, 2002. [Online]. Available: https://doi.org/10.1023/A:1014411503170

[16] E. Doubbaneh, "Comportement mécanique des enrobés bitumineux des petites aux grandes déformations," *Thése de Doctorat, Institut National Des Sciences Appliquées de Lyon.*, 1995.

[17] B. Shiferaw, "Modélisation de la fissuration en milieu viscoélastique par approche thick level set pour application au cas des enrobés bitumineux," *Thése de Doctorat, L'École Centreale de Nantes*, 2019. [Online]. Available: https://theses.hal.science/tel-03027068

[18] H. Leaderman, "Elastic and creep properties of filamentous materials and other high polymers." *The Textile Founda-Tion, Washington*, 1943. [Online]. Available: https://doi.org/10.1021/j150453a029

[19] F. Schwarzl and A. Staverman, "Time-temperature dependence of linear viscoelastic behavior," *Journal of Applied Physics*, vol. 23, no. 8, pp. 838–843, Aug. 1952. [Online]. Available: https://doi.org/10.1063/1.1702316

[20] M. Williams and R. Landel, "The temperature dependence of relaxation mechanisms in amorphous polymers and other glass-forming liquids." *Journal of the American Chemical Society*, vol. 77, p. 3701–3706, 1995. [Online]. Available: https://doi.org/10.1021/ja01619a008

[21] D. Anderson and R. Dongre, "The shrp direct tension specification test-its development and use." *Physical Properties of Asphalt Cement Binders. 100 Barr Harbor Drive, PO Box C700, West Conshohocken, PA 19428-2959: ASTM International.*, pp. 51–66, 1995.

[22] F. Doucet and A. Bruno, "Détermination du module complexe des enrobés au ministère des transports du québec," *MATÉRIAUX ET INFRASTRUCTURES, ÉTUDES ET RECHERCHES EN TRANSPORT.*, 2010.

[23] C. Huet, ""Étude par une méthode d'impédance du comportement viscoélastique des matériaux hydrocarbonés."," *Thèse de Docteur Ingénieur, Faculté Des Sciences de l'Université de Paris*, 1963.

[24] G. Sayegh, ""viscoelastic properties of bituminous mixtures."," *2nd International Conference on the Structural Design of Asphalt Pavements. University of Michigan, Ann Arbor 743–55*, 1967.

[25] X. Qinwu and S. Mansour, "Modelling linear viscoelastic properties of asphalt concrete by the huet–sayegh model," *International Journal of Pavement Engineering*, vol. 10:6, pp. 401–422, 2009. [Online]. Available: https://doi.org/10.1080/10298430802524784

[26] F. Olard and H. Benedetto, "General '2s2p1d' model and relation between the linear viscoelastic behaviours of bituminous binders and mixes." *Road Materials and Pavement Design*, vol. 4(2), p. 185–224, 2003. [Online]. Available: https://doi.org/10.1080/14680629.2003.9689946

[27] J. Simo and T. Hughes, *Computational inelasticity.* Springer, 1998.

[28] H. T. T. Nguyen, D.-L. Nguyen, V.-T. Tran, and M.-L. Nguyen, "Finite element implementation of huet-sayegh and 2s2p1d models for analysis of asphalt pavement structures in time domain," *Road Materials and Pavement Design*, vol. 23, no. 1, pp. 22–46, 2022. [Online]. Available: https://doi.org/10.1080/14680629.2020.1809501

[29] V. Van, Thang, ""Étude expérimentale et numérique du comportement au gel et au dégel des enrobés bitumineux partiellement satures-application à l'interprétation de dégradations subites de chaussées bitumineuses en période hivernale."," *Thèse de Doctorat, Ecole Centrale de Nantes.*, 2017. [Online]. Available: https://theses.hal.science/tel-02149945

[30] J. Miller and W. Bellinger, "Distress identification manual for the long-term pavement performance program," *U.S. Department of Transportation: Federal Highway Administration*, 2003.

[31] G. Nsengiyumva, Y.-R. Kim, and T. You, "Development of a semicircular bend (scb) test method for performance testing of nebraska asphalt mixtures," 2015.

[32] M. P. Wagoner, W. G. Buttlar, and G. H. Paulino, "Development of a single-edge notched beam test for asphalt concrete mixtures," *Journal of Testing and Evaluation*, vol. 33, no. 6, p. 452, 2005.

[33] M. Wagnoner, W. Buttlar, and G. Paulino, "Disk-shaped compact tension test for asphalt concrete fracture," *Experimental mechanics*, vol. 45, pp. 270–277, 2005. [Online]. Available: https://doi.org/10.1007/BF02427951

[34] C. M. Stewart, J. G. Reyes, and V. M. Garcia, "Comparison of fracture test standards for a super pave dense-graded hot mix asphalt," *Engineering Fracture Mechanics*, vol. 169, pp. 262–275, 2017. [Online]. Available: https://doi.org/10.1016/j.engfracmech.2016.10.016

[35] H. Radeef, N. A. Hassan, A. Z. Abidin, M. Mahmud, M. M. Satar, M. M. Warid, and Z. Al Saffar, "Determining fracture energy in asphalt mixture: A review," in *IOP Conference Series: Earth and Environmental Science*, vol. 682, no. 1. IOP Publishing, 2021, p. 012069. [Online]. Available: https://dx.doi.org/10.1088/1755-1315/682/1/012069

[36] A. Tabaković, A. Karač, A. Ivanković, A. Gibney, C. McNally, and M. D. Gilchrist, "Modelling the quasi-static behaviour of bituminous material using a cohesive zone model," *Engineering Fracture Mechanics*, vol. 77, no. 13, pp. 2403–2418, 2010. [Online]. Available: https://doi.org/10.1016/j.engfracmech.2010.06.023

[37] Z. P. Bazant and J. Planas, *Fracture and size effect in concrete and other quasibrittle materials*. CRC press, 1997, vol. 16.

[38] R. D. Recommendation, "Determination of the fracture energy of mortar and concrete by means of three-point bend tests on notched beames," *Materials and structures*, vol. 18, no. 106, pp. 285–290, 1985.

[39] I. L. Al-Qadi, S.-H. Yang, J.-F. Masson, K. K. McGhee *et al.*, "Characterization of low temperature mechanical properties of crack sealants utilizing direct tension test." Illinois Center for Transportation, Tech. Rep., 2008. [Online]. Available: https://rosap.ntl.bts.gov/view/dot/16705

[40] M. Merbouh *et al.*, "Contribution à la modélisation du comportement rhéologique des enrobés bitumineux: influence des conditions extrêmes de température et de trafic en fatigue," Ph.D. dissertation, Bordeaux 1, 2010. [Online]. Available: https://www.theses.fr/2010BOR14214

[41] A. A. Griffith, "Vi. the phenomena of rupture and flow in solids," *Philosophical transactions of the royal society of london. Series A, containing papers of a mathematical or physical character*, vol. 221, no. 582-593, pp. 163–198, 1921.

[42] T. L. Anderson, *Fracture mechanics: fundamentals and applications*. CRC press, 2017.

[43] C.-T. Sun and Z. Jin, *Fracture mechanics*. Academic press, 2011.

[44] G. R. Irwin, "Onset of fast crack propagation in high strength steel and aluminum alloys," 1956.

[45] J. R. Rice, "A path independent integral and the approximate analysis of strain concentration by notches and cracks," 1968. [Online]. Available: https://doi.org/10.1115/1.3601206

[46] Z. Zhuang, Z. Liu, B. Cheng, and J. Liao, "Chapter 2 - fundamental linear elastic fracture mechanics," in *Extended Finite Element Method*, Z. Zhuang, Z. Liu, B. Cheng, and J. Liao, Eds. Oxford: Academic Press, 2014, pp. 13–31.

[47] R. A. Schapery, "Correspondence principles and a generalized j integral for large deformation and fracture analysis of viscoelastic media," *International journal of fracture*, vol. 25, pp. 195–223, 1984. [Online]. Available: https://doi.org/10.1007/BF01140837

[48] R. Schapery, "On some path independent integrals and their use in fracture of nonlinear viscoelastic media," *International Journal of Fracture*, vol. 42, pp. 189–207, 1990. [Online]. Available: https://doi.org/10.1007/BF00018386

[49] F. Dubois and C. Petit, "Modelling of the crack growth initiation in viscoelastic media by the gθv-integral," *Engineering Fracture Mechanics*, vol. 72, no. 18, pp. 2821–2836, 2005. [Online]. Available: https://doi.org/10.1016/j.engfracmech.2005.04.003

[50] T. Belytschko and T. Black, "Elastic crack growth in finite elements with minimal remeshing," *International journal for numerical methods in engineering*, vol. 45, no. 5, pp. 601–620, 1999. [Online]. Available: https://onlinelibrary.wiley.com/doi/abs/10.1002/%28SICI%291097-0207%2819990620%2945%3A5%3C601%3A%3AAID-NME598%3E3.0.CO%3B2-S

[51] N. Moës, J. Dolbow, and T. Belytschko, "A finite element method for crack growth without remeshing," *International journal for numerical methods in engineering*, vol. 46, no. 1, pp. 131–150, 1999. [Online]. Available: https://doi.org/10.1002/(SICI)1097-0207(19990910)46:1%3C131::AID-NME726%3E3.0.CO;2-J

[52] H. Zhang and L. Li, "Modeling inclusion problems in viscoelastic materials with the extended finite element method," *Finite Elements in Analysis and Design*, vol. 45, no. 10, pp. 721–729, 2009. [Online]. Available: https://doi.org/10.1016/j.finel.2009.06.006

[53] H. Zhang, G. Rong, and L. Li, "Numerical study on deformations in a cracked viscoelastic body with the extended finite element method," *Engineering Analysis with Boundary Elements*, vol. 34, no. 6, pp. 619–624, 2010. [Online]. Available: https://doi.org/10.1016/j.enganabound.2010.02.001

[54] D. S. Dugdale, "Yielding of steel sheets containing slits," *Journal of the Mechanics and Physics of Solids*, vol. 8, no. 2, pp. 100–104, 1960. [Online]. Available: https://doi.org/10.1016/0022-5096(60)90013-2

[55] G. I. Barenblatt, "The mathematical theory of equilibrium cracks in brittle fracture," *Advances in applied mechanics*, vol. 7, pp. 55–129, 1962. [Online]. Available: https://doi.org/10.1016/S0065-2156(08)70121-2

[56] L. Kachanov, *Introduction to continuum damage mechanics*. Springer Science & Business Media, 1986, vol. 10.

[57] J. Lemaitre, "How to use damage mechanics," *Nuclear engineering and design*, vol. 80, no. 2, pp. 233–245, 1984. [Online]. Available: https://doi.org/10.1016/0029-5493(84)90169-9

[58] E. V. Dave and B. Behnia, "Cohesive zone fracture modelling of asphalt pavements with applications to design of high-performance asphalt overlays," *International Journal of Pavement Engineering*, vol. 19, no. 3, pp. 319–337, 2018. [Online]. Available: https://doi.org/10.1080/10298436.2017.1353393

[59] X. Li and M. Marasteanu, "The fracture process zone in asphalt mixture at low temperature." *Engineering Fracture Mechanics*, vol. 77 (7), p. 1175–1190, 2010. [Online]. Available: https://doi.org/10.1016/j.engfracmech.2010.02.018

[60] K. Yong-Rak, "Cohesive zone model to predict fracture in bituminous materials and asphaltic pavements: state-of-the-art review," *International Journal of Pavement Engineering*, vol. 12, no. 4, pp. 343–356, 2011. [Online]. Available: https://doi.org/10.1080/10298436.2011.575138

[61] A. R. C. Murthy, G. Palani, and N. R. Iyer, "State-of-the-art review on fracture analysis of concrete structural components," *Sadhana*, vol. 34, pp. 345–367, 2009. [Online]. Available: https://doi.org/10.1007/s12046-009-0014-0

[62] Z. Bazant and J. Planas, "Fracture and size effect in concrete and other quasibrittle materials." *Boca Raton, FL: CRC Press.*, 1998.

[63] D. Dugdale, "Yielding of steel sheets containing slits," *Mechanics and Physics of Solids*, vol. 8 (2), p. 100–104, 1960. [Online]. Available: https://doi.org/10.1016/0022-5096(60)90013-2

[64] G. Barenblatt, "The mathematical theory of equilibrium cracks in brittle fracture," *Advances in applied mechanics*, vol. 7 (1), p. 55–129, 1962. [Online]. Available: https://doi.org/10.1016/S0065-2156(08)70121-2

[65] H. Espinosa and P. Zavattieri, "A grain level model for the study of failure initiation and evolution in polycrystalline brittle materials. part i: theory and numerical implementation," *Mechanics of Materials*, vol. 35 (3–6), p. 333–364, 2003. [Online]. Available: https://doi.org/10.1016/S0167-6636(02)00285-5

[66] F. Soares, J. de Freitas and D. Allen, "Considering material heterogeneity in crack modeling of asphaltic mixtures." *Transportation Research Record: Journal of the Transportation Research Board*, p. 113–120, 1832. [Online]. Available: https://doi.org/10.3141/1832-14

[67] G. Paulino, S. Song, and W. Buttlar, "Cohesive zone modeling of fracture in asphalt concrete." *In: Proceedings of the 5th international RILEM conference-cracking in pavements: mitigation, risk assessment, and preservation, Limoges, France*, pp. 63–70, 2010.

[68] S. Song, G. Paulino, and W. Buttlar, "A bilinear cohesive zone model tailored for fracture of asphalt concrete considering viscoelastic bulk material," *Engineering Fracture Mechanics*, vol. 73, no. 18, p. 2829–2848, 2006a. [Online]. Available: https://doi.org/10.1016/j.engfracmech.2006.04.030

[69] E. V. Dave and W. G. Buttlar, "Low temperature cracking prediction with consideration of temperature dependent bulk and fracture properties," *Road Materials and Pavement Design*, vol. 11, no. sup1, pp. 33–59, 2010. [Online]. Available: https://doi.org/10.1080/14680629.2010.9690326

[70] T. M.G., B. Sluys, and E. Van der Giessen, "Numerical simulation of quasi-brittle fracture using damaging cohesive surfaces," *European Journal of Mechanics, A/Solids*, vol. 19(5), p. 761–779, 2000. [Online]. Available: https://doi.org/10.1016/S0997-7538(00)00190-X

[71] F. Zhou and J. Molinari, "Dynamic crack propagation with cohesive elements: a methodology to address mesh dependency," *International Journal for Numerical Methods in Engineering*, vol. 59(1), p. 1–24, 2004. [Online]. Available: https://doi.org/10.1002/nme.857

[72] L. Kachanov, "On rupture time under condition of creep (in russian)," *Izvestia Akademi Nauk SSSR, Otd. Tekhn. Nauk, No.8*, pp. 26–31, 1958.

[73] ——, "Creep problems in structural members," *North-Holland, Amsterdam*, 1969.

[74] M. Sumio, *Continuum Damage Mechanics A Continuum Mechanics Approach to the Analysis of Damage and Fracture*. Springer, 2012.

[75] J. Lemaitre and J. Chaboche, "Aspect phénoménologique de la rupture par endommagement," *Journal de Mécanique Appliquée*, vol. 2, p. 317–365, 1978.

[76] J. Milan, "Mathematical analysis of strain localization," *Revue europÃ©enne de gÃ©nie civil*, vol. 11, pp. (7–8), 2007. [Online]. Available: https://doi.org/10.1080/17747120.2007.9692973

[77] I. Stefanou and E. Gerolymatou, "Strain localization in geomaterials andregularization: rate-dependency, higher order continuum theories and multi-physics," *In J. Sulem, C. Viggiani (Eds.), ALERT Doctoral School 2019:The legacy of Ioannis Vardoulakis to Geomechanics. chapter 3.*, p. 47–85, 2019.

[78] Z. Bažant and B. Oh, "Crack band theory for fracture of concrete." *Mat. Constr.*, vol. 16, p. 155–177, 1983. [Online]. Available: https://doi.org/10.1007/BF02486267

[79] J. Červenka, V. Červenka, and S. Laserna, "On crack band model in finite element analysis of concrete fracture in engineering practice," *Engineering Fracture Mechanics*, vol. 197, pp. 27–47, 2018. [Online]. Available: https://doi.org/10.1016/j.engfracmech.2018.04.010

[80] Z. P. Bažant and G. Pijaudier-Cabot, "Nonlocal Continuum Damage, Localization Instability and Convergence," *Journal of Applied Mechanics*, vol. 55, no. 2, pp. 287–293, 1988. [Online]. Available: https://doi.org/10.1115/1.3173674

[81] A. Needleman, "Material rate dependence and mesh sensitivity in localization problems," *Computer methods in applied mechanics and engineering*, vol. 67, no. 1, pp. 69–85, 1988. [Online]. Available: https://doi.org/10.1016/0045-7825(88)90069-2

[82] R. de Borst and T. Duretz, "On viscoplastic regularisation of strain-softening rocks and soils," *International Journal for Numerical and Analytical Methods in Geomechanics*, vol. 44, no. 6, pp. 890–903, 2020. [Online]. Available: https://doi.org/10.1002/nag.3046

[83] A. Stathas and I. Stefanou, "The role of viscous regularization in dynamical problems, strain localization and mesh dependency," *Computer Methods in Applied Mechanics and Engineering*, vol. 388, p. 114185, 2022. [Online]. Available: https://doi.org/10.1016/j.cma.2021.114185

[84] Z. P. Bazant, "Crack band model for fracture of geomaterials." in *Unknown Host Publication Title*. AA Balkema, 1982, pp. 1137–1152.

[85] Z. P. Bažant and B. H. Oh, "Crack band theory for fracture of concrete," *Matériaux et construction*, vol. 16, pp. 155–177, 1983. [Online]. Available: https://doi.org/10.1007/BF02486267

[86] G. Pijaudier-Cabot and Z. P. Bažant, "Nonlocal damage theory," *Journal of engineering mechanics*, vol. 113, no. 10, pp. 1512–1533, 1987. [Online]. Available: https://doi.org/10.1061/(ASCE)0733-9399(1987)113:10(1512)

[87] E. Lorentz and S. Andrieux, "Analysis of non-local models through energetic formulations," *International Journal of Solids and Structures*, vol. 40, no. 12, pp. 2905–2936, 2003. [Online]. Available: https://doi.org/10.1016/S0020-7683(03)00110-0

[88] M. Jirásek, "Nonlocal damage mechanics," *Revue européenne de génie civil*, vol. 11, no. 7-8, pp. 993–1021, 2007. [Online]. Available: https://doi.org/10.1080/17747120.2007.9692974

[89] A. Simone, "Explicit and implicit gradient-enhanced damage models," *Revue européenne de génie civil*, vol. 11, no. 7-8, pp. 1023–1044, 2007. [Online]. Available: https://doi.org/10.1080/17747120.2007.9692975

[90] R. H. Peerlings, R. de Borst, W. M. Brekelmans, and J. de Vree, "Gradient enhanced damage for quasi-brittle materials," *International Journal for numerical methods in engineering*, vol. 39, no. 19, pp. 3391–3403, 1996. [Online]. Available: https://doi.org/10.1002/(SICI)1097-0207(19961015)39:19%3C3391::AID-NME7%3E3.0.CO;2-D

[91] H. Amor, J.-J. Marigo, and C. Maurini, "Regularized formulation of the variational brittle fracture with unilateral contact: Numerical experiments," *Journal of the Mechanics and Physics of Solids*, vol. 57, no. 8, pp. 1209–1229, 2009. [Online]. Available: https://doi.org/10.1016/j.jmps.2009.04.011

[92] C. Kuhn and R. Müller, "A continuum phase field model for fracture," *Engineering Fracture Mechanics*, vol. 77, no. 18, pp. 3625–3634, 2010. [Online]. Available: https://doi.org/10.1016/j.engfracmech.2010.08.009

[93] C. Miehe, M. Hofacker, and F. Welschinger, "A phase field model for rate-independent crack propagation: Robust algorithmic implementation based on operator splits," *Computer Methods in Applied Mechanics and Engineering*, vol. 199, no. 45-48, pp. 2765–2778, 2010. [Online]. Available: https://doi.org/10.1016/j.cma.2010.04.011

[94] C. Miehe, F. Welschinger, and M. Hofacker, "Thermodynamically consistent phase-field models of fracture: Variational principles and multi-field fe implementations," *International journal for numerical methods in engineering*, vol. 83, no. 10, pp. 1273–1311, 2010. [Online]. Available: https://doi.org/10.1002/nme.2861

[95] F. Dammaß, M. Ambati, and M. Kästner, "A unified phase-field model of fracture in viscoelastic materials," *Continuum Mechanics and Thermodynamics*, vol. 33, no. 4, pp. 1907–1929, 2021. [Online]. Available: https://doi.org/10.1007/s00161-021-01013-3

[96] B. Yin, J. Storm, and M. Kaliske, "Viscoelastic phase-field fracture using the framework of representative crack elements," *International Journal of Fracture*, vol. 237, no. 1-2, pp. 139–163, 2022. [Online]. Available: https://doi.org/10.1007/s10704-021-00522-1

[97] R. Shen, H. Waisman, and L. Guo, "Fracture of viscoelastic solids modeled with a modified phase field method," *Computer Methods in Applied Mechanics and Engineering*, vol. 346, pp. 862–890, 2019. [Online]. Available: https://doi.org/10.1016/j.cma.2018.09.018

[98] N. Moës, C. Stolz, P.-E. Bernard, and N. Chevaugeon, "A level set based model for damage growth: the thick level set approach," *International Journal for Numerical Methods in Engineering*, vol. 86, no. 3, pp. 358–380, 2011. [Online]. Available: https://doi.org/10.1002/nme.3069

[99] I. Stefanou and E. Gerolymatou, "Strain localization in geomaterials and regularization: rate-dependency, higher order continuum theories and multi-physics," p. 41.

[100] B. Shiferaw, O. Chupin, J.-M. Piau, and N. Moës, "Development of a damage viscoelastic model using the thick level set approach to fracture: 1d modeling and comparison to uniaxial tension stress tests on bituminous specimens," *Engineering Fracture Mechanics*, vol. 257, p. 108026, 2021. [Online]. Available: https://doi.org/10.1016/j.engfracmech.2021.108026

[101] N. Moës and N. Chevaugeon, "Lipschitz regularization for softening material models: the lip-field approach," *Comptes Rendus. Mécanique*, vol. 349, no. 2, pp. 415–434, 2021. [Online]. Available: https://doi.org/10.5802/crmeca.91

[102] N. Chevaugeon and N. Moës, "Lipschitz regularization for fracture: The lip-field approach," *Computer Methods in Applied Mechanics and Engineering*, vol. 402, p. 115644, 2022. [Online]. Available: https://doi.org/10.1016/j.cma.2022.115644

[103] N. Moës, B. Lé, and A. Stershic, "Fragmentation analysis of a bar with the lip-field approach," *Mechanics of Materials*, vol. 172, p. 104365, 2022. [Online]. Available: https://doi.org/10.1016/j.mechmat.2022.104365

[104] J. Lemaitre and J.-L. Chaboche, *Mechanics of solid materials*. Cambridge University Press, 1990.

[105] P. Germain, *Cours de mécanique des milieux continus. 1. Théorie générale*. Masson, 1973.

[106] B. Halphen and Q. S. Nguyen, "Sur les matériaux standard généralisés," *Journal de mécanique*, vol. 14, no. 1, pp. 39–63, 1975.

[107] P. Germain, P. Suquet, and Q. S. Nguyen, "Continuum thermodynamics," *ASME Journal of Applied Mechanics*, vol. 50, pp. 1010–1020, 1983.

[108] N. Lahellec and P. Suquet, "On the effective behavior of nonlinear inelastic composites: I. incremental variational principles," *Journal of the Mechanics and Physics of Solids*, vol. 55, no. 9, pp. 1932–1963, 2007. [Online]. Available: https://doi.org/10.1016/j.jmps.2007.02.003

[109] M. Ortiz and L. Stainier, "The variational formulation of viscoplastic constitutive updates," *Computer methods in applied mechanics and engineering*, vol. 171, no. 3-4, pp. 419–444, 1999. [Online]. Available: https://doi.org/10.1016/S0045-7825(98)00219-9

[110] E. Fancello, J.-P. Ponthot, and L. Stainier, "A variational formulation of constitutive models and updates in non-linear finite viscoelasticity," *International Journal for Numerical Methods in Engineering*, vol. 65, no. 11, pp. 1831–1864, 2006. [Online]. Available: https://doi.org/10.1002/nme.1525

[111] R. Radovitzky and M. Ortiz, "Error estimation and adaptive meshing in strongly nonlinear dynamic problems," *Computer Methods in Applied Mechanics and Engineering*, vol. 172, no. 1-4, pp. 203–240, 1999. [Online]. Available: https://doi.org/10.1016/S0045-7825(98)00230-8

[112] A. A. L. Baldelli and C. Maurini, "Numerical bifurcation and stability analysis of variational gradient-damage models for phase-field fracture," *Journal of the Mechanics and Physics of Solids*, vol. 152, p. 104424, 2021. [Online]. Available: https://doi.org/10.1016/j.jmps.2021.104424

[113] P. Virtanen, R. Gommers, T. E. Oliphant, M. Haberland, T. Reddy, D. Cournapeau, E. Burovski, P. Peterson, W. Weckesser, J. Bright *et al.*, "Scipy 1.0: fundamental algorithms for scientific computing in python," *Nature methods*, vol. 17, no. 3, pp. 261–272, 2020.

[114] J. Sulem, I. Stefanou, E. Papamichos, and M. Veveakis, "Modelling of instabilities and bifurcation in geomechanics," p. 302.

[115] R. Borst and T. Duretz, "On viscoplastic regularisation of strain-softening rocks and soils," vol. 44, no. 6, pp. 890–903. [Online]. Available: https://onlinelibrary.wiley.com/doi/10.1002/nag.3046

[116] A. Meurer, C. P. Smith, M. Paprocki, O. Čertík, S. B. Kirpichev, M. Rocklin, A. Kumar, S. Ivanov, J. K. Moore, S. Singh *et al.*, "Sympy: symbolic computing in python," *PeerJ Computer Science*, vol. 3, p. e103, 2017.

[117] R. Gopalsamy, N. Chevaugeon, O. Chupin, and F. Hammoum, "Variational approach to viscoelastic fracture: comparison of a phase-field and a lip-field approach." [Online]. Available: https://doi.org/10.1007/s10704-023-00725-8

[118] R. Gopalsamy, N. Chevaugeon, O. Chupin, J.-M. Piau, and F. Hammoum, "Lip-field approach for modeling fracture in viscoelastic materials," in *25ème Congrès Français de Mécanique (CFM 2022)*, Nantes, 2022.

[119] R. Gopalsamy, N. Chevaugeon, O. Chupin, and F. Hammoum, "Fracture in viscoelasticity: Comparison of a phase-field and a lip-field approach," in *The Seventh International Conference on Computational Modeling of Fracture and Failure of Materials and Structures (CFRAC 2023)*, Prague, 2023.

[120] C. Geuzaine and J.-F. Remacle, "Gmsh: A 3-d finite element mesh generator with built-in pre-and post-processing facilities," *International journal for numerical methods in engineering*, vol. 79, no. 11, pp. 1309–1331, 2009.

[121] K. Pham, H. Amor, J.-J. Marigo, and C. Maurini, "Gradient damage models and their use to approximate brittle fracture," *International Journal of Damage Mechanics*, vol. 20, no. 4, pp. 618–652, 2011. [Online]. Available: https://doi.org/10.1177/1056789510386852

[122] G. Molnár, A. Doitrand, A. Jaccon, B. Prabel, and A. Gravouil, "Thermodynamically consistent linear-gradient damage model in abaqus," *Engineering Fracture Mechanics*, vol. 266, p. 108390, 2022. [Online]. Available: https://doi.org/10.1016/j.engfracmech.2022.108390

[123] J. R. Shewchuk, "Triangle: Engineering a 2d quality mesh generator and delaunay triangulator," in *Workshop on applied computational geometry*. Springer, 1996, pp. 203–222.

[124] M. S. Andersen, J. Dahl, L. Vandenberghe *et al.*, "Cvxopt: A python package for convex optimization," *Available at cvxopt. org*, vol. 54, 2013.

[125] F. Johansson, V. Steinberg, S. B. Kirpichev, K. L. Kuhlman, A. Meurer, O. Čertík, C. Van Horsen, P. Masson, J. Arias de Reyna, T. Hartmann *et al.*, "mpmath: a python library for arbitrary-precision floating-point arithmetic," *Zenodo*, 2013.

[126] J. Ahrens, B. Geveci, and C. Law, "ParaView: An end-user tool for large data visualization," in *Visualization Handbook*. Elesvier, 2005, ISBN 978-0123875822.

[127] M. Geers, R. De Borst, W. Brekelmans, and R. Peerlings, "Strain-based transient-gradient damage model for failure analyses," *Computer methods in applied mechanics and engineering*, vol. 160, no. 1-2, pp. 133–153, 1998. [Online]. Available: https://doi.org/10.1016/S0045-7825(98)80011-X

[128] Q. Yang, L. Stainier, and M. Ortiz, "A variational formulation of the coupled thermo-mechanical boundary-value problem for general dissipative solids," *Journal of the Mechanics and Physics of Solids*, vol. 54, no. 2, pp. 401–424, 2006. [Online]. Available: https://doi.org/10.1016/j.jmps.2005.08.010

[129] F. Brauer and J. A. Nohel, "The qualitative theory of ordinary differential equations," w. a. benjamin, inc., new york, 1969."

[130] S. Strogatz, "Nonlinear dynamics and chaos: With application to physics, biology, chemistry and engineering. perseus books publishing, cambridge, 1994."

[131] G. Lancioni and G. Royer-Carfagni, "The variational approach to fracture mechanics. a practical application to the french panthéon in paris," *Journal of elasticity*, vol. 95, pp. 1–30, 2009. [Online]. Available: https://doi.org/10.1007/s10659-009-9189-1

List of publications

[1] R. Gopalsamy, N. Chevaugeon, O. Chupin, and F. Hammoum, "Variational approach to viscoelastic fracture: comparison of a phase-field and a lip-field approach," *International Journal of Fracture*. [Online]. Available: https://doi.org/10.1007/s10704-023-00725-8

[2] R. Gopalsamy, N. Chevaugeon, O. Chupin, J.-M. Piau, and F. Hammoum, "Lip-field approach for modeling fracture in viscoelastic materials," in *25ème Congrès Français de Mécanique (CFM 2022)*, Nantes, 2022.

[3] R. Gopalsamy, N. Chevaugeon, O. Chupin, and F. Hammoum, "Fracture in viscoelasticity: Comparison of a phase-field and a lip-field approach," in *The Seventh International Conference on Computational Modeling of Fracture and Failure of Materials and Structures (CFRAC 2023)*, Prague, 2023.

Titre : Approche variationnelle pour modéliser la rupture dans des matériaux viscoélastiques de type bitumineux

Mots clés : Endommagement, Viscoélasticité, Lip-field, Matériaux bitumineux, Approche variationnelle

Résumé : La détérioration des chaussées due à la fissuration des couches de matériaux bitumineux représente un défi majeur, nécessitant une compréhension plus approfondie des mécanismes et des facteurs associés. Aborder cette problématique implique le développement de modèles théoriques dédiés et leur implémentation dans des outils numériques. Les matériaux bitumineux sont largement reconnus pour leurs caractéristiques viscoélastiques. Dans ce contexte, la présente thèse se concentre sur la fissuration des matériaux viscoélastiques dans un cadre quasi-statique. Une nouvelle approche variationnelle thermodynamiquement cohérente est introduite pour modéliser l'endommagement dans les solides viscoélastiques. Cette approche permet l'intégration des équations constitutives locales dans un potentiel global incrémental, dont la minimisation conduit à la résolution du problème mécanique. Afin de surmonter les problèmes de dépendance au maillage associés aux modèles d'endommagement adoucissants, l'approche du lip-field a été utilisée pour régulariser le problème. Une mise en œuvre numérique dans des codes à éléments finis (FE) basés sur Python est présentée pour des scénarios à une dimension (1D) et à deux dimensions (2D). Les résultats de simulation pour le cas en 2D démontrent la capacité du modèle à reproduire les courbes force-déplacement expérimentales (pour la rupture en mode I) et à prédire les trajectoires de fissuration (pour la rupture en mode mixte). Ce travail fournit non seulement une base théorique et numérique solide pour d'éventuelles applications futures en mécanique des chaussées, mais étend également sa pertinence au-delà des matériaux bitumineux. La méthodologie développée ici peut être efficacement utilisée pour modéliser la fissuration dans divers matériaux viscoélastiques.

Title : Variational approach to model fracture in viscoelastic materials of bituminous type

Keywords : Damage, Viscoelasticity, Lip-field approach, Bituminous materials, Variational approach

Abstract : The deterioration of pavement due to the fracturing of layers made of bituminous materials is a significant challenge, necessitating a deeper understanding of the associated mechanisms and factors. Addressing this issue involves the development of essential theoretical models and numerical tools. Bituminous materials are widely acknowledged for their viscoelastic characteristics. In this context, the present thesis focuses on the cracking of viscoelastic materials in a quasi-static setting. A novel, thermodynamically consistent variational approach is introduced to model damage within viscoelastic solids. This approach enables the integration of local constitutive equations into a global incremental potential, the minimization of which yields the solution to the mechanical problem. To overcome the spurious mesh-dependent results associated with softening damage models, the lip-field approach has been used to regularize the problem. A detailed numerical implementation for both one-dimensional (1D) and two-dimensional (2D) scenarios is presented, complemented by Python-based finite element (FE) codes. The simulation results for the 2D case show the ability of the model to fit experimental force-displacement curves (for mode-I fracture) and to predict the crack paths (for mixed mode fracture). This work not only provides a robust theoretical and numerical foundation for potential future applications in pavement mechanics but also extends its relevance beyond bituminous materials. The methodology developed here can be applied effectively to model cracking in various viscoelastic materials.